Quantum Spin Systems and Magnetic Frustration Investigated with High Frequency AC Susceptibility and Muons

A thesis submitted in partial fulfilment of the requirements for the degree of

Doctor of Philosophy

by

Edward Arthur Joseph Riordan

October 2020

Abstract

An ac susceptometer is described that can measure up to 3.5 MHz at temperatures ≥ 2 K and in dc magnetic fields up to 1 T by integration with a Quantum Design PPMS. The susceptometer is described with a detailed explanation of the calibration procedure. ac susceptibility data on MgB_2 and $Dy_2Ti_2O_7$ measured by the high frequency susceptometer is presented and compared with data recorded using a commercial susceptometer which shows good agreement. FeraSpin XS magnetic nano particles are measured and the ac susceptibility is used to determine the mean particle radius, which shows good agreement with the literature.

The quantum tunnelling plateau is measured in powder $CdEr_2Se_4$ and $CdEr_2S_4$ using the high frequency susceptometer. ac susceptibility measurements in dc magnetic fields reveal field induced coexisting relaxation mechanisms, a thermally activated and a quantum process. $CdEr_2Se_4$ is measured at down to 70 mK and the two mechanisms are shown to persist to the spin freezing temperature which is also measured. Single crystal samples of $CdEr_2Se_4$ do not show any sign of the field induced relaxation mechanism at any temperature or field. The single crystal spin freezing temperature is found to be lower than in the powder. A muon spin rotation experiment in powder $CdEr_2Se_4$ finds that the spin fluctuation rates are orders of magnitude faster than those seen with ac susceptibility.

Muon spin rotation experiments in PVDF and $LiY_{0.95}Ho_{0.05}F_4$ are performed where the F-μ and F-μ-F quantum states form respectively. Measurements are performed in zero field and in the presence of an RF photon field. Multiple

approaches to fitting the zero field data are discussed, including by considering the state as an open quantum system. A close fit is achieved in $LiY_{0.95}Ho_{0.05}F_4$ but not in PVDF which is attributed to difficulty in accounting for amorphous regions. The application of the RF field is shown to alter the measured muon asymmetry. It is shown that the effect of the RF field cannot be accounted by a rotating magnetic field and therefore the RF field must be manipulating the occupation probabilities of the state.

Acknowledgements

Firstly I would like to thank my supervisor Sean Giblin for his excellent supervision. In particular I would like to thank him for his patience, expertise and willingness to discuss/argue physics at almost any time. Additionally I'd like to thank Dave and the other PhD students in my group for many helpful discussions and practical assistance. Thank you to the guys in the electronics workshop for helping maintain the HF and to the diamond group for my use of the PPMS. I'd also like to thank all my friends who have supported me throughout my time in Cardiff from the people I met as an undergraduate to those I met during my PhD. A big thank you to Gemma for her invaluable help and english skills as well as to my fellow patrons of the Green Dandelion for helping to keep me sane whilst writing up under lock down. Finally I'd like to extend a big thank you to my family for reasons too inumerable to mention.

Publications

- Gao, S., Zaharko, O., Tsurkan, V., Prodan, L., Riordan, E., Lago, J., Fåk, B., Wildes, A.R., Koza, M.M., Ritter, C. and Fouquet, P., 2018. Dipolar Spin Ice States with a Fast Monopole Hopping Rate in CdEr 2 X 4 (X= Se, S). Physical review letters, 120(13), p.137201.

- Riordan, E., Blomgren, J., Jonasson, C., Ahrentorp, F., Johansson, C., Margineda, D., Elfassi, A., Michel, S., Dell'ova, F., Klemencic, G.M. and Giblin, S.R., 2019. Design and implementation of a low temperature, inductance based high frequency alternating current susceptometer. Review of Scientific Instruments, 90(7), p.073908.

- Chen, H., Billington, D., Riordan, E., Blomgren, J., Giblin, S.R., Johansson, C. and Majetich, S.A., 2020. Tuning the dynamics in Fe3O4 nanoparticles for hyperthermia optimization. Applied Physics Letters, 117(7), p.073702.

Contents

List of Figures

List of Tables

Chapter 1

Introduction

This thesis focuses primary on two experimental techniques: ac susceptibility and muon spin rotation. They are applied in the study of magnetic spin systems where the true understanding of the resulting data lies in a microscopic description. Measurements will be discussed across a wide range of temperatures and magnetic fields in both the classical and quantum limits. Typified by the microscopic emergent properties of spin ice and quantum to thermal cross overs in spin flip time scales. Or the explicitly quantum treatment required to understand the entanglement of individual particles during muon spin rotation experiments in fluorinated materials. An outline of the remaining chapters of this thesis is as follows:

- In the first part of the second chapter there is an introduction to magnetism and a brief explanation of the origin of magnetism in simple materials. Following this is an introduction to spin ice materials and an explanation of the properties that has made them the subject of scientific interest. Namely, the finite residual entropy at 0 K and "magnetic monopole" excitations. Lastly an explanation of the muon spin rotation technique is given. Cover-

ing the core principles of an experiment and some models commonly used in the analysis of experimental data.

- The third chapter details the development of an ac susceptometer capable of measuring up to MHz frequencies with a temperature and field range previously difficult to measure at. Initially there is an explanation of the ac susceptibility technique including a discussion of different techniques, conventions and the principles of operation in the induction technique which is the one used in the aforementioned susceptometer. The design considerations required to measure at high frequency are discussed as well as how they were overcome. Finally some test measurements are presented to demonstrate good functionality.

- The fourth chapter is concerned with ac susceptibility measurements in dipolar spin ice materials: $CdEr_2S_4$ and $CdEr_2Se_4$. There is an introduction to the materials with a brief discussion of the existing literature. ac susceptibility measurements in zero field are used to measure the temperature independent plateau. Then ac susceptibility measurements in an applied magnetic field are presented which demonstrate some unexpected behaviour. This behaviour is characterised using ac susceptibility across a range of temperatures and fields in both powder and single crystal samples. A muon spin rotation experiment in $CdEr_2Se_4$ in zero and longitudinally applied magnetic fields is also performed and discussed.

- The fifth chapter focuses on an entangled quantum state that can occur in muon spin rotation experiments between the muon and Fluorine nuclei. It focuses primarily on attempts to accurately fit to experimental data using multiple approaches to modelling the decay of the state. It also covers two

experiments in which an RF coil was used to excite the systems between energy levels, in an attempt to manipulate the state populations of the system.

Chapter 2

Background Theory

2.1 Magnetism

Semi-classically, magnetic fields are produced by two main mechanisms[1]. Firstly they emerge any time you have a movement of charged particles. Perhaps the most well known instance of this is the movement of charges when a current is present in a wire, in which case a circular magnetic field is produced around the wire. In the case that this wire is a small loop connected at both ends, then the loop produces a magnetic dipole the strength of which is proportional to the current and the area of the loop. This dipole is known as the magnetic dipole moment of the loop. This is true even for a single charged particle moving in a loop, all that is required is that the charged particle has some momentum[1].

All particles that make up every day matter have an intrinsic magnetic moment associated with them. This magnetic moment does not come from motion of the particle but is instead an intrinsic property, indicative of an intrinsic angular momentum[1]. The magnetic dipole moment is given by

$$\vec{\mu} = g\frac{q}{2m}\vec{S} \tag{2.1}$$

where $\vec{\mu}$ is the particle magnetic moment, g is the g-factor which is a dimensionless constant, q is the particle charge, m is the particle mass and $\vec{S}$ is the particle's spin angular momentum. The particle angular momentum is related to the spin quantum number[1] s by $|\vec{S}| = \hbar\sqrt{s(s+1)}$, where $\hbar$ is the reduced Planck's constant. The spin quantum number is the number being referred to when a particle is described as having a certain spin value, for instance a spin-1/2 particle has s=1/2.

Spin is the fundamental property of the particle that gives it its magnetic moment. It is so named because it was once thought the moment was produced by the particles spinning about their axes[1]. The spin of a particle is indicative of it having some angular momentum however it is now known that particles such as electrons are point particles and so such rotations are not well defined. Spin is the second mechanism by which magnetic fields are produced.

2.2 Magnetic Materials

Magnetic materials get their properties from the magnetic properties of the atoms within them, typically from the electrons around the atoms although the nuclei can also be magnetic. The magnetic properties of an atom's electrons are produced by both of the aforementioned mechanisms, with contributions from the electron spin and from the electron orbital angular momentum, $\vec{L}$, where $|\vec{L}| = \hbar\sqrt{l(l+1)}$. The electron orbital angular momentum comes from the orbitals that the electrons occupy, with the l quantum number indicating the occupied electron shell: $l = 0$ for s-shell, $l = 1$ for p-shell etc[1].

The total angular momentum of the atom, $\vec{J}$ is given by $\vec{J} = \vec{L} + \vec{S}$. The atoms total dipole moment is given by

$$\vec{\mu} = g_J \mu_B \vec{J} \tag{2.2}$$

where g_J is the Landé g-factor and μ_B is the Bohr magneton which is a constant derived from the magnetic moment of an electron. Similarly to before $|\vec{J}| = \sqrt{j(j+1)}$, where j is the total angular momentum quantum number. In an atom with multiple electrons $\vec{L}$ and $\vec{S}$ will generally be determined by Hund's rules (explained in the following section), assuming the atom is in the ground state[1].

2.3 Hund's Rules

Hund's rules are used to determine the ground state of an atom with multiple electrons[2]. When determining the electron configuration with the lowest energy (the ground state) first one fills all of the electron orbitals in order of their energy until a point is reached at which there are not enough electrons to fill the next shell. Hund's rules are then used to determine the electron configuration in that shell and are as follows.

The first rule is that the electron orbitals in an electron shell should be filled such that the total spin, S, is maximised. Intuitively this can be understood as using as many orbitals in the shell as possible, filling each one with one electron first before adding to each orbital a degenerate electron with their spins in the opposite alignment. This minimises the Coulomb repulsion between them.

The second rule is that the total angular momentum, L, should be maximised. This allows the electrons to stay farther apart from one another, reducing the

energy cost associated with the electrostatic repulsion between them.

For the third rule the lowest energy state is dependent on whether the electron shell is more or less than half full. If it is more than half full then the lowest energy state is given by $J = |L + S|$, if it is less than half full the lowest energy state is given by $J = |L - S|$. The physical origin for this is less clear but is the result of the spin-orbit interactions and is only really relevant for larger atoms.

As an example of Hund's rules in action we will consider the Pr^{3+} ion. Praseodymium has an atomic number of 59 and so for Pr^{3+} there are 56 electrons to place[2]. Filling all the electron shells in terms of energy first we find that all the shells up to and including the 5p shell are filled. Leaving 2 electrons to go into the 4f shell.

Firstly we arrange the electrons such that S is maximised, which is achieved by arranging the electrons with S=1. This can be done by putting each electron in its own orbital, the 4f shell has 7 available orbitals (for a possible maximum of 14 electrons) so there is no need to doubly occupy them. Secondly L is maximised, the f orbital has $l = 3$ with $2l + 1$ possible states allowed which are indicated by the quantum numbers $m_l = -l, -l + 1, ..., l - 1, l$. To maximise L the first electron will take $m_l = 3$ and the second $m_l = 2$ to give $L = 5$. Lastly because the shell is less than half full the total angular momentum J is given by $|L - S|$ and so $J = 4$ for Pr^{3+} in the ground state.

In some cases (such as in the spin ice materials discussed later) the crystal electric field (CEF) can change the lowest energy configuration of $\vec{L}$ and $\vec{S}$ such that Hund's rules do not lead to the ground state[3]. The CEF is the static electric field from the charge distribution in the crystal and is considered as a continuous position dependent field. It describes the electrostatic interaction between an ion and its environment.

2.4 Susceptibility and Ordering

The magnetisation, $\vec{M}$, is a measure of the total magnetic moment of a sample from all of its constituent magnetic ions, normalised by the sample volume (or occasionally mass)[1]. If the spins are unpolarised they will cancel out over the full sample and in which case $\vec{M} = 0$, this is the case in a paramagnetic material that is not in the presence of any magnetising magnetic fields, $\vec{H}$. If a magnetic field is applied to a paramagnetic material it will tend to align the spins along its axis such that $\vec{M}$ becomes non-zero. In small magnetic fields the relationship between $\vec{M}$ and $\vec{H}$ is often linear and related by a constant of proportionality called the magnetic susceptibility, χ. If $\chi > 0$ then the sample is said to be paramagnetic. For an ideal paramagnetic material the relationship between $\vec{M}$ and $\vec{H}$ will be governed by the Brillouin function [1], which is also a function of temperature and j of the magnetic ions.

For some materials, $\chi < 0$ and the application of a magnetic field causes the spins to align in opposition to the magnetic field. Diamagnetism is a quantum mechanical effect that is present in all materials.

In some materials the spins can experience long range order and be aligned ($\vec{M} > 0$) without an applied magnetic field. These materials are called ferromagnets (or occasionally permanent magnets). The magnetisation can be the result of an applied magnetic field that has since been removed, or the result of spontaneous alignment if the sample is cooler than its Curie temperature. These materials exhibit hysteresis between $\vec{M}$ and $\vec{H}$ so χ is not well defined.

Long range order can also be realised in materials for which $\vec{M} = 0$. This can occur when the spins align antiparallel to their neighbours in a repeating pattern. This phenomenon is called antiferromagnetism and can occur spontaneously when

the sample is cooled below its Néel temperature. Similar to antiferromagnetism is ferrimagnetism in which not all the magnetic moments have the same amplitude and so $\vec{M}$ can be non-zero.

2.5 Superparamagnetism

Superparamagnetism is a phenomenon that can occur in particulate samples made from ferromagnetic or ferrimagnetic materials[2]. It can occur when the particle size is small enough for the whole particle to be composed of a single magnetic domain, typically particle sizes of the order of 10 nm or less are required depending on the material in question. In the absence of a magnetic field the net magnetisation of the sample is 0 (despite the moments being ordered) because the particle magnetisations are all in random alignments. However the application of a magnetic field will cause a net magnetisation in the direction of the field as if the sample were paramagnetic. The iron oxide nanoparticles briefly discussed toward the end of the following chapter are an example of this.

2.6 Curie-Weiss Law

At temperatures well above any magnetic transition the magnetic susceptibility of a material with localised magnetic moments will typically obey a simple Curie-Weiss law which is given by

$$\chi = \frac{C}{T - \Theta_{CW}} \tag{2.3}$$

where, C is the Curie constant and Θ_{CW} is the temperature at which the material is expected to undergo a transition. If Θ_{CW} is positive then the material is

expected to undergo a transition to a ferromagnetic sate, in this case Θ_{CW} is typically referred to as the Curie temperature, T_C. If Θ_{CW} is negative then the material will undergo a transition to an antiferromagnetic state, in which case Θ_{CW} is known as the Néel temperature, T_N.

2.7 μ_{eff}, μ_{FI} and μ_{sat}

Often the purpose of measuring $\vec{M}$ is to determine information about the individual magnetic moments in the sample, such as their magnitude and any anisotropies. In this case $\vec{M}$ is often presented as the magnetic moment per ion, for which there are three related values of interest μ_{eff}, μ_{FI} and μ_{sat}.

μ_{eff} is the effective magnetic moment of an ion. It is often used in cases where the measured magnetic moment of an ion is not the same as the actual magnetic moment of an ion (it can also be used in cases where it is not known whether the measured moment is the same as the actual moment). This can happen because of a number of reasons, as an example it can occur if magnetic anisotropy in the material prevents the moments from orienting in the measurement direction. If the magnetic moments were able to freely align with the field then their measured moment may be different, this moment is known as the free ion moment μ_{FI}.

If the moments in the material are able to freely align with the magnetic field then μ_{FI} will be the same as the saturated moment, μ_{sat}, which is the moment per ion when the sample has been magnetically saturated. Magnetic saturation in this case meaning that the sample magnetisation has reached its maximum value, and further increasing the applied magnetic field yields no increase in the magnetisation.

2.8 Ac Susceptibility

In an ac susceptibility measurement a magnetic field, $H(t)$, oscillating sinusoidally at a frequency, f, is applied to the sample under investigation and its dynamic magnetisation, $M(t)$, is measured[4, 5, 6]. This allows for a frequency dependent measurement of the susceptibility that can provide information about dynamic magnetic processes within the sample. The ac susceptibility can be represented as a complex quantity: $\chi_{ac}(\omega) = \chi'(\omega) - i\chi''(\omega)$, where $\omega = 2\pi f$. $\chi'(\omega)$ is referred to as the real part or the in phase component and is in phase with the excitation field. $\chi''(\omega)$ is referred to as the imaginary part or the out of phase component and is 90 degrees out of phase with the excitation field. The negative sign is a convention. For the remainder of this chapter $\chi'(\omega)$ and $\chi''(\omega)$ will be written without the brackets as a shorthand.

Calculating the amplitude of the ac susceptibility at a given frequency can be done by dividing the amplitude of the oscillating sample magnetisation by the amplitude of the oscillating magnetic field. If the amplitude of the oscillating field is small and the frequency is slow compared to any intrinsic relaxation mechanisms in the sample then $\chi_{ac} = dM/dH$, where dM is the amplitude of the magnetisation, dH is the amplitude of the oscillating magnetic field and dM/dH is the gradient of the $M(H)$ curve. For this relationship to be true it is assumed that the sample magnetisation responds linearly to the excitation field. Whether the response is linear or not will depend on how rapidly the gradient of the $M(H)$ curve is changing and the magnitude of dH. Ensuring that dH is small enough to stay within the linear region is important to maintaining accurate results.

Another important concept that underpins ac susceptibility is the fluctuation-dissipation theorem. The fluctuation-dissipation theorem is that if the system

under investigation is in equilibrium with a small field then any response to that field could also occur due to random intrinsic processes [7].

Most magnetic materials will have some internal magnetic dynamics that occurs on some typical time scale, τ, which is often referred to as the relaxation time. When performing an ac susceptibility measurement at frequencies that are small compared to the inverse of the relaxation time ($\omega << 1/\tau$) then the system under investigation can respond in phase with the excitation field and so $\chi'' = 0$. This purely real susceptibility is often referred to as the isothermal susceptibility, χ_T, which is defined as $\chi'(\omega \to 0)$ and provides information about the gradient of the $M(H)$ curve at the current applied DC field and temperature. In simple paramagnetic materials this relaxation time is often very short and so χ_T can be measured up to very high frequencies (often beyond the upper frequency range of the instrument).

If the current measurement frequency is comparable to $1/\tau$, then the real time response of the system will begin to lag behind the excitation field. This is the reason for the $\chi' - i\chi''$ convention and is required so that the value of χ'' is positive as illustrated in figure 2.1. In this regime χ'' will be non-zero and χ' will gradually roll off with increasing frequency. χ'' will have a peak centred on a frequency corresponding to $1/\tau$ and any asymmetry or broadening of this peak provides information about the distribution of internal relaxation times if one is present [8, 9, 10, 11].

At $\omega >> 1/\tau$ then χ'' is 0 and χ' will now be a quantity known as the adiabatic susceptibility, χ_s, which is measured as $\chi'(\omega \to \infty)$. The adiabatic susceptibility is a thermodynamic property and represents the spin-spin response to the excitation field, and contains no spin-lattice or thermal contributions.

Ac susceptibility has many uses in the field of condensed matter research. It

can be used for thermometry [12] where the known temperature evolution of a sample is used to determine environment temperature or superconductivity [13] where it can provide information about the critical temperature, geometry and penetration depth. Example applications in magnetism include the study of spin glasses [14], magnetic nanoparticles[15] and magnetic phase transitions[16].

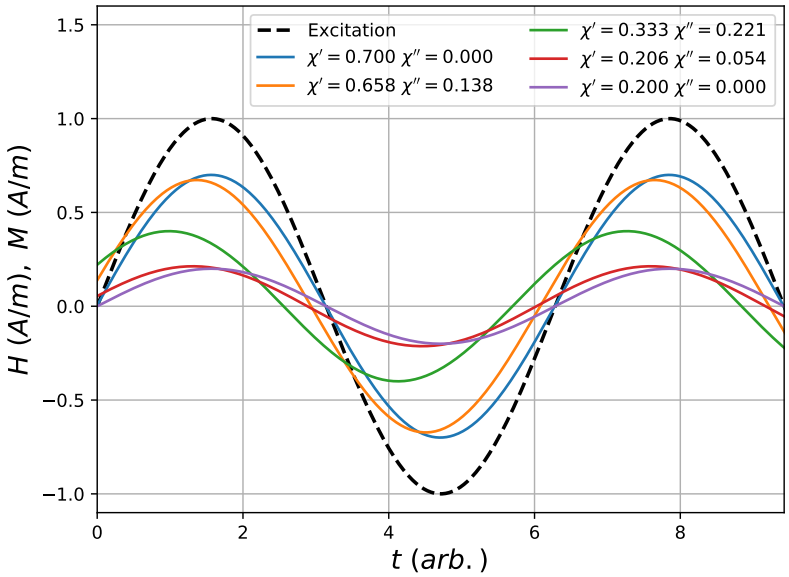

Figure 2.1: *Real time response of a magnetic material to an ac excitation field for typical values of* χ' *and* χ'' *with* χ_T*=0.7 and* χ_s*=0.2 using the convention* $\chi = \chi' - i\chi''$

2.9 The Debye, Cole-Cole, Cole-Davidson & Havriliak-Negami Equations

In an ac susceptibility measurement it is often useful to fit to the experimental data in order to determine the parameters of the system such as χ_s or τ. For instance χ_s maybe of interest because it is representative of some thermodynamic properties[17]. Some typical models for doing so are discussed here.

If the sample exhibits only a single well defined relaxation time then the ac susceptibility can be modelled by the Debye equation which is given by

$$\chi' - \chi'' = \chi_s + \frac{\chi_T - \chi_s}{1 + i\omega\tau}. \tag{2.4}$$

If there is not a single well defined relaxation time but instead a distribution of them, the shape of the response will be slightly different. One model for such a scenario is given by the Cole-Cole model where the ac susceptibility response is modified by the introduction of a parameter α

$$\chi' - \chi'' = \chi_s + \frac{\chi_T - \chi_s}{1 + (i\omega\tau)^{(1-\alpha)}}. \tag{2.5}$$

The effect of α is to broaden the peak in the imaginary part and it can take values between 0 and 1. If α=0 then there is no distribution in relaxation times and equation 2.5 reduces to Debye relaxation.

The Cole-Cole model assumes a distribution of relaxation times that is symmetric on a logarithmic scale however this is not necessarily the case. An asymmetric distribution of relaxation times can be modelled using the Cole-Davidson model which instead introduces a parameter β

$$\chi' - \chi'' = \chi_s + \frac{\chi_T - \chi_s}{(1 + i\omega\tau)^{\beta}}. \tag{2.6}$$

β has the effect of skewing the imaginary part of the ac susceptibility can take values between 0 and 1. For β=1 it again reduces to Debye relaxation.

Finally a more general equation exists that encompasses both cases and is known as the Havriliak-Negami equation

$$\chi' - \chi'' = \chi_s + \frac{\chi_T - \chi_s}{\left(1 + (i\omega\tau)^{(1-\alpha)}\right)^{\beta}}. \tag{2.7}$$

2.10 Relaxation Processes

The magnetic relaxation processes represented by τ can be the result of many different mechanisms. Often some information about those mechanisms may be gleaned by determining the temperature dependence. If there is temperature dependence then it is likely that the relaxation is thermally activated, thermally activated meaning that the energy for the response is obtained from the thermal energy of the system. In this thesis two models for thermally activated processes are employed as part of the analysis.

The first model is the Arrhenius law which is a general model for a thermally activated process and is not based on a specific feature or behaviour of the system under investigation. The temperature evolution of an Arrhenius law is given by

$$\tau = \tau_0 e^{\frac{E_a}{k_B T}} \tag{2.8}$$

where τ_0 is an intrinsic relaxation time scale of the system, E_a is an energy scale associated with the relaxation, k_B is Boltzmann's constant and T is the temperature.

The second model is similar and is the Orbach process[18], which is relevant when you have a ground state doublet with a small energy energy difference between the states of the doublet but a large energy gap to the first excited state[19]. In this case the system can go from being in one state to the other by absorbing a phonon of the correct energy which excites it to the first excited level, from which it re-emits the phonon relaxing back into the ground state doublet in

the different state to the initial one. The temperature evolution of the Orbach process is given by

$$\tau = \tau_0 \left(e^{\frac{\Delta}{k_B T}} - 1 \right) \tag{2.9}$$

where Δ is the energy gap to the first excited level.

If there are no phonons of the correct energy present to mediate an Orbach process (and no other mechanisms are possible) then classically it is expected that there should be no relaxation. That is, in the absence of energy to mediate a relaxation the system should become static. However this is not always the case and it is possible that relaxation can still occur through non-classical means. Relaxation could occur as the result of quantum tunnelling events between the two states of the ground state doublet without the need to go via the first excited level[6]. In this case the relaxation time depends only on the size of the energy difference between the doublet states and not on the temperature[20]. Because the relaxation time will be independent of the temperature then if temperature independence is observed then that is evidence the relaxation is the result of non-classical behaviour.

2.11 Demagnetising Fields

The magnetic flux in the region of a magnetised material is given [21] by

$$\vec{B} = \mu_0 \left(\vec{H} + \vec{M} \right) \tag{2.10}$$

where μ_0 is the permeability of free space and $\vec{B}$ is the magnetic flux. Outside of the sample, the $\vec{H}$ field and the $\vec{B}$ field are the same except for the constant

of proportionality μ_0 because free space cannot be magnetised. In contrast, $\vec{M}$ is the result of the magnetisation of the sample and only exists in the interior of the sample. This has the consequence that at the surface of the material the $\vec{M}$ field suddenly stops which causes its divergence to be non-zero there. So if $\boldsymbol{\nabla} \cdot \vec{M} \neq 0$ at the surface of a material, in order not to violate Maxwell's equations (which require $\boldsymbol{\nabla} \cdot \vec{B} = 0$) then $\boldsymbol{\nabla} \cdot \vec{H} = -\boldsymbol{\nabla} \cdot \vec{M}$. The same must be true at the opposing surface but $\boldsymbol{\nabla} \cdot \vec{H}$ and $\boldsymbol{\nabla} \cdot \vec{M}$ will have different signs there. This means that on the surfaces of the material in question there are sources and sinks of the magnetic field provided that those surfaces are perpendicular to $\vec{M}$. Figure 2.2 is an illustration of the $\vec{B}$, $\vec{H}$ and $\vec{M}$ fields in the interior and exterior of a uniformly magnetised cylindrical bar magnet. It shows how the $\vec{M}$ field suddenly stops at the surface and how $\vec{H}$ opposes $\vec{M}$ in the interior such that $\boldsymbol{\nabla} \cdot \vec{B} = 0$ at the surface.

The surface divergences in $\vec{H}$ will produce a $\vec{H}$ field between them (through the sample) which is in an opposing direction to the applied magnetising field, $\vec{H_a}$, and to the sample magnetisation. The produced field is referred to as the demagnetising field, $\vec{H_D}$, which acts to reduce the total field, $\vec{H_T}$, in the interior of the sample. The strength of $\vec{H_D}$ depends only on the strength of $\vec{M}$ and on the geometry of the sample. The strength and direction of $\vec{H_D}$ is not necessarily a simple function of $\vec{M}$ and it can be different at different positions within a sample.

If a sample has an ellipsoidal shape then the demagnetisation effect will be uniform in its interior. Additionally, if a sample has a uniform susceptibility and a high symmetry shape then it is usually sufficient to consider an average demagnetising field[23]. In both of these cases the demagnetising field is given by

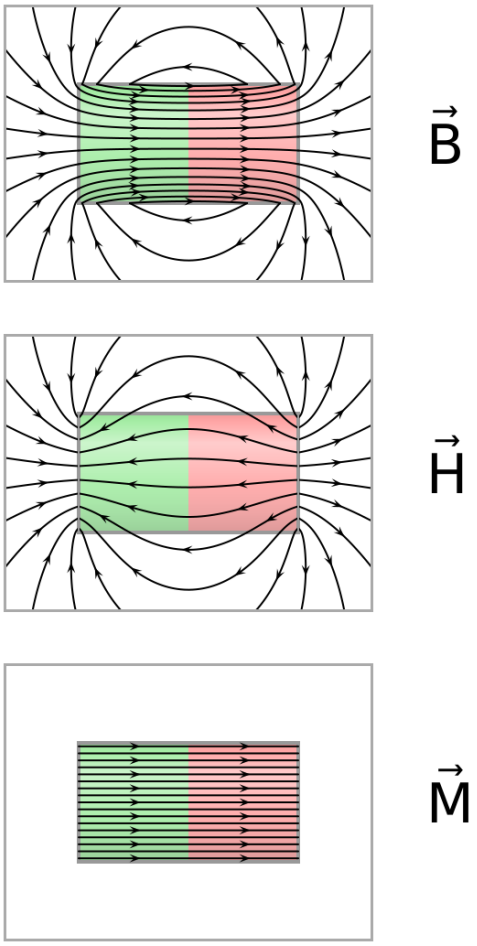

Figure 2.2: *Illustrations of lines of $\vec{B}$, $\vec{H}$ and $\vec{M}$ in the vicinity of a magnetised cylindrical bar magnet. Contour lines are shown with field directions. Figure re-used from ref. [22].*

$$\vec{H_D} = -\boldsymbol{N}\vec{M} \tag{2.11}$$

where $\boldsymbol{N}$ is the demagnetisation factor that depends on the geometry of the sample only. $\boldsymbol{N}$ is in bold because it is a tensor quantity as its value is dependent on the relative orientations of the sample and $\vec{H_a}$. In SI units $\boldsymbol{N}$ can take values between 0 and 1. If the sample is shaped like a needle aligned with $\vec{H_a}$ then $\boldsymbol{N} = 0$ along the long sample axis, this is true for any long and thin sample.

At the other end of the scale, in the case of an infinitely wide and thin sample perpendicular to $\vec{H}_a$ (such as a thin disc) $\boldsymbol{N} = 1$ in the direction of the field. Analytic solutions for N exist for ellipsoidal samples [24][25]. Analytic solutions for the average $\boldsymbol{N}$ in a sample exist for cylinders [26] and for prisms[27], for other sample shapes it is usually necessary to perform a finite element analysis. When measuring powder samples it is also necessary to consider how tightly packed the powder is[28, 29]. In the case of a powder with spherical grains then the demagnetisation factor is given by

$$\boldsymbol{N} = \frac{1}{3} + f\left(\boldsymbol{N_S} - \frac{1}{3}\right) \tag{2.12}$$

where, f is the relative density or packing fraction and $\boldsymbol{N_S}$ is the demagnetisation factor the sample would have if it were not made up of a powder.

It can be essential to take demagnetisation effects into account when calculating the susceptibility of a sample because the field experienced by the atoms in the sample is smaller than the one being applied. Simply dividing the measured magnetisation by the applied field will result in a quantity called the apparent susceptibility, χ_{app}, which differs from the true or intrinsic susceptibility, χ_{tru}, which is generally the quantity of interest. Assuming the magnetisation is in the same direction as the applied magnetic field the two quantities are related to each other through[30]

$$\chi_{tru} = \frac{M}{H_a - NM} = \left(\frac{1}{\chi_{app}} - N\right)^{-1} \tag{2.13}$$

where M and H_a are the magnitudes of $\vec{M}$ and $\vec{H}_a$. N is the demagnetisation factor which is no longer a tensor because only one direction is being considered.

The same effect will also occur when performing ac susceptibility measure-

ments. For ac susceptiblity measurements the relationship between the complex apparent susceptibility, $\chi'_{app} - i\chi''_{app}$, and complex true susceptibility, $\chi'_{tru} - i\chi''_{tru}$, is given by

$$\chi'_{tru} - i\chi''_{tru} = \frac{\chi'_{app} - N\left({\chi'_{app}}^2 + {\chi''_{app}}^2\right) - i\chi''_{app}}{1 - 2N\chi'_{app} + N\left({\chi'_{app}}^2 + {\chi''_{app}}^2\right)}. \tag{2.14}$$

This has the important consequence that both of χ'_{tru} and χ''_{tru} depend on both χ'_{app} and χ''_{app}. Which means that the value of N can impact the location of the peak in χ''_{app}, and therefore the measured value of τ if the correction is not applied properly.

Because χ_{tru} is almost always the quantity of interest, it is usually the quantity meant when the distinction is not made i.e. $\chi \equiv \chi_{tru}$ and $\chi' - i\chi'' \equiv \chi'_{tru} - i\chi''_{tru}$. Additionally it has been assumed in this section that χ and M values are normalised by volume and not by mass. When working with mass magnetisations and mass susceptibilities equations 2.13 and 2.14 are slightly different and also depend on the density of the material, ρ. The versions of equations 2.13 and 2.14 for mass susceptibility can be obtained by substituting in $\chi_{tru,mass} = \chi_{tru}/\rho$ and $\chi_{app,mass} = \chi_{app}/\rho$. Additionally equation 2.14 is slightly different in the cgs unit system[31].

2.12 Magnetic Interactions

2.12.1 Dipole-dipole Interaction

When magnetic ions are present in a material they may interact with one another. There are many mechanisms by which this can occur however for this thesis it will only be necessary to consider two of the simplest mechanisms; the magnetic

dipole-dipole interaction and the exchange interaction.

The first, the dipole-dipole interaction is a direct result of the magnetic field produced by a magnetic moment. Surrounding each magnetic moment is a magnetic flux given by

$$\mathbf{B}(\mathbf{r}) = \frac{\mu_0}{4\pi}\left(\frac{3\mathbf{r}\,(\mathbf{m}\cdot\mathbf{r})}{r^5} - \frac{\mathbf{m}}{r^3}\right). \tag{2.15}$$

Any other magnetic moments present in the vicinity of that magnetic field then have a potential energy given by

$$\mathcal{H} = -\mathbf{m}\cdot\mathbf{B} \tag{2.16}$$

so that the potential energy of the interaction between two dipoles is given by

$$\mathcal{H} = \frac{\mu_0}{4\pi}\left(\frac{\mathbf{m_1}\cdot\mathbf{m_2}}{r^3} - \frac{3\,(\mathbf{m_1}\cdot\mathbf{r})\,(\mathbf{m_2}\cdot\mathbf{r})}{r^5}\right). \tag{2.17}$$

A key feature of equation 2.17 is the presence of $\mathbf{r}$ which has two key implications. Firstly, the relative spatial positions of the two moments has an impact on the nature of the interaction, if there exists some anisotropy in the orientations the moments can take then this can have a significant influence on their behaviour. Secondly, the r dependence also indicates that eq. 2.17 is long range and can lead to interactions across many moments at once.

The dipole-dipole interaction is essentially the same interaction as can be seen when two bar magnets are brought into the vicinity of one another.

2.12.2 Exchange Interaction

Unlike the dipole-dipole interaction, there is no similar macroscopic version of the exchange interaction which is completely quantum mechanical in nature. For fermions the exchange interaction occurs because the total wave function of a pair of identical fermions must be anti-symmetric with respect to exchange of the particles. The total spatial wavefunction of two identical fermions will be symmetric as a result of their being identical. Because the particles are indistinguishable then swapping their positions cannot change their spatial wavefunction. This means that in order for their total wavefunction to be antisymmetric, the spin wavefunction will have to be antisymmetric. This can be realised by having their spins in opposition to one another. The Hamiltonian of the exchange interaction between two fermions is given by

$$\mathcal{H} = -2J\mathbf{S_1} \cdot \mathbf{S_2} \tag{2.18}$$

where, J is the exchange constant, $\mathbf{S_1}$ is the spin of the first particle and $\mathbf{S_2}$ is the spin of the second particle.

2.13 Geometric Frustration

Geometric frustration occurs in systems where there exists some geometric constraint that prevents the system from satisfying all of the present interactions. In other words, there are competing interactions attempting to impose different conditions that cannot all be realised simultaneously.

A common example of a geometrically frustrated system is found in figure 2.3, which depicts three spins on the vertices of an equilateral triangle. Here spins is

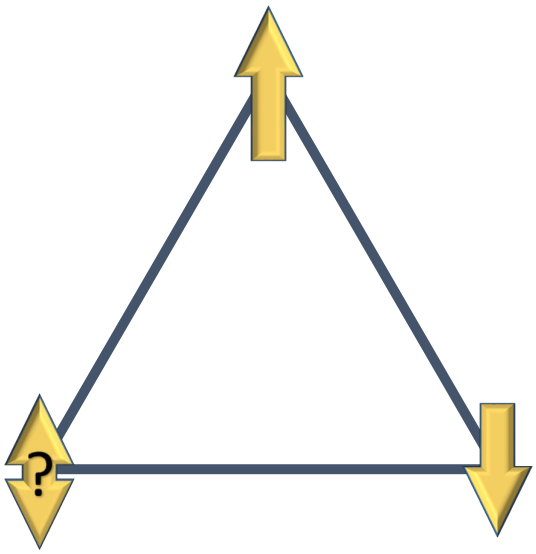

Figure 2.3: *Example of a frustrated magnetic system with AFM interactions between magnetic moments on the corners of an equilateral triangle.*

used as a shorthand for particles with spin. In this example the spins have anti-ferromagnetic (AFM) correlations with each other, meaning that they will try to align anti-parallel to each other. The spins at the top and lower right vertices have aligned anti-parallel and have therefore satisfied the AFM correlation between them, however it is not clear which way the spin in the lower left vertex should point. It cannot be anti-parallel with both of the other spins and so it is frustrated. There is no reason for that spin to be the frustrated one instead of the other two and so each of the spins experiences the same dilemma and are frustrated.

Scaling the problem up to three dimensions a similar problem is realised for spins on the vertices of a tetrahedron [32]. In this case each spin has three neighbours that it will try to align anti-parallel with, a condition which cannot be realised.

In both of these systems there is no single preferred state that minimises the

energy of the system. In fact this is a common feature of frustrated systems, that the ground state (lowest energy state) of the system will be degenerate.

In frustrated materials it is typical that they will not order magnetically even as they are cooled below their value of T_C or T_N. The susceptibility will continue to obey the Curie-Weiss law to lower temperatures until the system reaches a temperature at which the moments freeze out and deviates from the Curie-Weiss law, this temperature is known the spin freezing temperature, T_f. The ratio of these parameters is sometimes used as a measure of how frustrated a system is and is known as the frustration index, f, which is given by $f = |\Theta_{CW}|/T_f$.

2.14 Spin Ice

Frustration can still occur on a tetrahedron if there are ferromagnetic (FM) interactions but there must also be some other geometric constraints on the system. In spin ice there are Ising-like rare earth ions sitting on the vertices of a network of corner sharing tetrahedra (as in figure 2.4 c), with net FM interactions. The additional geometric constraint takes the form of a strong anisotropy in the CEF. The CEF constrains the ion spins to point along their local $\langle 111 \rangle$ directions which are directly toward the centre of their tetrahedron (pointing in) or directly away (pointing out). The CEF constraint prevents the ion spins from simply aligning to satisfy their FM interactions. As a result the system is frustrated.

The ground state of spin ice is realised when each tetrahedron has two spins pointing in and two spins pointing out, a condition referred to as the Bernal-Fowler ice rules[34] or simply the ice rule. The ice rule is so named because it was first discovered governing the positioning of hydrogen atoms in water ice (H_2O)[35]. In water ice, each oxygen ion is near to four hydrogen ions. For each

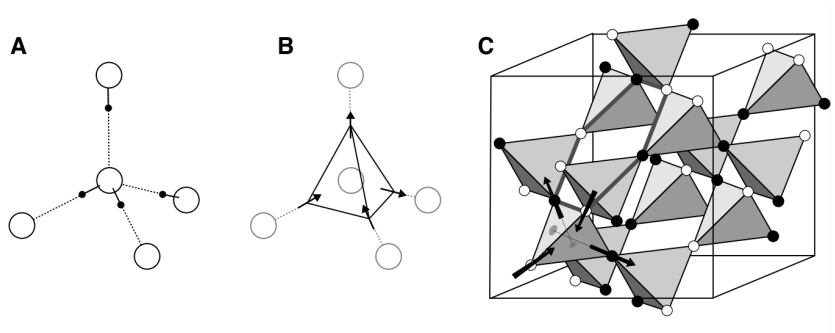

Figure 2.4: *a) Bernal-Fowler ice rules obeyed by oxygen ions (hollow circles) and hydrogen ions (black circles). b) Equivalent mapping to spin orientations in spin ice. c) pyrochlore structure of rare earth ions in spin ice with spin orientations indicated in the lower left tetrahedron, elsewhere the spin orientation is indicated by a white circle for 'in' or black circle for 'out'. Figure re-used from ref [33].*

oxygen ion there are two hydrogen ions that are close, and two that are farther away [34], one such configuration is shown in figure 2.4 a). There are 6 ways to position the hydrogen ions around an oxygen ion that satisfy the ice rules. By mapping close hydrogen ions to spins pointing in and far ions to spins pointing out (figure 2.4 b), the rules are the same in spin ice. This is where the ice part of the name spin ice comes from.

The degeneracy of the ground state also leads to a residual entropy at 0 K. To calculate the value of the entropy, first consider that for each rare earth ion there are two possible configurations, in and out. Based on that the multiplicity of the ground state would be 2^{2N} where N is the number of tetrahedra (or a quarter of the number of rare earth ions). However this does not account for the effect of the ice rules. Without the ice rules there are 16 possible ways to orientate the spins on a tetrahedron, but only 6 that satisfy the ice rules condition. To account for that it is necessary to multiply by $(6/16)^N$, meaning that the final multiplicity of the state is $2^{2N}\,(6/16)^N$. Inputting the multiplicity into Boltzmann's entropy formula gives a residual entropy of $R\ln(3/2)/2$ per mole (or Hydrogen in ice) [36] where

R is the gas constant and the factor of 1/2 is to avoid double counting as each spin is in two tetrahedra. The entropy value is the same in spin ice and water ice. Figure 2.5 shows experimental evidence of the ground state entropy in a spin ice material. The change in the entropy of a material over some temperature range $(T_1 - T_0)$ can be measured by integrating the specific heat divided by temperature (C/T) over that temperature range, i.e.

$$\Delta S = \int_{T_0}^{T_1} \frac{C}{T} dT. \tag{2.19}$$

The expected entropy if the ice rules are not obeyed is $R\ln(2)$[36], so if $S = 0$ at $T = 0$ then that should be the recovered value. In spin ice however integrating C/T (figure 2.5 a) yields $\Delta S \approx R\,(\ln(2) - \ln(3/2)/2)$ (figure 2.5 b) indicating that there was a residual entropy of $R\ln(3/2)/2$ at the lowest temperature of the integration and given that $C \approx 0$ at the lowest temperature in figure 2.5 a) then this likely extends to $T = 0$.

The first discovered and most well studied spin ice materials are $Ho_2Ti_2O_7$[37] (HTO) and $Dy_2Ti_2O_7$[36] (DTO). In both materials the rare earth ions Ho and Dy sit on a network of corner sharing tetrahedra, owing to the pyrochloric crystal structure. Strong CEFs in both materials constrain the spins to orient along their local $\langle 111 \rangle$ directions[38]. The CEF ground state is separated from the first excited state by an energy gap of the order of 240 K and 380 K in HTO and DTO respectively[39]. The charge structure in the spin ice pyrochlores means the rare earth ions lose 3 electrons (to become Ho^{3+} and Dy^{3+}), emptying their filled outer 6s electron shells and leaving the 4f shell partially filled. In HTO the free ion ground state has total angular momentum of $J = 8$, from quantum numbers of $L = 6$ and $S = 2$[3, 39]. In DTO the free ion ground state has a total

angular momentum of J=15/2, from $L = 5$ and $S = 5/2$ [3, 39]. The rare earth ions have magnetic moments $\approx 10\mu_B$ in both HTO and DTO.

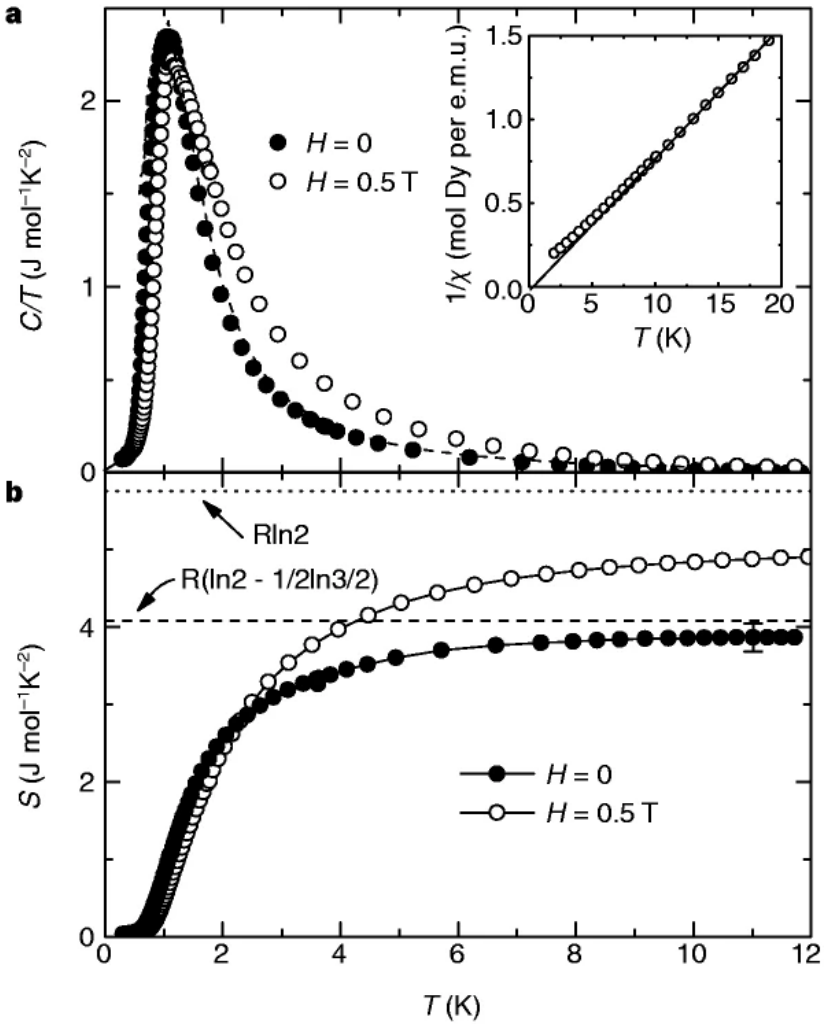

Figure 2.5: *Specific heat and entropy in the spin ice material $Dy_2Ti_2O_7$. a) Specific heat divided by temperature in H=0 T and H=0.5 T. b) Entropy change S obtained by integrating C/T with respect to T again in H=0 T and H=0.5 T. Figure re-used from ref. [36]*

The spin ice Hamiltonian has terms for the exchange interaction and the dipole-dipole interaction. Therefore it is given by [40]

$$\mathcal{H} = -J \sum_{\langle ij \rangle} \boldsymbol{S}_i^{\hat{z}_i} \cdot \boldsymbol{S}_j^{\hat{z}_j} + D r_{nn}^3 \sum_{i>j} \left[\frac{\boldsymbol{S}_i^{\hat{z}_i} \cdot \boldsymbol{S}_j^{\hat{z}_j}}{|\boldsymbol{r}_{ij}|^3} - \frac{3(\boldsymbol{S}_i^{\hat{z}_i} \cdot \boldsymbol{r}_{ij})(\boldsymbol{S}_j^{\hat{z}_j} \cdot \boldsymbol{r}_{ij})}{|\boldsymbol{r}_{ij}|^5} \right] \tag{2.20}$$

where, $\boldsymbol{r}_{ij}$ is the vector from the i^{th} to the j^{th} ion. $\boldsymbol{S}_i^{\hat{z}_i}$ denotes the spin for the i^{th} ion, the superscript indicates that the spin vector is in the local $\langle 111 \rangle$ direction which is labelled as $\hat{z}_i$. r_{nn} is the nearest neighbour distance between ions. J is the exchange coupling constant and D is the dipolar coupling constant. This model was first examined by refs. [41] and [40] and determined that although there is some influence of longer range interactions in these materials (particularly in HTO) the spin ice state can be well described by considering nearest neighbour interactions only. Taking account of the relative geometries of the nearest neighbour spins the Hamiltonian can be rewritten as

$$\mathcal{H} = J_{eff} \sum_{\langle ij \rangle} \sigma_i \sigma_j. \tag{2.21}$$

Where, J_{eff} is given by $J_{eff} = J_{nn} + D_{nn}$ in which, J_{nn} and D_{nn} are the effective exchange and effective dipolar coupling constants at the nearest neighbour distance. They are given by $J_{nn} = J/3$ and $D_{nn} = 5D/3$. σ_i represents the spin orientations and can have a value ± 1. In HTO those constants were found to be [42] $J_{nn} = -0.52$ K and $D_{nn} = 2.35$ K, meaning that net interactions at the nearest neighbour distance are ferromagnetic. In DTO those values are [43] $J_{nn} = -1.24$ K and $D_{nn} = 2.35$ K. Interestingly in both materials the AFM exchange interaction is stronger ($J > D$) however the geometry ensures that the dominant interaction is FM ($J_{nn} < D_{nn}$).

Other pyrochlore spin ice materials include $Ho_2Sn_2O_7$[44, 45] and $Dy_2Sn_2O_7$[46,

47], which behave similarly to their titanate counterparts but are less studied. $CdEr_2S_4$ and $CdEr_2Se_4$ are also spin ice materials [48, 49] but have a spinel structure, they will be discussed at length later in this thesis.

2.15 Magnetic Monopoles

In spin ice the ideal ground state is to have a 2-in 2-out state on each tetrahedron of the crystal as shown in figures 2.4 b) and 2.6 a). However if in a tetrahedron one spin were to change its orientation, which could occur due to a thermal excitation or quantum tunnelling between states, then on that tetrahedron there is a 3-in 1-out (or vice versa) state and the opposite configuration on the neighbouring tetrahedron (figure 2.6 b). This possibility was first discussed by Ryzhkin *et al.* [50] who identified the possibility of the formation of 3-in 1-out "defects", discerning that excitations of this kind would behave as magnetic analogues of ionic defects in water ice and raise the energy of the crystal by $4J_{eff}$. Castelnovo *et al.* [51] later expanded upon this idea to point that that Ryzhkin's defects were in fact quasi-magnetic charges or magnetic monopoles. It is important to note that these magnetic monopoles represent divergences in $\vec{M}$ and $\vec{H}$ not in $\vec{B}$ so $\boldsymbol{\nabla} \cdot \vec{B} = 0$ still holds[52]. Castelnovo *et al.* also introduced the dumbbell model, illustrated in figures 2.6 c) and d), in which the spins are instead thought of as "dumbbells" with opposing magnetic charges on each end.

At the centre of each tetrahedron on which there is a 3-in 1-out arrangement of spins, there exists a net magnetic charge, and an opposing net magnetic charge exists at the centre of the neighbouring 3-out 1-in tetrahedron. The net magnetic charges behave like monopoles and can be separated from one another by continually flipping spins leaving a chain of flipped spins connecting the two monopoles

as shown in figure 2.6 e) in the dumbbell model. This chain of flipped spins is similar to a Dirac string, although the chain of spins is observable (and has been observed with neutron scattering [53]) where as a true Dirac string would not be[54]. The energy cost of separating the two created monopoles is a finite quantity meaning that separation is possible up to arbitrarily large distances. The separated monopoles can interact at long range via a Coulomb-like interaction that is not screened by the lattice.

The potential energy of the monopole Coulomb interaction is given by [51, 55]

$$V\left(r_{\alpha\beta}\right) = \frac{\mu_0}{4\pi}\frac{Q_\alpha Q_\beta}{r_{\alpha\beta}} \tag{2.22}$$

where, Q_α and Q_β are the magnetic charges of the two monopoles labelled α and β. $r_{\alpha\beta}$ is the distance between them. Q_α and Q_β are given by

$$Q_\alpha = \pm Q_\beta = \pm \mu/a \tag{2.23}$$

where μ is the magnetic moment of the rare earth ions and a is the distance between the centres of neighbouring tetrahedra.

The peak in the specific heat is well modelled by Debye-Hückel theory [53, 56] which is a model for ions moving through an electrolyte solution of fixed volume where the ions interact at long range via a Coulomb interaction[57]. Debye-Hückel theory has also been used to model monopole densities [49] and spin fluctuation rates [58]. The monopoles have also been observed to carry magnetic charge in a phenomenon dubbed 'magnetricity' [59] and observed exhibiting a magnetic analogue of the Wien effect [60], an effect that can be used to demonstrate interactions of the form of equation 2.22 through the application of small magnetic fields[55].

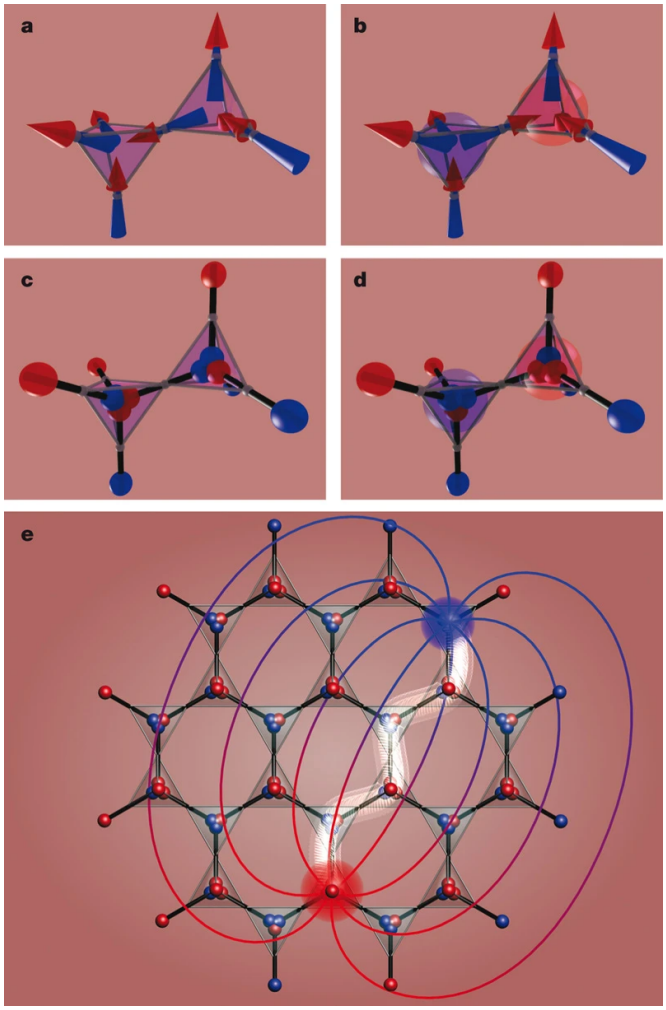

Figure 2.6: *a) Two neighbouring tetrahedra in a configuration allowed by the ice rules. b) The shared spin connecting the tetrahedra has flipped creating a 3-in 1-out defect on the right tetrahedron and a 3-out 1-in defect on the other. c) The same situation as in a in the dumbell representation. d) The same situation as in b in the dumbell model. e) Two monopole defects (highlighted blue and red) that have separated from one another by flipping a chain of spins (illuminated), flux lines indicate the Coulomb field between them. Figure re-used from ref. [51].*

2.16 Spin Dynamics in Spin Ice

Measurements of the spin relaxation time, τ, (or τ's reciprocal quantity, the spin fluctuation rate ν) in spin ice typically yield a temperature dependence of the form in figure 2.7.

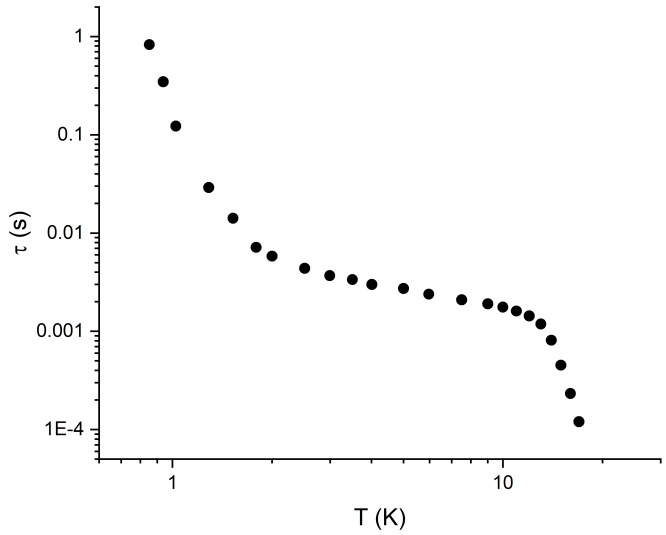

Figure 2.7: *τ against T in the spin ice material $Dy_2Ti_2O_7$. Figure adapted from reference [61].*

The relaxation time shows three distinct regimes across the temperature range shown. At higher temperatures the relaxation time varies exponentially with temperature, indicating a thermally activated process. In this high temperature regime, there is enough thermal energy in the material to allow for thermally activated spin flips which are mediated by exciting spins over the energy barrier. This is an Orbach process [62][18] which is when the absorption of thermal phonons excite the spins to higher crystal field levels from which they relax again. The relaxation time will have a temperature dependence given by

$$\tau(T) = \tau_0 \left(e^{\Delta/(k_B T)} - 1\right)^{-1}. \tag{2.24}$$

Where, τ_0 is know, as the rate constant or characteristic relaxation time, Δ is the energy barrier to be overcome, k_B is Boltzmann's constant and T is the temperature. It is also common to see this regime modelled with an Arrhenius

law [44] in which the -1 term is removed giving $\tau(T) = \tau_0 \exp(-\Delta/(k_B T))$.

At slightly lower temperatures there is a quasi-temperature independent plateau in the relaxation time. In this temperature regime the thermal energy of the system is too low for phonon mediated flipping of spins and the relative temperature independence suggests that spin flips occur as a result of quantum tunnelling events[63] between the two states of the ground state doublet. Tunnelling between the two states of the ground state doublet can only occur if there is an energy splitting between the levels. This splitting is provided by the effect of internal transverse magnetic fields [20, 64]. The spin flip time scale is well described as being mediated by the creation of monopole excitations[52]. The temperature dependence of the relaxation time on the plateau is given by an Arrhenius law with an energy barrier of $\Delta = 2J_{eff}$ which is the energy cost of a single free monopole or half the cost to flip a spin. There is a high density of monopoles in this regime and long range interactions between them are effectively screened[39, 59, 62]. The quantum tunnelling plateau is a key feature of spin ice materials that has been observed in all of them so far.

At the very lowest temperatures the relaxation time again becomes strongly temperature dependent with a re-entrant thermally activated process (re-entrant meaning that the sample returns to thermally activated processes upon cooling further). In this regime the relaxation time rapidly grows with decreasing temperature as the system approaches the spin freezing temperature[61]. The monopole density is much lower at low temperature and the monopoles that are present are unscreened. In this region the relaxation time is again well described by an Arrhenius law.

At the very lowest temperatures there is not enough energy for any spin flips to occur and the spins become frozen (with one caveat). Below the spin freezing

temperature, the spins are static, any monopole defects are frozen in and the system broadly settles into one of the configurations allowed by the ice rules[65]. The caveat is that the presence of nuclear magnetic moments has been shown to mediate tunnelling between spin orientations at lower temperatures[66] by hyperfine splitting.

Measurements in DTO using the muon spin rotation technique have detected spin fluctuations at temperatures well below the spin freezing temperature[67] hinting at the possibility of persistent spin dynamics at temperatures where the spins should be frozen. However it has been argued [68] that these are the result of thermal excitations induced by the measurement technique. Persistent spin dynamics have been observed in other frustrated magnetic materials, although their origin is unexplained[69].

2.17 Spin Ice in Applied Magnetic Fields

The application of a dc magnetic field can have a significant impact on the magnetic properties of spin ice. This is evident from Ramirez *et al.*'s [36] confirmation of the ground state entropy, where the application of a magnetic field was found to significantly alter the specific heat (see figure 2.8).

Harris *et al.*'s [37] neutron scattering measurements indicated that the orientation of the crystal relative to an applied magnetic field will affect whether or not any order is detected. Figure 2.8 is performed on a powder sample and so contributions from all crystallographic orientations are present.

Magnetisation measurements performed by Fukazawa *et al.* [70] and Petrenko *et al.* [71] provided further evidence for the anisotropic response of spin ice to a dc magnetic field and gave a discussion of the behaviour with the field along

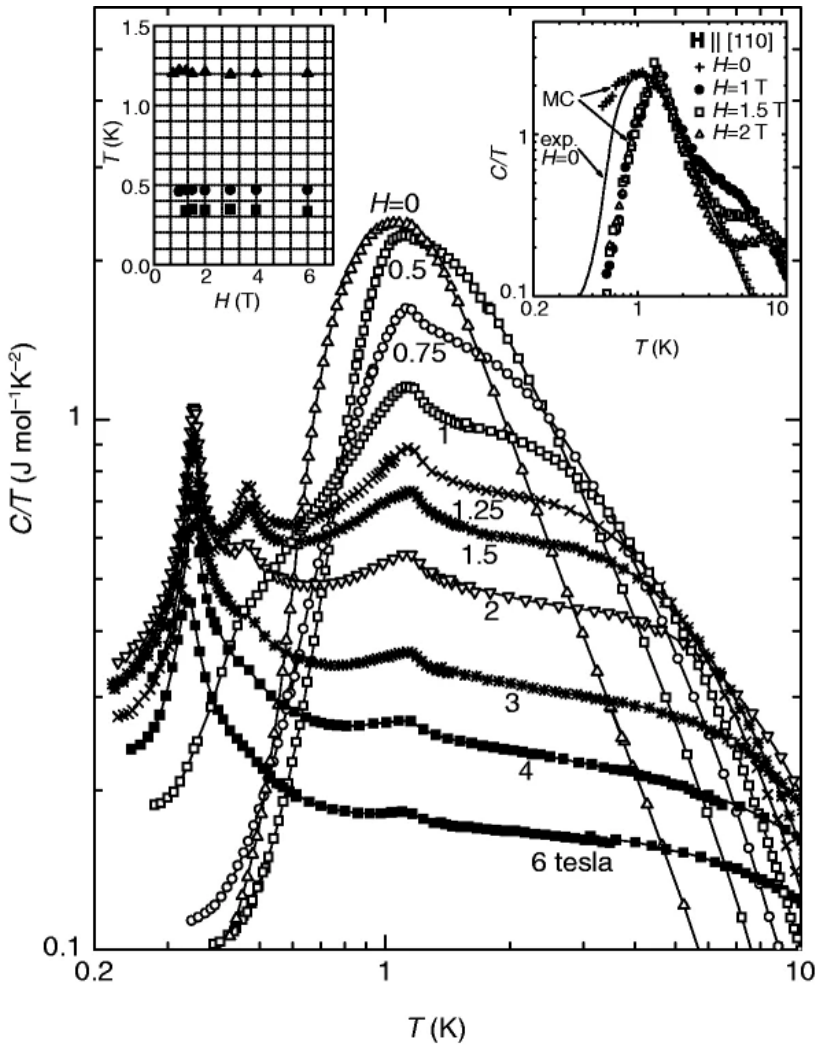

Figure 2.8: *Specific heat divided by temperature in powder $Dy_2Ti_2O_7$ in the application of magnetic fields. Top left inset: Field and temperature locations of the features in C/T. Top right inset: Monte-Carlo simulations of C/T. Figure re-used from ref. [36].*

the [100], [110] and [111] orientations. Their measurements confirmed that the saturation magnetisation is also dependent on field orientation.

For a magnetic field applied parallel to the [111] direction of the crystal there will be a quarter of the spins for which their local easy axis is aligned with the magnetic field. For the remaining spins the magnetic field is perpendicular to the triangular plane they lie on. For a field along the [111] direction there are

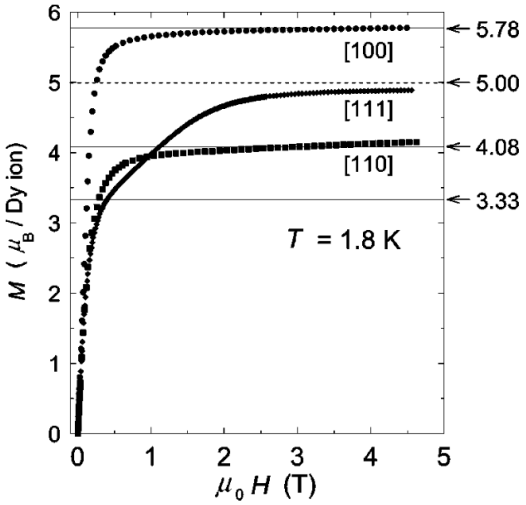

Figure 2.9: *dc magnetisation measurements on single crystal $Dy_2Ti_2O_7$ along the [100], [110] and [111] directions. Saturation values in Bohr magnetons per dysprosium ion are also indicated. Figure re-used from ref. [70].*

two saturation values, the Kagomé ice plateau and full saturation. In the plateau region the spins parallel to the field (of which there is one per tetrahedron) will tend to align with the field, creating a plane of aligned spins. The other spins on each tetrahedron are arranged on triangles that are perpendicular to the field. They will continue to obey the ice rules and are still frustrated so they form a Kagomé lattice[72, 73, 74, 71]. The magnetisation per rare earth ion is given by $\mu_{FI}(1 + 1/3)/4$ where μ_{FI} is the free ion value of one of the rare earths. The free ion value or free ion moment is the magnetic moment per ion that would be measured if the ions had no anisotropic constraints i.e. if they could all freely align with the field. At low temperatures the plateau is clearly visible however at higher temperatures (as in figure 2.9) it will generally manifest as a change in gradient of the $M(H)$ curve[75]. If the field is increased further it can break the ice rules and each tetrahedron will have a 3-in 1-out (or vice versa) state. All the spins in the Kagomé planes align with the field (or as close as they can

get whilst staying on their local $\langle 111 \rangle$ direction). The saturation magnetisation is now $\mu_{FI}/2$. The effect of a [111] field on the specific heat is complex and is discussed in detail in ref. [76]. The Kagomé ice phase is itself an area of intense interest and research in spin ice and other materials[77]. Other research along this direction has investigated the possibilities of a Kasteleyn transition [78] as well as a monopole liquid-gas type transition [58].

For a field along one of the [110] or equivalent directions, the effect of a field is quite different. For each tetrahedron there will be two spins that are almost aligned with the magnetic field and two spins that will be perpendicular[70]. Both of these groups of spins form long chains of spins that cross many tetrahedra. The ice rules are still obeyed [79].The chains are split into two categories: α-chains which are parallel to the field and β-chains which are perpendicular [80, 81]. The two chains lead to two peaks forming in the specific heat that become further separated with increasing field, each chain type contributes its own peak to the specific heat [82]. Yoshida *et al.* [82] were able to build up a phase diagram in temperature and field. In larger magnetic fields the α-chains are FM aligned with the β-chains either AFM or paramagnetic depending on temperature. They also predicted the presence of a phase with both α and β-chains being AFM ordered at the lowest temperatures and fields. In the dc magnetisation the saturation value is expected to be given by $\mu_{FI}(2\sqrt{2/3})/4$.

A magnetic field applied along the [100] direction can cause the spins on a tetrahedron to align with the field in a 2-in 2-out fashion that obeys the ice rule [70]. All of the spins $\langle 111 \rangle$ directions make the same angle with the applied field [73] so all spins react in the same manner to the field. The application of the field changes the Zeeman splitting of the spins meaning that the peak in the specific heat is field dependent[83]. The saturation magnetisation is given by $\mu_{FI}(1/\sqrt{3})$.

For a magnetic field along the [211] direction the field is parallel to one of the triangular faces of the tetrahedrons. Therefore there are three spins (those on that triangular face) for which the field has a pinning effect and one spin that is perpendicular to the field [84]. The spin that is perpendicular to the field will have its orientation determined by the ice rules [73]. This field orientation also contributes a single peak to the powder specific heat. Ruff *et al.* [85]performed a theoretical calculation on this field orientation finding that if the field is canted off the [211] direction by a few degrees then the perpendicular spins can be decoupled from their neighbouring spins and become paramagnetic (in its $\langle 111 \rangle$ direction). The paramagnetic spins interact with one another through long range dipole-dipole interactions.

2.18 Muons as Magnetic Probes

The commonly used short hand μSR stands for muon spin rotation, relaxation or resonance which is an experimental technique that uses positive muons as microscopic probes of the internal magnetic nature of a material[86][87][88] [89]. μSR is used throughout this thesis so a brief introduction to the technique is given here. The technique requires a particle accelerator (as naturally occuring cosmic ray muons are not practicable). Currently there are several facilities where this is possible: ISIS (UK), Paul Scherrer Institute (Switzerland), J-PARC (Japan) and TRIUMF (Canada).

Muons are fundamental particles that form part of the second generation of leptons in the standard model. They are similar to electrons in that their charge is $\pm$e, are spin-1/2 and have an antiparticle, however their mass is approximately 200 times greater and they decay after a mean lifetime of 2.2 μs. Their large mass

means that positive and negative muons behave more similarly to protons and anti-protons than to their electronic counterparts. In almost all cases positively charged muons are used although in the last few years negative muons have found some applications[90] including as magnetic probes[91].

In a μSR experiment muons are produced from the decay of positive pions (at ISIS these pions are produced by accelerating high energy protons into a graphite block). The pions then decay via the weak interaction after a mean lifetime of 26 ns. The products of this decay are predominantly given by:

$$\pi^+ \rightarrow \mu^+ + \nu_\mu \tag{2.25}$$

An electronic version of the above decay happens in approximately 0.01% of decays, but the positrons produced in that decay are not brought onto the sample and do not have an effect on the experiment. Because the decay is a two body decay and the pion has no net spin, the two decay products must be produced with their spins antiparallel to one another. The produced neutrinos have left handed helicity[92] and so their spin is aligned antiparallel to their momentum. Because momentum is conserved in the decay, this means the muons are also produced with their spin anti parallel to their momentum. The combination of these two effects means that large numbers of spin polarised muons can be reliably produced.

The spin polarised muon 'beam' is then directed onto the sample with steering magnets where they implant into the sample. The direction of the incoming muons is usually taken to be parallel to the z direction by convention. They come to a stop in the sample at a site dictated by the internal electric field of the sample, generally at interstitial sites because they are repelled by the

positive nuclei, and thermalise with little loss of polarisation[93]. After some time the muon will decay via the following process that is mediated by the weak interaction[92]:

$$\mu^+ \rightarrow e^+ + \nu_e + \bar{\nu_\mu} \tag{2.26}$$

Because it is a weak decay, the positron is preferentially emitted along the direction of the muon spin's orientation [94]. The probability of the positron being emitted in a particular direction is given by

$$p(\theta) \propto 1 + a_0(E)cos(\theta) \tag{2.27}$$

where, θ is the angle between the muon spin and the positron emission direction, E is the energy of the emitted positron and $a_0(E)$ describes the intrinsic asymmetry of the decay which is given by

$$a_0(E) = \frac{2E/E_{max} - 1}{3 - 2E/E_{max}} \tag{2.28}$$

where, E_{max} is the maximum possible positron energy having a value of approximately 52 MeV[88].

Integrating over possible emission energies a_0 averages to be 1/3. Example muon distributions are shown in figure 2.10 for E=0 ($a_0 = -1/3$), E=3/4E_{max} ($a_0 = 1/3$) and E=E_{max} ($a_0 = 1$). The emitted positrons can then be detected by the beamline detectors [88]. Usually there are two sets of detectors, one 'forward' of the sample and one 'backward' of the sample. By counting for large numbers of decays and taking the difference between the forward and backward detectors it is possible to effectively track the orientation of the muon spins as a function

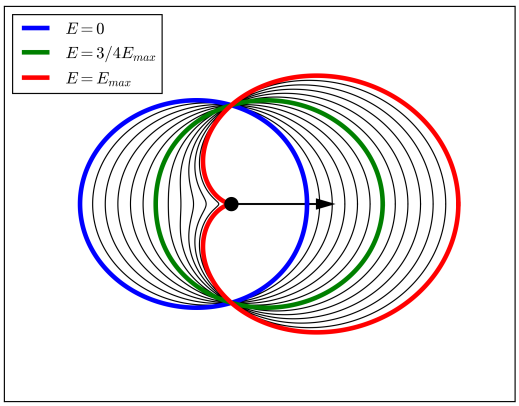

Figure 2.10: *Decay asymmetry of the muon (black dot) compared to its spin orientation (black arrow). Contour lines show the probability that the positron will be emitted in a given direction based on its energy.*

of time. The difference between the forward and backward detectors is referred to as the asymmetry, $A(t)$, or polarisation, $P_z(t)$, which are given by equation 2.29. The subscript z indicates the axis along which the sample and detectors lie, here the forward and backward detectors are taken to be in the $+z$ and $-z$ directions from the sample respectively. α is a calibration parameter to account for any instrumental asymmetry. Strictly speaking $P_z(t)$ refers to the average spin orientation of the muons and $A(t)$ refers to the measured signal, but for large numbers of positron detections they can be considered the same.

$$P_z(t) = A(t) = \frac{N_F(t) - \alpha N_B(t)}{N_F(t) + \alpha N_B(t)} \tag{2.29}$$

There are two approaches taken to delivering the muons to the sample. The first is to produce a continuous stream of muons arriving one after another, this is the technique employed at TRIUMF and PSI. This approach allows for a high time resolution, but limits the number of muons that can be used because it is

necessary to wait for the previous muon to decay before sending another one. In practice (at PSI) a wait time of 10 μs is used and a veto counter employed that means the next muon is ignored if a positron is not detected before the 10 μs window is over. The second technique is to produce a burst of muons that are all implanted in the sample at once, this is known as the pulsed technique and is used at ISIS and J-PARC. In this case large numbers of muons can be detected but the time resolution is limited by the length of each pulse.

The orientation of the muon spins as a function of time is of interest because it contains information about about their local magnetic environments. In the simplest case, a muon will experience some static internal field and will precess about the field direction at its Larmor frequency, given by[88]

$$\omega_L = -\gamma_\mu |\vec{B}| \tag{2.30}$$

where ω_L is the Larmor frequency, γ_μ is the muon gyromagnetic ratio ($\gamma_\mu = 135.5 \times 2\pi \ MHz/T$) and $|\vec{B}|$ is the magnitude of the net $\vec{B}$ field at the muon site. If there is only one suitable stopping site for the muons in a given sample or multiple magnetically equivalent sites, all the muons in an experiment are likely to experience the same internal field $|\vec{B}|$ and so the measured asymmetry will ideally be a sinusoid given by

$$P_z = \cos^2(\theta) + \sin^2(\theta)\cos\Big(\gamma_\mu |\vec{B}| t\Big) \tag{2.31}$$

where θ is the angle between the $|\vec{B}|$ field direction and the initial muon spin direction or z-axis which are typically chosen to be the same. If the sample under investigation has multiple possible muon sites, or multiple equivalent crystal sites with inequivalent magnetic environments, then the measured asymmetry will be

an average of all the muon polarisations.

If the muons experience a range of magnetic fields that is approximately Gaussian in shape, an assumption that is usually be justified by the central limit theorem, then the measured asymmetry will be described by a Kubo-Toyabe function. Mathematically if the Gaussian field distribution is given by

$$P(|B_i|) = \frac{1}{\sqrt{2\pi}\Delta} \exp\left(\frac{|B_i|^2}{2\Delta^2}\right) \ , \ i = x, y, z \tag{2.32}$$

where, $|B_i|$ is the x y z components of $\vec{B}$. Then by integrating equation 2.31 and equation 2.32 over all field directions one arrives at the Kubo-Toyabe function:

$$P_z = \frac{1}{3} + \frac{2}{3}(1 - \gamma_\mu^2 \Delta^2 t^2) \exp\left(\frac{-\gamma_\mu^2 \Delta^2 t^2}{2}\right). \tag{2.33}$$

An example Kubo-Toyabe asymmetry is shown in figure 2.11, exhibiting the exponential relaxation from full asymmetry at short times and the characteristic 1/3 tail.

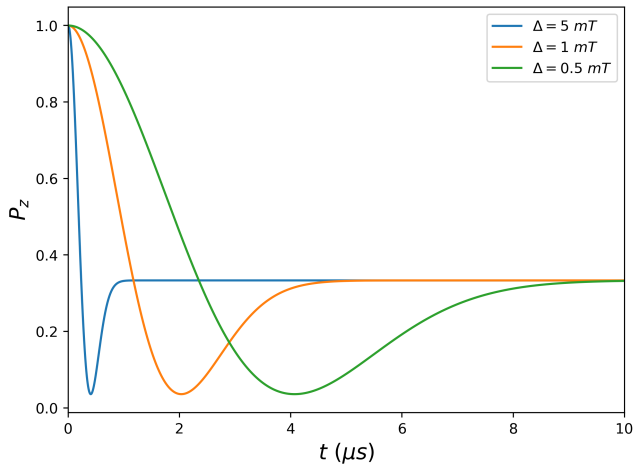

Figure 2.11: *Example Kubo-Toyabe functions.*

Most μSR instruments allow for the application of a DC magnetic field to the

sample. This is usually done in one of two possible geometries: transverse (TF) and longitudinal (LF). The field is said to be transverse when it is applied perpendicular to the orientation of the incoming muon spins, similarly a longitudinal field is one that is applied parallel to the incoming muon spins. The application of a transverse field is likely to lead to an oscillatory muon polarisation, as the muons precess about the applied field. This is especially true if the applied field is large compared to any internal fields. A longitudinal field however tends to try and pin the muon spins along its axis. Figure 2.12 shows the impact of a longitudinal field on the Kubo-Toyabe distribution, where the lines have been calculated from equation 2.34. The application of the field modifies the field distribution that the muons see, increasing the z component. In large longitudinal fields (relative to Δ) the z component is dominated by the field, pinning the spins along their initial orientations[89].

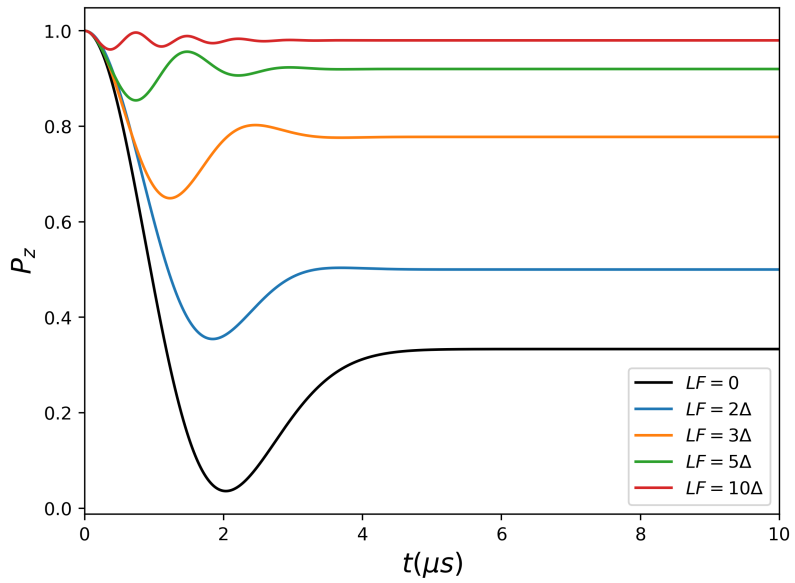

Figure 2.12: *Example longitudinal field Kubo-Toyabe functions for* $\Delta = 1\ mT$

$$P_z(t, B_{ext}) = 1 - \frac{2\Delta^2}{B_{ext}^2}\left(1 - \cos\left(\gamma_\mu B_{ext} t\right)\exp\left(-\gamma_\mu^2\Delta^2 t^2/\,2\right)\right) + \frac{2\gamma_\mu\Delta^4}{B_{ext}^3}\int_0^t \sin\left(\gamma_\mu B_{ext}\tau\right)\exp\left(-\gamma_\mu^2\Delta^2\tau^2\right)d\tau. \tag{2.34}$$

It is possible that the magnetic field at a given muon site will not be static and is instead dynamic (changing over time). For example the muons could experience a changing magnetic field due to spin fluctuations of nearby magnetic moments (electronic or nuclear). A muon could also experience a changing magnetic environment by 'hopping' to a new site in the sample due to a thermal excitation. An analytic form for the dynamic polarisation in a longitudinal field exists and is given by the Keren function [95], which is discussed later in this thesis. In the absence of an applied magnetic field the dynamic muon polarisation is given by[96]

$$P_z(t) = P_{z,KT}(t)e^{-\nu t} + \nu\int_0^t P_z(t-t')P_{z,KT}(t')e^{-\nu t'}dt'. \tag{2.35}$$

Where $P_{z,KT}$ is the static Kubo-Toyabe polarisation, and ν is the frequency of the fluctuations. Note that the quantity of interest $P_z(t)$ is on both sides of the equation. Equation 2.35 can be difficult to compute and so typically approximations are used.

In the case of slow fluctuations, usually defined as $\nu/(\gamma_\mu\Delta) < 1$ only the 1/3 tail is affected and the relaxation in the region of the tail is given by equation 2.36.

$$P_z\left(t,\nu\right) = \frac{1}{3}\exp\left(\frac{-2\nu t}{3}\right). \tag{2.36}$$

In the limit of fast fluctuations ($\nu/(\gamma_\mu\Delta) >> 1$), the initial dip and recovery

of the asymmetry characteristic of the Kubo-Toyabe is not observed and the polarisation is simply an exponential given by equation 2.37. In the fast fluctuation limit, the decay of the muon polarisation is inversely proportional to ν because of motional narrowing. Motional narrowing in μSR is similar to the process of the same name in nuclear magnetic resonance (NMR)[97] [86] except in the time domain rather than the frequency domain.

$$P_z\left(t,\nu\right) = \exp\left(\frac{-2\gamma_\mu^2\Delta^2}{\nu}\right). \tag{2.37}$$

In the intermediate regime ($\nu/(\gamma_\mu\Delta) > 1$) the polarisation is given by the Abragam form (equation 2.38). Examples of each of these cases are shown in figure 2.13.

$$P_z\left(t,\nu\right) = \exp\left(\frac{-2\gamma_\mu^2\Delta^2 t}{\nu^2}\left(\exp(-\nu t) - 2 + \nu t\right)\right) \tag{2.38}$$

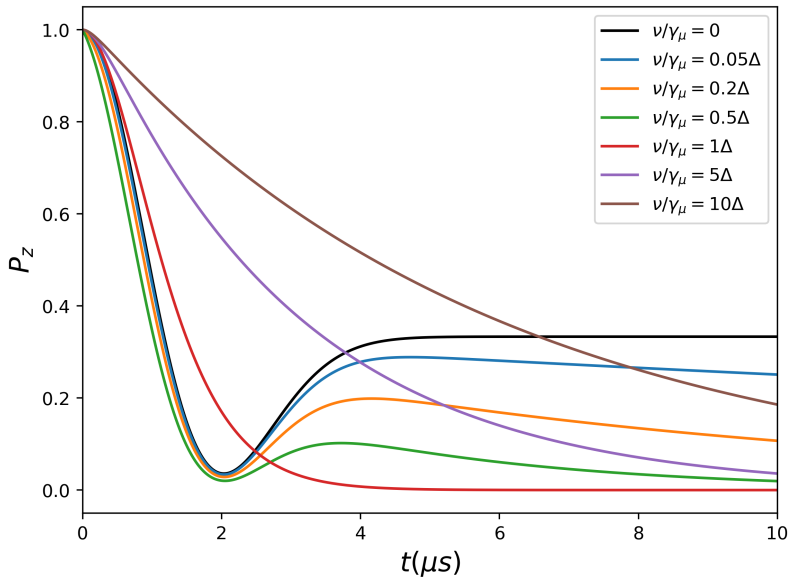

Figure 2.13: *Example dynamic Kubo-Toyabe functions for* $\Delta = 1$ mT *and no applied magnetic fields.*

Chapter 3

High Frequency ac Susceptometry

3.1 Operational Principle

An ac susceptometer must have two key components: a method of applying an oscillating magnetic field and a method of measuring the oscillating response from the sample. There are several techniques for achieving this, such as using tank resonators[98, 99, 100], mutual inductance bridge[101], SQUIDs or inductive coils.

In the tank resonator technique a circuit with some known inductance and capacitance is used and its resonant frequency, ω_{res} measured. Some of the inductance will be from the presence of a coil of some sort and during a measurement the sample under investigation is inserted into this coil. This changes the inductance of the circuit by an amount that is proportional χ', which changes the resonant frequency of the circuit because $\omega_{res} \approx (LC)^{-1/2}$. This change in ω_{res} is measured and χ' can then be calculated.

In a mutual inductance bridge the circuitry is quite complicated (see fig. 1 of

ref. [101]), however as a simple overview it consists of a primary and secondary circuit. The primary circuit contains a coil of wire with an oscillating current running through it, the secondary circuit is not driven and contains two counter wound coils. The sample is placed between the primary coil and one of the secondary coils, changing the mutual inductance between them. The susceptibility can be calculated from the change in mutual inductance.

In the inductive coils technique there are two circuits: the excitation circuit and the detection circuit. In the most basic form the excitation circuit consists of a source of ac voltage as well as an excitation coil of some kind, usually (but not always) a solenoid. In the detection circuit there will be at least one detection coil which is/are connected to an instrument capable of detecting the voltage at the measurement frequency as well as any phase shifts compared to the excitation circuit. A common set up for the detection circuit is to have two counter wound detection coils that are both in series with a lock-in amplifier (this configuration is known as a first order gradiometer). The purpose of having two counter wound coils is that this in principle allows for any background offsets present in both coils to be easily corrected for. It is also possible to have higher order detection coils, for instance a second order gradiometer has three coils, which can afford greater sensitivity and noise cancellation. For now however only the simplest first order case with be discussed. During the measurement the sample is initially placed in the centre of one of the detection coils. The flux through this coil is then given by

$$\Phi_1(t) = \mu_0 A(M(t) + H(t)) \tag{3.1}$$

and the flux through the other coil given by

$$\Phi_2(t) = \mu_0 A H(t) \tag{3.2}$$

where, A is the area of the coils (we will assume that A is the same for both coils). By Lenz's law this then leads to an e.m.f. in the detection circuit given by

$$\mathcal{E}(t) = -\mu_0 N A \alpha \frac{\partial}{\partial t} \left[M(t) + H(t) - H(t) \right] \tag{3.3}$$

where, N is the number of turns in each of the two detection coils and α is a complex coupling constant that is dependent on the coil geometry and sample properties. Example sample properties include shape, size and in the case of a powder sample: filling factor. In the case of a sample that has a symmetric cross-section along its length, uniform thickness for the length of the detection coil and a uniform internal $M(t)$ field then $\alpha = 1$.

The sample is then moved so that it is in the centre of the second coil. The emf induced in the circuit is now

$$\mathcal{E}(t) = -\mu_0 N A \alpha \frac{\partial}{\partial t} \left[-M(t) + H(t) - H(t) \right] \tag{3.4}$$

the difference between these two voltages is then taken giving

$$\Delta V(t) = -2\mu_0 N A \alpha \frac{\partial M(t)}{\partial t} \tag{3.5}$$

where $\Delta V(t)$ is the difference in the emf between when the sample is in the first and second coils and is a complex quantity. Then substituting in

$$M(t) = (\chi' - i\chi'') H_0 e^{i\omega t} \tag{3.6}$$

where H_0 is the amplitude of the excitation field. We have an equation for the complex susceptibility given by

$$\Delta V(t) = -2\mu_0 NA\alpha(\chi' - i\chi'')H_0 \frac{\partial}{\partial t}\left[e^{i\omega t}\right] \tag{3.7}$$

When measuring using a lock-in amplifier one measures the amplitudes of the in phase and out of phase as opposed to the time varying voltages so finally, by performing the derivative and considering only the amplitude we have

$$\Delta V(t) = 2\mu_0 NA\alpha H_0\omega(\chi'' + i\chi') \tag{3.8}$$

The SQUID technique is quite similar to the inductive coils technique. An oscillating magnetic field is applied to the sample which is positioned close to some detection coils, the signal induced in the detection coils is then measured by the SQUID (see diagram in ref. [102]). The voltage output of the SQUID can then be converted to ac susceptibility.

3.2 Motivation for High Frequency

Magnetic systems with dynamics on different time scales of measurement lend themselves best to different techniques. Figure 3.1 shows the typical dynamic ranges for different magnetic measurement techniques, for example it shows muon spin rotation is best for measurements in the microsecond range. For nanosecond to picosecond dynamics either Mössbauer spectroscopy or neutron scattering is the most appropriate technique. In the 10^0 s^{-1} to 10^4 s^{-1} dynamic window we can see that there are two available techniques, nuclear magnetic resonance (NMR) and ac susceptibility. NMR measures the response of the nuclear spins

in the sample and requires the use of a large DC magnetic field, so its potential applications are distinct from those of ac susceptibility. The similar technique nuclear quadrupole resonance (NQR) does not require magnetic fields but is only applicable to samples where there is a nuclear quadrupole moment.

For samples with dynamics faster than this ($> 10^4$ s^{-1}), muon spin rotation is most suitable. In some samples the perturbative nature of muon spin rotation (from the presence of the muon) can alter the system under investigation so significantly that its results are not representative of the unperturbed sample[103] adding significant difficult to the interpretation of data. In order to perform accurate measurements in these samples it is therefore required to invent either an entirely new technique or to extend the range of existing ones. Pyrochlores are an example of such a system in which the implantation of a muon can distort the crystal structure [103]. This is a particular concern in the rare earth pyrochlores with non-Kramers ions as the magnetic ion such as $Ho_2Ti_2O_7$ and $Pr_2Sn_2O_7$. A Kramers ion (such as the Dy ion in $Dy_2Ti_2O_7$) has an odd number of electrons[1] and so because of Kramers theorem cannot have its ground state split by an electric field. A non-Kramers ion has no such protection against splitting and so the muons can have a significant impact. In some cases the muon causes a change in spin fluctuation rates and can even fundamentally change the crystal field levels of the rare earth ions completely changing the physics of the system the muons were intended to measure. Some of the materials discussed in this thesis have a pyrochloric or similar structure and provided the motivation to develop a technique capable of measuring in the 10^4 s^{-1} to 10^7 s^{-1} dynamic range. These are not the only samples in which this device is expected to have applications however, for example it has already seen use in the measurement of magnetic nano particles [104][105].

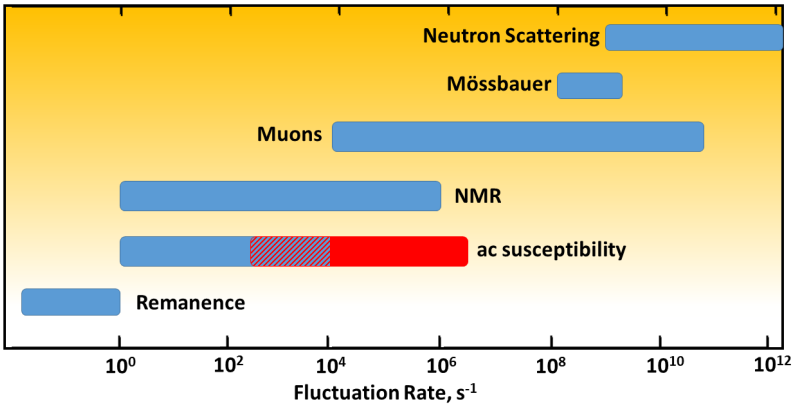

Figure 3.1: *Typical timescales of measurement techniques that detect dynamic magnetic processes in materials. The red regions indicate the new dynamic range made available by the instrument that is the focus of this chapter. Based on the diagram in ref. [6].*

3.3 Design Considerations

Most commercially available ac susceptometers are limited to the kHz range. There is no intrinsic physical reason for this limit, it is instead a product of the desire to balance easily changed drive frequencies, ease of integration with the sample environment, good frequency stability, good sensitivity and the ability to produce a (relatively) large excitation field. Previous attempts to achieve ac susceptibility measurement at high frequency have included tunnel diode circuits[98], resonant LC circuits[100] and helical resonators[106] but all of these techniques are limited by long measurement times as they require physically changing the circuit to measure at a new frequency. Another design is to use torroidal coils[107, 108] however these are plagued by difficulties in mounting the sample and can begin to radiate at their highest measurement frequencies. Inductance based designs [109] that meet the above criteria exist but are limited to room temperature. Micro-SQUID designs have been successful for measurement of microscopic samples[110]

but not for bulk samples.

For the high frequency susceptometer described in this chapter we have managed to extend the frequency range without significant sacrifices in any of these areas.

The first thing to consider when designing a high frequency ac susceptometer is that it is inductive and capacitive to some degree. The source of the inductive contribution is obvious with both circuits containing at least one coil of wire. The source of the capacitance is due to parasitic capacitance in the coils, wires and connections of the full circuit. Parasitic capacitance occurs due to charge building up across two different sections of conducting wire that come close to one another in the apparatus.

The inductance of a component is its propensity to resist a change in the electrical current flowing through the circuit of which it is a part. A component that adds inductance to a system is called an inductor and is usually a coil of wire that may or may not be wrapped around a core. When a current flows in an inductor some of the energy from the current is stored as potential energy in a produced magnetic field. If the current through the inductor is changed, then the magnetic field produced is also changed. The changing magnetic field through the inductor induces an e.m.f. in the circuit given by Lenz's law to be

$$\mathcal{E}(t) = -L\frac{dI}{dt} \tag{3.9}$$

where L is the inductance of the inductor and is measured in henrys (H). The negative sign in equation 3.9 shows that the induced e.m.f. will oppose the change in current, tending to sustain a current when the current in the circuit is being reduced and to reduce a current when it is being increased.

The capacitance of a component is its ability to store electric charge for a given voltage applied across them. A component that adds capacitance to a circuit is called a capacitor and will generally consist of two conductive surfaces separated by an insulating material or simply empty space. A capacitor will produce a current when the voltage across it is changed, this relationship is given by

$$I = C\frac{dV}{dt} \tag{3.10}$$

where C is the capacitance of the capacitor and is measured in farads (F). The absence of a negative sign shows that the current produced by a capacitor will work with a change in the applied voltage. Not immediately obvious from these equations however is that both inductors and capacitors cause a phase shift between the voltage and the current in the circuit. Assuming a sinusoidal drive voltage, an inductor will cause the current through it to lag behind the voltage by 90°. Similarly a capacitor causes the voltage across it to lag behind the current by 90°. This may be understood for the inductor by considering that the rate of change in current is greatest as it crosses through I=0 by equation 3.9 the voltage generated across the inductor will therefore be greatest at this time. Figure 3.2 illustrates this point. The phase lag from a capacitor may be understood in a similar way.

Another consequence of inductance and capacitance in an ac circuit is that they will make the response of the circuit frequency dependent. To see this, we will examine a circuit with a drive voltage given by $V(t) = V_0 \exp(i\omega t)$ that contains a single source of capacitance and then a circuit with a single source of

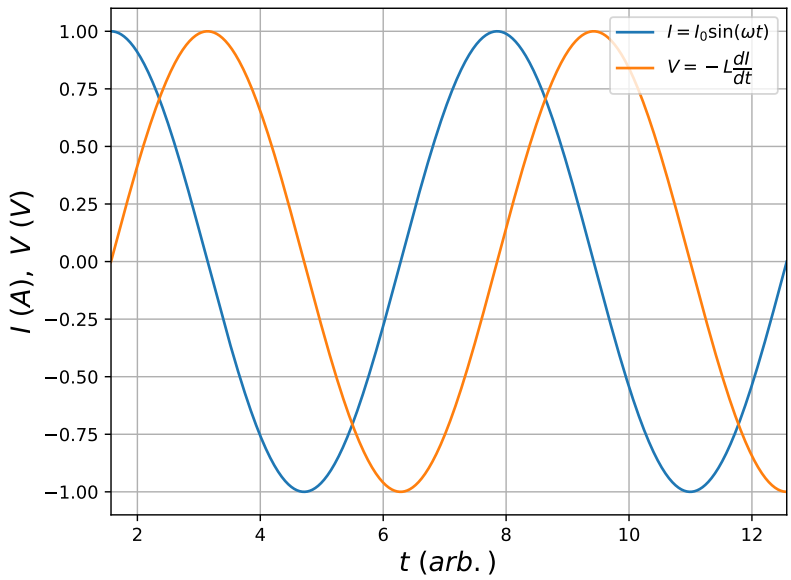

Figure 3.2: *Real time values of the voltage and current in a circuit consisting of an inductor and capacitor connected in series showing the 90° phase difference*

inductance. We will use phasor notation such that Ohm's law:

$$V = IZ \tag{3.11}$$

is valid. In this equation Z is the impedance of the circuit and can be complex. The current through a circuit with a capacitor is

$$I = C\frac{dV}{dt} \tag{3.12}$$

substituting in for V and performing the derivative we have

$$I = Ci\omega V_0 e^{i\omega t} \tag{3.13}$$

which is equivalent to

$$I = Ci\omega V \tag{3.14}$$

by comparison with equation 3.11 we then have

$$Z_C = \frac{1}{i\omega C}. \tag{3.15}$$

Similarly for a circuit with only an inductor the current will be given by

$$I = \int \frac{-V}{L} dt \tag{3.16}$$

substituting in for V and performing the integral we have

$$I = -V_0 \frac{e^{i\omega t}}{i\omega L}, \tag{3.17}$$

which by comparison with equation 3.11 gives

$$Z_L = -i\omega L. \tag{3.18}$$

Equations 3.15 and 3.18 have three important consequences. Firstly, they show that the behaviour of the circuit is frequency dependent. Secondly, because they contain the imaginary unit, i, they will affect the phase shift between the voltage and current in the circuit, and the extent of this phase shift will also be frequency dependent. Thirdly, because Z_L leads to an impedance that increases with frequency and Z_C leads to one that decreases with frequency, then if the inductance and capacitance are connected in series then there will be a minimum in the impedance at a particular frequency, known as the resonant frequency ω_0. If the components are in parallel then the resonant frequency will represent a

maximum in the impedance. In both cases the resonant frequency is given by

$$\omega_0 = \frac{1}{\sqrt{LC}}. \tag{3.19}$$

In a more complicated circuit the resonant frequency is not as simply defined.

Therefore when designing an ac susceptometer it is important to try and minimise the capacitance and inductance, in order to reduce frequency dependent effects in the circuit. In an ac susceptometer the largest source of inductance will be the excitation coil in the excitation circuit and the detection coils in the detection circuit. The inductance of a long tightly wound solenoid is given by

$$L = \frac{\mu N^2 A}{l} \tag{3.20}$$

where μ is the permeability of whatever is in the coil (such as air, a cryostat exchange gas or the sample), N is the number of turns of the coil, A is the cross-sectional area of the coil and l the length of the coil. Reducing the number of turns and reducing the cross sectional area seem like easy ways to reduce the inductance however as a result of equation 3.8 this will also reduce the sensitivity of the detection circuit. Increasing the length is a viable option, however, because the two detection coils have to be kept reasonably far apart this can cause problems if there is limited space available. For the excitation coil reducing the inductance by any mechanism will involve a reduction in the amplitude of the excitation field, reducing the minimum resolvable susceptibility.

Capacitors are not usually added to either circuit in an inductance ac susceptometer and so any capacitance present will be a parasitic capacitance. Parasitic capacitance can be very difficult to remove from a circuit, especially because the sources of it may not always be obvious. In order to reduce the parasitic ca-

pacitance it is best to try and keep different parts of the circuit away from each other and also from any other conductive materials. Whilst this can be achieved in the coils by increasing the separation between turns, trying to do this can be difficult for wiring connecting the coils to the instruments. Separating wires from one another means that they cannot be twisted round each other to create twisted pairs - a common practice for reducing crosstalk in ac circuits. Crosstalk is an effect where nearby wires can have undesired influences on each other due to capacitive, inductive or direct conductive effects. Getting the signal from the coils to the instruments without picking up significant noise and without adding a large capacitance was one of the biggest concerns when designing the instrument described in this chapter.

It is also important to consider the value of the resonant frequency. The resonant frequency should be much larger than the intended frequency range of the instrument in order to have a reliable response. The equivalent circuit for a solenoid is shown in figure 3.3. It shows that the capacitance and inductance of a solenoid are in parallel with one another and therefore the resonant frequency represents a maximum in the impedance. Consequently, as the excitation circuit begins to approach resonance the impedance increases which reduces the current flowing through it and in turn that reduces the amplitude of the excitation field.

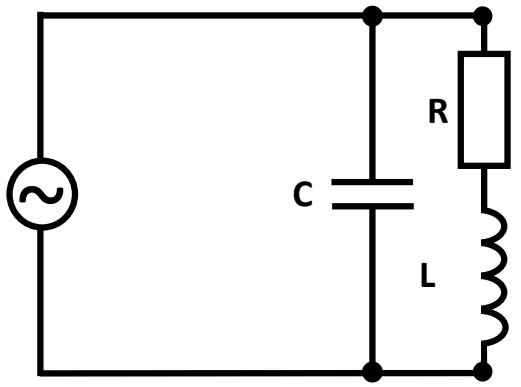

Figure 3.3: *Equivalent circuit diagram for a solenoid. Note that the parasitic capacitance acts in parallel to the inductance and not in series.*

3.4 Our Design

The ac susceptometer design discussed in this chapter is intended to be integrated into a Quantum Design Physical Property Measurement System (QD - PPMS). Integration with the QD-PPMS was chosen because this allows for our susceptometer to work across a wide temperature range from 2 K to 300 K. The QD-PPMS also contains a superconducting magnet which allows for measurements in an applied dc field. The coil set is designed to sit on the base of the QD-PPMS sample space, inside the variable temperature insert (VTI) so that the coil set is close to the QD-PPMS thermometers. The coils of the susceptometer are wrapped around a plastic former which is of small enough dimension that the field produced by the QD-PPMS magnets is uniform along their length. Figure 3.4 shows their approximate relative positions. The QD-PPMS also has a thermometer in the wall of the sample space that is at a height similar to the top of the coil set which allows for monitoring of any temperature gradients across the coil set.

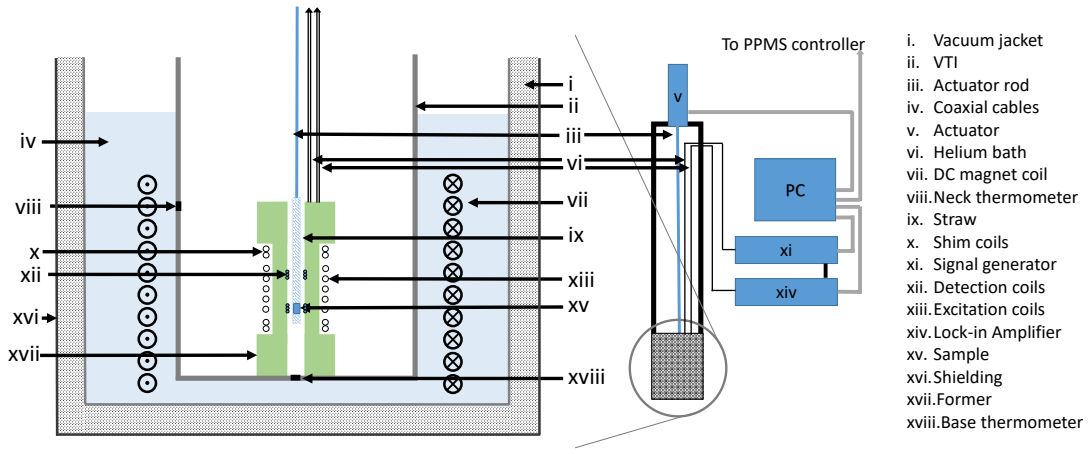

Figure 3.4: *Diagram of the high frequency susceptometer within the QD-PPMS sample space.*

The excitation coil is wound in two overlapping helixes such that the wires cross each other in a series of "X" like points and are not close to one another along their length. This allows for the separation between sections of wire to be maximised, reducing the parasitic capacitance of the coil. This coil design is similar to that developed by researchers at Research Institutes of Sweden (RISE) and discussed in reference [109]. Researchers involved in that project were also involved in the design stages of this high frequency project. The geometry of the excitation coil was designed in collaboration with researchers at RISE. In the original design the excitation coil is 80 mm in length, made up of 20 turns, and is made from NbTi wire. Two additional turns of shim coil are added at either end of the excitation coil to improve uniformity of the excitation field along its length as shown in figure 3.5. Later designs of the excitation coil were made from copper wire but other attributes of the coil design did not change significantly. As shown in figure 3.4, the detection coils are inside of the excitation coil and are connected in series and wound in opposite directions to one another. Each detection coil is 8 mm in length and their closest edges are separated by 20 mm which is sufficient

separation to avoid significant mutual inductance between them. Each coil is made up of 15 turns and is made of single core copper wire. The detection coils are also well away from the ends of the excitation coil meaning they do not experience any edge effects. A higher order gradiometer was not used because this would have had negative effects on the frequency range as a result of increased inductance in the detection circuit.

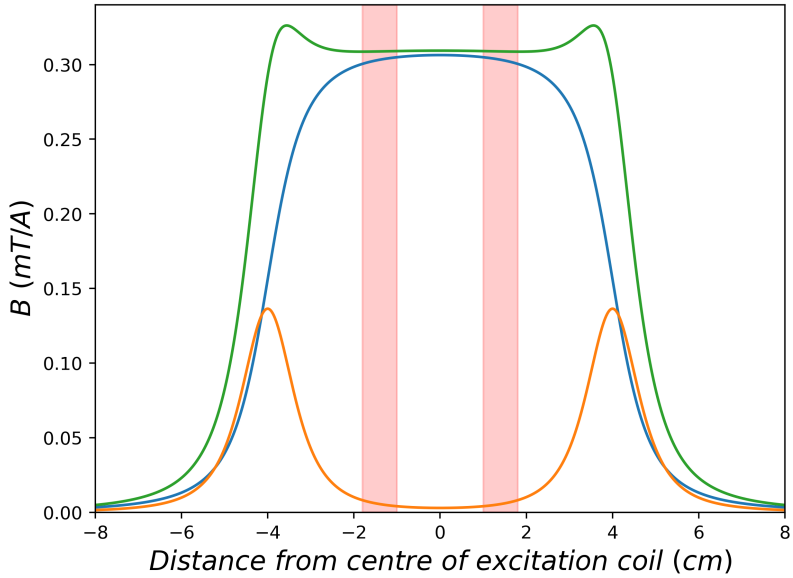

Figure 3.5: *Calculation of magnetic field per unit current applied to the excitation coil. The contribution from the main coil is shown in blue, the shim coils in orange and the total field in green. Red shaded regions indicate the locations of the detection coils.*

The inductance of the excitation coil in the first design was measured to be 3.58 μH (at 100 kHz) with a calculated parasitic capacitance of 9.2 pF resulting in a coil resonance at 27.8 MHz. A superconducting material was chosen in order to avoid resistive heating in the coil warming the the sample space. When in the resistive state the excitation coil has a resistance of 90.8 Ω. The superconducting material used (NbTi) has a critical temperature, $T_{C,NbTi}$, of 9.8 K and it was

found that measurements at temperatures near $T_{C,NbTi}$ encountered significant problems with unwanted heating, leading to a measurement blind spot. This is because the QD-PPMS has less cooling power at temperatures near $T_{C,NbTi}$ and so could not compensate for the heating effect of the coil. At temperatures well above $T_{C,NbTi}$ the QD-PPMS has more cooling power available and so the sample temperature is stable during measurement. In order to remove the temperature blind spot it was decided to construct a coil set with a copper excitation coil, of which more than one was eventually made. The copper designs had similar values of inductance and capacitance but with a much lower resistance, it was found they performed as well as the NbTi coil at base temperature (2 K). The excitation coil is connected to a Stanford Research Systems DS345 signal generator which has a series impedance of 50 Ω and can produce a periodic signal at frequencies up to 30 MHz with a maximum amplitude of 10 V peak-to-peak.

The detection coil circuit had an inductance of 5.3 μH (at 100 kHz) and a calculated parasitic capacitance of 9.9 pF resulting in a coil resonance at 22.0 MHz. The coils have a resistance of 0.86 Ω, their design was unchanged in later iterations of the coil. Originally the circuit was connected to a Stanford Research Systems SR844 which has a series impedance of 50Ω and can perform phase sensitive detection up to 200 MHz but has a minimum measurement frequency of 25 kHz which restricts the minimum measurement frequency. In later set ups a Stanford Research Systems SR865A was used which has a more suitable frequency range of 1 mHz to 4 MHz but has a series impedance of 10 MΩ and parallel capacitance of 25 pF, so in this set up a 50 Ω terminator is used.

When the coil set is in the QD-PPMS sample space it rests on the bottom, but the wires to connect to the instruments must come out at the top. The QD-PPMS does have connections at the base of the sample space that can be connected to

instruments, however early trials using these connections were unsuccessful. The inbuilt wiring was found to have insufficient noise and frequency stability for high frequency applications. This means that a significant length of wire is required in the circuit, which can introduce significant sources of noise (for example, by acting as an antenna for any electromagnetic noise in the vicinity) and be a source of capacitance. Even slight movement of the wires during a measurement can introduce noise which can be caused by the vibration of the QD-PPMS. We have found that by using mini-coaxial wire with a low capacitance per metre these problems can be minimised. The walls of the VTI provide the wires with a good amount of shielding from noise and as long as the wires are kept away from the walls then vibration is also not an issue.

Samples are mounted in plastic drinking straws, chosen because they have almost no magnetic response being only very weakly diamagnetic. The straws are attached to the end of a carbon fibre rod which extends the length of the sample space (≈ 1 m). The carbon fibre rod is also connected to an Accu-Glass 2" linear actuator, mounted on the top of the sample space. The actuator allows for the sample to be moved between the two detection coils during a measurement and is accurate to within 0.1 mm allowing the sample to be positioned very precisely. Because the motor is far away from the coil set it does not introduce significant noise when in use and the sample is always stationary during a measurement regardless.

The PPMS and ac susceptibility measurement are both controlled from the same computer (in this case the computer that comes as part of the PPMS). The ac susceptibility measurement is controlled using a National Instruments LabView program, with the instruments connected to the computer using GPIB cables or USB (in the case of the actuator). Several programs are used when

performing a measurement which can be collected into three main categories by their purpose.

The first category of programs convert the measured voltage into a susceptibility by applying the calibrations described in section 3.5, they also determine the next measurement frequency. This group of programs were produced by the Swedish team and were locked from editing, the remaining two groups were produced as part of this thesis.

The second category of programs manage the instruments required for the measurement. They manage things such as setting the lock-in amplifier parameters (time constant, sensitivity etc.), reading the voltage recorded by the lock in, setting the parameters on the signal generator and controlling the actuator.

The third category consists only of one program which allows for temperature and field scans to be performed by sending instructions to the PPMS to go to the required temperature or field and then waiting for it to arrive before triggering an ac susceptibility measurement to occur.

3.5 Calibration

In order to perform a measurement with the ac susceptometer it is necessary to perform two calibration measurements. The first consists of a background calibration in which a sample holder is measured with no sample, in order to detect and then account for any signal from the sample mounting, as well as any signal that arises due to intrinsic asymmetries in the detection coils. The operational principle for the background calibration is simple and involves moving the sample holder to the approximate centre of one of the detection coils and recording the voltage on the lock-in. The sample is then moved to the centre of

the other detection coil and the voltage is again recorded. The difference between these two values is then taken and subtracted from all future measurements. Example background calibrations are shown in figure 3.6.

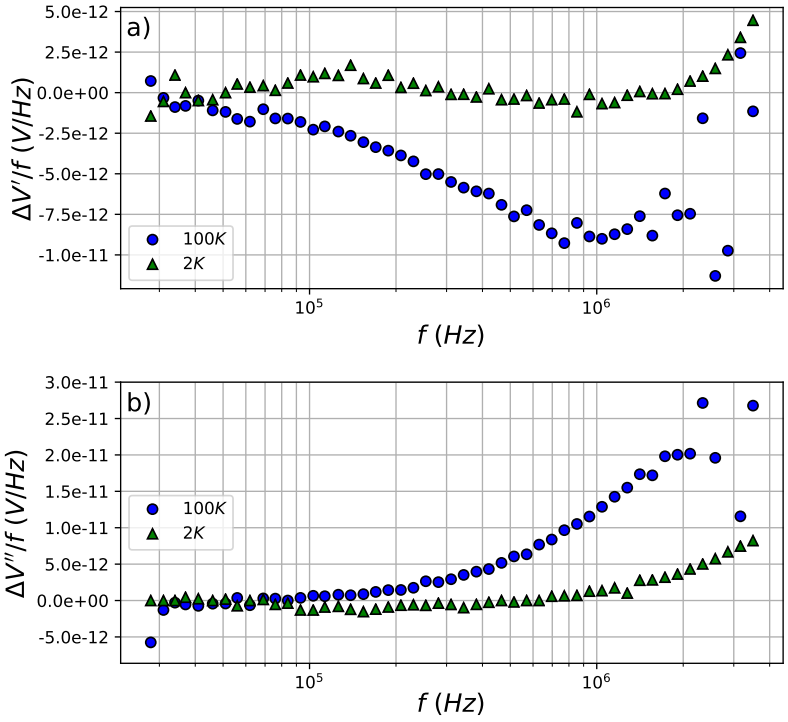

Figure 3.6: *Example background calibrations performed at 100 K (blue circles) and 2 K (green triangles). Figure a) shows the real part of the background voltage difference and figure b) shows the imaginary part. In both figures the voltage is divided by the measurement frequency.*

The other required calibration is the gain and phase calibration, which requires measuring a sample that has a well known susceptibility, χ_{calib}, at the frequencies to be measured at. For simplicity, the chosen samples will usually be ones that have no imaginary part to their ac susceptibility. The calibration sample is then measured and a calibration factor given by

$$G = \frac{\chi_{calib} V_{calib} H 2\pi f}{\Delta V_{cal} - \Delta V_b} \tag{3.21}$$

where G is the calibration factor which can be complex to allow for phase corrections, V_{calib} is the volume of the calibration sample, ΔV_{cal} is the voltage difference recorded on the lock in during the calibration measurement and ΔV_b is the background voltage correction from the background calibration. Because G is a complex factor it can be decomposed into polar form like: $G = ge^{i\phi}$ where g is the gain that is required and ϕ is the phase correction. Example gain and phase calibrations are shown in figure 3.7 using two different calibration samples at different temperatures.

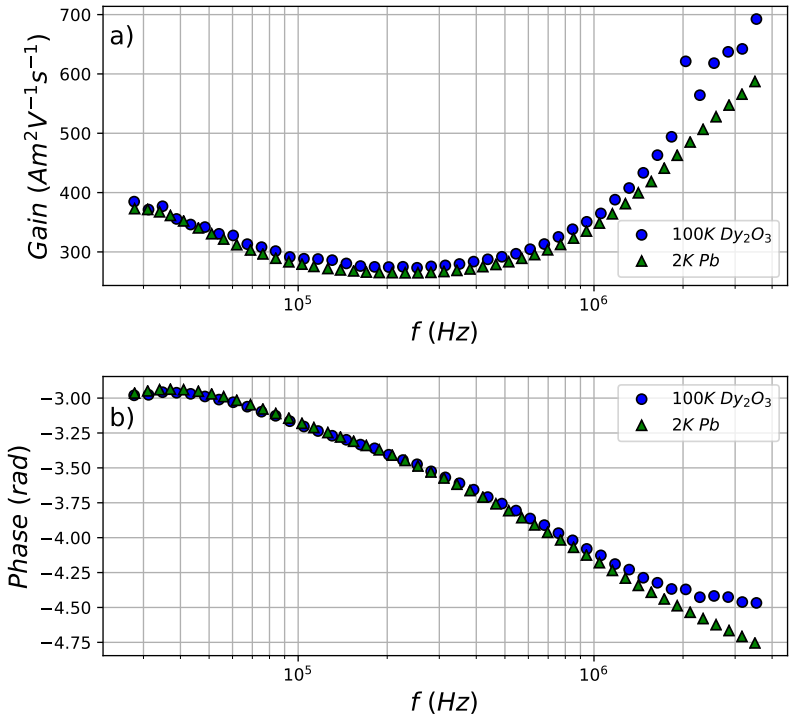

Figure 3.7: *Example gain and phase calibrations. Blue circles show calibrations performed at 100 K using the Dy_2O_3 sample, green triangles show calibrations performed at 2 K using the lead sample. Figure a) shows the gain, g, and figure b) shows the phase, ϕ.*

The two samples used for the calibrations shown in figure 3.7 are lead (Pb) and dysprosium oxide (Dy_2O_3). Pb is a suitable calibration sample because it is su-

perconducting below 7.2 K[111] and superconductors are perfectly diamagnetic. Its superconducting properties mean it will have χ'=-1 when in the superconducting phase (at least in principle) and this property is used for the calibration. Superconductors can have a peak in χ'' at temperatures close to their critical temperature however this is only expected in type-II superconductors[112] and Pb is type-I (the distinction between type-I and type-II superconductors is explained in section 3.6). Dy_2O_3 is a commonly used calibration standard for ac susceptibility devices[113, 114] due to the large magnetic moment of the Dy ions causing a large susceptibility. Fast relaxation times in Dy_2O_3 mean that χ''=0 up to very high frequencies. Dy_2O_3 has a Néel temperature of 16.8 K[115] (lower values have also been reported) and is therefore suitable for calibration at temperatures $\gtrapprox$70 K. Our Dy_2O_3 sample is a powder sample with a cylindrical shape. Measurements (figure 3.8) were performed using the ACMS option of the QD-PPMS at 10 kHz and find a Néel temperature of (15.04 $\pm$ 0.04) K using a demagnetisation factor of 0.37. The inset of figure 3.8 shows that the imaginary part of the ac susceptibility is very small across the entire temperature range measured, suggesting no imaginary part at higher frequencies than 10 kHz, at least in the intermediate temperature range.

The ACMS option was also used to measure the lead calibration sample at 10 kHz, shown in figure 3.9. The data has not been demagnetisation corrected as it is not necessary to know the "true" susceptibility of the sample for a gain and phase calibration which can be performed using the "apparent" susceptibility. Figure 3.9 shows the sample transitioning to superconductivity at the expected temperature (7.2 K), the sample is also found to be diamagnetic above this temperature as is expected. Below T_c no imaginary part is measured indicating the sample's suitability as a calibration sample.

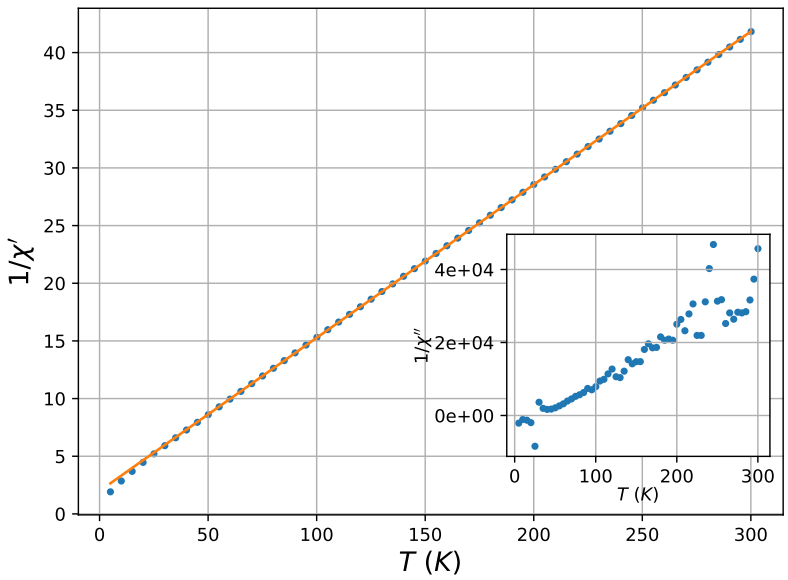

Figure 3.8: *AC susceptibility measurements on powder Dy_2O_3 at 10 kHz in an excitation field amplitude of 0.5 G. Main figure is the inverse of the real part of the AC susceptibility and inset is the inverse of the imaginary part.*

When calibrating for a measurement run it is standard practice to calibrate at temperatures similar to the ones to be measured at. Therefore the Dy_2O_3 is used to calibrate at higher temperatures of the order of 100 K and the lead is used to calibrate at lowest temperatures (usually at 2 K).

In order to perform a measurement (or calibration) it is first necessary to locate the sample relative to the two detection coils. In order to achieve this the QD-PPMS will be set to maintain a constant temperature and magnetic field and the sample will be slowly moved through the entire range available to the motor. As the sample is moved the excitation coil will produce an excitation field at a constant frequency and amplitude. At regular intervals the amplitude of the voltage detected by the lock in amplifier is recorded. Plotting this voltage against the motor position will produce a shape like the one in figure 3.10, where the maximum and minimum show when the sample is in the centre of a detection

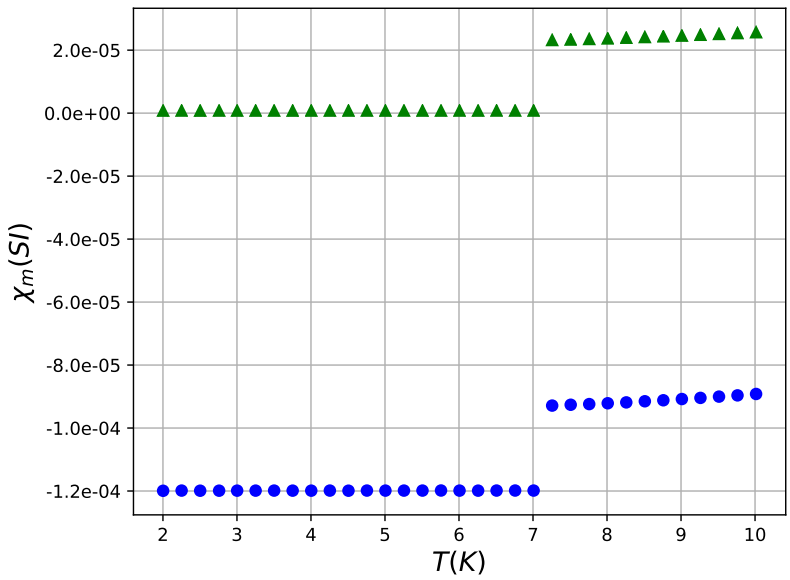

Figure 3.9: *ac susceptibility measurements on the lead calibration sample at 10 kHz. Blue circles indicate the real part of the mass susceptibility and green triangles the imaginary part.*

coil. It is therefore possible to extract the coil positions directly from these points, however if the sample has a small susceptibility then this trace may be noisy and so they will be more easily extracted by fitting. Finding the centre points of each of the detection coils accurately is important because a 0.5 mm position error in one coil leads to a 1% error in the recorded voltage in that coil, a position error of 2 mm in one coil leads to a 10% error in the recorded voltage.

To derive a fitting equation we need to know the flux through the detection coils. To calculate this we will consider a magnetic dipole with magnetic moment $\boldsymbol{\mu}$ at distance z from the centre point of a loop of wire, that is being cut by a flux, Φ_{loop}. We will assume that the dipole has no displacement in either the x or y directions, and has a negligible size. To find the flux we need to perform the integral given by

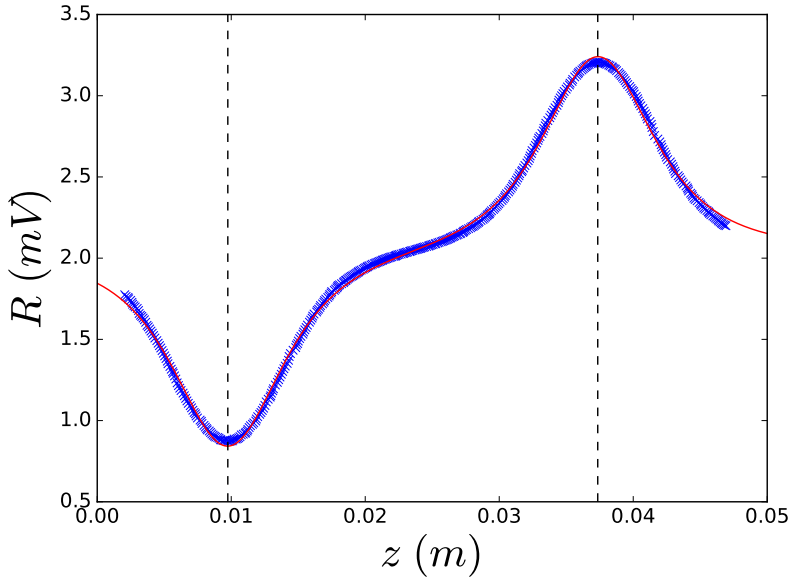

Figure 3.10: *Signal amplitude against motor position to locate a sample relative to the coils. Sample shown is the superconducting lead calibration sample. The red line is a fit to equation 3.27. Vertical dashed lines indicate detection coil positions* z_1 *and* z_2

$$\Phi_{loop} = \int_S \boldsymbol{B}_{dipole}.d\boldsymbol{A} \tag{3.22}$$

where $\boldsymbol{B}_{dipole}$ is the magnetic field from the magnetic dipole, $d\boldsymbol{A}$ is a surface element to be integrated over. In order to simplify the derivation we will instead consider the magnetic flux through a spherical cap of radius $\sqrt{a^2+z^2}$, where a is the radius of the loop of wire, the flux through the cap and the loop of wire will be the same because $\boldsymbol{\nabla}.\boldsymbol{B} = 0$. We will also use $\boldsymbol{B}_{dipole}$ in the spherical polar coordinate system which is given by

$$\boldsymbol{B}_{dipole} = \frac{\mu_0|\boldsymbol{\mu}|}{4\pi r^3}\left(2\cos(\theta)\hat{\boldsymbol{r}} + \sin(\theta)\hat{\boldsymbol{\theta}}\right). \tag{3.23}$$

We need only consider the component of the magnetic field that is perpendicular to the surface of integration (the spherical cap), which is given by the radial

component of equation 3.23. We therefore need to compute the following integral

$$\int_S \boldsymbol{B}_{dipole}.d\boldsymbol{A} = \int \frac{\mu_0|\boldsymbol{\mu}|}{4\pi r^3} 2\cos(\theta) 2\pi r^2 \sin(\theta) d\theta. \tag{3.24}$$

Performing the integral and then substituting in $\sin\theta = a/\sqrt{a^2+z^2}$, the flux through the coil is given by

$$\Phi_{loop} = \frac{\mu_0|\boldsymbol{\mu}|}{2} \frac{a^2}{(a^2+z^2)^{3/2}}. \tag{3.25}$$

We now consider that the magnetic moment $\boldsymbol{\mu}$ is a time dependent quantity that oscillates sinusoidally and so by Lenz's law induces an e.mf. in the loop. At this point we will also consider the fact that we do not have a single loop but instead a solenoid comprised of N turns of wire. Assuming an oscillating moment given by $|\boldsymbol{\mu}(t)| = |\boldsymbol{\mu}|\sin(\omega t)$ then the induced e.m.f in the solenoid is

$$\mathcal{E}(t) = -\frac{\mu_0 N\omega|\boldsymbol{\mu}|\cos(\omega t)}{2} \frac{a^2}{(a^2+z^2)^{3/2}} \tag{3.26}$$

from here we need only consider the amplitude of the oscillating signal because the measurement will be performed using a lock-in amplifier. We will also now consider that we have two detection coils wound in opposite directions that are at positions z_1 and z_2 as well as some background voltage induced in the detection coils from the excitation coil which we consider by adding a constant, C. The recorded voltage as a function of sample position is then given by

$$R = F\frac{A_1^2}{(A_1^2+(z-z_1)^2)^{3/2}} - F\frac{A_2^2}{(A_2^2+(z-z_2)^2)^{3/2}} + C \tag{3.27}$$

where $R = \sqrt{\mathrm{Re}(V)^2 + \mathrm{Im}(V)^2}$, A_1 and A_2 are the areas of the first and second detection coil respectively and $F = \frac{\alpha\mu_0 N\omega|\boldsymbol{\mu}|}{2}$ in which α is an additional constant

to account for any non-ideal behaviour of the coil. Equation 3.27 is the fitting equation used when locating the sample relative to the coil and an example of this is shown in figure 3.10 showing the coils located at z_1=0.0098 m and z_2=0.0374 m.

3.6 Characterisation & Test Measurements

Using the gain and phase calibration described in section 3.5 it is not necessary to know the magnitude of the excitation field to perform a measurement. This is because the value of the excitation field can be moved to the LHS of equation 3.21 and incorporated into G. This is the standard operating procedure when performing measurements, however in some cases it may be useful to know the magnitude of the excitation field. For instance it may be useful to know the amplitude of the field in order to ensure that measurements stay in the linear response regime. The field amplitude produced for a given drive voltage will be frequency dependent because the impedance of the coil is frequency dependent.

In order to measure the field amplitude two measurements are required. Firstly it is necessary to know the magnetic field produced for a given current, these quantities will be linearly proportional to each other by a factor which we will call the B/I factor. Secondly it is required to know how the current through the coil varies with frequency.

Determining the B/I factor was done by connecting the excitation coil to a DC power supply and then using a longitudinal Hall probe, placed in the centre of the excitation coil, to measure the DC magnetic field produced. This measurement was performed at room temperature. Figure 3.11 a) shows the values measured by the hall probe after correcting for any background signal. Fitting a straight line to the data yields a B/I factor of (0.358±0.008) mT/A. The fit does not pass

perfectly through the origin, instead there is an offset of (-3.47±2.14)×10^{-4} mT meaning some small systematic error will be present in B values calculated from the fit. Additionally there appears to be some weak non-linear trend in the measured data which is difficult to explain. One possible explanation could be the excitation coil cooling over the course of the measurement caused by the environment cooling. This seems unlikely due to the need for a fairly significant temperature drop and the short length of time it took to perform the measurement. In fact the opposite would be more likely due to ohmic heating in the coil however this would have the opposite effect in figure 3.11 a) and was not observed.

To determine the frequency dependence of the current through the coil an analogue differential input amplifier (DIA) was used across a 1 Ω resistor, placed in series with the excitation coil. The DIA output was connected to an oscilloscope to measure the drop in voltage amplitude across the resistor, which is then readily converted to the current through the entire circuit. The apparatus was calibrated by initially connecting only the resistor to the signal generator and measuring its frequency dependent behaviour, which is required because most standard resistors will have some inductance and capacitance of their own. Correcting for the 1 Ω added resistance is not required because these measurements were performed on the NbTi excitation coil which has a resistance of 98.1 Ω and so the added resistance is negligible. Once the voltage drop across the resistor is known as a function of frequency then the current through the circuit is easily calculated and then the B/I factor can be used to calcualte the frequency dependence shown in figure 3.11 b).

The frequency response of the coil set was also measured using a vector network analyser (VNA). A VNA is a device that measures the attenuation and

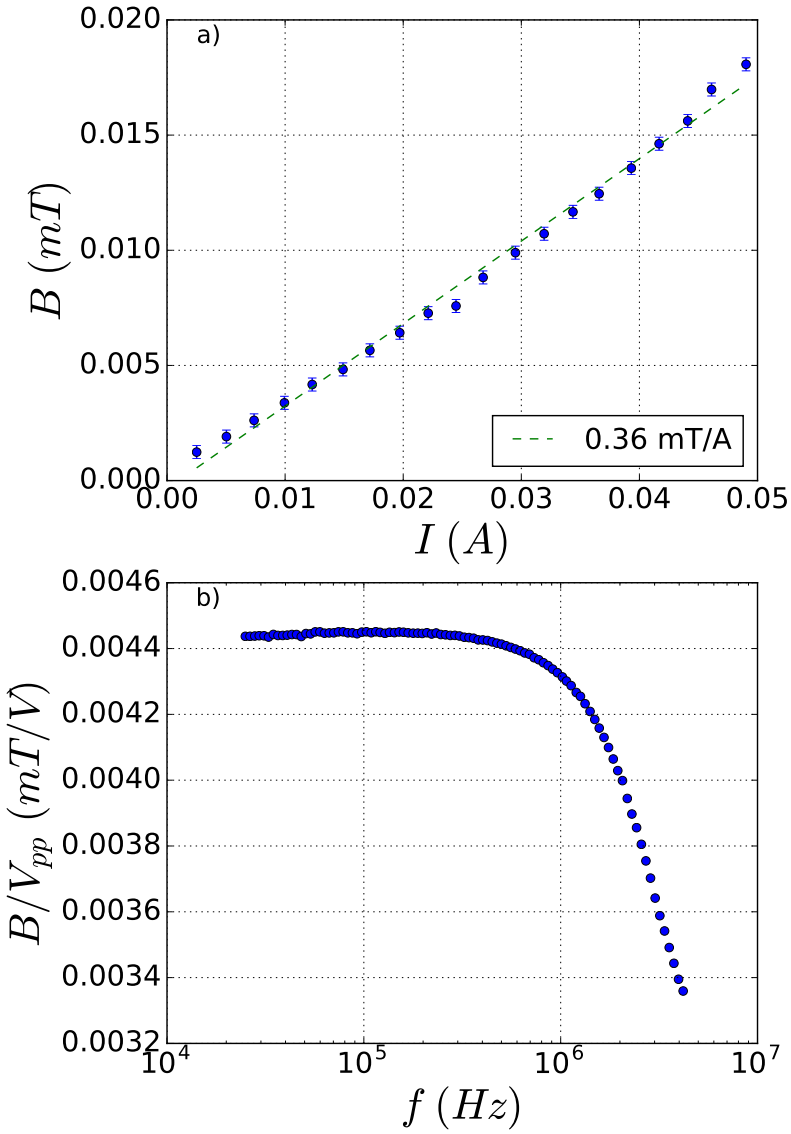

Figure 3.11: *a) Hall probe measurements of the DC magnetic field produced in the centre of the excitation coil for a DC current. Green dashed line is a straight line fit to determine the B/I factor. b) Magnetic field produced per volt (peak-to-peak) applied across the full excitation circuit as a function of frequency.*

phase shift of an ac signal through a circuit as a function of frequency. The VNA measurements shown in figure 3.12 were performed on a later iteration of the coil design than the coil measured in figure 3.11. The later iteration has a slightly altered winding such that the number of turns per unit length changes along its

length, both excitation coils are made of copper and have identical detection circuits. They also include the signal output wires of the circuit. The VNA results show that the detection circuit has a resonance at 8.15 MHz and the detection circuit exhibits a resonance at 10.35 MHz.

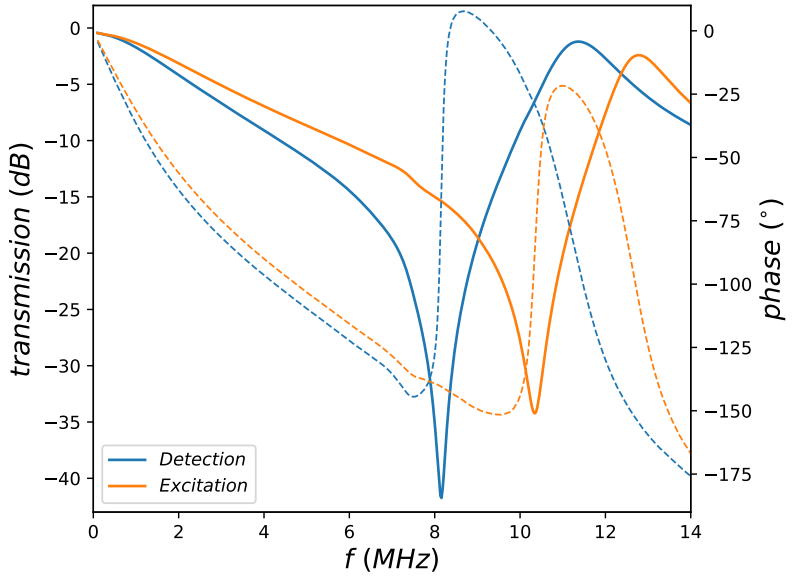

Figure 3.12: *VNA measurements performed on one of the high frequency susceptometer designs. Solid lines are transmission of the signal from one VNA terminal to the other, dashed lines show the phase shift. Showing resonant frequencies at 8.15 MHz and 10.35 MHz for the detection and excitation circuits respectively.*

Simulations of the resonances using the LTspice software predicted resonances approximately order of magnitude higher than measured by the VNA. From those calculations the resonances should be at approximately 100 MHz in both circuits. The reason for the discrepancy is not known, although it is possible to speculate based on differences between the simulation and the real circuit. The simulation takes into account the impedance and parallel capacitance of the signal generator and lock-in amplifier, where as the VNA measurements do not (as the VNA replaces them in the circuit). Additionally the LTspice simulation simulation

does not account for components such as the feed-through to the sample space or the connections between different sections of the circuit .

Test measurements were performed on three samples intended to illustrate the reliable operation of the susceptometer up to high frequency. The first such sample is magnesium diboride (MgB_2) which is a type-II superconductor with a high critical temperature of 39 K[116]. Type-I superconductors are materials which when cooled below their critical temperature, T_c, expel all magnetic flux from their interior and exhibit no electrical resistance. In a type-I superconductor there will be some critical magnetic field strength, H_c, above which the superconductivity will be broken and the material will become resistive again. In a type-II superconductor there are two critical fields, H_{c1} and H_{c2}. If the superconductor is in a magnetic field less than H_{c1}, then the material will behave in the same way as a type-I superconductor that is below H_c. If the magnetic field is increased beyond H_{c1} but is still less than H_{c2} then the superconductor enters a vortex phase. In the vortex state the material no longer expels all magnetic fields and instead allows magnetic flux to penetrate it through quantised vortices, when in the vortex phase the electrical resistance is still zero. Figure 3.13 shows high frequency ac susceptibility measurements performed on MgB_2 at 100 kHz, 300 kHz, 1 MHz and 3 MHz, no magnetic field was applied during this measurement and any stray magnetic fields were less than H_{c1}. Figure 3.13 shows that the sample becomes superconducting at approximately 39 K, as expected indicating reliable measurement of the diamagnetic susceptibility and good temperature stability. The lack of any frequency dependence is evidence that the intrinsic frequency dependent effects of the coils have been corrected for. It is not uncommon to measure a peak in the imaginary part near the transition, however one was not observed. This is because the width of the peak is dependent on the field ampli-

tude and the frequency[116], as the measurement frequency is very high and the field amplitude used is small, the peak would be much narrower than the temperature step size used (1 K). The reason for the slow drop off in the susceptibility is not known and was not investigated further because only the location of T_c was of interest.

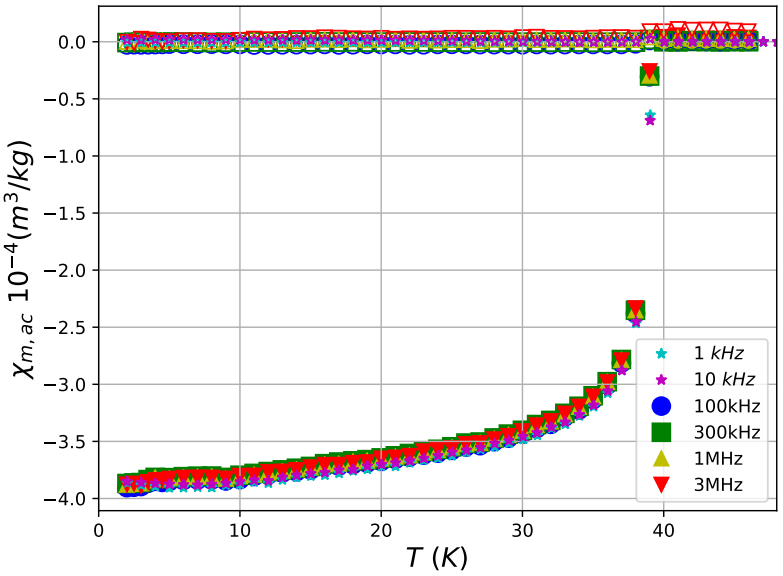

Figure 3.13: *Mass susceptibility data on powder MgB_2. Hollow markers indicate the imaginary part and solid markers the real part as measured by the high frequency susceptometer (100 kHz, 300 kHz, 1 MHz and 3 MHz) and ACMS (1 kHz and 10 kHz). The sample transitions to the superconducting state at the expected temperature (39 K).*

The second test sample we have measured is the spin ice material $Dy_2Ti_2O_7$, spin ice materials will be discussed at length in other parts of this thesis so their underlying physics will not be discussed here. $Dy_2Ti_2O_7$ has been measured at 15 K using both the commercially available ACMS option and the high frequency susceptometer. At above approximately 12 K relaxation times in $Dy_2Ti_2O_7$ vary exponentially with temperature, and so is a sensitive indicator of sample temperature. If the high frequency susceptometer was having some heating effect on

the sample or sample space then the location of the peak in the imaginary part would shift noticeably.

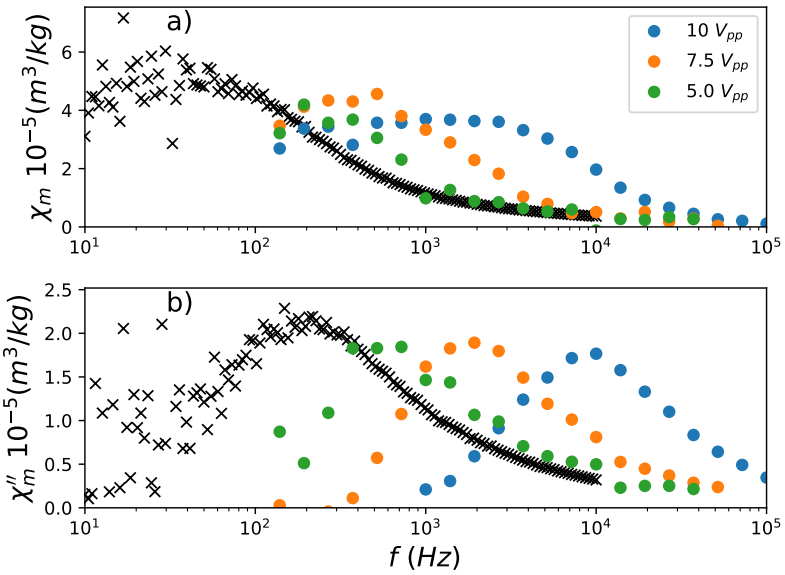

Figure 3.14: *a) and b) show the real and imaginary parts of the mass ac susceptibility of $Dy_2Ti_2O_7$ at 12 K. Black crosses were measured using the ACMS and the coloured dots were measured using the coil set with a NbTi excitation coil with different voltage amplitudes applied.*

Signs of heating were found in early measurements using the coil set with a NbTi excitation coil. Evidence of this is shown in figure 3.14, where measurements using the NbTi high frequency coil set (coloured points) do not agree with the ACMS data. In all the data sets shown in figure 3.14 the PPMS thermometers recorded a temperature of 12 K which was the set point. Clearly the data recorded by the high frequency susceptometer and the ACMS disagree. The source of the disagreement can be inferred from the dependence of the measured susceptibility on the voltage amplitude applied to the excitation coil. As the voltage amplitude is decreased the measured susceptibility comes closer to agreement with the ACMS. The most likely mechanism by which this should occur is

resistive heating in the excitation coil warming the sample, the heat output of which is reduced as the applied voltage is reduced. Since the sample is closer to the excitation coil than the thermometers and in weaker thermal contact with the cooling power of the PPMS, it is possible the sample is being warmed without warming the thermometers. The heating problem was solved by making a second coil set with a copper excitation coil because it has a much lower resistance.

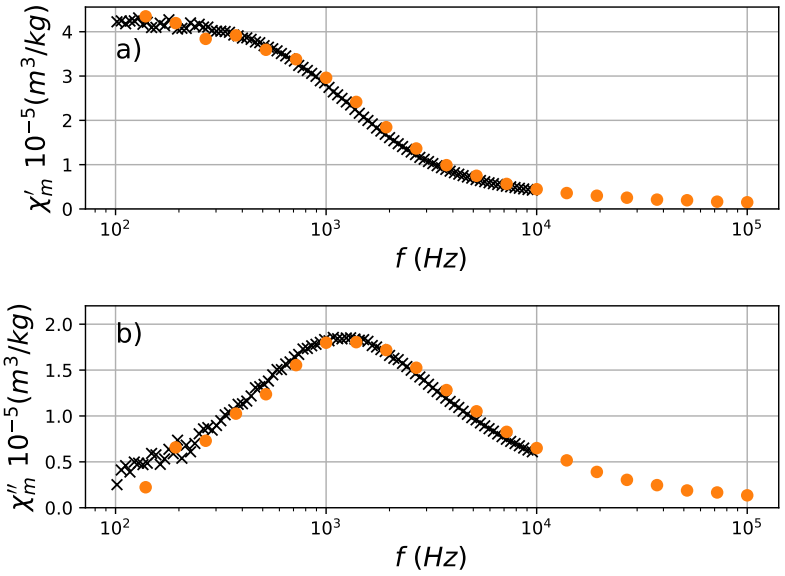

Figure 3.15: *a) and b) show the real and imaginary parts of the mass ac susceptibility of $Dy_2Ti_2O_7$ at 15 K. Black crosses were measured using the ACMS and orange dots measured using the high frequency with the copper excitation coil.*

Figure 3.15 shows ac susceptibility measurements on $Dy_2Ti_2O_7$ using the copper excitation coil at 15 K. The good overlap between ACMS data and high frequency data also shows good temperature stability and accurate calibration.

The third sample measured to check that the high frequency susceptometer is operating properly are FeraSpin XS magnetic nanoparticles produced by nanoPET Pharma GmbH. The nanoparticles are iron oxide and have a hydrodynamic particle diameter in the range 10-20 nm[117]. The hydrodynamic diameter

is the diameter that a perfect solid sphere would need to have in order to have the same hydrodynamic properties as the real particle. Iron oxide is strongly magnetic and due to the small particle sizes they are expected to be superparamagnetic (the entire particle is one domain)[118]. The nanoparticles are suspended in water. Magnetic nanoparticles have biomedical applications such as magnetic hypothermia and magnetic particle imaging[119, 120].

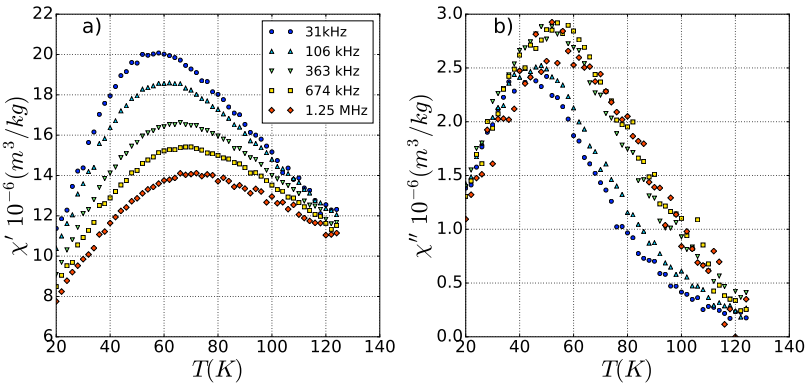

Figure 3.16: *Mass ac susceptibility data for FeraSpin XS nanoparticles. Figure a) shows the real part and figure b) shows the imaginary part.*

The peak in the imaginary part is expected to be broad, allowing the susceptometer to be tested over a wide temperature range. The suspension liquid was frozen by cooling to 250 K in atmospheric pressure and then holding the temperature constant for one hour. After an hour the sample will have been completely frozen and so the sample chamber was purged and cooling to the first measurement temperature started. During this whole process and subsequent measurement no magnetic field was applied.

Five frequencies were measured (31 kHz, 106 kHz, 363 kHz, 674 kHz and 1.25 MHz) as the sample temperature was increased from 20 K to 124 K and the results shown in figure 3.16. The peaks in the imaginary part indicate the temperature at which the current measurement frequency corresponds to the

relaxation time of the sample. With the sample medium frozen the relaxation time will be the Néel relaxation time which is reversal of the magnetic moment of the nanoparticles and not movement of the entire nanoparticle[121]. Néel relaxation is temperature dependent and the relationship is given by an Arrhenius equation given by

$$\tau(t) = \tau_0 \exp\left(\frac{KV}{k_B T}\right) \tag{3.28}$$

where T is temperature, τ_0 is the attempt frequency which is usually in the range of 10^{-9} - 10^{-10} s for iron oxide nanoparticle systems, K is the magnetic anisotropy constant and V is the magnetic core volume. This model assumes coherent magnetisation reversal, that each nanoparticle does not interact with any other and that the magnetic fields involved are small so as not to introduce hysteresis effects.

Peak locations were determined by fitting Lorentzian functions to the imaginary parts of the ac susceptibility in figure 3.16. The use of Lorentzians as fitting functions is phenomenological and not based on any expectation that the imaginary part should have that shape. The peak locations obtained from this analysis are shown in figure 3.17 with a fit to equation 3.28. For the Arrhenius fit the anisotropy constant suggested by Wetterskog *et al.*[122] (K=2.8×10^4 J/m^3) was used. The mean core diameter was found to be (8.86 ± 0.09) nm and τ_0=(2.50 ± 2.35)×10^{-13} s. This value of τ_0 is of a similar order of magnitude to that found by Wetterskog *et al.* however our core diameter is slightly larger than their value (≈6 nm) which was measured using electron microscopy analysis. However our particle diameter is similar to that found by Bender *et al.*[123] where X-ray diffraction, neutron powder diffraction and small angle x-ray scat-

tering were used to determine a mean core diameter of ≈9 nm. This again shows reliable operation of the high frequency susceptometer across a wide temperature and frequency range.

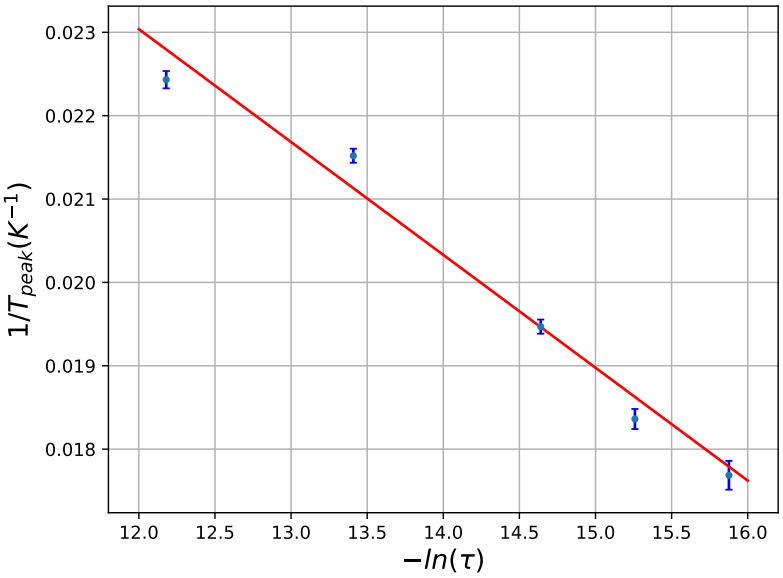

Figure 3.17: *Analysis of figure 3.16. Blue markers are peak locations from the Lorentzian fits, the red line is a best fit to equation 3.28.*

3.7 Summary and Future Work

To conclude, an ac susceptometer has been built that is capable of measuring up to MHz frequencies at temperatures as low as 2 K by integration with a QD-PPMS. The design of the coil set has been described and the calibration procedure explained. A summary of the specifications of the most recent iteration of the susceptometer is given in table 3.1. Reliable temperature stability has been demonstrated with the onset of diamagnetism in MgB_2 at the expected temperature (39 K) and good agreement between this device and the ACMS when measuring $Dy_2Ti_2O_7$ at 15 K. Measurements on FeraSpin XS nano particles have

shown that the real and imaginary parts of the ac susceptibility can be reliably determined up to high frequency across a wide range of temperatures. The fitted value of the mean particle diameter shows good agreement with that determined using other techniques indicating that the location of the peak in the imaginary part is accurately determined.

The susceptometer is also capable of measuring in magnetic fields up to 1 T, using the magnet of the QD-PPMS. This capability that has not yet been proven but will be demonstrated in the following chapter.

Parameter	Value	Unit
Materials	Cu	-
Lowest measurement frequency	1	kHz
Maximum measurement frequency	4	MHz
Temperature range	2 - 300	K
Field range	$\lessapprox 1$	T
Minimum detectable moment (@ 1 MHz)	5×10^{-10}	Am^2
Detection circuit inductance	4.81818	μH
Excitation circuit inductance	2.99146	μH
Detection circuit capacitance	21.023	pF
Excitation circuit capacitance	79.846	pF
Detection circuit measured resonance	8.15	MHz
Excitation circuit measured resonance	10.35	MHz

Table 3.1: Table of specifications for the final high frequency susceptometer design.

Worthwhile future developments would include altering the design of the high frequency susceptometer such that it can be integrated with a dilution refrigerator, and therefore be used at much lower temperatures. A prototype is currently under development that will integrate with a dilution refrigerator available in Cardiff. When finished it will in principle allow high frequency measurement down to 4 mK. Measuring at millikelvin temperatures introduces new difficulties, particularly with regard to thermalisation of the coils and sample without eddy

current or resistive heating warming the sample. Even moving the sample between detection coils presents a new challenge not present at higher temperatures because mechanical vibration can warm the sample.

It should also be possible to extend the upper frequency range of the susceptometer. LTspice calculations (not included in this thesis) have found that by introducing resistors in parallel with the coil set it should be possible to move the resonances to higher frequency and therefore improve the upper measurement range. Attempts to do so thus far have been unsuccessful for unknown reasons, however it remains a technical feasibility. Improvements to the frequency range could also be achieved through changes in the coil design. One way to do this could be by reducing the number of turns and therefore reducing the inductance and increasing the resonance, at the cost of reduced sensitivity.

Chapter 4

Spinel Spin Ice

4.1 Crystal Structure

The materials $CdEr_2Se_4$ and $CdEr_2S_4$ that form the focus of this chapter both have a spinel crystal structure[124, 125]. The spinels are a class of material that have a chemical formula of the type AB_2X_4 and a cubic unit cell. The A and B cations occupy octahedral and tetrahedral positions in the lattice respectively with the X anions occupying the 32e sites. The A and B sites can be occupied by the same species provided they have different valences, such as in magnetite ($Fe^{2+}Fe_2^{3+}O_4$). A sketch of the crystal structure of $CdEr_2Se_4$ is shown in figure 4.1, the structure of $CdEr_2S_4$ is the same but with the selenium atoms replaced with sulphur atoms.

$CdEr_2Se_4$ and $CdEr_2S_4$ both form in the $Fd\bar{3}m$ (#227) crystal group. The erbium B site ions sit at the 16b site and form a network of corner sharing tetrahedra, in an identical manner to the positions of rare earth ions in the pyrochlore spin ices. The charge structure in both materials is $Cd^{2+}Er_2^{3+}X_4^{2-}$. The outermost unfilled electron shell of the Er^{3+} ions is the 4f shell which contains

11 electrons allowing for the ions to be strongly magnetic.

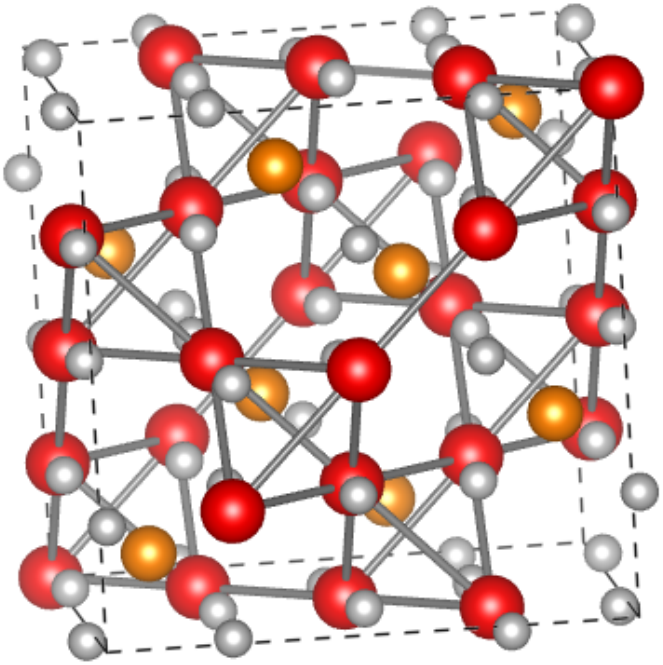

Figure 4.1: *Crystal structure of $CdEr_2Se_4$ generated using the VESTA software. Orange spheres respresent Cd ions, red spheres represent Er ions and silver spheres represent Se ions. Dashed lines indicate the unit cell, solid bars indicate the Er-Er bonds which make up the network of corner sharing tetrahedra. Note some atoms have been removed from the illustration to aid clarity.*

4.2 Magnetic Properties

DC magnetisation measurements were first performed on $CdEr_2S_4$ and $CdEr_2Se_4$ by Fuji *et al.* [126], which indicated that crystal field affects may have a significant impact on their magnetic behaviour at low temperature. Their measurements found a saturation magnetisation value (measured up to 15 T) of 5.4 μ_B per Er ion and 5.1 μ_B per Er for $CdEr_2S_4$ and $CdEr_2Se_4$ respectively, much less than

their calculated free ion value of $9.0\mu_B$. Ben-Dor *et al.*[127] used Mössbauer spectroscopy at 4.2 K to determine that the magnetic moment of the Er ions in $CdEr_2S_4$ is close to that of the free ion value.

Lau *et al.*[128] measured a number of chalcogenide spinels including $CdEr_2S_4$ using x-ray scattering and DC magnetisation measurements to determine the crystal and magnetic structure. Their measurements indicated little structural disorder, and indicated the presence of a magnetisation plateau which they suggested could be caused by XY planar anisotropy as in $Er_2Ti_2O_7$ (ETO)[129].

ETO is an XY antiferromagnet [130, 128, 131] meaning that the erbium magnetic moments exhibit antiferromagnetic interactions with one another and can take any orientation in the plane perpendicular to their local $\langle 111 \rangle$ directions. ETO is not a spin ice material.

Lago *et al.*[48] identified that the crystal field environment of the magnetic ions in the spinels is different to that in pyrochlores despite their similar sublattices. This change in the crystal field environment changes the symmetry of the Er sites from XY planar (as in ETO) to Ising-like as in the pyrochlore spin ices. Lago *et al.* [48] performed specific heat and DC magnetisation measurements on $CdEr_2Se_4$, confirming the presence of the residual ground state entropy expected for the spin ice state. Their specific heat measurements are shown in figure 4.2. They subtract the phonon and crystal field contributions to the specific heat to leave only the magnetic contribution which they then integrate to get the change in entropy. The recovered entropy is close to the expected $R\ln(2) - R/2\ln(3/2)$, differing by $0.0147R$. They then use their DC magnetisation measurements to calculate the crystal field parameters, from which they calculate the ground state wave function of the Er ions as: $|\pm\rangle = 0.8792\,|\pm 15/2\rangle \mp 0.4418\,|\pm 9/2\rangle + 0.1571\,|\pm 3/2\rangle \pm 0.0843\,|\mp 3/2\rangle$ where $|J_{<111>}\rangle = \left|{}^4I_{15/2}, J_{<111>}\right\rangle$.

They also calculated that $g_{xx} = g_{yy} = 0$ and $g_{zz} = 16.05$ providing strong evidence for the existence of large moment Ising spins as required for the dipolar spin ice model. Their work provided very compelling evidence that $CdEr_2Se_4$ is a dipolar spin ice material.

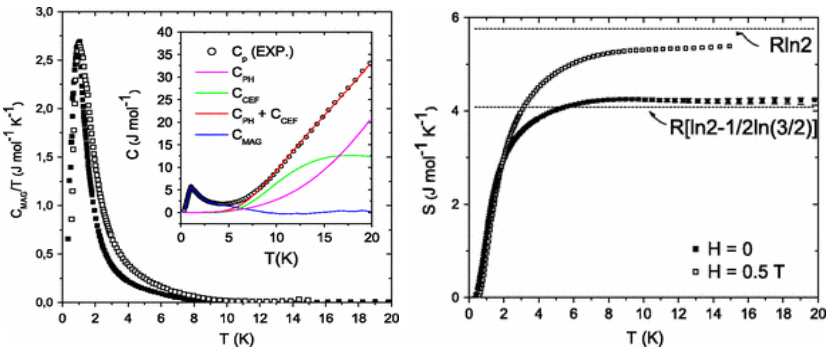

Figure 4.2: *Specific heat measurements in $CdEr_2Se_4$ showing the residual ground state entropy. Figure is from ref. [48], it has been altered for formatting purposes.*

In 2015, Ben-Dor *et al.*'s measurements were confirmed by Legros *et al.*[132] who performed Mössbauer measurements on $CdEr_2S_4$ at 4.2 K measuring an effective moment of 9.51 μ_B per Er ion, close to the expected free ion value of 9.57 μ_B. Their measurements indicated a $J = 15/2$ ground state for the Er ions with a large energy gap (∼100 K) between the ground and first excited crystal field states. The measurements performed by Legros *et al.* illustrated that $CdEr_2S_4$ behaves similarly to $CdEr_2Se_4$ and may also be a spin ice sample.

Gao *et al.* [49] performed a detailed study on both $CdEr_2Se_4$ and $CdEr_2S_4$ in which multiple neutron techniques and ac susceptibility were used to characterise both samples fully. Including measurements performed by the instrument described in chapter 3, and detailed in this thesis. They performed inelastic neutron scattering measurements on powder samples, providing microscopic evidence for the Ising character of the Er^{3+} ions in $CdEr_2Se_4$ and $CdEr_2S_4$. They determined that the ground states transform as the $\Gamma_5^+ \oplus \Gamma_6^+$ dipole-octupole doublet

under D_{3d} site symmetry[133]. The ground state wave functions in both materials are dominated by the $|15/2, \pm 15/2\rangle$ components with the coefficients of the full wave function given in table 4.1. They also report anisotropic g-factors ($g_\perp = 0$ and $g_\parallel = 16.4$) consistent with those reported by Lagos *et al.*

J_z	$\|\pm 15/2\rangle$	$\|\pm 9/2\rangle$	$\|\pm 3/2\rangle$	$\|\mp 3/2\rangle$	$\|\mp 9/2\rangle$
$CdEr_2Se_4$	± 0.906	0.386	0.159	-0.073	± 0.004
$CdEr_2S_4$	± 0.904	0.391	± 0.145	-0.094	± 0.006

Table 4.1: Doublet coefficients in the ground state wave function from ref. [49]

Gao *et al.* [49] also performed polarised diffuse neutron scattering to determine the spin-spin correlation lengths, and confirm the power-law correlations required of a dipolar spin ice. Using the Hamiltonian given by:

$$\mathcal{H} = J_1 \sum_{\langle ij \rangle} \boldsymbol{\sigma}_i \boldsymbol{\sigma}_j + J_2 \sum_{\langle\langle ij \rangle\rangle} \boldsymbol{\sigma}_i \boldsymbol{\sigma}_j + D r_0^3 \sum_{ij} \left[\frac{\boldsymbol{n}_i . \boldsymbol{n}_j}{|r_{ij}|^3} - \frac{3(\boldsymbol{n}_i . \boldsymbol{r}_{ij})(\boldsymbol{n}_j . \boldsymbol{r}_{ij})}{|r_{ij}|^5} \right] \boldsymbol{\sigma}_i \boldsymbol{\sigma}_j \quad (4.1)$$

where, $\boldsymbol{r}_{ij}$ is the vector between spins i and j, J_1 and J_2 are the exchange interactions for nearest neighbour (NN) $\langle ij \rangle$ and next nearest neighbours (NNN) $\langle\langle ij \rangle\rangle$ respectively, $\boldsymbol{n}_i$ is the unit vector pointing along the local $\langle 111 \rangle$ axes, $\boldsymbol{\sigma}_i = \pm 1$, r_0 is the NN distance and D is the dipolar interaction. D is reported to be 0.62 K and 0.69 K for $CdEr_2Se_4$ and $CdEr_2S_4$ respectively. For $CdEr_2Se_4$ they derive J_1=-0.03 K from specific heat measurements and then J_2=0.04 K from fitting to diffuse neutron scattering, showing that dipolar interactions are clearly dominant and therefore the dipolar spin ice state is realised. Diffuse scattering measurements on $CdEr_2S_4$ have a similar Q dependence also indicating the presence of the dipolar spin ice state.

Reig-i-Plessis *et al.* [134] used the crystal field parameters reported by Gao *et*

al. to refine the magnetic contribution to the specific heat data taken by Lago *et al.*. This led to a ground state entropy less than the expected value ($R/2ln(3/2)$) which they speculated could be caused by some two-in-two-out configurations being less favoured because of interaction terms not considered in the dipolar spin ice model.

4.3 Fast Dynamics

The magnetic fluctuation rates in $CdEr_2Se_4$ and $CdEr_2S_4$ are similar to one another and follow the same trend as observed in other spin ice materials. The evolution of the relaxation time is shown in figure 4.3, indicating the presence of the three distinct regimes.

In the high temperature regime (T>10 K) spin flipping is mediated by an Orbach process with temperature dependence given by $\tau = \tau_0 \left[\exp\left(\Delta/k_B T\right) - 1\right]$, where, Δ is the activation energy (77.1 K and 96.3 K for $CdEr_2Se_4$ and $CdEr_2S_4$ respectively) and τ_0 is the attempt frequency (9.93×10^{-11} s and 2.73×10^{-11} s for $CdEr_2Se_4$ and $CdEr_2S_4$ respectively)[135]. Neither Δ value matches a transition to a specific energy level, however in both materials there are 4 crystal field levels between $E/k_B = 45$ K and 130 K and the fitted Δ values likely represent the effect of multiple possible transitions.

Between 2 and 5 K a temperature independent plateau is observed at $\tau \approx 4.9 \times 10^{-7}$ s. These measurements were performed as part of this thesis and are discussed again in section 4.4.1. τ being temperature independent is a sign that spin fluctuations at these temperatures are mediated by quantum tunnelling between the two orientations of the ground state doublet.

At low temperatures (T< 1 K) the relaxation time obeys an Arrhenius law

given by $\tau = \tau_0 \exp(\Delta/k_B T)$ with $\tau = 1.01 \times 10^{-10}$ s and $\Delta = 10.07$ K for $CdEr_2Se_4$, and $\tau = 2.9 \times 10^{-10}$ s and $\Delta = 10.2$ K for $CdEr_2S_4$. Both of these activation energies are more than $6J_{eff}$ (0.8 K or 1 K for $CdEr_2Se_4$) as is also the case in $Dy_2Ti_2O_7$ (DTO).

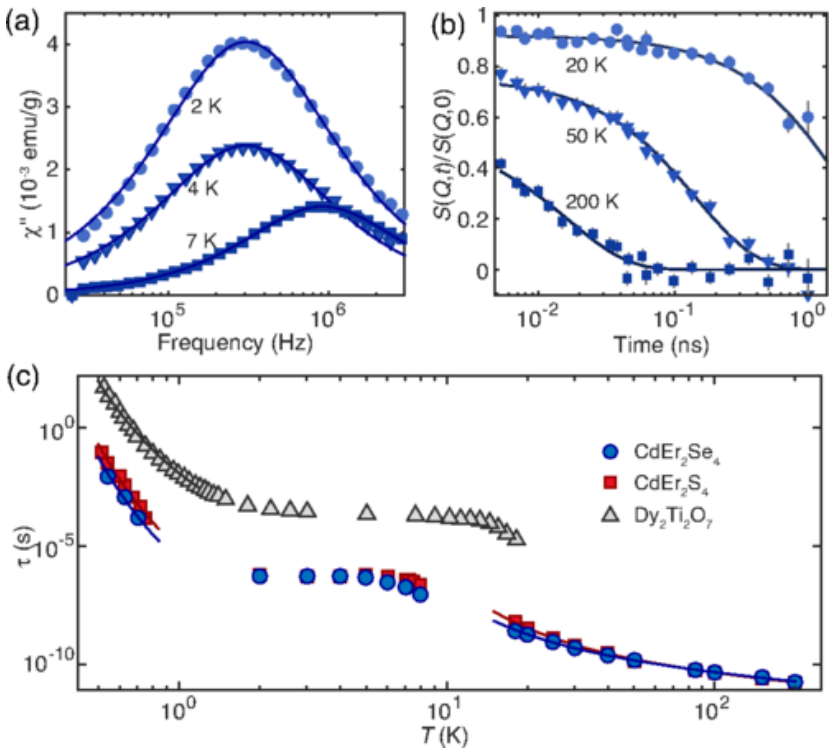

Figure 4.3: *a) ac susceptibility measurements in $CdEr_2Se_4$. b) Neutron spin echo measurments in $CdEr_2Se_4$. c) τ vs temperature in $CdEr_2Se_4$ and $CdEr_2S_4$ with $Dy_2Ti_2O_7$ for comparison. The data in a) and τ values between 2 and 8 K in c) were produced as part of this thesis. Figure reused from ref. [49]*

Despite similarities in the qualitative behaviour of relaxation times in DTO and $CdEr_2Se_4/CdEr_2S_4$, there is a factor of 10^3 difference between them. This can be explained by two properties of both systems. Firstly, if we consider that in spin ice materials, the monopole excitations behave like a dilute electrolyte or Coulomb gas then from Debye-Hückel theory, the fluctuation rate, f, is given by $f \propto u\rho$, where u is the monopole mobility and ρ the monopole density. ρ is

assumed to be given by $\rho \propto \exp(-v_0/k_BT)$ where v_0 is the chemical potential of a monopole anti-monopole pair and is 2.93 K and 3.84 K for $CdEr_2Se_4$ and $CdEr_2S_4$ respectively (in DTO $v_0 = 4.35$ K), meaning that ρ is up to a factor of 10 greater. This means that in order to account for the 10^3 difference there must be a 10^2 increase in u. u can be calculated by examining the splitting effect of the internal magnetic fields on the crystal field ground state doublet[20]. This is because the rate at which spin flips occur (which allow the monopoles to move) is proportional to the ground state splitting for a quantum process[64] (for a thermally activated process the opposite is true). From Tomasello *et al.*, the splitting of the ground state doublet for a Kramers ion (such as Er^{3+}) is given by $\Delta E = \alpha\left[1 + A\cos\left(6\phi\right)\right]H^3$, where ΔE is the ground state splitting, H is the magnetic field amplitude, ϕ is the angle between the transverse field and the x direction and α and A are fitting constants. It has been calculated that whilst the internal magnetic fields in $CdEr_2Se_4$ and $CdEr_2S_4$ are similar to that in DTO, the parameter α is 2.80×10^{-4} meV/T^3 and 1.95×10^{-4} meV/T^3 for $CdEr_2Se_4$ and $CdEr_2S_4$ respectively. In DTO $\alpha = 2.14 \times 10^{-6}$meV/T^3 which is two orders of magnitude smaller, explaining the fast dynamics in $CdEr_2Se_4$ and $CdEr_2S_4$.

4.4 Magnetic Susceptibility

Our samples were given to us by collaborators at the Paul Scherrer Institut, Switzerland and were prepared by the solid state reaction method. This method used CdSe and Er_2Se_3 or CdS and Er_2S_3 for $CdEr_2Se_4$ and $CdEr_2S_4$ respectively, which were mixed together in an argon atmosphere at a temperature of 800 °C. More information on sample preparation can be found in the supplemental information of ref. [49].

The initial motivation for these measurements was to measure the ac susceptibility of $CdEr_2Se_4$ $CdEr_2S_4$ at high frequency to determine the behaviour of the relaxation time at temperatures of the order of 1 K. Measurements at this temperature range will have the potential to demonstrate that $CdEr_2Se_4$ and $CdEr_2S_4$ have a temperature independent quantum tunnelling plateau as observed in other dipolar spin ices. The high frequency susceptometer described in the previous chapter is an ideal tool to use for this measurement, as the relaxation time at these temperatures is expected to be exactly in the centre of its frequency range.

4.4.1 Zero Field

The ac susceptibility of powder $CdEr_2Se_4$ and $CdEr_2S_4$ was measured at temperatures between 2 K and 8 K, in the absence of an applied magnetic field. The sample was cooled using the Quantum Design PPMS cryostat and the ac susceptibility measurements were performed using the instrument described in the previous chapter (for $f > 25$ kHz) and the ACMS option of the PPMS for frequencies $f < 10$ kHz. At the time of these measurements 25 kHz was the lowest possible measurement frequency of the high frequency susceptometer. The samples were contained in gelatine capsules with one half of the capsule inverted and inserted into the other half. The capsules were further sealed with Kapton tape and Parafilm. The sample containment was checked and found to have a negligible contribution to the measured susceptibility.

The ac susceptibility measurements are shown in figures 4.4 and 4.5 for $CdEr_2Se_4$ and $CdEr_2S_4$ respectively. Some of the data from figure 4.4 is also shown in figure 4.3 a) because these measurements were published in [49]. The relaxation times, τ, were extracted using fits to the Cole-Cole model [9], they are shown in

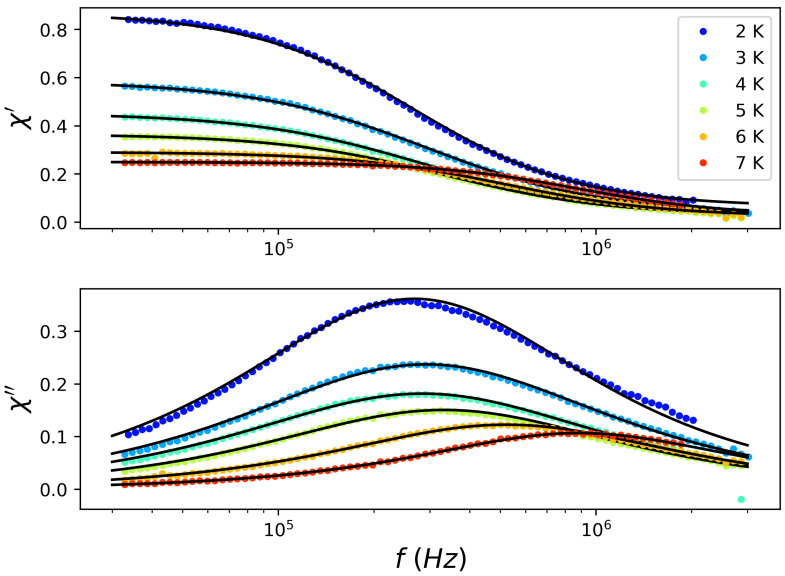

Figure 4.4: *Ac susceptibility measurements in $CdEr_2Se_4$ in the absence of an applied magnetic field. Black lines are fit to a Cole-Cole model.*

figure 4.3 c) and in more detail in figure 4.6.

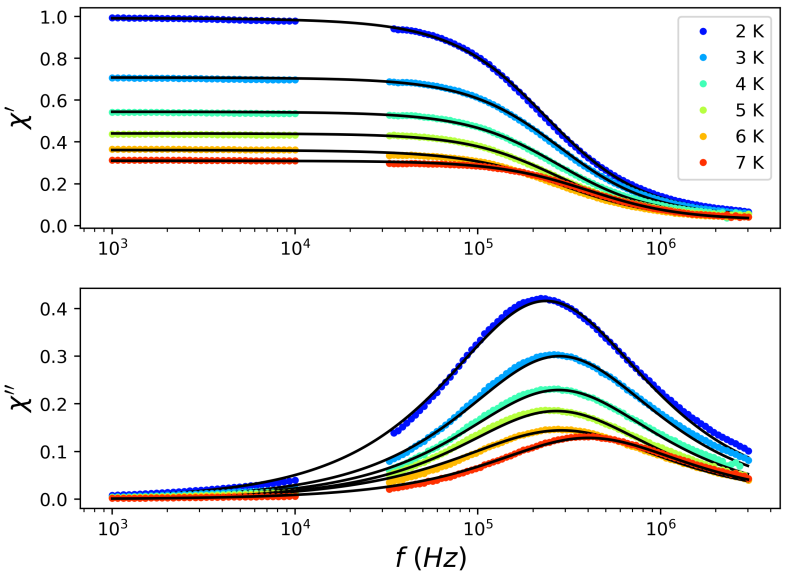

Figure 4.5: *Ac susceptibility measurements in $CdEr_2S_4$ in the absence of an applied magnetic field. Black lines are fit to a Cole-Cole model.*

In both materials the temperature independence of the peak in the imaginary part is quite clear between 2 K and 5 K and the magnitude is inversely proportional to T as expected. The quantum temperature independent plateau occurs with a relaxation time of $\tau \approx 4.9 \times 10^{-7}$ s. Indicating that quantum tunnelling events between the orientations of the ground state doublet occurs on a much faster time scale than in $Dy_2Ti_2O_7$. Above 5 K the relaxation time becomes thermally activated in both materials and by 9 K the location of the peak in χ'' is beyond the upper limit of the susceptometer. These measurements provide further evidence that $CdEr_2Se_4$ and $CdEr_2S_4$ are dipolar spin ices by demonstrating they have the expected temperature dependence for such materials.

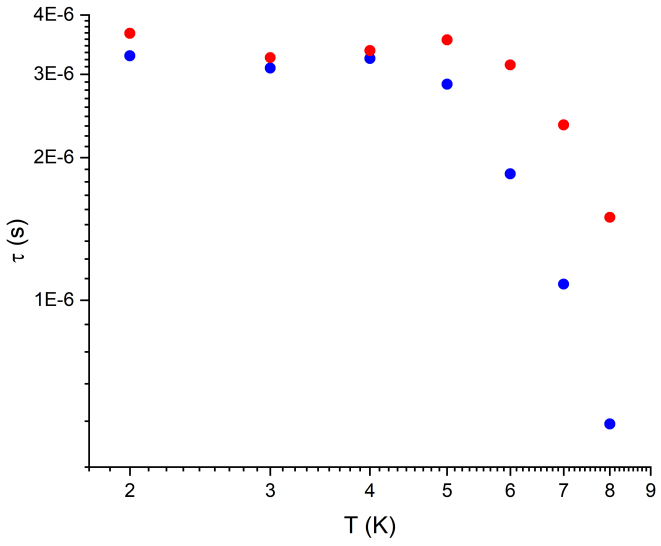

Figure 4.6: *Temperature dependence of the relaxation time in $CdEr_2Se_4$ (blue points) and $CdEr_2S_4$ (red points), showing the temperature independent plateau. These points are also featured in figure 4.3.*

4.4.2 Applied dc Magnetic Fields

The measurements discussed so far were performed in the absence of an applied magnetic field (residual fields were <1 mT). Spin ice materials have been shown to exhibit interesting behaviour in the presence of applied DC magnetic fields along high symmetry axes. Examples include Kagome Ice behaviour[78], ordering of spin chains[80] and quasi-liquid-gas monopole transitions[58]. In powder samples it has been shown that application of magnetic fields in $Dy_2Ti_2O_7$ can alter the spin freezing temperature [61] as well as introduces spikes in the specific heat[36].

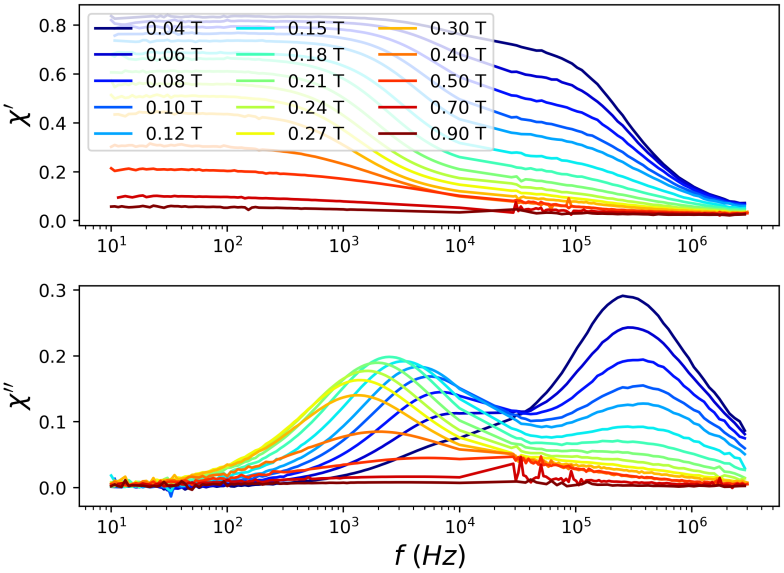

Figure 4.7: *ac susceptibility measurements in $CdEr_2Se_4$. Upper and lower panels show χ' and χ'' respectively, both against frequency. All shown measurements were at 2 K*

AC susceptibility measurements were performed on $CdEr_2Se_4$ and $CdEr_2S_4$ in a PPMS crytostat with the superconducting 9 T magnet option used to apply a constant magnetic field. The magnetic field was aligned with the ac excitation field. The samples were mounted in the same way as for the zero field measurements. The measurements were first performed at 2 K up to 1 T, but the most

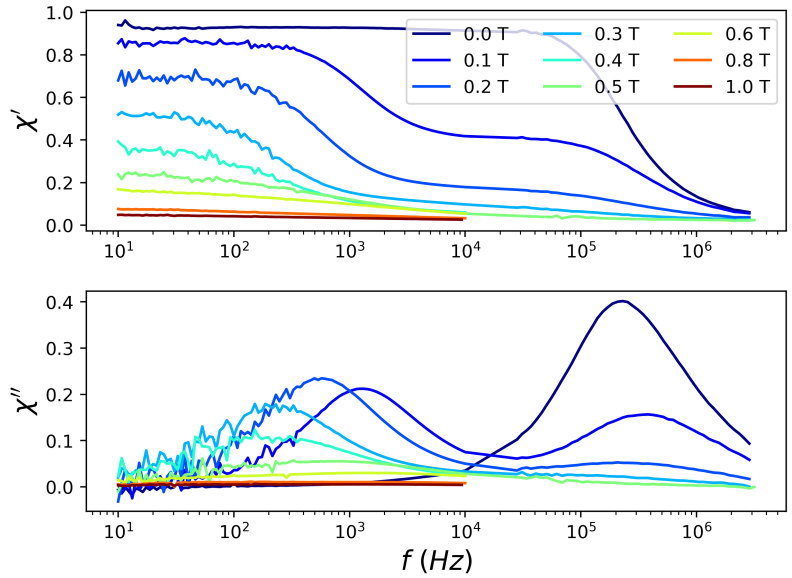

Figure 4.8: *ac susceptibility measurements in $CdEr_2S_4$. Upper and lower panels show χ' and χ'' respectively, both against frequency. All shown measurements were at 2 K*

interesting behaviour occurs in fields smaller than 0.5 T. As can be seen in figures 4.7 and 4.8 upon the application of a magnetic field at 2 K the peak in χ'' at $f \approx 300$ kHz becomes gradually subdued and a new peak emerges at lower frequencies. The 300 kHz peak will be referred to as the fast peak/fast relaxation mechanism and the slower field induced peak as the slow peak/slow relaxation mechanism.

At 2 K the increasing magnetic field subdues the fast peak almost entirely by 0.4 T, without significantly altering its frequency location. The slow peak initially grows in amplitude with increasing field up to around 0.18 T above which it is gradually suppressed. By 1 T the peak amplitude is almost completely supressed. The location of the slow peak is highly dependent on the field amplitude varying by at least an order of magnitude. The frequency location of the peak decreases with increasing field, which continues up to approximately 0.3 T above which

increasing the field increases the frequency. This field evolution at 2 K is virtually identical in both $CdEr_2Se_4$ and $CdEr_2S_4$.

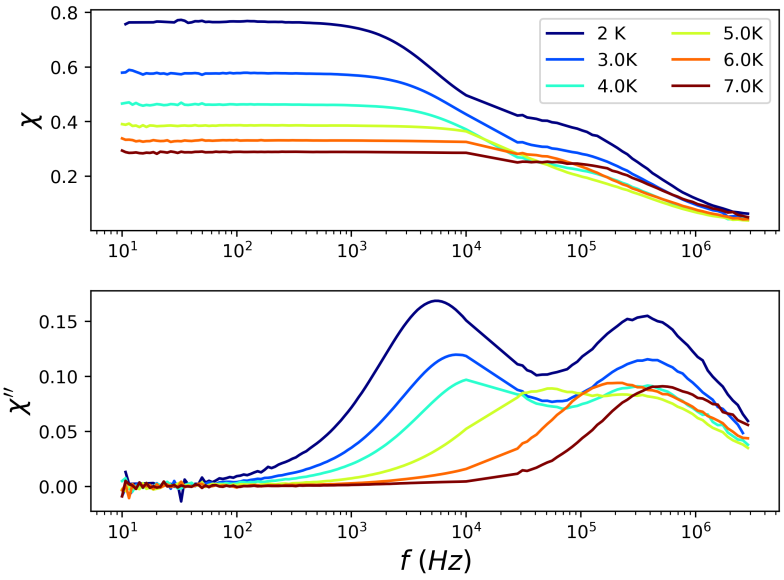

Figure 4.9: *ac susceptibility measurements in $CdEr_2Se_4$. Upper and lower panels show χ' and χ'' respectively, both against frequency. All shown measurements were in a magnetic field of 0.1 T*

Figures 4.9 and 4.10 show the temperature dependence in a constant field of 0.1 T. The behaviour is consistent across both samples again and indicates that the fast mechanism continues to be temperature independent in the presence of a magnetic field but the slow mechanism does not. The slow peak varies exponentially with temperature, indicating that it is a thermally activated process.

Building this up to higher temperatures and fields, it becomes possible to examine the full behaviour of the two peaks. First the behaviour in $CdEr_2S_4$ will be discussed because there is a greater range of fields and temperatures measured. Figure 4.11 shows heat maps of χ'' with the natural logarithm of frequency on the x-axis and the magnetic field on the y-axis.

The fast and slow peaks can be clearly distinguished from one another up to

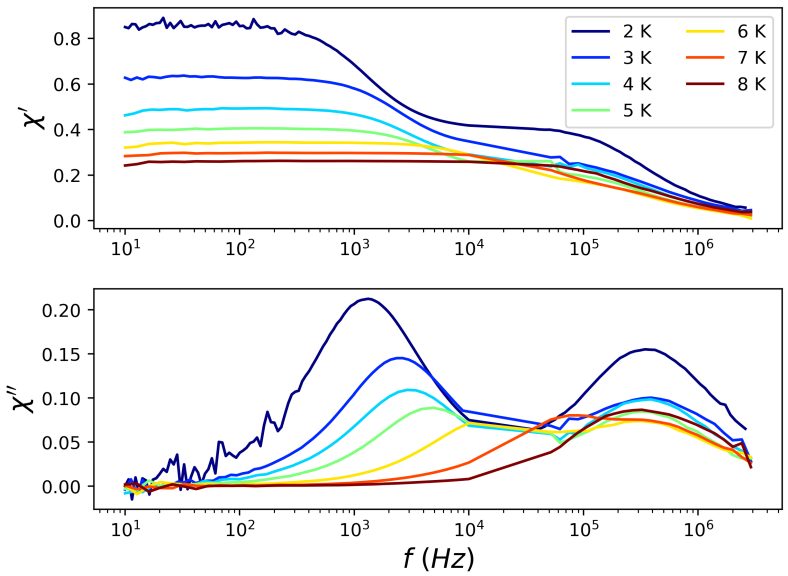

Figure 4.10: *ac susceptibility measurements in $CdEr_2S_4$. Upper and lower panels show χ' and χ'' respectively, both against frequency. All shown measurements were in a magnetic field of 0.1 T*

7 K. By 8 K the two peaks are too close to one another to distinguish and cannot be reliably separated when fitting to the data. Between 2 K and 7 K the fast peak is very small in amplitude by 0.3 T and completely suppressed by 0.5 T. The slow peak persists to much higher fields and is still present up to 0.6 T. In order to extract the dependence of the relaxation times, two Cole-Cole models were fitted to the data with some example fits shown in figure 4.12. τ_{fast} is the relaxation time of the fast peak and τ_{slow} is the relaxation time of the slow peak.

From the Cole-Cole fits the behaviour of the relaxation times with temperature and field can be plotted (figures 4.13). Fitting finds that τ_{fast} stays temperature independent in all fields up to suppression. Exact determination of τ_{fast} in larger fields and higher temperatures is difficult due to its small amplitude and close proximity to τ_{slow}, explaining the quite significant noise seen in figure 4.13 at $B \geqslant 0.14$ T and $T \geqslant 4$ K.

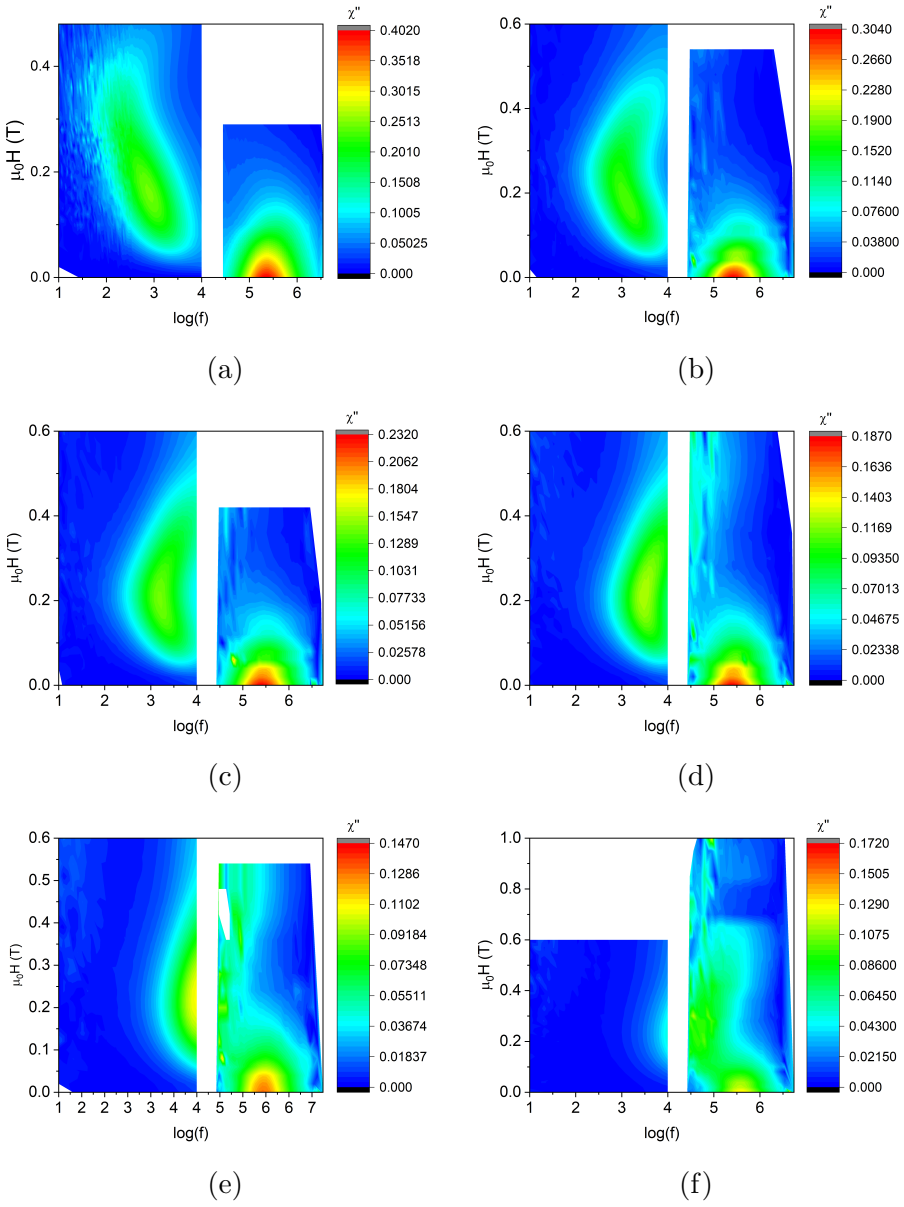

Figure 4.11: *χ'' in $CdEr_2S_4$ at 2 K, 3 K, 4 K, 5 K, 6 K, and 7 K in panels a, b, c, d, e and f respectively. x-axes are the logarithm of the frequency in Hz and y-axes the magnetic field.*

It appears that τ_{fast} maintains temperature independence up to at least 0.3 T, although it is possible some weak trend is hidden by the noise. There is some clear dependence of τ_{fast} on the field. The value of τ_{fast} changes by less than an order of magnitude before it is suppressed by the field however it varies with a

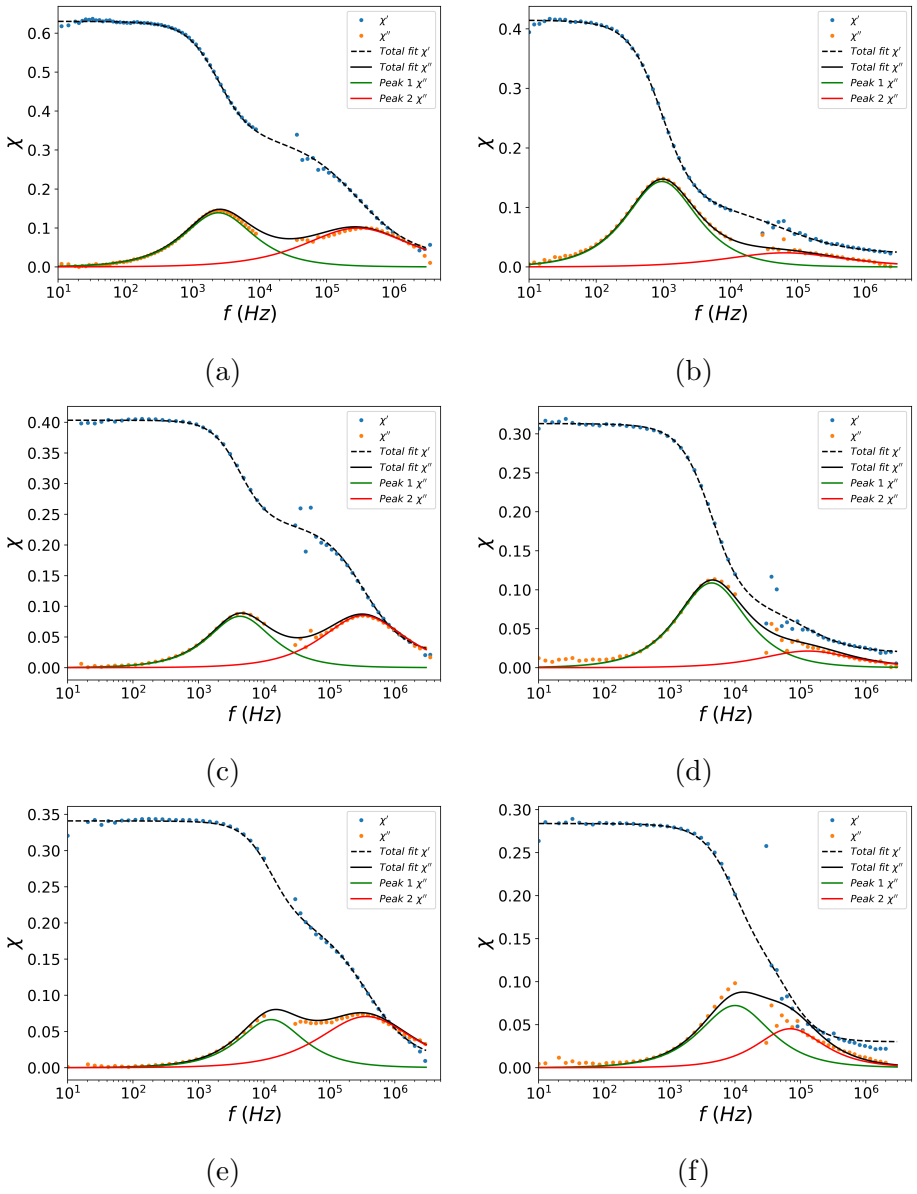

Figure 4.12: *Cole-Cole fits to χ' (blue circles) and χ'' (yellow circles) in $CdEr_2S_4$. Black lines are the combined model, red and green lines are the imaginary parts of the component Cole-Cole fits to illustrate each peak. plots a) and b) are at 3 K in 0.1 T and 0.3 T. c) and d) are at 5 K in 0.1 T and 0.3 T. e) and f) are at 6 K in 0.1 T and 0.3 T*

greater than exponential dependence.

At 5 K and colder τ_{fast} initially increases exponentially with increasing field before turning around and decreasing exponentially. The location of the turn

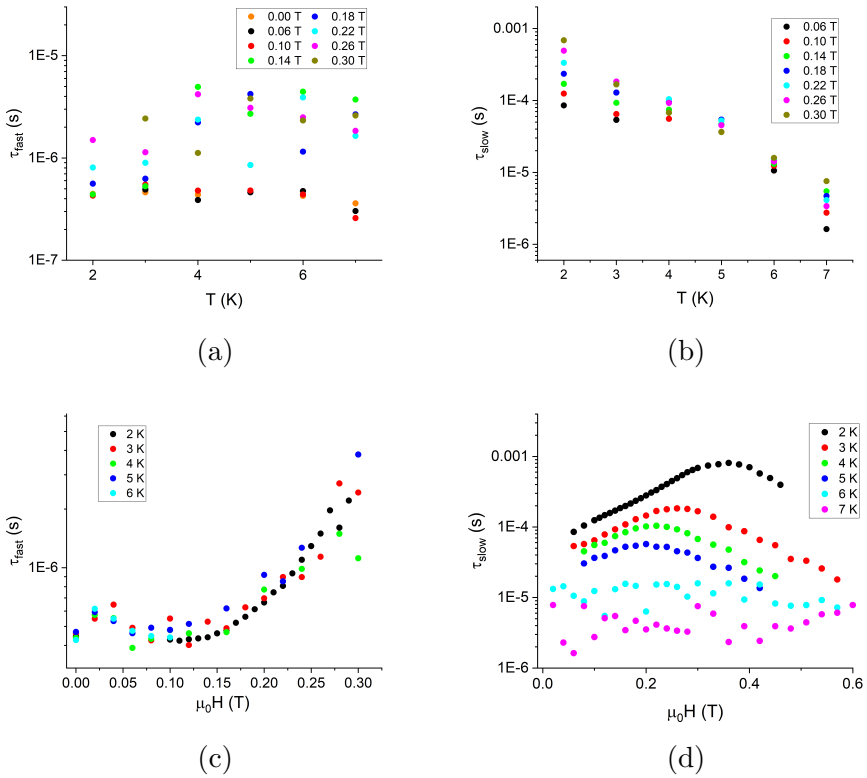

Figure 4.13: *τ_{fast} and τ_{slow} as a function of temperature in $CdEr_2S_4$, (a and b respectively) and magnetic field, (c and d respectively)*

around is temperature dependent occurring at approximately 0.36 T, 0.26 T, 0.22 T and 0.2 T for 2 K, 3 K, 4 K and 5 K respectively, suggesting that the location of the turn around may follow a trend given by $\sim \exp(1/T)$ (as shown in figure 4.17). At 6 K and 7 K τ_{slow} appears to be independent of field although it is possible that any field dependence is lost in noise and the frequency gap of the data which make accurate determination of τ_{slow} difficult. τ_{slow} is clearly temperature dependent as seen in figure 4.13 b) and there are either one or two regimes visible depending on the magnetic field. In magnetic fields less than 0.36 T, τ_{slow} shows a transition between Arrhenius laws at approximately 5 K. Above 0.36 T the entire temperature range is well described by a single Arrhenius fit.

Fitting an Arrhenius law to τ_{slow} (figure 4.14) finds that increasing the magnetic field causes an increase in E_a up to 0.3 T where it plateaus until the field reaches 0.45 T. Above 0.45 T, increasing the magnetic field reduces the energy barrier. τ_0 instead peaks at a lower field of approximately 0.2 T.

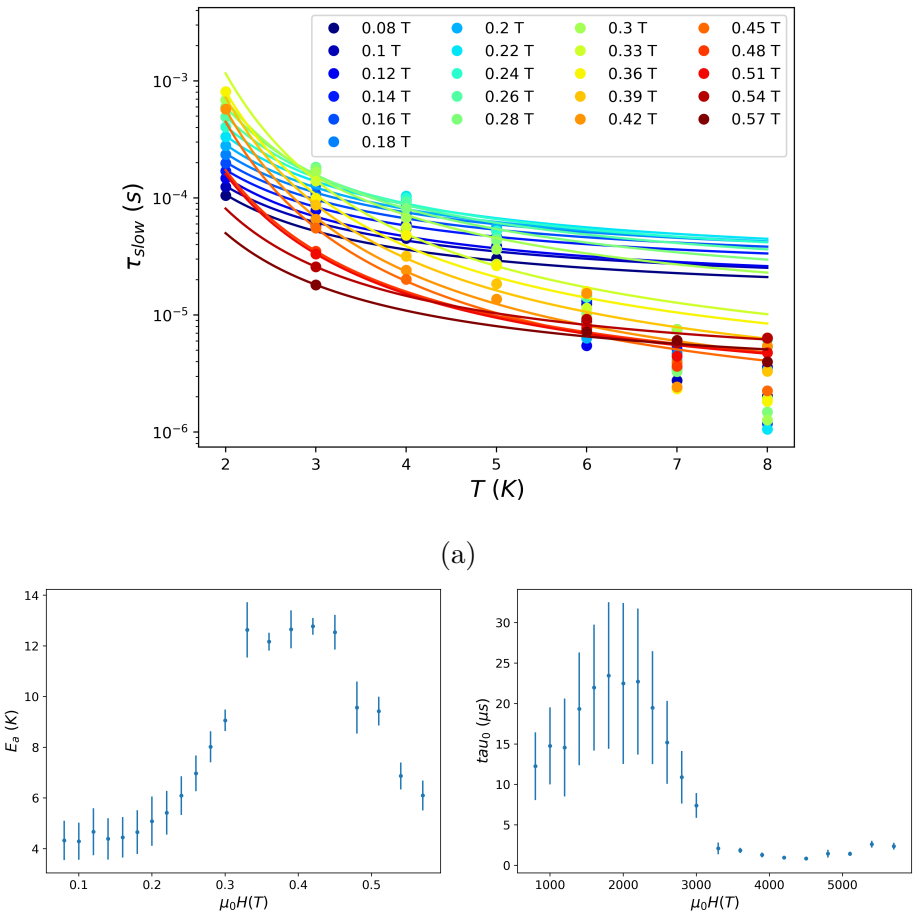

Figure 4.14: *a) Arrhenius fits to τ_{slow} against T in $CdEr_2S_4$ for varying fields between 0.08 T (darkest blue) and 0.57 T (darkest red). Fits are only to $T < 5$ K data below 0.45 T and the full range in greater fields. b) Activation energies, E_a, from Arrhenius fits. c) Characteristic relaxation times, τ_0, from Arrhenius fits.*

The behaviour in a magnetic field in $CdEr_2Se_4$ is similar. The location of the slow peak is at higher frequency than in $CdEr_2S_4$. As can be seen in figure 4.15 this puts the slow peak closer to the frequency blind spot, making accurate de-

termination of the peak more difficult. Furthermore there is a smaller range of data available in $CdEr_2Se_4$ than in $CdEr_2S_4$. The fast and slow peaks can be easily distinguished from one another up to 7 K where they are too close to reliably separate. At 5 K the peak in the imaginary part is almost entirely contained within the frequency gap between instruments. The field at which the fast peak is suppressed is approximately 0.3 T, which is temperature independent. 2 K is the only temperature where it is possible to observe the slow peak being suppressed completely by the magnetic field as the data do not extend to high enough fields at other temperatures.

As in $CdEr_2S_4$, the Cole-Cole model was used to fit the data, with two Cole-Cole functions combined to fit both peaks. The slow peak is particularly close to the frequency blind spot in this sample which makes accurate determination of the location of the slow peak difficult. This can be clearly seen in the 6 K measurements of figure 4.16 where the location of the slow peak is not easily determined.

Figure 4.18 shows τ_{fast} and τ_{slow} as a function of magnetic field and temperature. τ_{fast} shows some weak temperature dependence, although it is over a very small range and could be caused by the temperature dependence of τ_{slow} affecting the fit. The field dependence of τ_{fast} at 2 K matches the trend seen in $CdEr_2S_4$. At higher temperatures the trend is different to that observed in $CdEr_2S_4$. τ_{fast} in $CdEr_2Se_4$ appears mostly field independent above 4 K, although given the small range of variation τ_{fast} had at 2 K in $CdEr_2S_4$ it is possible that the fits have just not fully captured the true behaviour.

The fast peak shows a strong temperature dependence that gets stronger with increasing field suggesting that the field is activating a thermal process. The dependence on magnetic field is similar to that in $CdEr_2S_4$ with τ_{slow} exhibiting

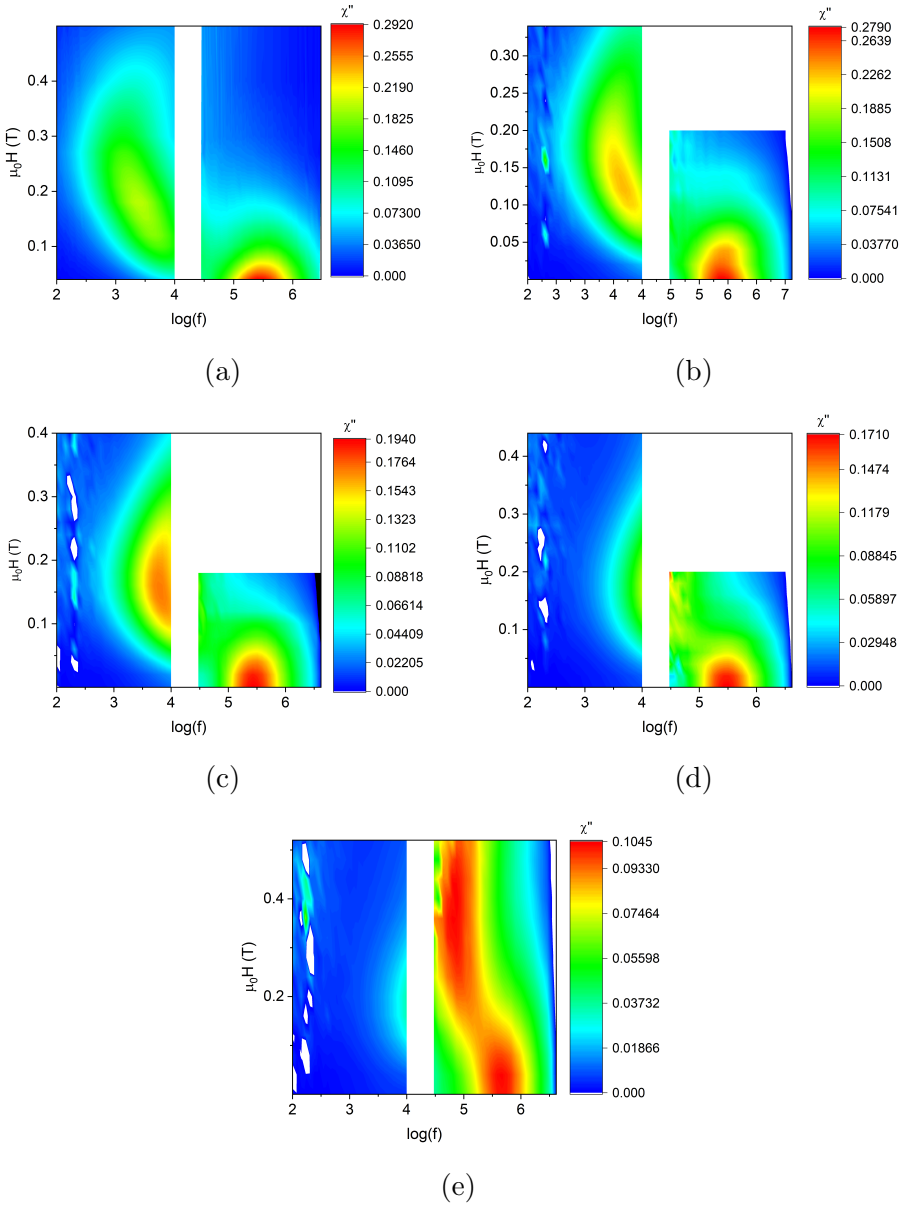

Figure 4.15: *χ'' in $CdEr_2Se_4$ at 2 K, 3 K, 4 K, 5 K and 6 K in panels a, b, c, d and e respectively. x-axes are the logarithm of the frequency in Hz and y-axes the magnetic field. Not all the data is shown.*

a turn around with increasing field. The field dependence of τ_{slow} at 5 K is not shown because it could not be reliably determined due to the slow peak being almost entirely in the frequency blind spot. The turn around occurs at approximately 0.26 T, 0.20 T, 0.18 T and 0.14 T for 2 K, 3 K, 4 K and 6 K

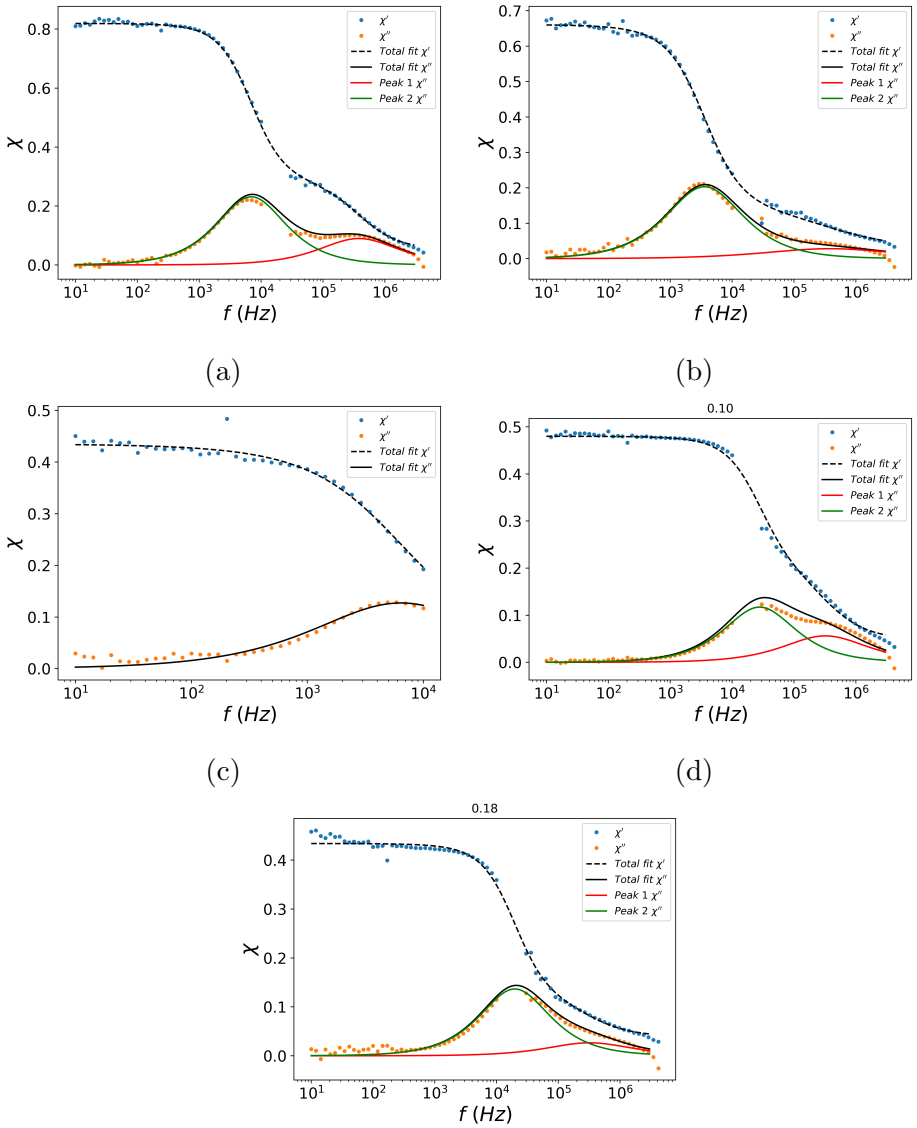

Figure 4.16: *Example Cole-Cole fits to χ' (blue circles) and χ'' (yellow circles) in $CdEr_2Se_4$. Black lines are the combined model, red and green lines are the imaginary parts of the component Cole-Cole fits to illustrate each peak. plots a), b) and c) are at 3 K in 0.1 T, 0.18 T and 0.3 T. d) and e) are at 5 K in 0.1 T and 0.18 T.*

respectively. As in $CdEr_2S_4$ this suggests that the location of the turn around goes like $\sim \exp(1/T)$. This trend can be seen in figure 4.17, note that the y-axis values are only approximate.

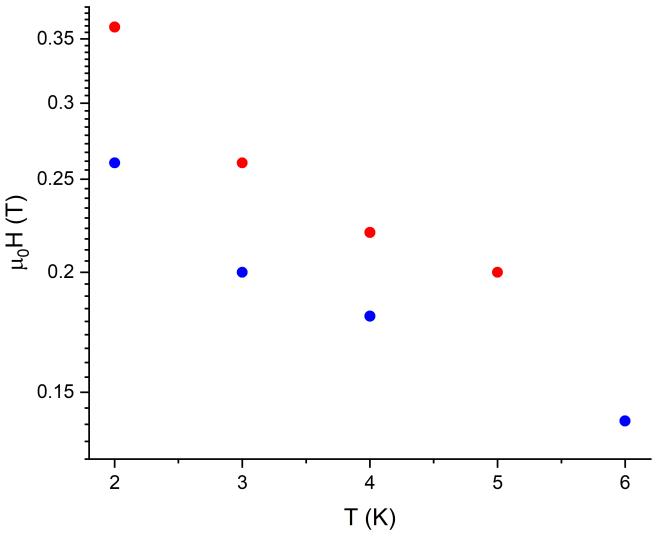

Figure 4.17: *Approximate magnetic field values at which τ stops increasing with field and starts decreasing plotted against temperature for $CdEr_2S_4$ (red circles) and $CdEr_2Se_4$ (blue circles).*

As in $CdEr_2S_4$ and Arrhenius law is fitted to τ_{slow} at T<5 K, the results of which are shown in figure 4.19. In $CdEr_2Se_4$ the Arrhenius fits do not resemble the data as well as in $CdEr_2S_4$. Figure 4.19 shows that increasing field leads to a steady increase in the fitted activation energy, and that τ_0 does not show much dependence on field.

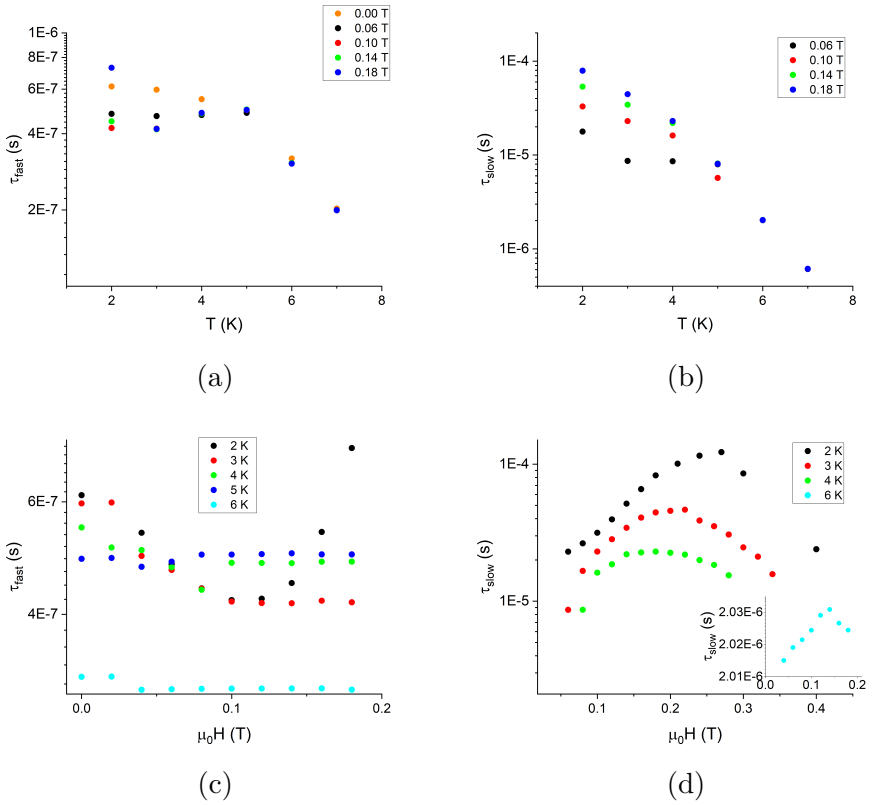

Figure 4.18: *τ_{fast} and τ_{slow} as a function of temperature in $CdEr_2Se_4$, (a and b respectively) and magnetic field, (c and d respectively)*

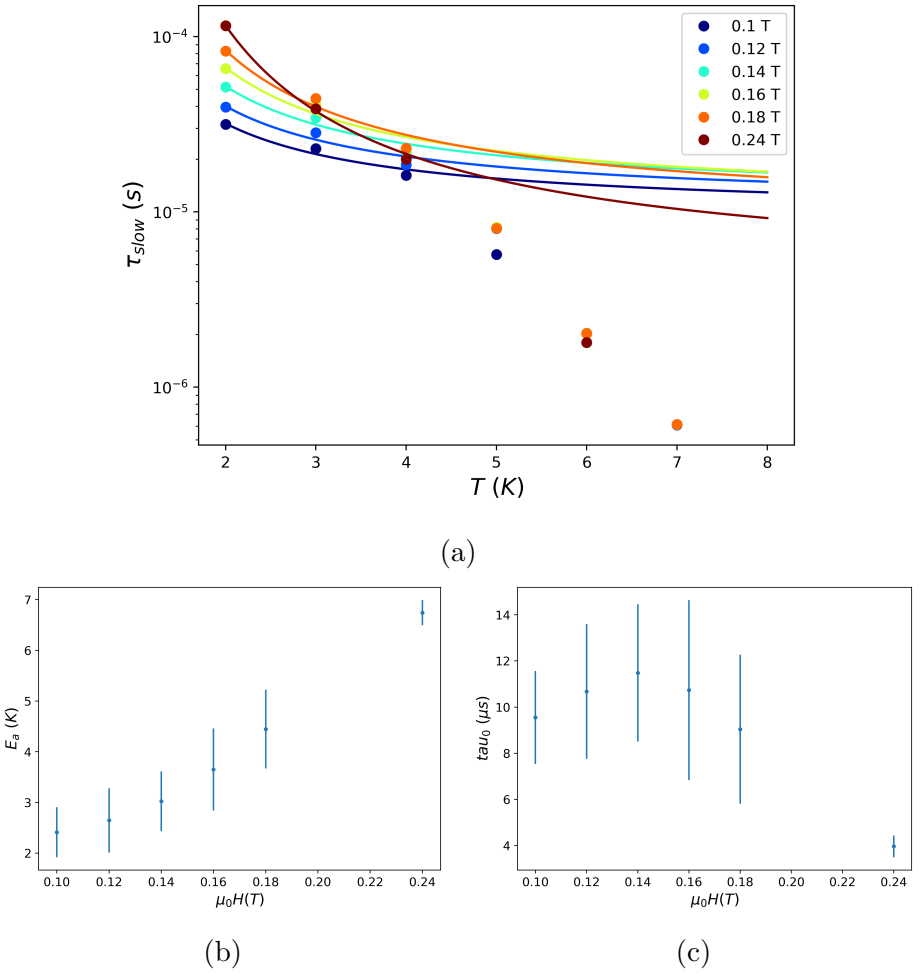

Figure 4.19: *a) Arrhenius fits to τ_{slow} against T in $CdEr_2Se_4$ for varying fields between 0.1 T (darkest blue) and 0.24 T (darkest red). Fits are only to $T < 5$ K data. b) Activation energies, E_a, from Arrhenius fits. c) Characteristic relaxation times, τ_0, from Arrhenius fits.*

4.5 Grease Measurement

In order to check that the slow peak is not caused by movement of the powder grains due to the application of the magnetic field (as in [136]), some $CdEr_2Se_4$ powder sample was mixed with vacuum grease. Mixing with vacuum grease is intended to fix the powder grains in place as well as allow some distance between grains provided the grease and powder are well mixed. ac suceptibility measurements were performed using the ACMS only as the intention is only to observe the existence of the slow peak.

The grease-$CdEr_2Se_4$ mixture was measured at 2 K in a 0.1 T magnetic field (figure 4.20). The mass of the sample was not precisely determined (as some of the grease-$CdEr_2Se_4$ mixture was left over during mounting of the sample) and so χ'' is normalised to its maximum value to make comparison with the capsule mounted sample easier. There is a slight difference between the two measurements, however this is likely due to demagnetisation effects (which have not been accounted for) or possibly pressure effects from the vacuum grease at low temperature. The important conclusion of figure 4.20 is that the slow peak is present in the grease mounted sample. This means that it is unlikely to be the result of powder movement, and is an intrinsic magnetic response of the sample.

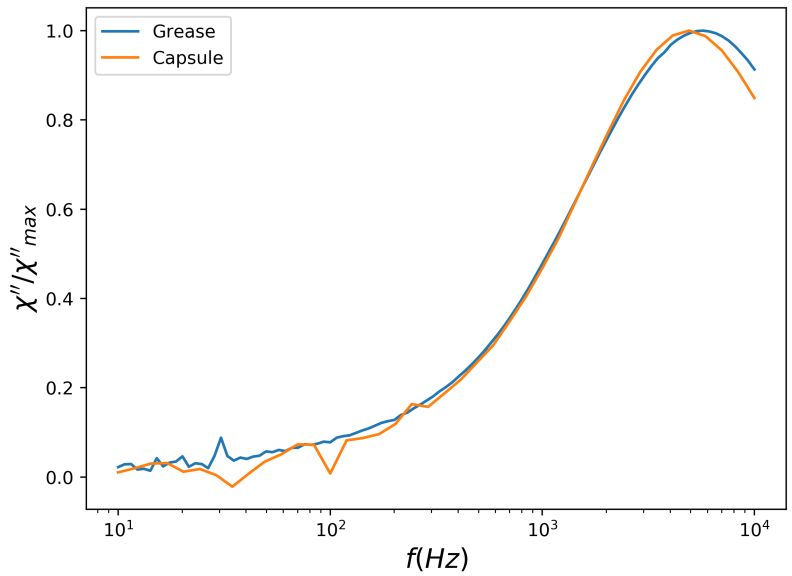

Figure 4.20: *Ac susceptibility in $CdEr_2Se_4$ for the capsule mounted powder and the vacuum grease-$CdEr_2Se_4$ mixture. Both measurements were performed at 2 K and in a magnetic field of 0.1 T. Both peaks are normalised to their maximum value to make comparison easier.*

4.6 Low Temperature Measurements

Powdered $CdEr_2Se_4$ was measured at the Néel institut, CNRS in Grenoble as part of a European Microkelvin Platform project. The sample was mounted in a dilution refigerator to achieve measurement temperatures between 7 mK and 4 K. A zero field cooled (ZFC) - field cooled (FC) measurement was performed in order to determine the spin freezing temperature. The measurement procedure is to perform the ZFC measurement first and initially cool the sample to base temperature in the absence of an applied magnetic field. At base temperature the field is turned on and the sample is warmed, as it is warmed the sample magnetisation is measured. Eventually the warming is stopped and the sample is cooled to base temperature again, still in the presence of the magnetic field. At base temperature the sample is again warmed whilst measuring the magnetisation,

these two measurements form the FC portion.

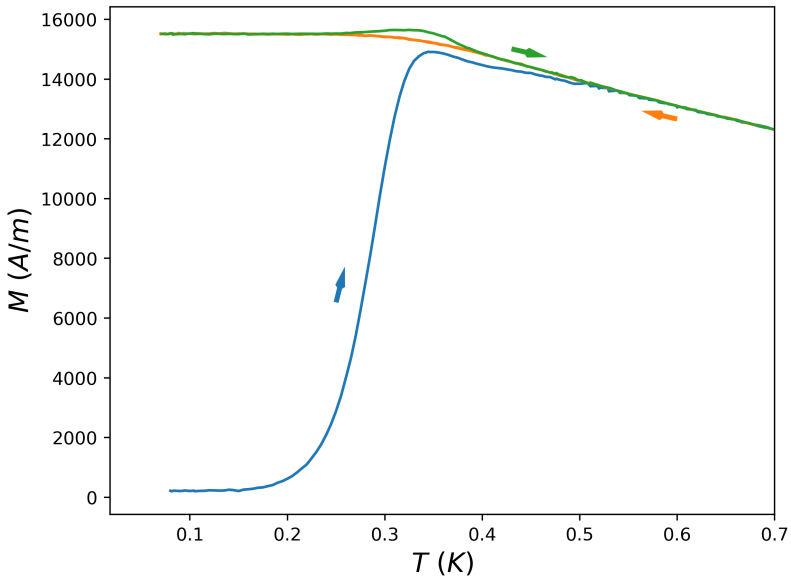

Figure 4.21: *ZFC and FC dc magnetisation measurements in $CdEr_2Se_4$. Blue line shows the ZFC measurement measured on warming, orange line is the FC measurement on cooling and the green line is the FC measurement on warming.*

The ZFC-FC measurement in figure 4.21 shows a separation of the ZFC and FC curves at 500 mK although the difference between them is small until temperatures below 330 mK where there is a strong bifurcation. The applied magnetic field in this measurement was 0.01 T. Unusual behaviour was observed in the form of a temperature hysteresis in the magnetisation between the cooling and warming portion of the FC magnetisation curve, seen as a gap between the green and orange lines. This can occur if the temperature of the sample changes too quickly for it to maintain an equilibrium state, however attempts to change the warming/cooling rate were not successful in closing the gap.

The ac susceptibility was measured using a superconducting quantum interference device (SQUID) in DC magnetic fields up to 0.5 T. In 0 T the imaginary part of the ac susceptibility (figure 4.22) was fitted with a Gaussian peak to de-

termine the peak location. It is important to note that the use of a Gaussian is a phenomenological model to capture the peak and not an expected behaviour of χ'' vs temperature. The peak location varies exponentially with temperature and shows very close agreement with the relaxation times reported by Gao *et al.*. Fitting an Arrhenius law finds a low temperature activation energy of (8.72±0.07) K which differs slightly from the value reported by Lago *et al.*.

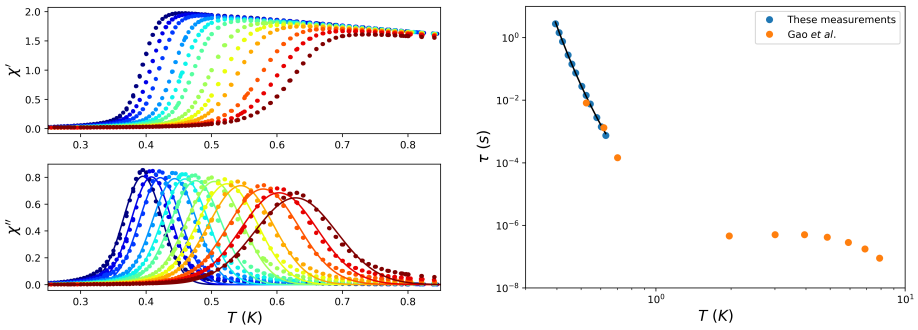

(a) (b)

Figure 4.22: *Zero field ac susceptibility measurements at low temperatures in $CdEr_2Se_4$. a) χ' (upper) and χ'' (lower) panel at frequencies between 0.057 Hz (dark blue) and 211 H (dark red) with Gaussian fits to χ''. b) τ against temperature extracted from Gaussian fits in panel. b) (blue circles) with fit to Arrhenius law (black line), orange circles are τ from ref. [49] in which the values at $T \geq 2$ K were measured as part of this thesis.*

When a magnetic field is applied, evidence of two relaxation mechanisms emerges as is clear in figure 4.23. The temperature separation between the two peaks in χ'' is highly dependent on frequency and field.

The dependence of the two peaks with changing magnetic fields can be seen more clearly in figure 4.24 where only single frequencies are shown.

Extracting the peak locations from this data is difficult because the true centres of the peaks can be obscured by the tails of each other. For this reason, accurate fits to the underlying distributions are required. The difficulty is finding a suitable distribution to fit the data. Plotting the data as a function of fre-

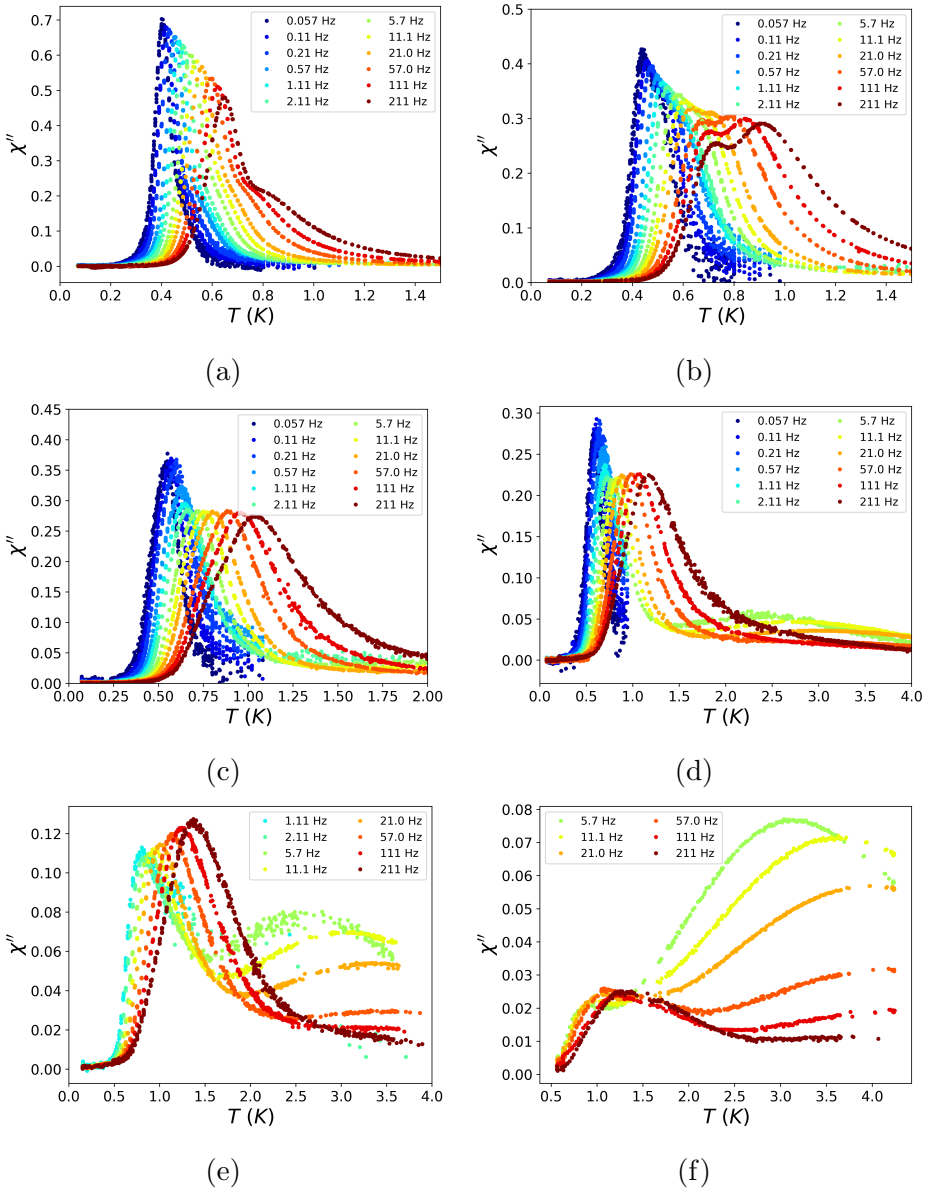

Figure 4.23: χ'' *in* $CdEr_2Se_4$ *at low temperature, in magnetic fields of a) 0.5 T, b) 0.1 T, c) 0.15 T, d) 0.2 T, e) 0.3 T and f) 0.5 T. Colours indicate frequency from dark blue (low frequency) to dark red (high frequency), colours are consistent through all panels. The frequencies measured at are: 0.057, 0.12, 0.21, 0.57, 1.11, 2.1, 5.7, 11.1, 21.1, 57, 110 and 211 Hz.*

quency allows for the Cole-Cole model to be applied, however the small number of frequencies measured at makes accurately fitting τ difficult, especially with two peaks. Fitting to the ac susceptibility as a function of temperature provides

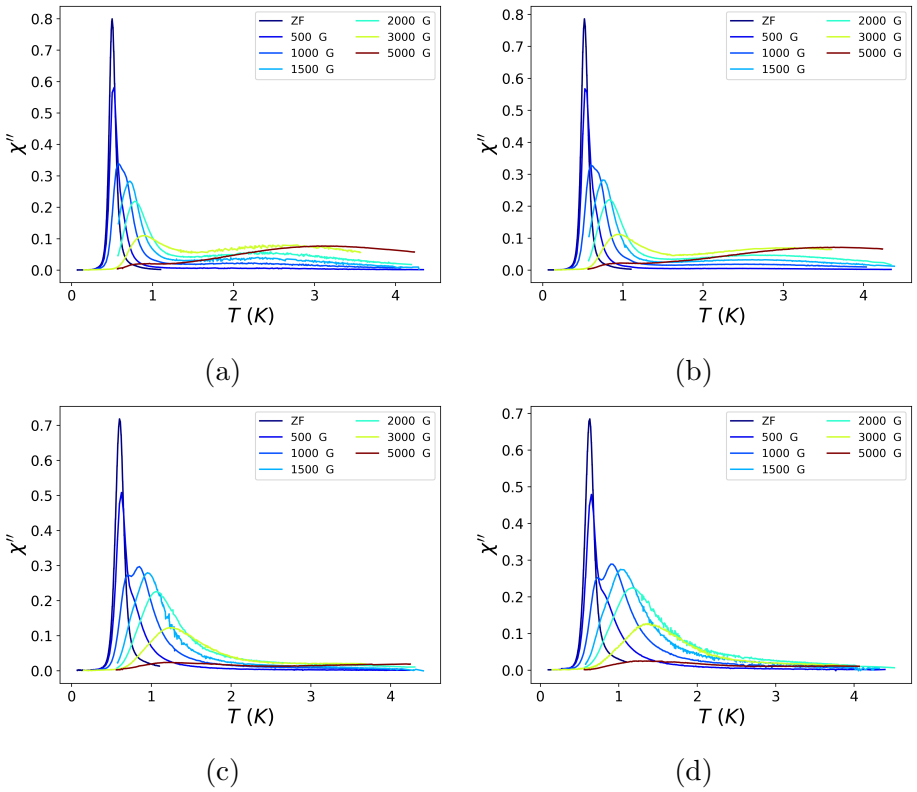

Figure 4.24: χ'' *at low temperature in powder* $CdEr_2Se_4$*. In this instance each panel shows a single frequency. a) 5.7 Hz. b) 11.1 Hz. c) 110 Hz. d) 211 Hz.*

a large number of data points to fit to but has the problem that any model used will be phenomenological. For this reason, fitting using both methods have been used and are compared. For the temperature dependent data two logarithmic normal distributions in addition are used for the fit. Gaussians were not used as in zero field because they did not achieve a good fit to the data. For the frequency dependent data two Cole-Cole models were used to fit the data.

Comparisons of the two fitting techniques are shown in figures 4.25, 4.26, 4.27, 4.28 and 4.29 for applied fields of 0 T, 0.05 T, 0.1 T, 0.15 T and 0.2 T respectively. In each case only a sample of the fits are shown.

There is good agreement between the fits to a Cole-Cole model and to the temperature dependent data in zero field 4.25, in a field of 0.05 T (figure 4.30 a)

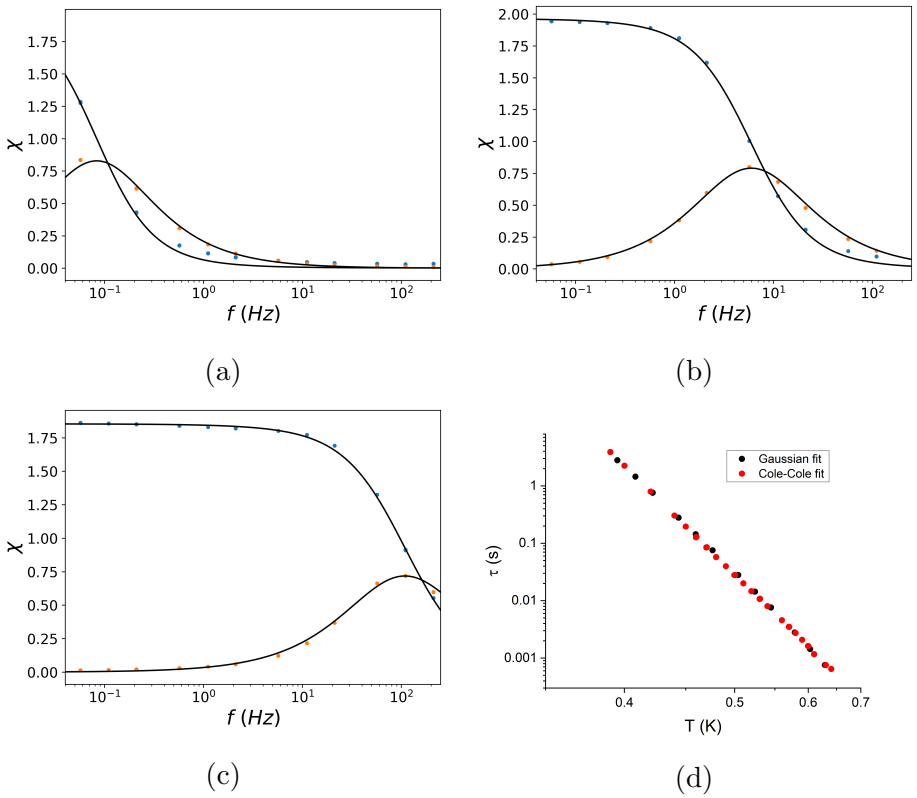

Figure 4.25: *0 T ac susceptibility data in $CdEr_2Se_4$ from figure 4.22 arranged vs frequency. Blue circles are χ' and yellow circles are χ'', black lines are a Cole-Cole fits. a), b) and c) are measurements with fits at 0.4, 0.5 and 0.6 K respectively. d) Comparison between fitting to temperature dependent data and frequency dependent Cole-Cole fits.*

and 0.1 T(fig. 4.30 b). At 0.15 T (fig. 4.30c) there is some disagreement between the two fitting methods. Additionally, at 0.15 T the temperature dependent fit has not fitted to the faster relaxation well at some frequencies, instead fitting a small peak at lower temperatures that does not resemble the data. See for example the bump at approximately 0.35 K in the fit line in figure 4.28 d). τ values resulting from these peaks are not included in figure 4.30 c). At 0.2 T (fig. 4.30d) the Cole-Cole fits could only capture the slow peak which agrees well with the temperature dependent fits.

Fitting an Arrhenius law to the fast peak finds activation energies of (8.78±0.05) K

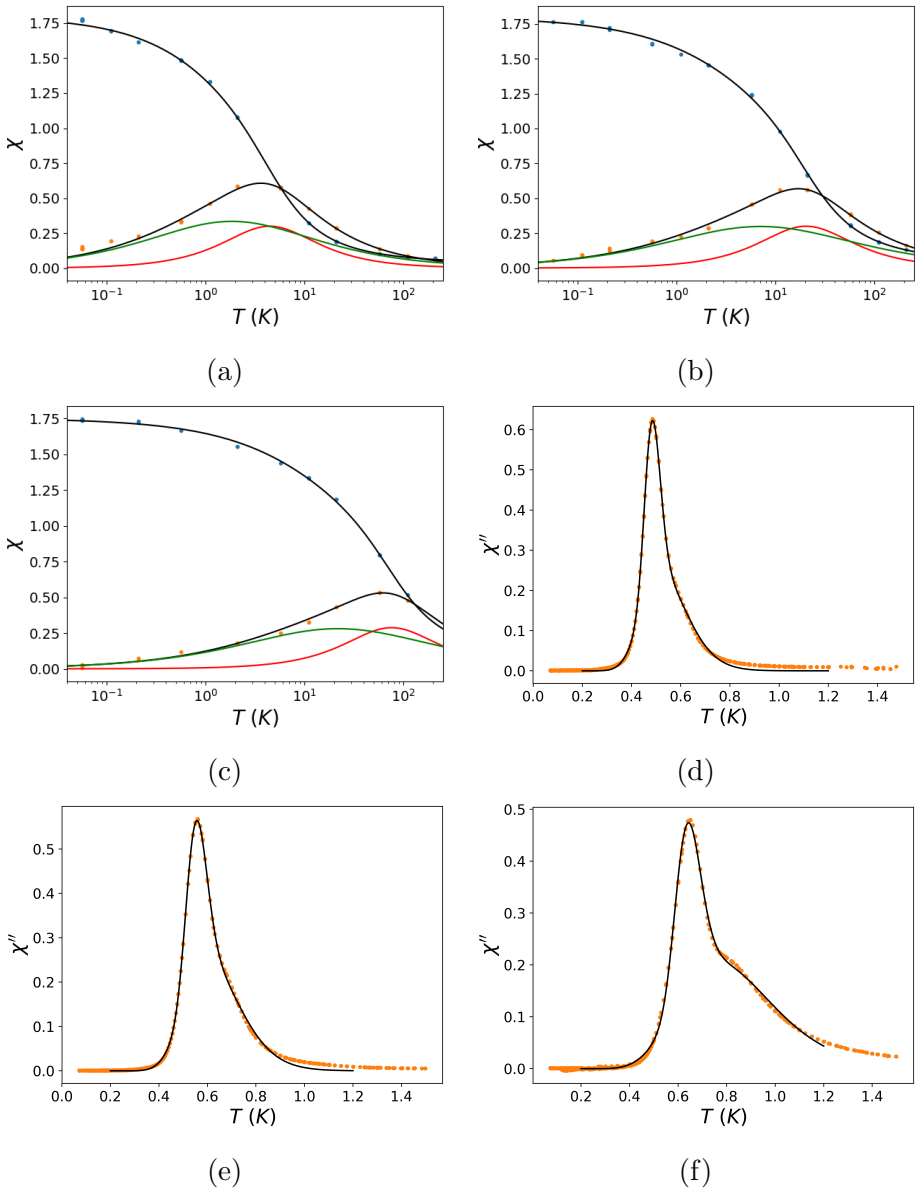

Figure 4.26: *Low temperature ac susceptibility measurements in $CdEr_2Se_4$ with a magnetic field of 0.05 T. Blue circles are χ' and orange circles are χ'' in all panels. a), b) and c) show the frequency dependent data at 0.5 K, 0.55 K and 0.6 K respectively with combined Cole-Cole fits (black lines) and individual peaks from the Cole-Cole fit (red and green lines). d), e) and f) show the temperature dependent data (χ'' only) at 2.1, 21.1 and 211 Hz respectively.*

and (9.36±0.16) K at 0.05 T and 0.1 T respectively for the temperature dependent fits. The Cole-Cole fits find activation energies of (8.85±0.04) K and

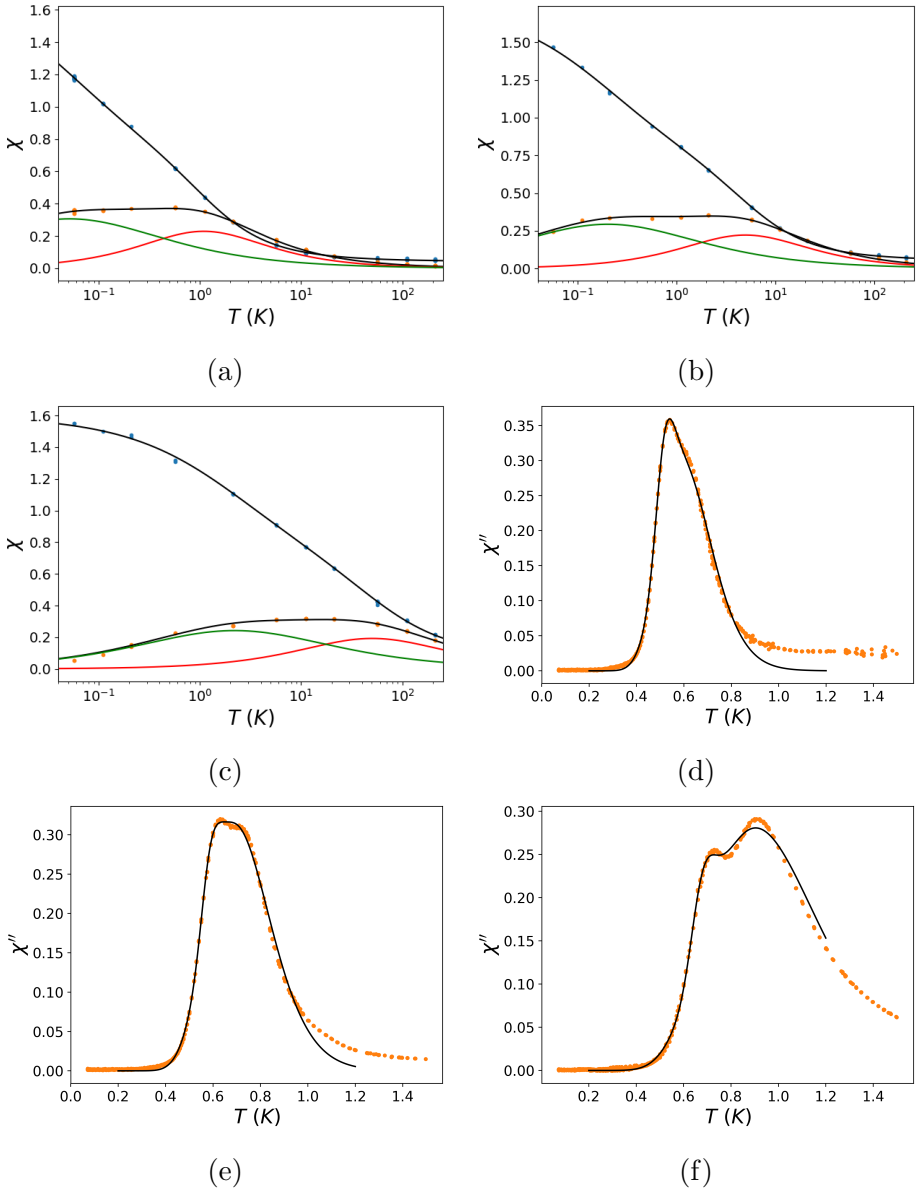

Figure 4.27: *Low temperature ac susceptibility measurements in $CdEr_2Se_4$ with a magnetic field of 0.1 T. Blue circles are χ' and orange circles are χ'' in all panels. a), b) and c) show the frequency dependent data at 0.5 K, 0.55 K and 0.65 K respectively with combined Cole-Cole fits (black lines) and individual peaks from the Cole-Cole fit (red and green lines). d), e) and f) show the temperature dependent data (χ'' only) at 2.1, 21.1 and 211 Hz respectively.*

(8.38±0.05) K at 0.05 T and 0.1 T respectively. At 0.15 T the relaxation times from fitting to the temperature dependent data do not show Arrhenius-

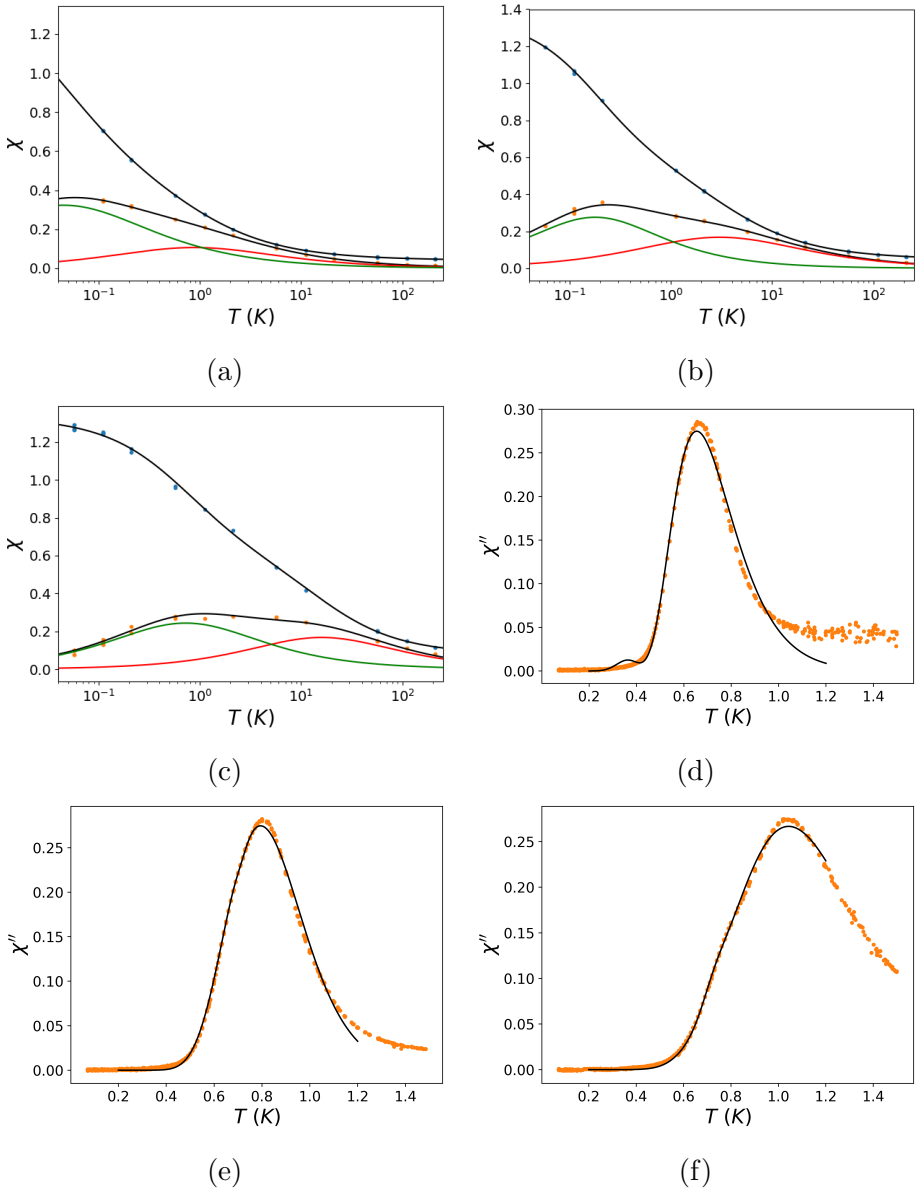

Figure 4.28: *Low temperature ac susceptibility measurements in $CdEr_2Se_4$ with a magnetic field of 0.15 T. Blue circles are χ' and orange circles are χ'' in all panels. a), b) and c) show the frequency dependent data at 0.55 K, 0.61 K and 0.69 K respectively with combined Cole-Cole fits (black lines) and individual peaks from the Cole-Cole fit (red and green lines). d), e) and f) show the temperature dependent data (χ'' only) at 2.1, 21.1 and 211 Hz respectively.*

like behaviour, but fitting to the Cole-Cole points finds an activation energy of (8.60±0.12) K. At 0.2 T the Cole-Cole fits could not reliably capture the location

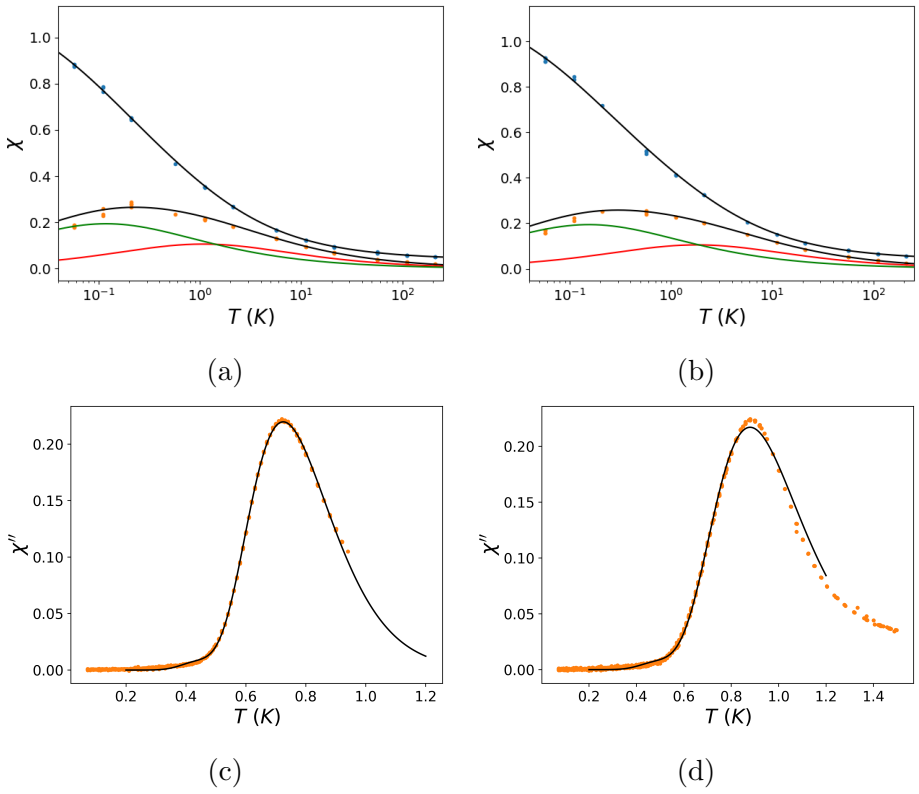

Figure 4.29: *Low temperature ac susceptibility measurements in $CdEr_2Se_4$ with a magnetic field of 0.2 T. Blue circles are χ' and orange circles are χ'' in all panels. a) and b) show the frequency dependent data at 0.65 K and 0.7 K respectively with combined Cole-Cole fits (black lines) and individual peaks from the Cole-Cole fit (red and green lines). c) and d) show the temperature dependent data (χ'' only) at 2.1 and 21.1 Hz respectively.*

of the fast peak (likely due to its small amplitude) but the temperature dependent relaxation times have an activation energy of (8.09±0.47) K. This suggests that at low temperature, spin fluctuations are mediately by a thermally activated process as in zero field and the energy gap for spin flipping does not change significantly with the magnetic field.

For the slow field induced peak, the behaviour of the relaxation time is more complex with less agreement between the Cole-Cole fits and temperature dependent fits. For the temperature dependent fits in each magnetic field value, the

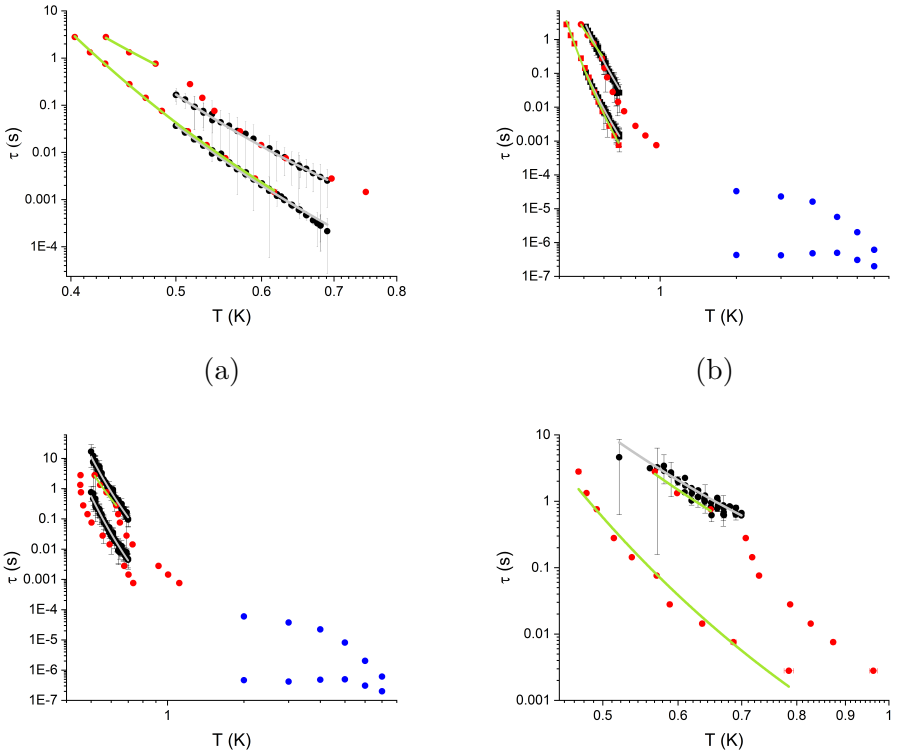

Figure 4.30: *τ against temperature in $CdEr_2Se_4$ in a magnetic field of 0.05, 0.10, 0.15 and 0.20 T for panels a), b), c) and d) respectively. Blue circles are from the high temperature data in section 4.4. Black circles are from the Cole-Cole fits to the frequency dependent data and red circles are the results of temperature dependent fits. Light grey lines are Arrhenius fits to the black cirlces and light green lines are Arrhenius fits to the red circles.*

relaxation times have a region in which the relaxation time grows faster than expected for a thermally activated process between 0.5 K and 2 K. Below 0.6 K, the relaxation times are again governed by an Arrhenius law with activation energies given in table 4.2.

	E_a (K)	
B (T)	Temp. dep.	C-C
0.05	(5.59 ± 0.58)	(7.56 ± 0.06)
0.10	(5.85 ± 0.23)	(8.40 ± 0.13)
0.15	(6.56 ± 0.70)	(8.11 ± 0.09)
0.20	(5.74 ± 1.00)	(5.14 ± 0.20)

Table 4.2: Activation energies at low temperature in $CdEr_2Se_4$ from Arrhenius fits to τ values extracted via temperature dependent fits and via fitting to the Cole-Cole model.

suggesting that the energy barrier increases with increasing field until a point between 0.15 T and 0.2 T above which the barrier decreases. From the Cole-Cole fits the activation energies are given in table 4.2 and suggest that the activation energy instead begins decreasing between 0.1 T and 0.15 T.

4.7 Specific Heat

Specific heat measurements were carried out on powdered $CdEr_2Se_4$ in a PPMS cryostat at the London Centre for Nanotechnology, University College London in collaboration with Steven Bramwell and Daan Arroo. The measurements were performed using the heat capacity option of the PPMS. The sample was affixed to the calorimeter puck using vacuum grease.

Preliminary results are shown in figure 4.31. The raw experimental data is shown without any correction for the background. It has also not been calibrated for the mass of the sample and so is shown in arbitrary units. Additionally the magnetic contribution C_{mag} to the specific heat, C, has not been isolated meaning that contributions from phonons, C_{ph}, nuclear magnetic moments, C_{nuc},

and crystal field, C_{CEF}, are included. Lago *et al.* [48] found in their specific heat measurements (shown here in figure 4.2) that below approximately 5 K C_{ph} and C_{CEF} have a small contribution. In $Er_2Ti_2O_7$ C_{nuc} is only significant at $T < 0.4$ K [130], if it is assumed to be similar in $CdEr_2Se_4$ then it should not affect the data in figure 4.31. A measurement of the vacuum grease is also shown which indicates that its contribution is small below 2 K, the specific heat of the grease is field independent at least up to and including 0.5 T. Therefore between 0.4 K and 2 K, C can be assumed to be approximately equal to C_{mag}.

The purpose of these measurements is to look for evidence of any magnetic phase transitions in $CdEr_2Se_4$ as observed in $Dy_2Ti_2O_7$[36, 73] and other spin ices over the field range measured here, which would be visible as sharp peaks in C. The application of the magnetic field increases the height and width of the broad peak in C up to 0.3 T. At 0.5 T the peak in C is lower and has moved to higher temperature. However in none of the measurements does any indication of a magnetic phase transition appear. This suggests that the applied fields are not inducing any significant phase changes that could be responsible for the field induced slow mechanism.

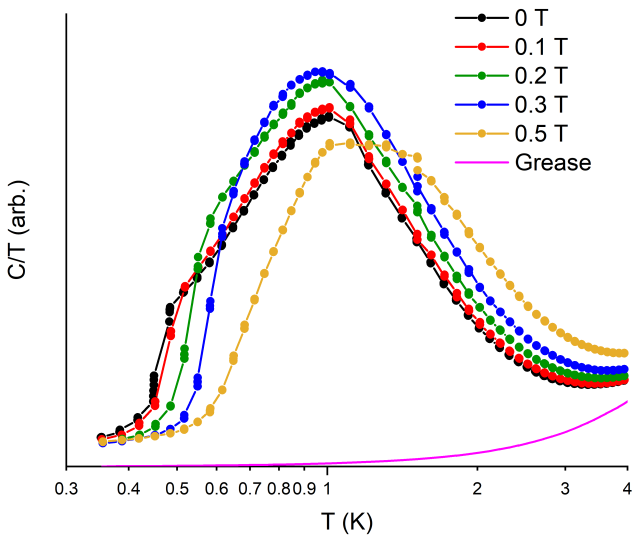

Figure 4.31: *Specific heat measurements in $CdEr_2Se_4$ at the indicated dc magnetic fields.*

4.8 Single Crystals

Recently, single crystal samples of $CdEr_2Se_4$ have become available thus enabling the measurement of ac susceptibility along specific crystallographic axes. Only small crystals are available with masses of the order of 1 mg. The $CdEr_2Se_4$ single crystal samples were grown by Vladimir Tsurkan via the chemical transport reaction method using a preliminary synthesized polycrystalline ternary material and iodine as a transport agent at temperatures between 850 and 900°C.

The crystal was aligned using an X-ray Laue camera in the materials characterisation laboratory at ISIS, RAL. The samples provided were very fragile and awkwardly shaped meaning that only one crystal could be properly aligned. This sample had a mass of close to 1 mg and had a triangular prism shape approximately 0.34 mm thick with sides of the order of 1 mm long. The sample was mounted to a plastic screw with GE varnish to hold it in place. The intention

was to mount the sample in such a way as to have access to the [111], [110] and [100] directions (or equivalent) by rotating the screw without having to realign the sample.

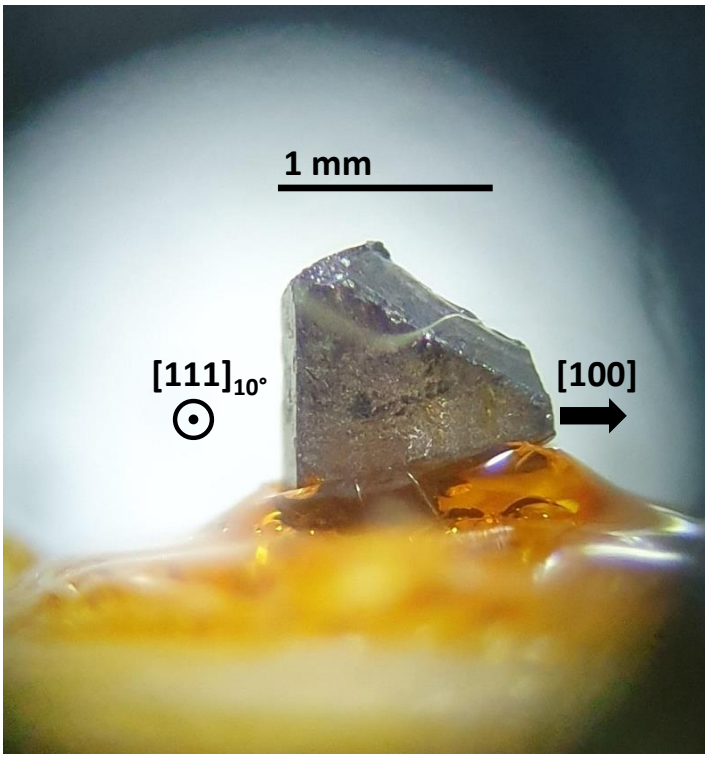

Figure 4.32: *Image of sample in situ on the screw mount with scale.*

The Laue camera images are shown in figure 4.33. The [111] crystallographic axis was aligned with the face of the sample and so presented the largest surface area for X-ray scattering allowing the clearest pattern. The [110] pattern is less clear and is also partially obscured by the isotropic background from the Blu Tac used to mount the sample to the goniometer. A pattern for the [100] was recorded but has unfortunately since been lost. The alignment of the [100] axis can also be inferred from the shape of the crystal however as it should lie along one of the "points" of the sample.

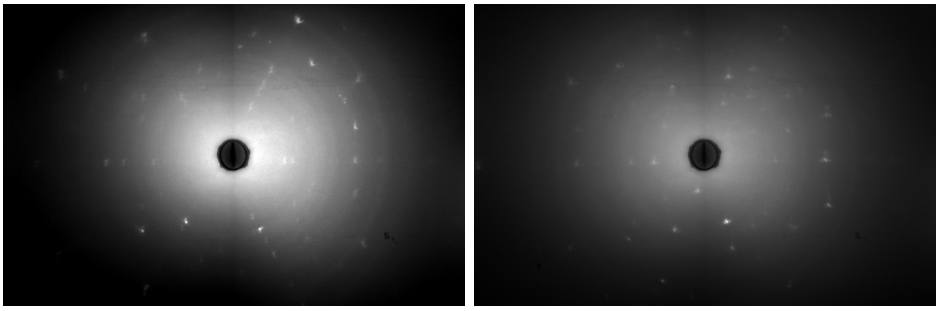

(a) (b)

Figure 4.33: *Laue camera X-ray scattering patterns of the $CdEr_2Se_4$ single crystal sample. Showing the [111] and [110] crystallographic alignments in a) and b) respectively.*

Because of the low quality of the Laue camera images, it is prudent to check the alignment using another method. This is possible using DC magnetisation measurements, as the expected saturation values of the [111], [110] and [100] are known and easily calculated from the free ion value [70]. The free ion value, μ_{FI} in $CdEr_2Se_4$ is $9\mu_B$ [48]. The saturation values per erbium ion are expected to be 0.5 μ_{FI}, 0.408 μ_{FI} and 0.577 μ_{FI} for the [111], [110] and [100] directions respectively, with an additional plateau at 0.333 μ_{FI} along the [111] direction.

DC magnetisation measurements were performed at 2 K using the vibrating sample magnetometer (VSM) option of the PPMS (figure 4.34). The crystal was measured along the orientations expected to be the [111], [110] and [100] directions, owing to difficulties in mounting the [111] direction is known to be approximately 10° off the measurement axis and so those measurements will be labelled as $[111]_{10^\circ}$ from now on. Due to the awkward shape of the samples, demagnetisation effects are difficult to account for. Because the sample is thin compared to its surface dimensions, demagnetisation effects are expected to be significant for the $[111]_{10^\circ}$ direction (face on) and insignificant for the [100] direction (edge on) with the [110] direction somewhere in between. Demagnetisation

effects should not affect the saturation value, only the magnetic field that need be applied by the magnet to achieve saturation. For this reason no demagnetisation corrections have been applied in figure 4.34.

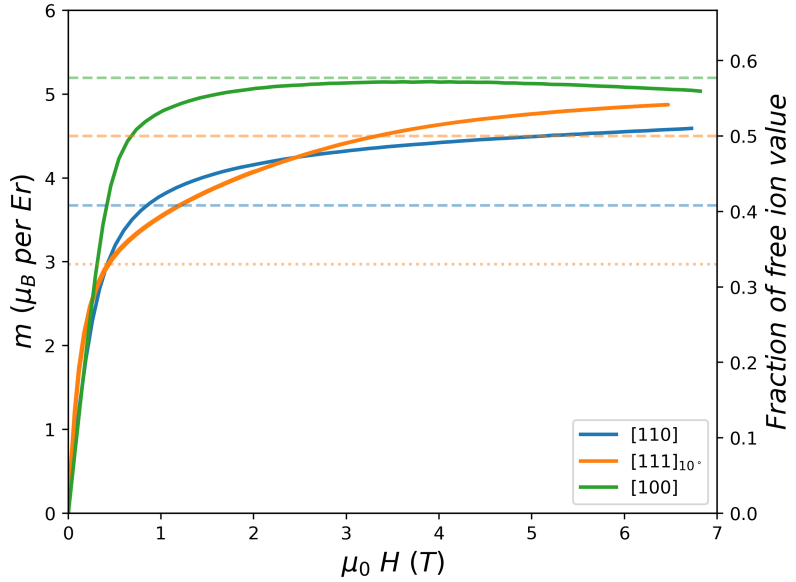

Figure 4.34: *DC magnetisation at 2 K for the three alignments indicated in the key. Solid lines are the data, dashed lines indicate expected saturation values for each alignment, the dotted line indicates the expected magnetisation of the Kagomé plateau.*

The $[111]_{10^\circ}$ measurement shows behaviour roughly consistent with that expected for the [111] direction. The measured magnetisation does not fully saturate but slowly increases at a similar value to the expected saturation value, which is consistent with being several degrees off axis. The [111] plateau is not expected at 2 K although a change in gradient is expected at approximately the plateau magnetisation which is observed. The [110] measurement is not consistent with expected behaviour and exceeds the expected magnetisation before saturation is reached by approximately 1 μ_B per Er suggesting that the [110] direction is not properly aligned. The [100] direction magnetisation saturates at almost exactly

the expected value which is a strong indicator that it has been well aligned.

Ac susceptibility measurements were performed on the single crystal sample in fields up to 0.5 T. It was measured along the $[111]_{10^\circ}$, [100] and the direction that was thought to be the [110] but that will now be labelled as [unknown]. The purpose of these measurements was to determine if the slow peak induced by the magnetic field could be attributed to a particular direction. An unaligned sample was also crushed in order to see if that would replicate the powder measurements, it should be noticed the average grain size in the crushed sample is still quite large and is not a true powder measurement. As in the DC magnetisation measurements, demagnetisation effects are expected to be significant but have not been accounted for.

In each orientation measured as well as the crushed sample, the peak in χ'' is at a frequency an order of magnitude larger than in the powder. This could be due to demagnetisation effects although a demagnetisation factor large enough to shift the peak in χ'' to its location in the powder results in an infeasibly large real part($\chi' > 2$). The high frequency susceptometer used can experience phase instability at high frequencies when measuring samples with very small moments (as is the case here) and is very sensitive to the background calibration used, so the precise centre of the peak may not be perfectly accurate. This issue is also known to get worse over the course of a series of measurements, so measurements taken later are more likely to be affected. If phase instability or background calibrations are an issue, the high frequency susceptometer will tend to underestimate the susceptibility and roll off at high frequencies. The Cole-Cole model can be fit to the $[111]_{10^\circ}$ and [unknown] alignments to reveal the true signal from the noise however this is not possible for the [100] measurement suggesting that the apparent peak in χ'' may be due to the aforementioned high frequency

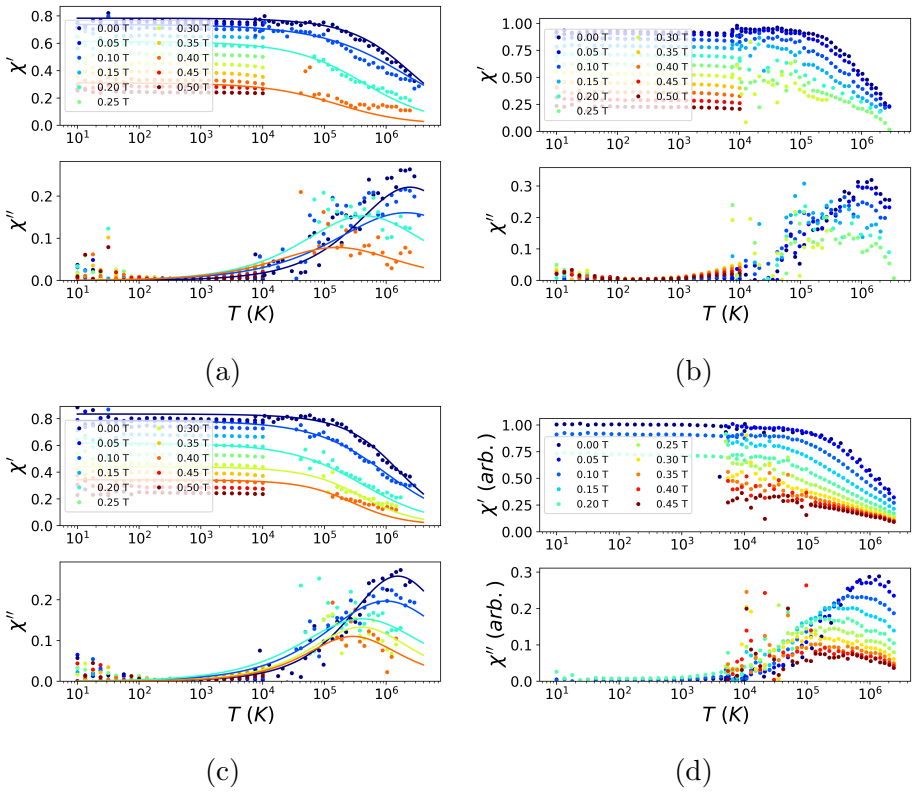

Figure 4.35: *a), b) and c) ac susceptibility measurements on the single crystal* $CdEr_2Se_4$ *at 2 K along the* $[111]_{10°}$*, [100] and [unknown] directions respectively. Lines are Cole-cole fits to the data, fits were not possible to the [100] data. d) ac susceptibility in the crushed crystal sample at 2 K, arbitrary units are used because the sample mass is not known.*

issues, the [100] measurement was performed last of all the measurements.

It is possible that the slow peak would emerge in the single crystal in greater magnetic fields than in the powder, however there is no reason to expect this to be the case and those measurements were not carried out due to concerns about the sample mounting in strong magnetic fields. The application of a magnetic field broadens the peak in the imaginary part and shifts it to lower frequency in each measured alignment.

The most important consequence of the measurements in figure 4.35 is that the slow field induced peak was not observed in any of the measured alignments.

Even more significantly the slow peak was not observed in the crushed sample.

4.9 Low Temperature Single Crystals

The single crystal $CdEr_2Se_4$ sample was also measured in Elsa L'Hotel's lab at the Néel institut, CNRS in Grenoble as part of a European Microkelvin Platform project. A dilution refrigerator was used to achieve temperatures down to 0.12 K. The same sample as before was intended to be used but it broke during mounting, the largest piece of it was used instead. The alignment was maintained but the sample is much smaller and a different shape to earlier measurements.

DC magnetisation measurements were performed along the [111] direction up to 7.5 T at 70 mK. The sample alignment is expected to be much improved with the magnetic field direction very close to the [111] direction. The results of the DC magnetisation measurements are shown in figure 4.36, no demagnetisation correction has been applied. There is a clear step in the magnetisation between 0.18 T and 1.5 T which is similar to that seen in other spin ice materials as they enter the Kagomé ice phase. Above 1.5 T there a rapid increase in the magnetisation up to 2 T above which the magnetisation increases gradually. In this phase the ice rules have been broken and the sample should be saturated. Clearly the sample has not saturated, the gradual increase in the magnetisation could be indicative of the spins being gradually canted away from their local $\langle 111 \rangle$ axes. This could also explain why the magnetisation is not field independent in the Kagomé phase.

At 70 mK between -0.2 T and 0.2 T there are jumps in the magnetisation and an asymmetry between the sweep directions. It is expected that the these jumps are the result of the erbium moments falling out of equilibrium with the magnetic

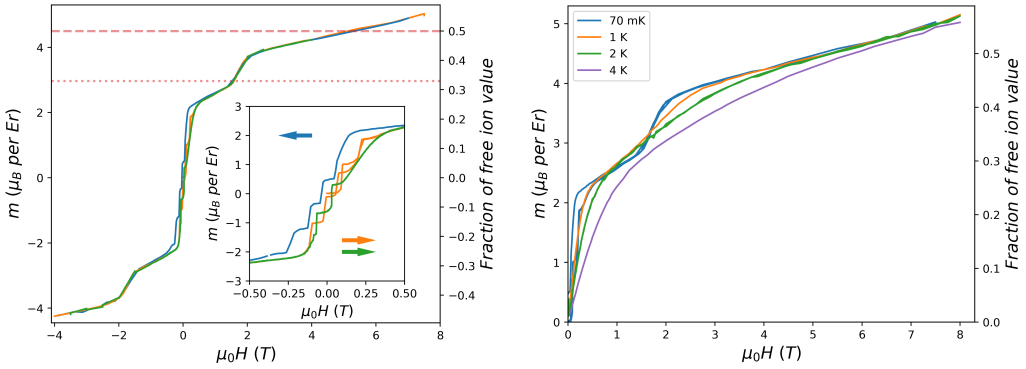

(a) (b)

Figure 4.36: *a) dc magnetisation in moment per Er ion vs field at 70 mK along the [111] direction of $CdEr_2Se_4$, inset shows the same data on a different scale. The green line represents the data with a slower sweep rate in the magnetic field compared to the blue and orange data which have the same sweep rate but differing sweep directions. Coloured arrows indicate the sweep direction of their colour matched line. Dashed line is the expected saturation value and dotted line is the expected value of the Kagomé plateau. b) dc magnetisation in moment per Er ion vs field at varying temperatures*

field due to the low temperature. The process by which this occurs is that the moments do not have sufficient energy to respond to changes in the magnetic field at the rate at which it is being swept, so the magnetisation 'lags behind' the magnetic field. As the field continues to change the system falls further behind the magnetic field until eventually the energy cost of the non-equilibrium state is great enough to allow the system to rapidly 'catch up' appearing as a sudden change in the magnetisation. It is possible that the jumps are the result of magnetic avalanches as seen in $Dy_2Ti_2O_7$ in reference [137].

This phenomenon can be investigated by performing measurements with a different sweep rate of the magnetic field. In figure 4.36 a) the green line represents data in which the magnetic field was changed at a rate approximately half that of the blue and orange lines. As can be seen in the inset, halving the sweep rate reduces the number of jumps in the magnetisation which is strong evidence that

they are not indicative of an intrinsic phenomenon but instead the result of the aforementioned non-equilibrium behaviour. The jumps in the magnetisation do not appear in the higher temperature measurements which is further evidence that they result from non-equilibrium behaviour. This is because the phenomenon of magnetic avalanches is related to the specific heat of the sample [137] with them being more likely to occur when the specific heat is small. As can be seen in figure 4.31 at 70 mK the specific heat in powdered $CdEr_2Se_4$ is small. At 1 K, the temperature of the next magnetisation measurement, the specific heat is much greater being consistent with the absence of magnetic avalanches.

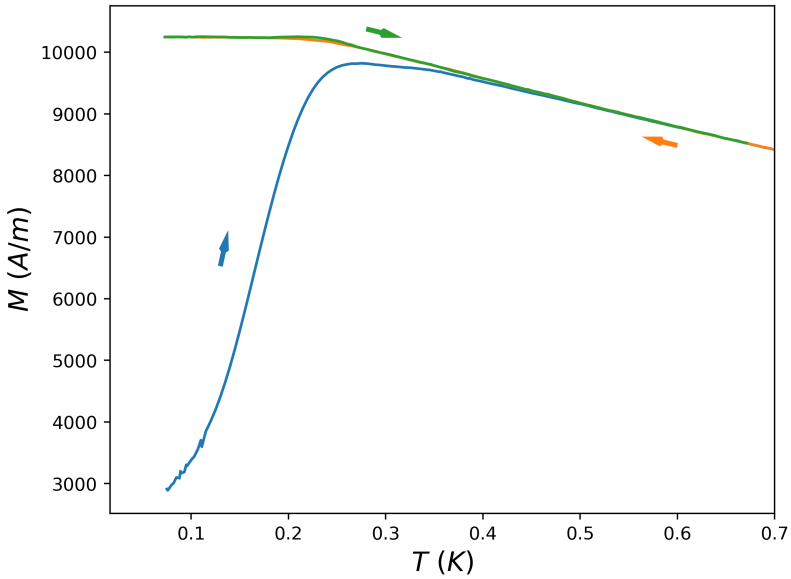

Figure 4.37: *ZFC and field cooledFC DC magnetisation measurements along the [111] axis of single crystal $CdEr_2Se_4$. Blue line shows the ZFC measurement measured on warming, orange line is the FC measurement on cooling and the green line is the FC measurement on warming.*

A ZFC-FC measurement was also performed on the single crystal sample which is shown in figure 4.37, the applied dc field was 0.01 T. There is a difference between the ZFC and FC curves below 350 mK with a strong bifurication below

250 mK, these values are both much lower that in the powder sample suggesting that the spin freezing temperature in the single crystal is less than in the powder. As in the powder there is a temperature hysteresis between the warming and cooling portions of the FC curve.

AC susceptibility measurements were also performed using a SQUID along the [111] axis of the single crystal sample. Owing to difficulties in the calibration of the SQUID the location of the peaks in χ'' can be trusted but not the absolute value of χ so the data is presented here in arbitrary units. Peak locations were estimated by fitting a Gaussian distribution to the peak of the imaginary part for the 0 T and 0.1 T measurements whereas the peak locations were taken by eye for the 0.2 T measurement as Gaussian distributions provided a poor fit. The extracted peak locations are shown in figure 4.38 d). Arrhenius fits give an activation energy of (5.71±0.2) K in 0 T which is smaller than in the powder. In a magnetic field of 0.1 T and 0.2 T the activation energies are (5.99±0.06) K and (8.56±0.76) K respectively.

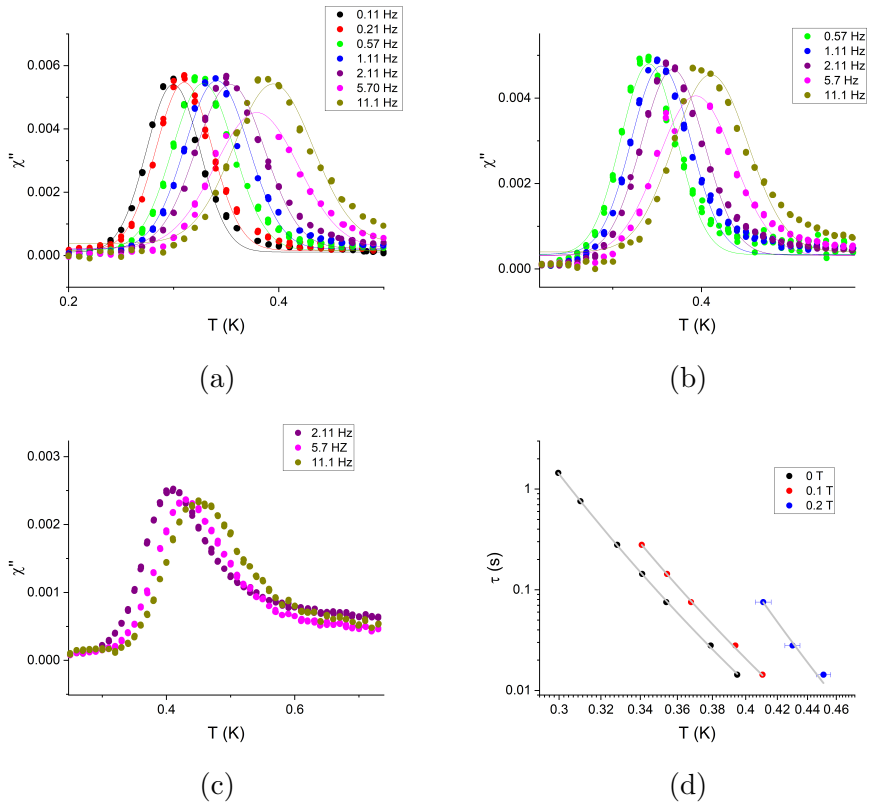

Figure 4.38: Low temperature ac susceptibility in single crystal $CdEr_2Se_4$ along the [111] crystal direction in: a) No applied magnetic field. b) 0.1 T applied magnetic field. c) 0.2 T magnetic field. Lines are Gaussian fits to the data. d) Relaxation times vs temperature with fits to Arrhenius law (grey lines)

4.10 Previous Observations in the Literature

The emergence of a second relaxation mechanism in the application of a magnetic field has been previously observed in powder diluted spin ice $Dy_{2-x}Y_xTi_2O_7$ [138][139] and powder undiluted spin ice $Dy_2Ti_2O_7$ [140]. Yttrium was used as the doping element because it is non-magnetic and has a similar atomic radius to Dy. All of these measurements were made using ac susceptibility and found very similar behaviour of both peaks in the region of the time independent plateau to the behaviour of both peaks in $CdEr_2Se_4$ and $CdEr_2S_4$. The field required to cause both mechanisms to have equal weight is much larger ($\approx$1 T) than in the

spinels.

In reference [138] the field induced mechanism is attributed to the magnetic field reducing/increasing the net transverse magnetic field at the rare earth ions. They also observed a minimum in τ with increasing field and found the location of the minimum to be temperature dependent. The behaviour of both mechanisms was found to be dependent on the level of doping.

In reference [140] the effect of spin dilution was further examined. Measurements in undoped $Dy_2Ti_2O_7$ powder set in epoxy resin also observed both mechanisms, however the slow mechanism was observed at a much higher frequency than in loose powder measurements. A phenomenon they explained by contraction of the epoxy exerting pressure on the sample as it was cooled.

Xing *et al.* [139] performed the most recent study to have observed coexisting relaxation mechanisms in a spin ice material. They studied $Dy_{1.6}Y_{0.4}Ti_2O_7$ only and attempted to capture the temperature dependence of both mechanisms more accurately than in earlier papers by fitting to two Havriliak-Nagami[11] functions (a more generalised version of the Cole-Cole model). They found that both mechanisms were thermally activated (as opposed to a quantum and a thermal mechanism) and they explained their measurements as the result of spin clustering. Where two groups of spin clusters respond differently to the field depending on their orientation.

In all of these measurements the available frequency range was much smaller than available for the measurements presented in this chapter. To the best of my knowledge the field induced effect has never been observed in a single crystal spin ice sample.

4.11 Discussion of Field Induced Mechanism

Based on the measurements so far the precise nature of the slow mechanism is still an open question. Some possible explanations are discussed below however it is not possible to prove or disprove any of them currently.

It is possible that the crystal anisotropy that is the source of the coexisting mechanisms. The single crystal measurements suggest that the [111] and [100] axes are not responsible for the slow mechanism as no field induced peak was observed with the field applied along those directions.

It is possible that the slow peak would have been observed when measuring along a different axis. Possible candidates for orientations where the slow peak could be observed are the [110] and [112] directions. Both of these orientations have spins that would be perpendicular to the applied magnetic field, and can become decoupled from their environment [85, 82] interacting amongst themselves. Measurements in DTO along the [110] and [111] crystallogrpahic axes are shown in figure 4.39. With the field along the [110] direction (figure 4.39) the relaxation time moves to lower frequency in magnetic fields greater than 0.6 T which is approximately consistent with the phase diagram in ref. [82]. The relaxation time rapidly diverges from that measured with the magnetic field along the [111] direction, indicating that τ depends strongly on the crystal orientation of the DC magnetic field. It is possible that the transition happens at a low enough field in $CdEr_2Se_4$ to be the slow peak although this cannot be confirmed without specific heat measurements on single crystal samples.

The absence of the slow peak in the crushed sample is harder to explain. If the slow peak can be attributed to any particular crystal direction then there should be some contribution from that direction in the crushed sample. Therefore the

fact it has not been observed in the crushed sample suggests that the slow peak mechanism does not exist at all in the single crystal materials. This could be explained by crystal defects or impurities in either the powder or single crystal sample. Defects or impurities are more likely in the single crystals than the powders as the powders are very high quality (see the supplementary information in ref. [49]). Another explanation could be that there was only a small fraction of the axis responsible for the slow peak in the crushed sample and its response was too small to be detected.

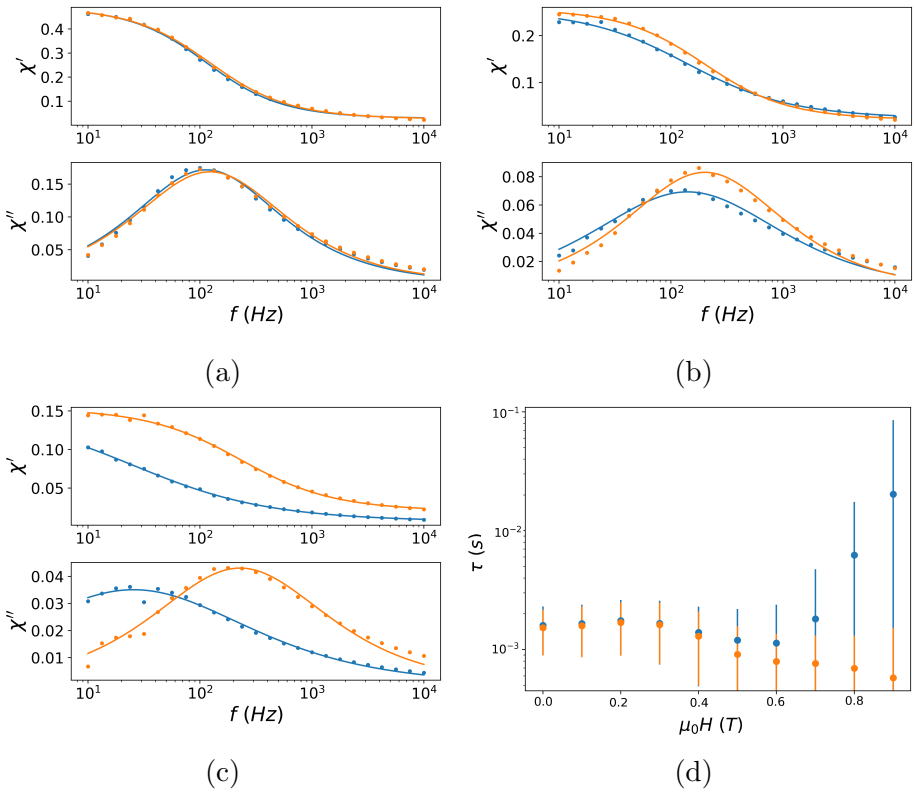

Figure 4.39: *ac susceptibility data in $Dy_2Ti_2O_7$ along the [110] (blue markers) and [111] (orange markers) directions. Lines are fits to the Cole-Cole model. Example data with fits are shown in a) 0.4 T, b) 0.6 T and c) 0.8 T. The full behaviour of, τ, with H is shown in d).*

Field anisotropy is thought to be the most likely explanation but it cannot be confirmed until large and more accurately aligned single crystal samples can be

measured.

It is possible that the isotopes of erbium that have a nuclear magnetic moment could be responsible for the observed behaviour. The ^{167}Er isotope of erbium has a natural abundance of 22.93% and is the only stable isotope to have a nuclear magnetic moment with a spin number of 7/2. It could be the case that the application of a magnetic field is splitting the hyperfine levels on erbium ions that have a nuclear magnetic moment. This splitting could lead to an avoided level crossing as seen for example in Holmium doped $LiYF_4$ [141, 142]. The behaviour of the slow mechanism with increasing field is roughly consistent with a thermally activated transition between two levels in the region of an avoided crossing. The main problems with this explanation however is that it ought to be the case in the single crystal sample too, but that has not been observed. Nuclear moments have previously been observed to affect spin dynamics in other spin ice materials [66] [143].

Another possible explanation could be modification of the CEF levels by the magnetic field. The application of a magnetic field could alter the CEF environment and change the available states and gaps. A significant change in the CEF levels is considered unlikely as a fairly large change in the first excited level would be required to account for a thermal process. Additionally preliminary inelastic neutron scattering results on $CdEr_2Se_4$ in a magnetic field were performed in collaboration with Tom Fennell at the Paul Scherrer Institut, Switzerland that did not indicate any change in the CEF levels. It is quite plausible however that the field could be altering the splitting of the ground state doublet. As discussed in section 4.3, the fast dynamics on the temperature independent plateau can be attributed to intrinsic magnetic fields splitting the ground state doublet. The application of a magnetic field could be changing the splitting in powder grains

in certain orientations relative to the magnetic field. If this is the case it could be investigated by measuring with a magnetic field applied perpendicular to the [111] direction. As before, in order to perform such a measurement would require a well aligned single crystal sample along such a direction.

It could be that the origin for the slow mechanism lies in the fact that the ground state wave function is not a pure $\pm|15/2\rangle$ state but has some smaller contributions from lower spin states that are still highly anisotropic (see table I in ref. [49]). The magnetic field could be amplifying the contributions of those states by making them more energetically favourable in powder grains of certain alignments. This possibility may be best investigated using a theoretical investigation, however one has not yet been carried out.

Finally, another explanation could be that the field induced relaxation comes from defects in the sample, such structural defects or the presence of impurities. However this is considered unlikely. The large amplitude of the field induced relaxation mechanism (relative to the fast mechanism) would suggest that for defects to be responsible they would have to be present to a significant degree. The powder sample measured here is from the same batch as in ref.[49] which was investigated using X-ray scattering and found to contain $< 1\%$ magnetic impurities.

4.12 μSR

A muon spin rotation experiment was performed on powdered $CdEr_2Se_4$ as part of the investigation into the twin relaxation mechanism phenomenon. There were two reasons for doing so. Firstly, the μSR technique allows measurement of the fluctuation rate of nearby spins to the muon allowing us to confirm the relaxation

times measured by our ac susceptibility measurements. The second motivation is to take advantage of having a spin system where we can tune the relaxation time of the system through the application of a magnetic field, and see how this affects the muon. Another possible result was detection of persistent spin dynamics at low temperature.

The experiment was performed at the ISIS facility at Rutherford Appleton Laboratory, UK. The EMU instrument was used with a sorption refrigerator (sorp) for measurements between 355 mK and 20 K. A closed cycle refrigerator (CCR) was used for measurements between 25 K and 300 K. In both sets of measurements a magnet was used that is capable of producing magnetic fields up to 0.45 T and active field compensation was used for zero field measurements. The sample was stuck to the sample holder plate with GE varnish and covered with 1 layer of silver foil.

4.12.1 Zero Field Measurements

The high temperature CCR data is shown in figure 4.40 which shows that at the highest temperature, the muon asymmetry depolarises gradually with a line shape that is well fit by a stretched exponential:

$$P_z = A_0 \exp\Big(-(\lambda t)^{\beta}\Big) \tag{4.2}$$

where λ is the polarisation decay constant, t is time, A_0 is the initial asymmetry and β is the stretch parameter. As the sample temperature is lowered, the asymmetry depolarises faster, eventually moving into the instrumental dead time by 25 K. This is in contrast to the neutron spin echo measurements performed in ref. [49] which indicate that the relaxation time should decrease with increasing

temperature. This suggests that the fluctuations the muon is measuring are in the motionally narrowed fast fluctuation limit.

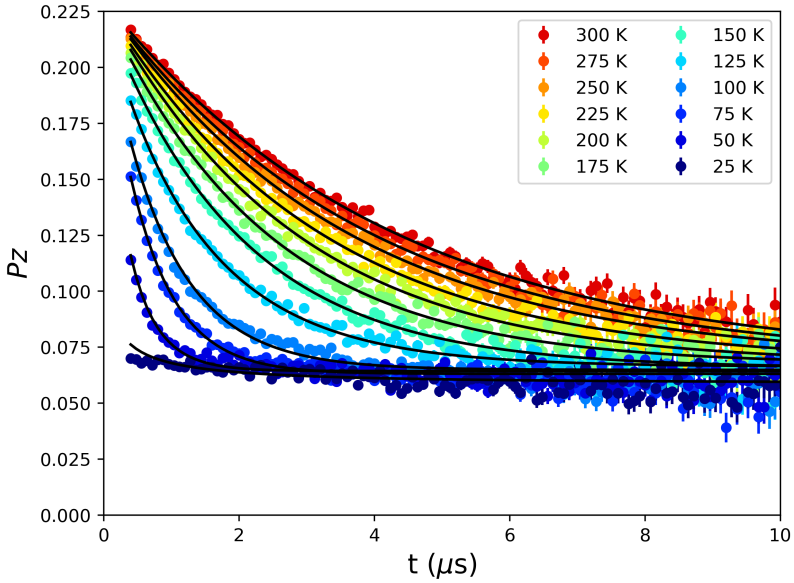

Figure 4.40: *Muon asymmetry in $CdEr_2Se_4$ as the sample is cooled. Black lines are stretched exponential fits to the data (coloured markers).*

In the fast fluctuation limit, λ is inversely proportional to the spin fluctuation rate, ν, which is in itself inversely proportional to the spin relaxation time τ. Figure 4.41 shows the results of the stretched exponential fits. The stretch parameter is approximately 1 for almost all temperatures, suggesting a narrow distribution of relaxation times. If a distribution of relaxation times exists, then the average fluctuation rate is related to the first moment of the stretched exponential by equation 4.3. In the fast fluctuation limit the relaxation time, τ, is proportional to the fluctuation rate by $2\Delta^2$ where Δ is the Kubo-Toyabe parameter. In order to avoid making assumptions about the value of Δ at this point the inverse of $\langle 1/\lambda \rangle$ is plotted in figure 4.41. Arrhenius fits to figure 4.41 will have incorrect values of τ_0 however E_a will be correct.

$$\left\langle \frac{1}{\lambda} \right\rangle = \int_0^\infty A_0 \exp\Big(-(\lambda t)^\beta\Big) dt = \frac{1}{\lambda\beta}\Gamma\left(\frac{1}{\beta}\right) \tag{4.3}$$

where $\Gamma()$ is the error function. There are two distinct energy regimes visible in λ, which are clearly discerned from one another in figure 4.41 with a transition region around 100 K. This transition is also visible in β. As the depolarisation moves into the instrumental dead time beta drops off rapidly from 1 and λ increases sharply. A probable explanation is that there is insufficient depolarisation to fit to accurately, rather than being the result of an intrinsic sample phenomenon.

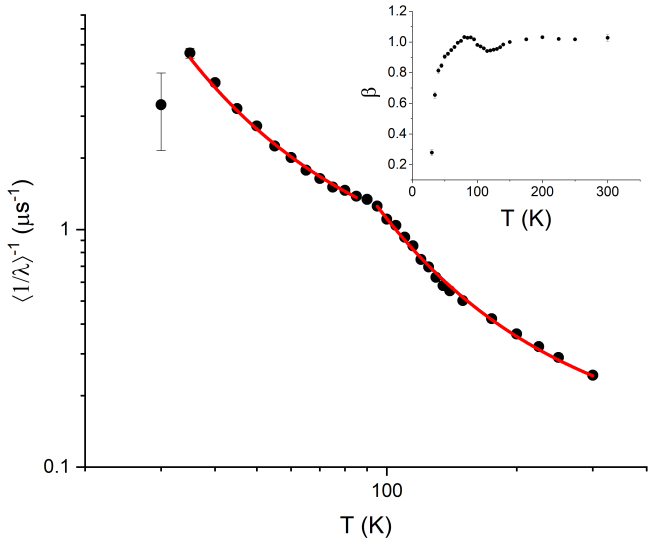

Figure 4.41: *Inverse of* $\langle 1/\lambda \rangle$ *against temperature from stretched exponential fits to figure 4.40. Red lines are fits to an Arrhenius law. Inset is the temperature dependence of the stretch parameter* β

Fitting to an Arrhenius law gives activation energies of (80.5±2.2) K for the 35 K to 90 K region and (228.5±4.7) K for the 105 K to 300 K region. An activation energy of 80.5 K is not consistent with any particular transition between crystal field levels[49] but is close to the average of the 1st (E_1 =45.2 K),

2^{nd}(E_2 =65.8 K), 3^{rd} (E_3 =102.8 K) and 4^{th} E_4 =112.4 K) excited levels so may represent some combination of thermal transitions. Similarly, 225.5 K could represent some combination of transitions between states except now also including the 5^{th} (E_5 =306.1 K) and 6^{th} (E_6 =338.0 K) crystal field levels, although the origin of this value is less clear. It is perhaps significant that the transition region aforementioned is consistent with the temperature at which the Boltzmann weight of the 5^{th} and 6^{th} levels start to become significant.

In the sorp measurements (figure 4.42) almost all of the muon depolarisation is lost in the instrumental dead time (the time between the muons arriving and the first good data bin). For instance, in the measurement at 20 K the first good bin is at 0.28μs with a muon asymmetry of 0.014, compared with a maximum asymmetry of the instrument of approximately 0.23 as seen in the early time data points of figure 4.40. This suggests that ν has slowed to the point where motional narrowing no longer reduces the decay constant enough for the depolarisation to be measured but also has not slowed enough to be measured. A significant number of counts ($\approx 150 \times 10^6$ events) were taken in order to ensure that the absence of a signal was not due to noise or low resolution.

The absence of any significant measured muon asymmetry continues down to 0.33 K, which was the lowest temperature measured. There is a slight exponential trend in the measured asymmetry in all the measurements between 0.355 K and 20 K, however because the relaxation is effectively temperature independent it is not likely to be a signal from the sample but a background signal. At 0.33 K and 0.75 K there is a small additional depolarisation at early times, which is greater in the 0.355 K measurement. Indicating that some temperature dependent depolarisation is occurring in the instrumental dead time, that may become visible at temperatures below 0.355 K.

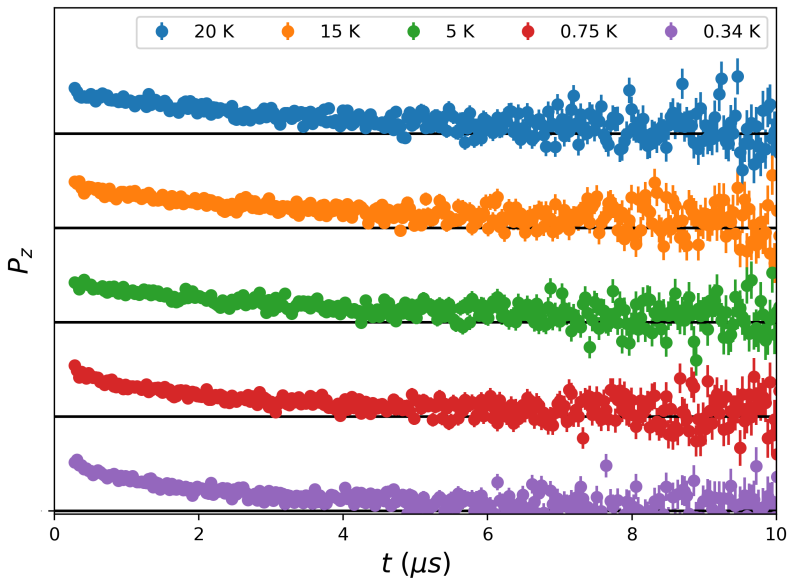

Figure 4.42: *Muon asymmetry in $CdEr_2Se_4$ at low temperature. Measurements have been shifted up the y-axis to separate them with the black lines representing $P_z = 0$ for each measurement.*

The absence of a measured signal in this temperature range is unexpected, ac susceptibility measurements suggest that the spin fluctuation rate should be easily measured using μSR. Between 2 K and 5 K, the fluctuation rate from ac susceptibility is 324.8 kHz which should be easily detectable in the muon data. This is even more pronounced at temperatures below 2 K where the fluctuation rate decreases exponentially with decreasing temperature. By 0.7 K, the fluctuation rate from ac susceptibility is expected to be 1.08kHz, effectively static compared to the lifetime of a muon. The implication therefore is that the spin fluctuation rate experienced by the muon is several orders of magnitude faster than expected.

This is not without precedent; Lago *et al.* [67] measured relaxation times 3 orders of magnitude faster than expected in another dipolar spin ice $Dy_2Ti_2O_7$. In fact, they measured similar behaviour at all temperatures, they measured

exponential depolarisation at high temperatures (70 - 280 K) which moved into the instrumental dead time upon cooling suggesting motional narrowing. Upon cooling below 40 K, the depolarisation re-emerges from the instrumental dead time, with behaviour consistent with the slow fluctuation limit (slow relaxation of the 1/3 tails). Lago *et al.* speculated that the 3 orders difference in their results could be due to the different Q-space sampling of ac susceptibility (Q=0) and μSR (average over all Q values) or due to measurement of different relaxation processes, however they considered both of these unlikely and left it an open question. The μSR measurements in $CdEr_2Se_4$ in this section provide no new insight, although the similarity in qualitative behaviour may suggest a similar cause. A possible explanation in both materials ($CdEr_2Se_4$ and $Dy_2Ti_2O_7$) is that the muon introduces a perturbation that alters the crystal and spin fluctuation rates. This possibility has been investigated before by Foronda *et al.* [103] in the pyrochlore $Pr_2Sn_2O_7$ (a quantum spin ice candidate [46, 144]) where the presence of the muon was found to pull nearby O^{2-} ions off their initial positions and split the CEF levels of the Pr^{3+} ions. In $CdEr_2Se_4$ and $Dy_2Ti_2O_7$ the magnetic ions are Kramers ions (Pr^{3+} is non-Kramers) so the ground state cannot be split by the muons electric field, however a structural distortion may alter the CEF environment of the rare earths whilst leaving the ground state doublet intact. For example such a perturbation could alter the energy gap to the first excited state. The exact mechanism will be different in $CdEr_2Se_4$ as there are no O^{2-} ions, however the muon could distort the positions of the Se^{2-} ions.

4.12.2 Longitudinal Field Measurements

Measurements in a longitudinal field (LF) were also performed in both the CCR and sorp. A sweep of the full temperature range of the CCR in a LF of 0.1 T

was performed and is shown in figure 4.43. As in zero field, the depolarisation is well fit by a stretched exponential at all temperatures. The polarisation decay constant is again decreasing with increasing temperature suggesting it is again in the fast fluctuation limit. In fast fluctuation limit with a LF the relationship between λ and ν is more complicated than in ZF, and in the case of very fast fluctuations is given by the Redfield formula [89] (a special case of the Keren function[95]):

$$\lambda = \frac{2\Delta^2\nu}{\nu^2 + \gamma_\mu^2 B_{LF}^2} \tag{4.4}$$

where Δ is the Kubo-toyabe parameter describing the width of the field distribution at the muon site, γ_μ is the muon gyromagnetic ratio and B_{LF} is the magnitude of the longitudinal magnetic field. The implication of this is that in order to determine how ν changes with temperature and field we need to know the value of Δ.

To measure Δ accurately, we need data taken on a continuous muon beam line (one that produces a steady stream of single muons) because they have much greater time resolution. A μSR experiment was performed in 2010 by Jorge Lago at the Paul Scherrer Institut (a continuous source) as part of reference [48] and the data was made available by them for analysis. The experiment was performed on the LTF instrument in zero field at 19 - 600 mK. A dynamic Kubo-Toyabe function (see section 2.18) was fitted to the data.

At 600 mK and below, only the crystal field ground state is expected to be occupied and therefore the distribution of magnetic fields experienced by the muon is assumed to be the same for all 5 measurements. Figure 4.44 b) supports the assumption of Δ being temperature independent as each fitted Δ is close

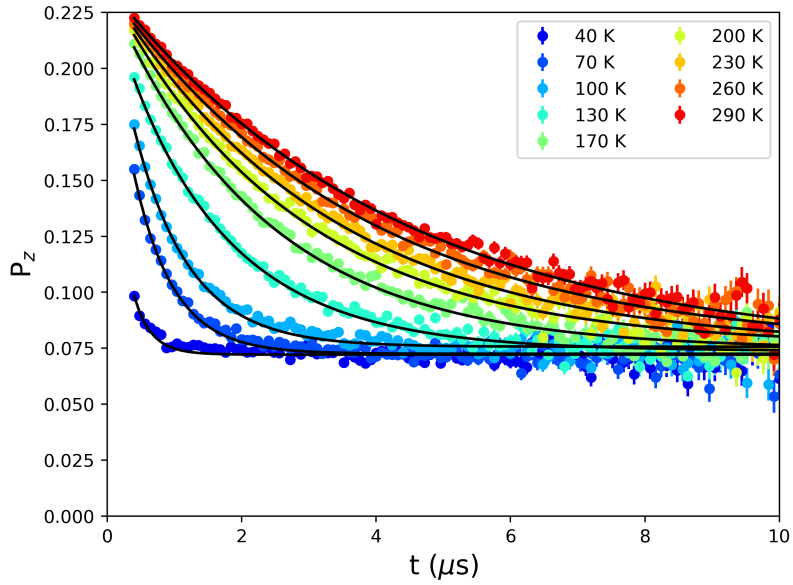

Figure 4.43: *Muon asymmetry in $CdEr_2Se_4$ in a longitudinal magnetic field of 0.1 T. Black lines are stretched exponential fits to the data (coloured markers).*

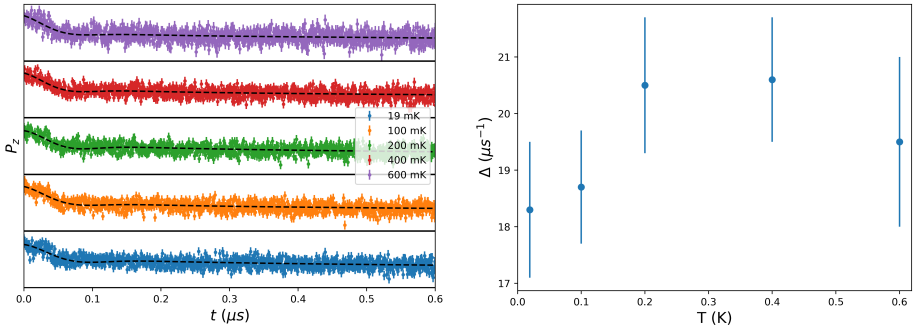

(a) (b)

Figure 4.44: *a) Muon asymmetry in $CdEr_2Se_4$ taken by Jorge Lago at PSI, Switzerland. Dashed black lines are dynamic Kubo-Toyabe fits to the data (coloured points). Solid black lines represent the zero points of each measurement which have been shifted up the y-axis for clarity. b) Internal field distribution Δ from dynamic Kubo-Toyabe fits as a function of temperature.*

to the average Δ of (19.52 $\pm$ 0.54) μs, which corresponds to an internal field distribution width of (143.9 $\pm$ 3.8) mT.

Using this value, the temperature evolution of the spin fluctuation rate can

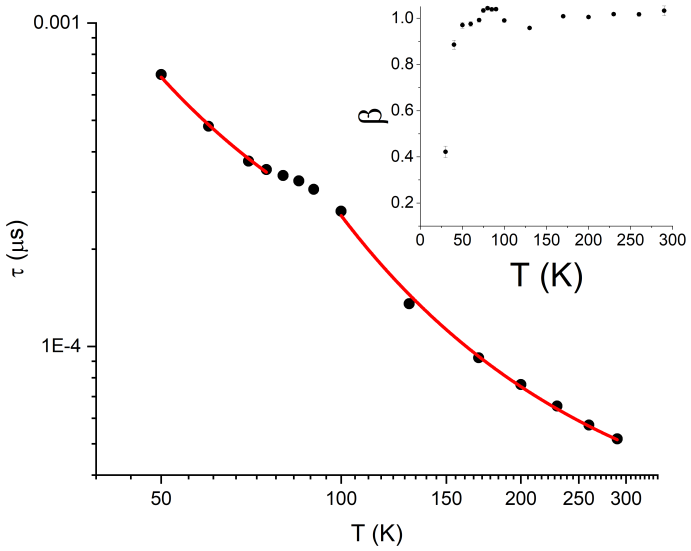

Figure 4.45: *Relaxation time τ calculated using the Redfield formula on λ from stretched exponential fits in figure 4.43 to the 0.1 T data. Red lines are fits to an Arrhenius law. Inset shows the temperature evolution of the stretch parameter β.*

be determined if the assumption is made that Δ does not change significantly up to 300 K. λ for equation 4.4 is assumed to be given by $1/\langle 1/\lambda \rangle$. τ is given by $1/(2\pi\nu)$ and the values of τ are shown in figure 4.45. As in zero field two clear Arrhenius laws can be observed with a with two clear regimes transitioning at approximately 95 K. In the high temperature case an Arrhenius law finds an activation energy of (243.7 $\pm$ 6.2) K, an increase of 18.6 K compared to the zero field case. At T<75 K the fit yields an activation energy of (101.6 $\pm$ 5.4) K an increase of 21 K on the zero field measurements. The increases in activation energies can by explained by there being some modification of the crystal field energy levels as a result of the field, or that Δ is not temperature independent.

Constant temperature field sweeps were performed at 35 K, 75 K, 110 K and 300 K up to 0.45 T. As can be seen in figure 4.46, as the field is swept there is little change in the decay rate, λ is effectively field independent for all values. β

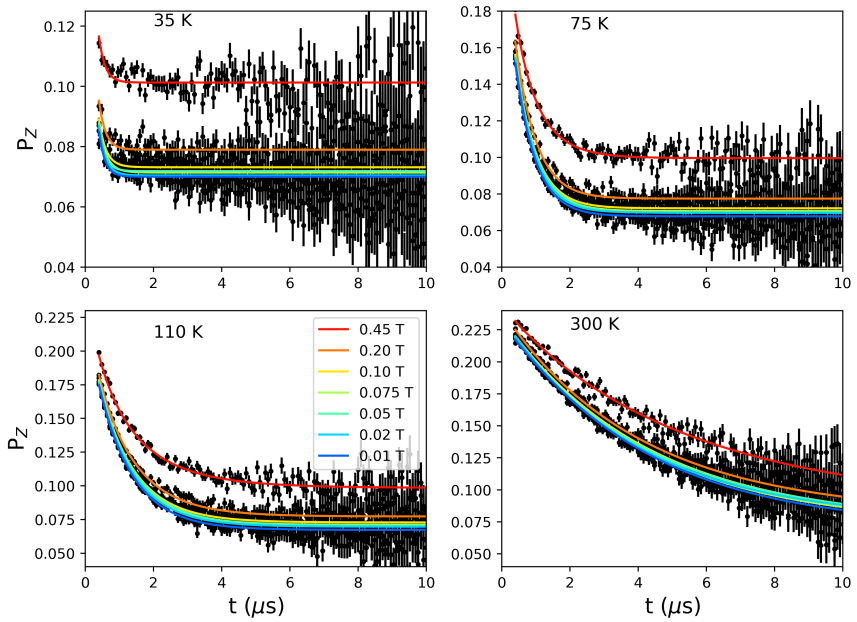

Figure 4.46: *Muon asymmetry data at 35 K, 75 K, 110 K and 300 K with stretched exponential fits (coloured lines). Legend in the lower left panel is applicable to all panels.*

is close to 1 for most measurements at 75 K, 110 K and 300 K except at 0.45 T where it drops off to 0.9. Using equation 4.4 to extract ν is not possible for all measurements, particularly those performed at 35 K. This is because equation 4.4 returns a complex value which is unphysical, suggesting that for those points the assumptions of the Redfield formula are no longer suitable. The results that could be calculated are shown in figure 4.47 and show that there is weak dependence on the magnetic field at 75 K and 110 K with a gradual reduction in ν as the field is increased. At 300 K there is no clear trend as a function of field and the data point at 0.45 T is believed to be an outlier. At 35 K there are few physical ν values, a probable explanation is that at 35 K the spins are not fluctuating sufficiently fast to be in the limit where equation 4.4 applies.

Field sweeps were also performed as part of the sorp measurement set. DC field measurements were taken at 355 mK, 1 K, 2 K and 5.4 K up to 0.45 T

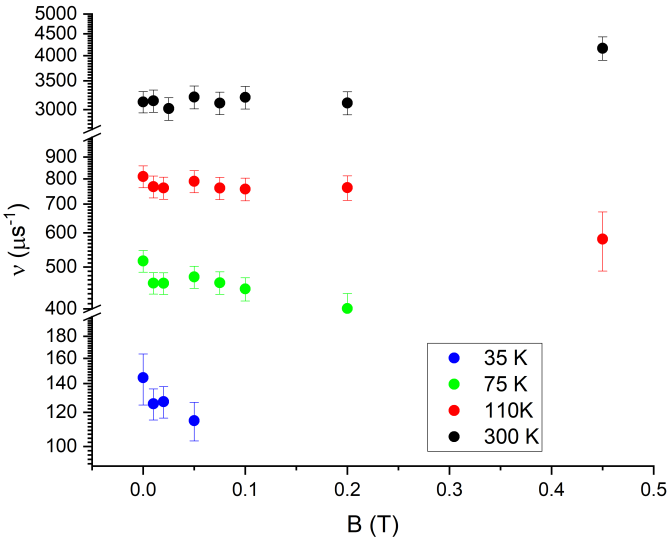

Figure 4.47: *ν as calculated from equation 4.4 against the applied magnetic field at 35 K, 75 K, 110 K and 300 K*

and are shown in figure 4.48. At all temperatures the application of a longitudinal magnetic field leads to a recovery of the tail asymmetry up to about half the expected initial asymmetry. Unfortunately the magnet was incapable of producing a magnetic field that would fully recover the asymmetry to provide another method of directly measuring Δ (the muons should not depolarise for $\gamma_\mu B_{LF}/\Delta \approx 10$). However, if the recovery of the asymmetry is assumed to be linear in field, then it is possible to estimate the field that would fully recover the asymmetry. A linear fit finds a gradient of (14.6 $\pm$ 1.8) T^{-1} with intercept (2.99 $\pm$ 0.58) suggesting that the full asymmetry is recovered in a field of (1.37 $\pm$ 0.18) T, implying an internal field width of approximately 140 mT. Given that somewhat shaky assumption of linearity, this value is remarkably close to the internal field width found from the fits to Jorge Lago's data.

The small additional depolarisation at early times observed previously in the

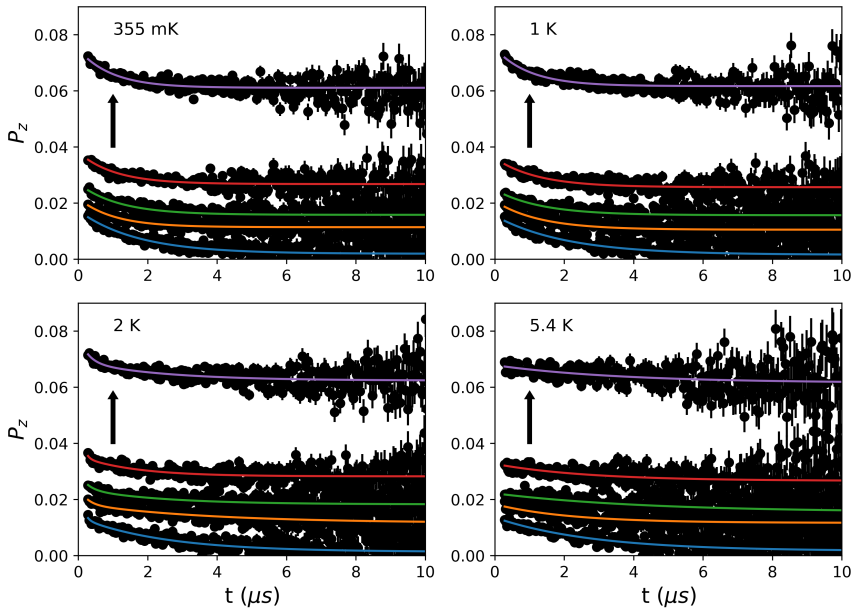

Figure 4.48: *Longitudinal field measurements at 355 mK, 1 K, 2 K and 5.4 K. Arrows indicate direction of increasing field each temperature has measurements at 0 T, 0.1 T, 0.18 T, 0.27 T and 0.45 T. Coloured lines are fits to equation 4.5.*

0.355 K and 0.75 K ZF data is visible in figure 4.48 at 0.355 mK and 1 K, and appears to change slightly with field. To attempt to quantify this phenomenon, exponential decay functions were fitted to the data (equation 4.5), one for the slow decay mentioned earlier and another to fit the depolarisation at early times. The first decay constant, λ_1, fits the slow relaxation and the second, λ_2, fits the early times depolarisation. As can be seen in figure 4.49 neither λ_1 nor λ_2 show a clear trend with field at either temperature.

$$Pz = a_1 \exp(-\lambda_1 t) + a_2 \exp(-\lambda_2 t) + A_{tail} \tag{4.5}$$

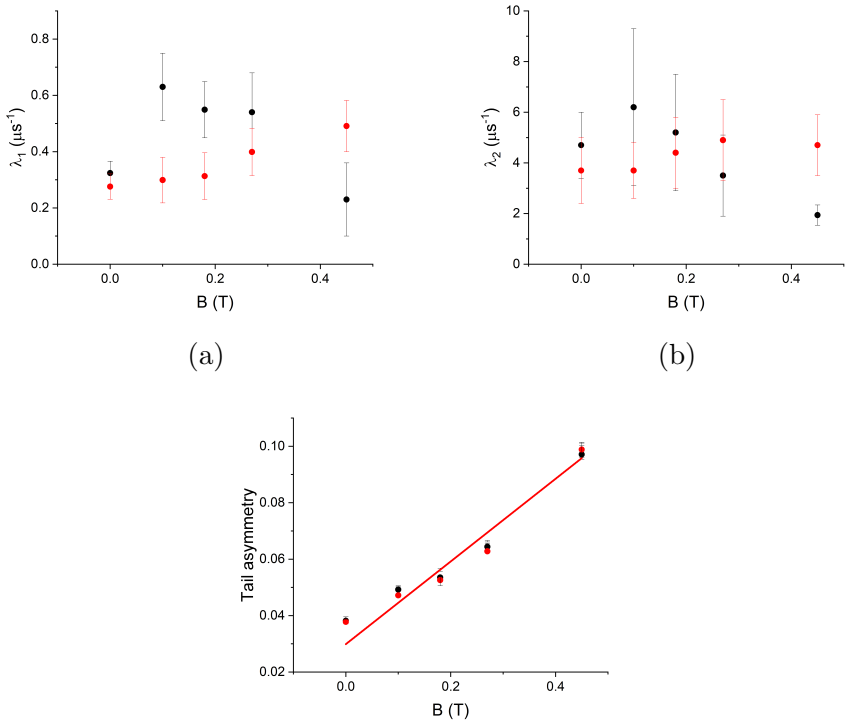

Figure 4.49: *Fit parameters from fits to equation 4.5 at 355 mK (black circles) and 1 K (red circles). a) Decay constant λ_1. b) Decay constant λ_2. c) Tail asymmetry A_{tail} with straight line fit to 1 K points.*

4.13 Summary and Future Work

The quantum tunnelling plateau has been measured using the high frequency susceptometer, providing further insight into the spin ice behaviour in $CdEr_2Se_4$ and $CdEr_2S_4$. ac susceptibility measurements in applied dc magnetic fields have uncovered coexisting relaxation mechanisms in the powder samples that were found to exist with differing temperature dependences and energy scales. ac susceptibility data was taken over a large range of fields and temperatures, including measurements taken at millikelvin temperatures at the Néel Institute, Grenoble.

Preliminary specific heat measurements in magnetic fields up to 0.5 T did not

show any sign of a magnetic phase transition that could be responsible for the field induced relaxation mechanism. These measurements are only preliminary and the magnetic contribution has not been separated out from the other contributions, however in the temperature range covered it is expected to be the dominant contribution.

Dc magnetisation measurements at 2 K in the $CdEr_2Se_4$ single crystal sample found saturation values approximately consistent with expected along the [100] and [111] directions. The dc magnetisation measurement at 70 mK found that the Kagomé plateau is not flat as in other spin ice materials, and the expected saturation value was exceeded.

At 2 K the field induced relaxation was not observed by ac susceptibility measurements of the $CdEr_2Se_4$ single crystal sample along any of the measured directions although the data is very noisy owing to the samples small size. However were the field induced relaxation present with a similar amplitude to the powder sample then the ACMS should have been sensitive enough to detect it. Measurements at low temperature however did find a weak relationship between the applied dc field and the activation energy.

The spin freezing temperature was measured in both powder and single crystal $CdEr_2Se_4$, and found to be lower in the single crystal sample.

The zero field μSR experiment in $CdEr_2Se_4$ has observed behaviour similar to that seen in another spin ice material $Dy_2Ti_2O_7$. The muon asymmetry depolarises orders of magnitude faster than is expected from ac susceptibility data such that no asymmetry is measured when the spin fluctuation rate should be well within the dynamic range of μSR. Measurements at higher temperatures did measure an asymmetry as the measured fluctuations entered the motionally narrowed limit. Those measurements found two distinct energy scales with a

transition at around 100 K.

Measurements in an applied magnetic field did not find any evidence of the slower field induced mechanism observed using ac susceptibility. Which suggests that either the muon is not able to measure that mechanism or that it is also too fast to be observed in this experiment. It is quite possible that whatever process increases the zero field relaxation rate would also increase the rate of the slower mechanism rendering it unmeasurable. An estimate of the internal field distribution was obtained however the magnet used in this experiment was not powerful enough to measure it directly.

Ultimately, this experiment has provided limited insight into $CdEr_2Se_4$ or the phenomenon of the coexisting peaks. It may however be worthwhile to perform a μSR experiment in $CdEr_2Se_4$ or $CdEr_2S_4$ using a continuous muon source to expand upon Jorge Lago's measurements. Measuring to higher temperatures and in applied magnetic fields with the time resolution available to a continuous source may reveal some information about both relaxation mechanisms.

Future investigation of the coexisting relaxation mechanisms in the powder sample could benefit from inelastic neutron scattering data to determine if the crystal field levels are affected by the application of the magnetic field. Additionally measuring the specific heat in larger magnetic fields could yield information about the presence of any anisotropic magnetic phase changes.

Measurements in a doped sample, were the magnetic erbium ion is replaced with some non-magnetic ion may be of interest. Doping of the magnetic ions has been shown to influence a field induced peak in powder $Dy_{2-x}Y_xTi_2O_7$, a similar experiment in $CdEr_2Se_4$ or $CdEr_2S_4$ may provide some explanation.

The most useful area of future research however is likely to be in further study of single crystal samples. Access to larger single crystal samples would

make accurate alignment and measurement easier. Measuring the single crystals with a magnetic field along the [110] and [211] directions may reveal the field induced slow mechanism.

Chapter 5

Quantum States in μSR

5.1 Introduction

So far this thesis has predominantly focused on a macroscopic measurement technique (Chapter 3) and on a magnetic spin system in which the microscopic properties of the system are evident and detectable at the macroscopic level (Chapter 4). This chapter focuses on a spin system in which the underlying physics can only be understood on the microscopic scale with a quantum mechanical treatment. This system occurs as a result of the quantum interaction between fluorine nuclei and implanted muons in a μSR experiment. This topic bears some relevance to the field of frustrated magnetism because one of the materials studied ($LiY_xHo_{1-x}F_4$) is an example of a frustrated Ising spin system (for $x = 0$). In this chapter however it is the non-magnetic fluorine atoms that are of interest.

5.2 Pure, Mixed & Entangled States

A group of particles are said to be in an entangled state if the state of a particle in the group cannot be written independently of the others. For instance, imagine two qubits that can each be in state $|0\rangle$ or $|1\rangle$ where, $|...\rangle$ represents a ket vector in Dirac's notation [145]. If the first qubit is in state $|0\rangle$ and the second qubit is in state $|1\rangle$ then the total state of the system can be written as $|\phi\rangle = |0\rangle \otimes |1\rangle = |01\rangle$ so the two qubits are not entangled[146, 147]. The symbol $\otimes$ represents the tensor product which is mathematically performed by the Kronecker product. However if the qubits are prepared in a state given by $|\psi\rangle = \frac{1}{\sqrt{2}}(|01\rangle - |10\rangle)$[148, 149] then it is not possible to write this as a product of individual states and it is impossible to discuss the state of one qubit without considering the other, this is an example of an entangled state.

Pure and mixed states describe the state of an ensemble of quantum systems[146]. If the ensemble reliably forms in a single state described by a single vector then (such as $|\phi\rangle$ or $|\psi\rangle$) then it is in a pure state. However if the ensemble is instead in a statistical mixture of allowed states, for instance 75% is in $|\phi\rangle$ and 25% is in $|\psi\rangle$, then it is said to be in a mixed state[150]. It is not possible to describe a mixed state with a single ket vector. Such a scenario is likely to occur in a composite quantum system where there is imperfect information about the initial state of all the particles or one of the particles has an entangled state as one of its available states.

5.3 Density Matrices

Throughout this chapter density matrices will be used to represent quantum states formed by implanted muons and other particles, in particular fluorine nu-

clei. The density matrix, ρ, for a particle that can exist in n states: $|\psi\rangle_1, |\psi\rangle_2, ..., |\psi\rangle_n$ is given[151][150]by

$$\rho = \sum_{j=1}^{n} p_j |\psi\rangle_j \langle\psi|_j \tag{5.1}$$

where p_j is the probability that the particle is in state $|\psi\rangle_j$. The probabilities p_j are normalised such that $\sum p_j = 1$. The advantage of density matrices is that they can easily describe both mixed and pure states.

The total density matrix of a composite quantum system is given by the tensor product of the density matrix of each particle so for N particles it is given by:

$$\rho_{tot} = \rho_1 \otimes \rho_2 \otimes ... \otimes \rho_N. \tag{5.2}$$

The expectation value of an observable, A, can be calculated by performing the product of the density matrix with the relevant operator and then taking the trace of the resulting matrix like so[147]:

$$\langle A \rangle = \mathrm{Tr}[\rho \hat{A}]. \tag{5.3}$$

If the system is not prepared in a pure state of one of the eigenstates of the system Hamiltonian,$\mathcal{H}$, then it will evolve over time[152]. This will mean that the density matrix is time dependent. Assuming that the quantum system in question is closed (it does not interact with its environment) then the time evolution of the density matrix is governed by the Liouville-von Neumann equation,

$$i\hbar \frac{\partial \rho}{\partial t} = [\mathcal{H}, \rho] \tag{5.4}$$

where, i is the imaginary unit and $\hbar$ the reduced Planck's constant. The square

brackets indicate a commutator which is defined as $[A, B] = AB - BA$. The solution to equation 5.4 is

$$\rho = U(t)\rho(0)U(t)^{\dagger} \tag{5.5}$$

where $U(t)$ is the unitary time propagator that evolves the state of the system: $|\psi(t)\rangle = U(t)|\psi(0)\rangle$. For a time independent Hamiltonian $\rho(t)$ is given by[153]

$$\rho(t) = e^{-i\mathcal{H}t/\hbar}\rho(0)e^{i\mathcal{H}t/\hbar} \tag{5.6}$$

which is a solution to equation 5.4. For a time dependent Hamiltonian a solution can be achieved by firstly integrating equation 5.4 between 0 and t over the dummy variable, t', to achieve

$$\rho(t) = \rho(0) - \frac{i}{\hbar}\int_0^t [\mathcal{H}(t'), \rho(t')]dt' \tag{5.7}$$

then by repeatedly substituting equation 5.7 into itself we can get

$$\rho(t) = \rho(0) - \frac{i}{\hbar}\int_0^t [\mathcal{H}(t'), \rho(0) - \frac{i}{\hbar}\int_0^{t'} [\mathcal{H}(t''), \rho(0) - \frac{i}{\hbar}\int_0^{t''} [\mathcal{H}(t'''), \rho(0) - ...]dt''']dt'']dt' \tag{5.8}$$

which through the Dyson series[154] is mathematically equivalent to

$$\rho(t) = \hat{T}_+ \left[\exp\left\{-\frac{i}{\hbar}\int_0^t \mathcal{H}(t')dt'\right\}\right] \rho(0) \hat{T}_- \left[\exp\left\{\frac{i}{\hbar}\int_0^t \mathcal{H}(t')dt'\right\}\right] \tag{5.9}$$

where $\hat{T}_+$ and $\hat{T}_-$ are time ordering operators (in different directions).

When simulating the density matrix of a system with a time dependent Hamil-

tonian it may be computationally favourable to instead use an iterative version of equation 5.4. One way of doing this is is using the following[155]

$$\rho(t) = e^{-i\mathcal{H}(t)dt/\hbar}\rho(t-dt)e^{i\mathcal{H}(t)dt/\hbar} \tag{5.10}$$

where dt is the time step used in the iteration. In order to show that equation 5.10 is also a solution to equation 5.4, the first step is to repeatedly substitute it into itself N times giving

$$\rho(t) = \prod_{n=0}^{N}\left[e^{-i\mathcal{H}(t-ndt)dt/\hbar}\right]\rho(t-Ndt)\prod_{n=N}^{0}\left[e^{i\mathcal{H}(t-ndt)dt/\hbar}\right]. \tag{5.11}$$

If we let $dt = t/N$, in the limit of $N \to \infty$ then dt becomes infinitesimally small and $\rho(t-Ndt)$ tends to $\rho(0)$. In this case in the exponent of the left exponential we have: $\sum_{n=0}^{\infty} -i\mathcal{H}(t-ndt)dt/\hbar$ which for infinitesimally small dt is mathematically equivalent to an integral. Therefore, equation 5.11 tends to

$$\rho(t) = \exp\left\{-\frac{i}{\hbar}\int_0^t \mathcal{H}(t')dt'\right\}\rho(0)\exp\left\{\frac{i}{\hbar}\int_0^t \mathcal{H}(t')dt'\right\} \tag{5.12}$$

which, because of the ordering of the products in equation 5.11, is equivalent to equation 5.9 and therefore a solution to equation 5.4. A more detailed derivation is given in reference [156] and in the appendix of reference [157].

5.4 Entangled Muon States

So far in this thesis, muons have been used to measure magnetic dynamics and internal fields. These experiments have been ones in which the muons experience some static or fluctuating magnetic environment and their response to it can be well described as an average response to the total muon environment. However,

this is not always the case, in some materials the muon couples strongly to a small number of nearby particles and interacts with them directly. When this occurs, the observed muon asymmetry cannot be explained simply as the result of classical magnetic fields at the muon site causing the muon to precess nor can it be explained by fluctuations in those classical fields. Instead to understand the asymmetry it must be treated as part of a quantum mechanical system.

5.4.1 Muonium

A simple case of an implanted muon interacting directly with a nearby particle is Muonium. The muonium state is formed when the implanted muon captures a nearby electron and forms an effective atom[158][93][93]. In Muonium, the muons behave similarly to a proton, meaning the muon-electron system behaves like a short lived version of Hydrogen[159]. It has even been observed forming compounds with other atoms such as MuCl[160], this field of research is often referred to as muonium chemistry[161].

In muonium, the spin of the muon and the spin of the captured electron become entangled with one another, interacting via the hyperfine interaction. The muonium state can be described with the following basis: $|\uparrow\uparrow\rangle$ $|\uparrow\downarrow\rangle$ $|\downarrow\uparrow\rangle$ $|\downarrow\downarrow\rangle$ [148]. The basis is defined such that $|\uparrow\rangle$ denotes a spin in the up orientation (positive z direction) and $|\downarrow\rangle$ is the down orientation. The basis state $|\uparrow\downarrow\rangle$ is a product state representing the $|\uparrow\rangle$ state for the muon and $|\downarrow\rangle$ for the election, it is given by $|\uparrow\downarrow\rangle = |\uparrow\rangle \otimes |\downarrow\rangle$. The other basis states are similarly defined.

The muons arrive spin polarised in the $|\uparrow\rangle$ state because their spins are antiparallel to their momentum which is in the $-z$ direction by convention. The electrons can initially be in either $|\uparrow\rangle$ or $|\downarrow\rangle$ orientation with equal probability. Therefore their initial density matrices are:

$$\begin{aligned} \rho_\mu(0) &= |\uparrow\rangle\langle\uparrow| \\ \rho_e(0) &= \frac{1}{2}\left(|\uparrow\rangle\langle\uparrow| + |\downarrow\rangle\langle\downarrow|\right) \end{aligned} \tag{5.13}$$

Their states then evolve over time according to the hyperfine interaction Hamiltonian:

$$\mathcal{H} = A_0 h \boldsymbol{I}.\boldsymbol{S} \tag{5.14}$$

where h is Planck's constant ($h/2\pi = \hbar$), A_0 is the hyperfine coupling constant, $\boldsymbol{I}$ is the muon spin operator and $\boldsymbol{S}$ is the electron spin operator. The spin operators are defined by

$$\begin{aligned} \boldsymbol{I} &= \frac{\hbar}{2}\left(\vec{\sigma} \otimes \mathbb{I}\right) \\ \boldsymbol{S} &= \frac{\hbar}{2}\left(\mathbb{I} \otimes \vec{\sigma}\right) \end{aligned} \tag{5.15}$$

where $\mathbb{I}$ is the identity matrix and

$$\vec{\sigma} = (\sigma_x, \sigma_y, \sigma_z) \tag{5.16}$$

where σ_x, σ_y and σ_z are the Pauli spin matrices.

The expectation value of the muon polarisation is therefore given by

$$P_z(t) = \mathrm{Tr}[\rho(t) I_z] \tag{5.17}$$

where I_z is the z component of $\boldsymbol{I}$.

The eigenstates of the Hamiltonian are indicated on the energy level diagram

in figure 5.1 a). Because the initial density matrix of the system does not commute with the Hamiltonian[152], the system should oscillate indefinitely, typically with a frequency proportional to the energy gap between the states. Figure 5.1 b) shows the muon polarisation as measured in an idealised μSR experiment. The measured signal oscillates with a frequency proportional to the energy gap ($\omega = \hbar\Delta E$) as the muon spins fluctuate between allowed states, as expected. Figure 5.1 b) also shows the expected signal for if the system was prepared in a pure $|\uparrow\uparrow\rangle$ state, which is an eigenstate of the Hamiltonian. In this case the system stays in that state and does not evolve over time.

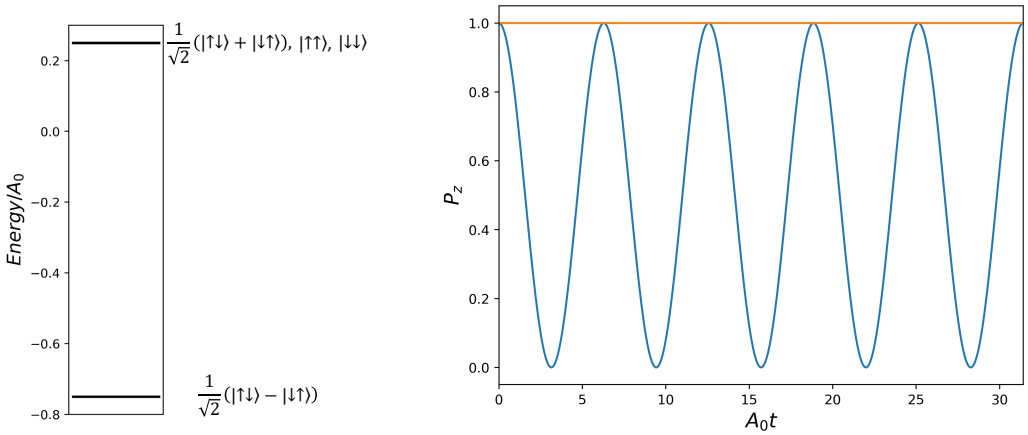

(a) (b)

Figure 5.1: *a) Energy level diagram of the solutions to the muonium Hamiltonian in units of $A_0 = 1$. b) Spin polarisation vs time for the initial conditions in equations 5.13 (blue line) and for muonium prepared in the pure $|\uparrow\uparrow\rangle$ state (orange line).*

5.4.2 F-μ

In a μSR experiment on a sample containing fluorine, the muon is likely to implant at a site very close to a fluorine atom. Fluorine is the most electronegative element meaning it creates a very dense electron cloud around it, this dense

cloud of negative charge is what attracts the muon. When this happens, the muon and fluorine nuclei interact via the dipole-dipole interaction and become entangled[162]. The only stable isotope of fluorine is ^{19}F which has nuclear spin 1/2.

The Hamiltonian describing their interaction is given by:

$$\mathcal{H}_{\mu F} = \frac{\mu_0 \gamma_\mu \gamma_F}{4\pi r^3}[\boldsymbol{I}.\boldsymbol{S} - 3(\boldsymbol{I}.\hat{\boldsymbol{r}})(\boldsymbol{S}.\hat{\boldsymbol{r}})] \tag{5.18}$$

where, γ_μ is the gyromagnetic ratio of the muon, γ_F is the gyromagnetic ratio of the fluorine nucleus ($\gamma_F = 40.05 \times 2\pi$ MHz/T), r is the F-μ separation, $\hat{\boldsymbol{r}}$ is a unit vector pointing between the fluorine nucleus and the muon, and $\boldsymbol{S}$ denotes the fluorine nuclear spin. Clearly in this case the relative positions of the two particles becomes significant, which was not the case in muonium, as is their positions relative to the incoming muon spins. The eigenvalues of equation 5.18 are shown in figure 5.2 a), with the allowed transitions indicated. As in section 5.4.1, units of A_0 have been used where $A_0 = \mu_0 \gamma_\mu \gamma_F / 4\pi r^3$. There are 4 eigenstates denoted $|0\rangle$, $|1\rangle$, $|2\rangle$ and $|3\rangle$ which depend on the orientation of the F-μ bond relative to the initial muon spin (z-axis). If $\hat{\boldsymbol{r}}$ is in the x-y plane (transverse to z) then these eigenstates are:

$$\begin{aligned}
|0\rangle &= \frac{1}{\sqrt{2}}\left(|\uparrow\downarrow\rangle + |\downarrow\uparrow\rangle\right) \\
|1\rangle &= \frac{1}{\sqrt{2}}\left(|\uparrow\uparrow\rangle + |\downarrow\downarrow\rangle\right) \\
|2\rangle &= \frac{1}{\sqrt{2}}\left(|\uparrow\downarrow\rangle - |\downarrow\uparrow\rangle\right) \\
|3\rangle &= \frac{1}{\sqrt{2}}\left(|\downarrow\downarrow\rangle - |\uparrow\uparrow\rangle\right)
\end{aligned} \tag{5.19}$$

whereas if $\hat{\boldsymbol{r}}$ is parallel to z then the states are:

$$\begin{aligned} |0\rangle &= |\uparrow\uparrow\rangle \\ |1\rangle &= |\downarrow\downarrow\rangle \\ |2\rangle &= \frac{1}{\sqrt{2}}\left(|\uparrow\downarrow\rangle - |\downarrow\uparrow\rangle\right) \\ |3\rangle &= \frac{1}{\sqrt{2}}\left(|\uparrow\downarrow\rangle + |\downarrow\uparrow\rangle\right). \end{aligned} \tag{5.20}$$

If the bond is in a different alignment to the two aforementioned, then the eigenstates will be different again (typically a superposition of all of the 4 basis states). Figure 5.2 b) shows some example muon polarisations for the F-μ bond in the parallel and transverse cases. The frequency of oscillation for the muon spin is again proportional to the energy gap of the relevant transitions, of which there are 2 for the transverse cases and 1 for the parallel case.

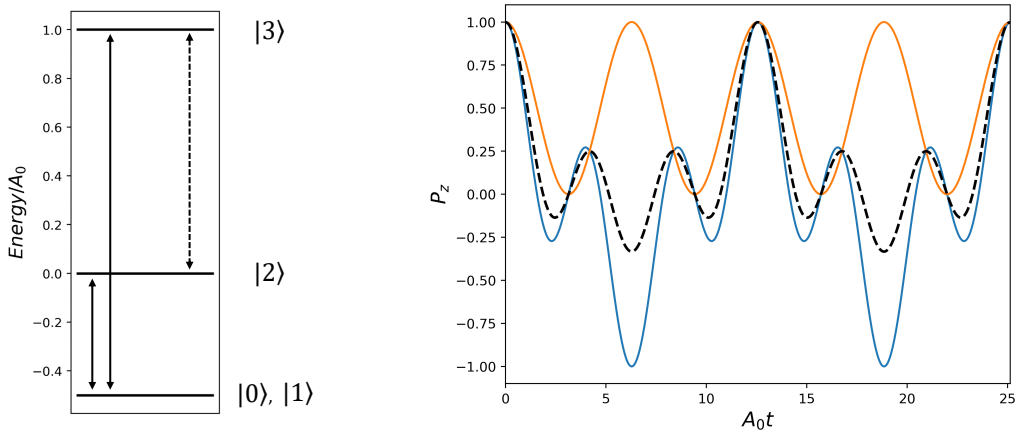

(a) (b)

Figure 5.2: *a) Energy level diagram of the solutions to the F-μ Hamiltonian in units of A_0. Arrows indicate allowed transitions in the transverse (solid arrow) and parallel (dashed arrow) geometries. b) Muon spin polarisation vs time in the case that the F-μ bond is transverse to z (blue line) or parallel to z (orange line) also shown is the polycrystal spatially averaged result (dashed black line).*

Analytic solutions can be obtained for the muon polarisation in the F-μ state and are given by

$$\begin{aligned} P_{z,parallel} &= \frac{1}{2} + \frac{1}{2}\cos(A\hbar t) \\ P_{z,transverse} &= \frac{1}{2}\cos(3A\hbar t/2) + \frac{1}{2}\cos(A\hbar t/2). \end{aligned} \tag{5.21}$$

In the case of a powder/polycrystalline sample there will not be a single bond orientation. Instead there is an average of all orientations and so both sets of transitions will be observed. An analytic equation for the powder case can be obtained by taking 1/3 of the parallel case and 2/3 of the transverse case to give:

$$P_{z,powder} = \frac{1}{6}\left[1 + \cos(A\hbar t) + 2\cos(3A\hbar t/2) + 2\cos(A\hbar t/2)\right]. \tag{5.22}$$

In an amorphous sample there may be a distribution of bond lengths as well as an averaging of orientations. An analytic solution for this has not been derived but the polarisation can be calculated by sampling a distribution of bond lengths and averaging them.

In June 2018, a μSR experiment was performed on a polyvinylidene fluoride (PVDF) sample on the EMU instrument at ISIS. The muons are expected to form the F-μ state. PVDF exhibits both amorphous and crystalline regions with approximately equal proportions of each[163]. If the polycrystalline regions are small and not mutually aligned, then the F-μ trace should resemble the powder case. A previous μSR experiment in PVDF found that the polarisation was well fitted by equation 5.22[164].

As can be seen in figure 5.3, the muon asymmetry is gradually lost over

the course of each measurement. This is not an intrinsic feature of the F-μ system, which should in principle oscillate forever (in isolation) because $\rho(0)$ and $\mathcal{H}_{\mu F}$ do not commute (as shown in figure 5.2 b). Therefore, the loss of muon polarisation must be due to the influence of other factors in the system. There are multiple possible sources of external influence, with examples including other nearby spins[165], muon hopping[166] or thermal effects. Properly accounting for these sources can be complicated, computationally expensive and may require assumptions be made about the system. So at this point their influence will be modelled by multiplying by a stretched exponential. A stretched exponential is used because it requires no assumptions about the form of the decay, it is purely phenomenological [167]. Additionally, accounting for the presence of a possible background signal can be done with the addition of an exponential term and a flat background. This gives the fitting function:

$$P_z(t) = Ae^{-(\lambda_1 t)^\alpha} P_{z,powder}(t) + Be^{-(\lambda_2 t)^\beta} + A_{bkg} \tag{5.23}$$

where α and β are stretch parameters and, A, B, λ_1, λ_2 and A_{bkg} are all fitting constants.

Fitting equation 5.23 yields the fit results in figure 5.3. The fit finds an F-μ separation of r=(0.11002 $\pm$ 0.00003) nm, the parameters of the decaying exponential are λ_1=(0.21$\pm$0.03) μs^{-1}, α=(1.29$\pm$0.02) and A=(0.1075$\pm$0.001). The value of α suggests more than one source of damping on the oscillations. r and λ_1 are close to values previously reported in PVDF [164] although they did not use a stretched exponential for damping. The value of A is smaller than expected, indicating that only around half of the muons form in the F-μ state described by $P_{z,powder}(t)$ (full initial asymmetry on EMU is $P_z \approx 0.23$). For the back-

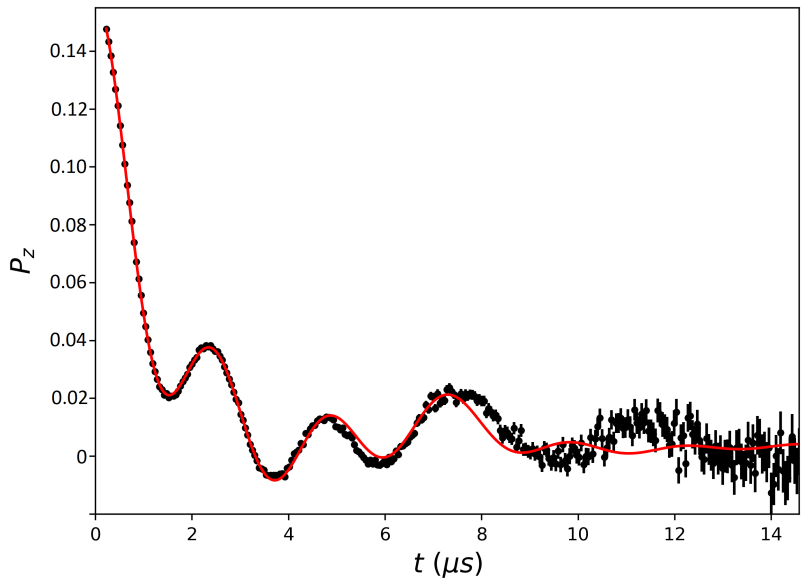

Figure 5.3: *Muon polarisation in PVDF at 10 K (black points) with fit to equation 5.23 (red line).*

ground, the fit finds B=(0.048±0.001), λ_2=(0.423±0.010) μs^{-1}, β=(1.61 ± 0.05) and A_{bkg}=(0.0028±0.0002). B is larger than expected, suggesting a significant fraction of the muons form states not described by $P_{z,powder}(t)$. Fitting was also tried with up to 5 $P_{z,powder}(t)$ terms (to account for other polycrystalline phases which may exist in PVDF), which was found to not improve the fit.

The comparatively large exponential background could be caused by muons stopping in the amorphous regions of the sample. In these areas there will still be a number of fluorine nuclei that the muons can become entangled with. Figure 5.4 shows some simulated traces from muons forming in the amorphous region. The polarisations in figure 5.4 were calculated by assuming a normal distribution of F-μ separations centred on 0.11 nm, with standard deviations of 0.1 nm, 0.2 nm and 0.3 nm. The normal distributions were each sampled 1×10^6 times, the polarisation was calculated for each sample r and then all of the polarisations were averaged and plotted. Figure 5.4 shows how this leads to a rapid initial drop in

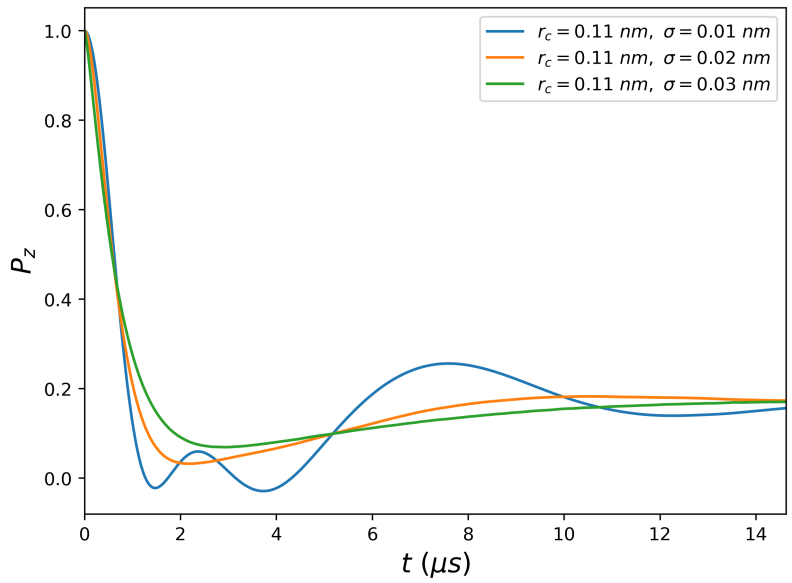

Figure 5.4: *Possible muon polarisations from the amorphous regions of PVDF for a normal distribution of F-μ distances. Distribution centres r_c and standard deviations σ are indicated in the figure legend.*

muon polarisation before tending to a constant value. If there is a signal of this nature in the experimental data, it may explain why there is a large exponential background, and also why the fit to the polarisation is poor beyond 8 μs. A similar proposition was examined in ref. [168] in poly-tetrafluoroethylene (PTFE) but was discounted. Fits to the data with an amorphous background term have been attempted but have not yet been successful.

It is also possible that some muons may be forming other states such as muonium which has been observed to coexist with the F-μ-F state in fluorinated salts[169]. This may explain why the initial asymmetry is less than expected[170] for EMU (0.23).

5.4.3 F-μ-F

It is also possible for the muon to localise at a site which is near to multiple fluorine atoms. Such as in the F-μ-F[162] state where a muon becomes entangled with 2 fluorine nuclei. It is the F-μ-F state of interest to us in this section, as this is the state that forms in the sample discussed later: $LiHo_{1-x}Y_xF_4$. As before, the muon and fluorine nuclei interact via the dipole-dipole interaction meaning that the Hamiltonian is made up of three terms of the form of equation 5.18.

$$\mathcal{H}_{F\mu F} = \mathcal{H}_{F_1\mu} + \mathcal{H}_{\mu F_2} + \mathcal{H}_{F_1F_2} \tag{5.24}$$

For $\mathcal{H}_{F_1F_2}$, A_0 should be altered to use only fluorine gyromagnetic ratios ($\gamma_F\gamma_F$ instead of $\gamma_\mu\gamma_F$). Because $\mathcal{H}_{F_1F_2}$ is typically small compared to $\mathcal{H}_{F_1\mu}$ and $\mathcal{H}_{\mu F_2}$ as a result of the smaller value of γ_F and greater distance between the fluorine nuclei, it is often neglected in the literature[162, 164, 171]. The spin operators must be updated to match the new dimensionality of the three particle Hilbert space and are now given by:

$$\begin{aligned} \boldsymbol{I} &= \frac{\hbar}{2}\left(\vec{\sigma}\otimes\mathbb{I}\otimes\mathbb{I}\right) \\ \boldsymbol{S_1} &= \frac{\hbar}{2}\left(\mathbb{I}\otimes\vec{\sigma}\otimes\mathbb{I}\right) \\ \boldsymbol{S_2} &= \frac{\hbar}{2}\left(\mathbb{I}\otimes\mathbb{I}\otimes\vec{\sigma}\right). \end{aligned} \tag{5.25}$$

The new basis is $|\uparrow\uparrow\uparrow\rangle$, $|\uparrow\uparrow\downarrow\rangle$, $|\uparrow\downarrow\uparrow\rangle$, $|\uparrow\downarrow\downarrow\rangle$, $|\downarrow\uparrow\uparrow\rangle$, $|\downarrow\uparrow\downarrow\rangle$, $|\downarrow\downarrow\uparrow\rangle$ and $|\downarrow\downarrow\downarrow\rangle$. Which is defined similarly to the F-μ basis.

The allowed transitions and energy levels of Hamiltonian are shown in figure 5.5 a), in units of A_0. The eigenstates of the Hamiltonian are generally

entangled states of several of the basis states, as an example for the cases of the F-μ-F bond being parallel to the initial muon spin they are:

$$\begin{aligned}
|0\rangle &= |\uparrow\uparrow\uparrow\rangle \\
|1\rangle &= |\downarrow\downarrow\downarrow\rangle \\
|2\rangle &= -a|\uparrow\downarrow\downarrow\rangle + b|\downarrow\uparrow\downarrow\rangle + b|\downarrow\downarrow\uparrow\rangle \\
|3\rangle &= -b|\uparrow\uparrow\downarrow\rangle - b|\uparrow\downarrow\uparrow\rangle + a|\downarrow\uparrow\uparrow\rangle \\
|4\rangle &= \frac{-1}{\sqrt{2}}\left(|\downarrow\uparrow\downarrow\rangle - |\downarrow\downarrow\uparrow\rangle\right) \\
|5\rangle &= \frac{-1}{\sqrt{2}}\left(|\uparrow\uparrow\downarrow\rangle - |\uparrow\downarrow\uparrow\rangle\right) \\
|6\rangle &= d|\uparrow\downarrow\downarrow\rangle + c|\downarrow\uparrow\downarrow\rangle + c|\downarrow\downarrow\uparrow\rangle \\
|7\rangle &= c|\uparrow\uparrow\downarrow\rangle + c|\uparrow\downarrow\uparrow\rangle + d|\downarrow\uparrow\uparrow\rangle
\end{aligned} \tag{5.26}$$

where,

$$\begin{aligned}
a &= \sqrt{\frac{1}{3+\sqrt{3}}} \\
b &= \sqrt{\frac{2+\sqrt{3}}{6\sqrt{3}}} \\
c &= \sqrt{\frac{1}{6+2\sqrt{3}}} \\
d &= \sqrt{\frac{2+\sqrt{3}}{3+\sqrt{3}}}.
\end{aligned} \tag{5.27}$$

The initial density matrix of the system is also defined similarly to before as

$$\rho(0) = |\uparrow\rangle\langle\uparrow| \otimes \frac{1}{2}\left(|\uparrow\rangle\langle\uparrow| + |\downarrow\rangle\langle\downarrow|\right) \otimes \frac{1}{2}\left(|\uparrow\rangle\langle\uparrow| + |\downarrow\rangle\langle\downarrow|\right) \tag{5.28}$$

assuming the muon is initially in the spin up orientation and the two fluorine spins are initially randomly orientated.

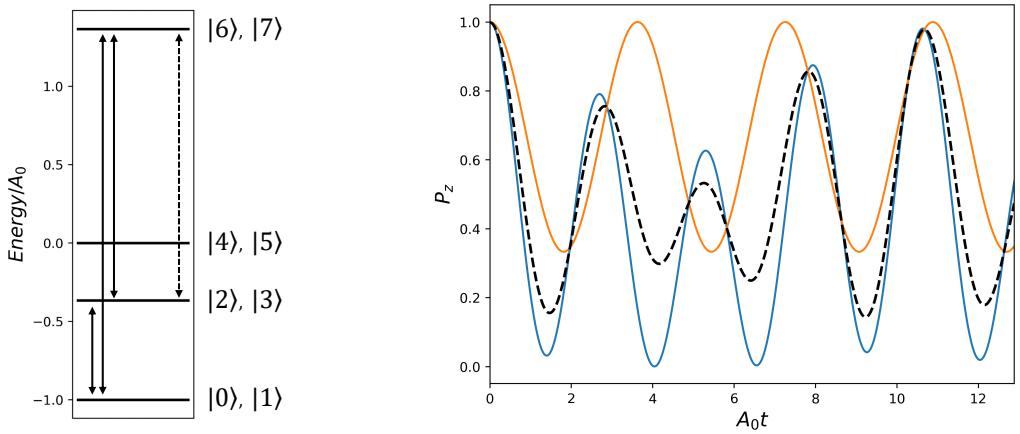

(a) (b)

Figure 5.5: *a) Energy level diagram of the solutions to the F-μ-F Hamiltonian in units of A_0. Arrows indicate allowed transitions in the transverse (solid arrow) and parallel (dashed arrow) geometries. b) Muon spin polarisation vs time in the case that the F-μ-F bond is transverse to z (blue line) or parallel to z (orange line) also shown is the polycrystal spatially averaged result (dashed black line).*

Continuing to neglect the $\mathcal{H}_{F_1F_2}$ term and assuming that the F-μ-F bond forms a straight line with the muon equidistant to both fluorine nuclei, then analytic solutions for the muon polarisation as a function of time can be obtained.

$$P_{z,parallel}(t) = \frac{2}{3} + \frac{1}{3}\cos\left(\sqrt{3}\omega_D t\right) \tag{5.29}$$

and transverse cases:

$$P_{z,trans}(t) = \frac{5}{12} + \frac{1}{12}\cos\left(\sqrt{3}\omega_D t\right) + \frac{1}{3}\Bigg(\left(1+\frac{1}{\sqrt{3}}\right)\cos\left(\frac{3+\sqrt{3}}{2}\omega_D t\right) + \left(1-\frac{1}{\sqrt{3}}\right)\cos\left(\frac{3-\sqrt{3}}{2}\omega_D t\right)\Bigg) \tag{5.30}$$

where $\omega_D = A\hbar$. An equation for the polarisation in the polycrystalline case can be found by taking 1/3 of the parallel case and 2/3 of the transverse case, giving [167]:

$$P_{z,powder}(t) = \frac{1}{6}\Bigg(3 + \cos\left(\sqrt{3}\omega_D t\right) + \left(1-\frac{1}{\sqrt{3}}\right)\cos\left(\frac{3-\sqrt{3}}{2}\omega_D t\right) + \frac{1}{3}\left(1+\frac{1}{\sqrt{3}}\right)\cos\left(\frac{3+\sqrt{3}}{2}\omega_D t\right)\Bigg) \tag{5.31}$$

a solution in the single crystal case is more complicated but can be expressed[171] as:

$$P_{z,crystal}(t) = \frac{1}{12}\Bigg[5 + 3\zeta + 2\left(1-\zeta\right)\Bigg(\left(\frac{3-\sqrt{3}}{2}\right)\cos\left(\frac{3-\sqrt{3}}{2}\omega_D t\right) + \left(1+\frac{1}{\sqrt{3}}\right)\cos\left(\frac{3+\sqrt{3}}{2}\omega_D t\right)\Bigg) + \left(1+3\zeta\right)\cos\Big(\sqrt{3}\omega_D t\Big)\Bigg] \tag{5.32}$$

where $\zeta = \cos^2\theta$ in which θ is the angle between the bond orientation and the z axis. A noteworthy feature of equation 5.32 is that it has no dependence on the azimuthal angle (the angle to the x or y axes), as such rotations of the bond around z do not alter the measured signal.

In February of 2017, a μSR experiment was performed on a sample of yttrium-

doped lithium holmium tetrafluoride (LYHF) $LiY_{0.95}Ho_{0.05}F_4$, using the EMU instrument at ISIS. One of the muon asymmetry results is shown in figure 5.6, which was taken at 50 K in zero field. LYHF is a single crystal sample, which has been previously observed to form the F-μ-F state[172, 171]. The sample is also of interest for studying single ion dynamics of rare earth ions, and has been measured using μSR in dc magnetic fields to observe the hyperfine splitting[173] and avoided level crossings of the rare earth ion[142].

Figure 5.6 shows that in LYHF, there is also a clear loss of polarisation over the course of the measurement. It is presumed that the loss of polarisation and the F-μ-F signal is due to similar processes as in PVDF and so it is again modelled by multiplying the signal by a stretched exponential. The background will again be modelled using exponential and constant terms.

$$P_z(t) = A\exp\left(-(\lambda_1 t)^{\alpha}\right) P_{z,crystal}(t) + B\exp\left(-(\lambda_2 t)\right) + A_{bkg} \tag{5.33}$$

Fitting equation 5.33 to the single crystal data in figure 5.6 yields an F-μ separation of (0.1203 ± 0.00009) nm at an angle of $\theta = (52.38 \pm 0.48)^\circ$ to the z axis. A and B are (0.179 ± 0.002) and (0.0373 ± 0.0038) respectively, indicating that almost all of the observed signal is from the F-μ-F state. λ_1 was fitted as 0.211 μs^{-1} (negligible uncertainty) with α=(1.38 ± 0.05), suggesting multiple sources of damping. λ_1 was fitted to be 0.848 μs^{-1} (negligible uncertainty) and A_{bkg}=(0.0447 ± 0.0009). An identical fit can be obtained using a modified version of equation 5.33 with two $P_{z,crystal}(t)$ terms using the same value of r, in this case, the two bond alignments are $(73.76 \pm 0.42)^\circ$ and $(35.29 \pm 0.75)^\circ$ and A is approximately doubled.

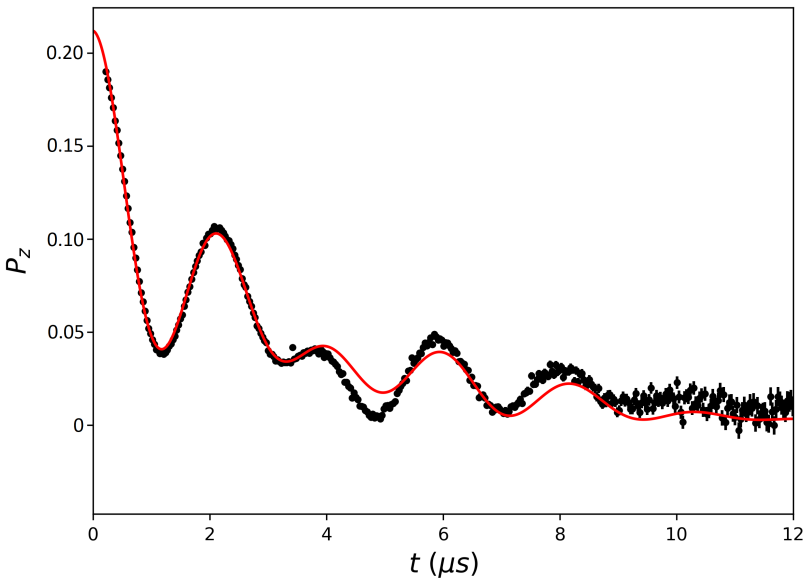

Figure 5.6: *F-μ-F state in single crystal LYHF at 50 K with fit to equation 5.33*

In the literature the F-μ-F state has been previously determined to have an F-μ separation of 0.119 nm in a sample with 5% holmium on the Y/Ho site[172]. In a 0.2% Ho sample the F-μ separation was found to be 0.1195 nm[142]. A study in 2011 on LYHF samples with varying levels of doping found a separation of 0.1185 nm that did not change with the doping level [171]. The above fitted parameters are approximately consistent with these values.

It is possible to check if these values are reasonable by examining the crystal structure of LYHF. A full treatment would entail performing density functional theory (DFT) calculations[174] in order to predict likely stopping places for the muon based on the electric field distribution in the material. However here just the fluorine-fluorine distances will be examined using their crystallographic positions. This process does not account for any movement of the fluorine atoms from the presence of the muon. A 3×3×3 unit cell of $LiYF_4$ (fully doped LYHF) was constructed and the F-F distances between all fluorine nuclei were calculated.

$LiYF_4$ was chosen because the sample of LYHF used was very dilute, and so it is expected to be more representative than $LiHoF_4$. The muon is likely to localise in the centre of these F-F distances, although it can pull the fluorine nuclei off their original positions slightly. Figure 5.7 a) is a histogram of those F-F distances (only F-F distrances less than 0.5nm are shown).

Naively, the most likely candidate for the muon stopping site is in the middle of the shortest fluorine-fluorine distance. In figure 5.7 a) it can be seen that there is a group of F-F vectors each slightly shorter than 0.26 nm, which are coloured blue, magenta and red in the histogram. The lengths of the short F-F distances are 0.2563 nm, 0.2583 nm and 0.2596 nm for blue, magenta and red respectively. In figure 5.7 b) the corresponding F-F vectors in a unit cell are shown (some of the bonds cross the unit cell border and their corresponding fluorines in the neighbouring cell are also shown). In figure 5.7 c) the three groups of bonds have been translated to pass through a central point such that their relative orientations can be more easily compared. The short F-F vectors have 5 orientations, the longer group of vectors (red, 0.2596 nm) form an angle of 68.8° with the crystallographic c axis and form angles of 90° to each other in the a-b plane. The medium length bond (magenta, 0.2583 nm) is co-linear with one of the long bonds. The shortest bond (blue, 0.2563 nm) is almost co-linear with the red bonds, instead forming an angle of 70.8° with the c axis. Each of the bond groups are similar enough that their resultant muon polarisations would be indistinguishable, however the four orientations of the red group could each lead to very distinct polarisations.

With this in mind, the fit in figure 5.6 is roughly consistent with the likely F-μ-F sites identified. It would suggest that the two fluorine nuclei have been pulled towards the muon by 7.85 fm (6.1%) which is plausible and approximately consis-

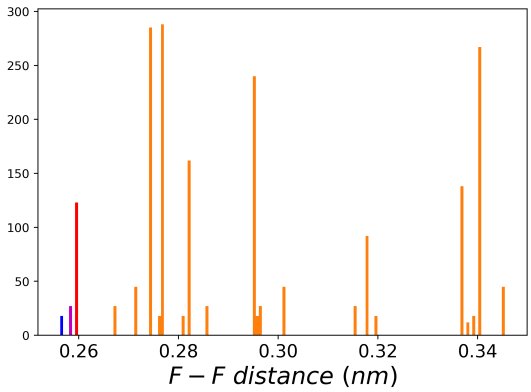

(a)

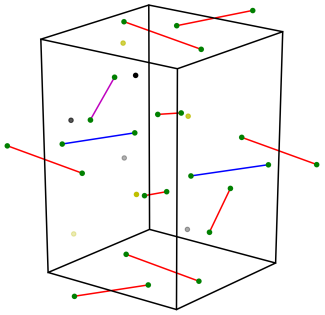

(b)

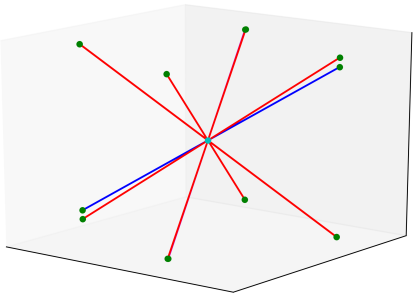

(c)

Figure 5.7: *a) Histogram of F-F distances in $LiYF_4$ found in a cell 3×3×3 unit cells in size. Indicating likely candidates for the F-μ-F bond. Blue, magenta and red bars indicate the shortest F-F distances and therefore the most likely candidates, their colours match with the bonds shown in b). b) Illustration of shortest bonds from a) between fluorine atoms (green). Lithium (yellow) and yttrium (black) atoms are also shown. Black box indicates the unit cell, atom sizes are not to scale. c) Shortest bonds shifted to pass through the same point to make comparison of their orientations easier. The magenta line is co-linear with the red lines and is therefore not visible. A cyan circle is used to symbolise the muon.*

tent with previous measurements[171]. Figure 5.7 does suggest that the inclusion of additional $P_z(t)$ terms to equation 5.33 would have a physical justification and would possibly improve the fit.

5.5 Modelling

It is clear from looking at figure 5.6 that equation 5.33 does not perfectly capture the experimental data. In order to improve the fit, a more rigorous treatment of the system was performed to calculate the muon polarisation with fewer simplifications.

Some of the computer code used in this and the following section is based on code written by Amal Vaidya for his M.Sci. dissertation at Durham University [175].

The assumptions used to produce the analytic solutions in the previous section were that the fluorine-fluorine interaction is negligible, the F-μ-F bond is straight and the muon is in the centre. Doing away with these simplifications puts analytic solutions out of reach and so the muon polarisation should be directly calculated from the density matrix. Doing so has previously been successful in fitting to the polarisation in other materials [176, 174].

The F-F interaction is easily accounted for by the reintroduction of the $\mathcal{H}_{FF}$ term of the Hamiltonian. Buckling of the F-μ-F bond can be included in the Hamiltonian using geometry to modify the relevant terms. Similarly it is possible to account for a muon position that is not equidistant from both fluorine nuclei by using geometry to modify the relevant terms.

The fitting function for the inclusion of multiple bonds is given by:

$$P_z(t) = A\exp\left(-(\lambda_1 t)^{\alpha}\right)\sum_{n}^{N_{bonds}}\mathrm{Tr}\left[\rho_n(t)I_z\right] + B\exp\left(-(\lambda_2 t)^{\beta}\right) + A_{bkg}. \qquad (5.34)$$

Because of the increased number of parameters, it was found during fitting that the χ^2 space of the problem has a large number of local minima that do not

provide a good fit. For this reason it was decided to use the differential evolution fitting algorithm [177] to find the global minimum, a task for which it is well suited as it searches the entire parameter space. Using differential evolution is not without downsides though; there is no guarantee that it will find the global minimum nor that it will always return the same result. Because differential evolution is stochastic and not based on the gradient of the χ^2 space, it does not provide parameter uncertainty estimates so fit parameters are given without errors hereafter.

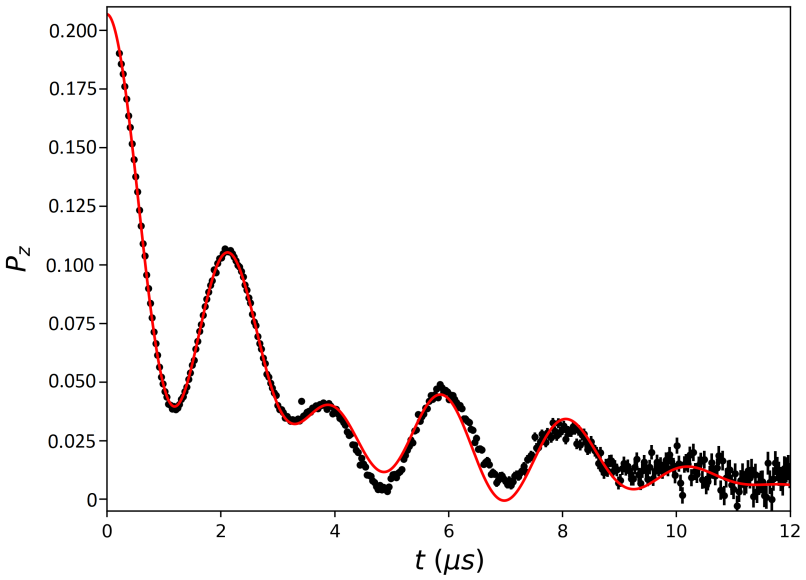

Figure 5.8: *Best fit to LYHF data at 50 K using equation 5.34 with four F-μ-F bonds.*

It has been found that using four bonds provides the best fit to the data, (shown in figure 5.8) which is consistent with the bond alignments in figure 5.7 b) (two bonds also provide a good fit but that is less consistent with figure 5.7). To reduce the number of fitting parameters, all four bonds used the same r and buckling angle. The fit finds an F-μ separation of $r = 0.11974$ nm with the F-μ-F bond buckled by 10.7°. The four bonds form angles with the z axis of 173.1°,

140.6°, 75.9° and 100.7°. The decay lifetime was found to be $\lambda_1 = 0.159\ \mu s^{-1}$ with stretch parameter α=1.615, suggesting a distribution of timescales is involved in the decay. For the background $\lambda_2 = 0.651\ \mu s^{-1}$ with $\beta = 1.546$. The amplitudes of the three terms were found to be $A = 0.04496$ (meaning a F-μ-F fraction of 0.1798, due to the four bonds effectively multiplying A by 4), $B = 0.0263$ and $A_{bkg} = 0.000736$. The reduced chi-square statistic was $\chi^2 = 7.79$.

The 0.11975 nm F-μ separation is consistent with figure 5.7 if the fluorine nuclei have each been pulled toward the muon by approximately 8% or 10 fm.

5.6 State Manipulation

As part of the experiments on PVDF and LYHF, a radio frequency (RF) photon field was applied to the samples in an attempt to manipulate the quantum state populations of the entangled muon-fluorine state. Because the initial conditions of the system cause a mixed state to form, each state has a definite probability of occupation. Whilst the wave functions of individual muons will oscillate between allowed states over the course of the experiment (this is the source of the observed oscillations), the probabilities of occupation across the full ensemble remain constant.

The intention was to investigate whether the eigenstate occupation probabilities could be altered by the application of RF field to the samples. Manipulation of the quantum state of a spin system has previously been demonstrated in other systems, for example in references [178, 179, 180]. The frequency of the RF field was chosen to correspond to one of the energy gaps, such that the photons of the field should excite the system to the higher level of the gap. The RF field was produced by a saddle RF coil (pictured in figure 5.9) in close proximity to

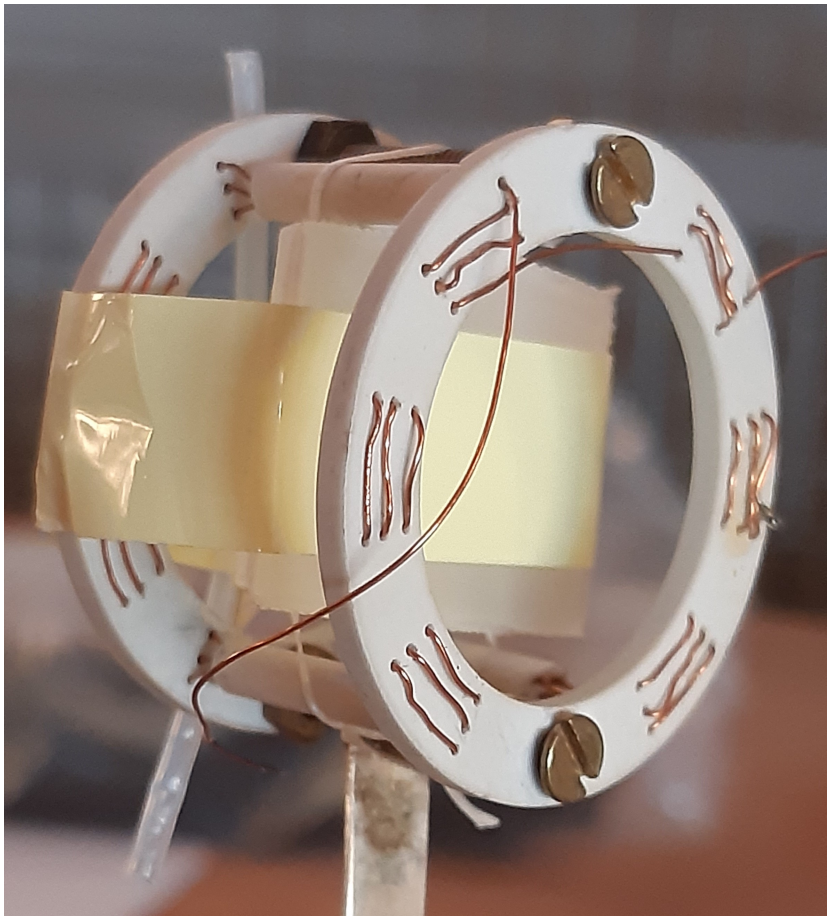

Figure 5.9: *Photograph of the coil use to produce the RF field. The incoming muons arrive perpendicular to the white rings.*

the sample[181], which produced circularly polarised photons. The emitters were orientated perpendicular to the incoming muon polarisation, and so the RF photons were circularly polarised in the x-y plane. The pulsed nature of the muons at ISIS was used to measure RF on and RF off data in tandem, so that the temperature profile of both measurements would be the same. This procedure will also automatically account for any experimental or calibration changes. The asymmetry was measured for 5 pulses with the RF field off and then 5 pulses with the RF field on, a pattern which was repeated for the full length of each measurement. In figures 5.10 and 5.11 measurements recorded in tandem are

always shown together.

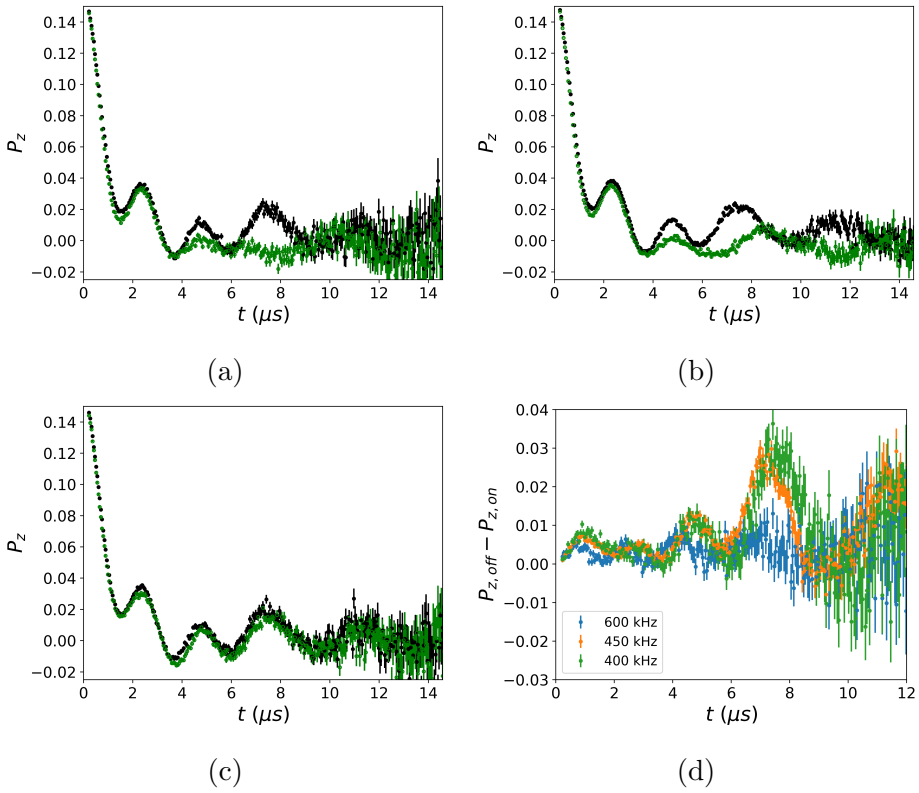

Figure 5.10: *a), b) and c) show the muon polarisation in PVDF with the RF field off (black) and RF field on (green) for 400 kHz, 450 kHz and 600 kHz respectively. d) Difference between the RF on and RF off measurements.*

In PVDF, the RF field was applied to excite the energy cap between the $|0\rangle$, $|1\rangle$ and $|3\rangle$ energy levels. From the energy level diagram for PVDF with $r = 0.11$ nm this corresponds to a frequency of approximately 400 kHz, however a Fourier transform of the RF off measurements suggests the gap is closer to 450 kHz, so measurements were performed at both of these frequencies. An additional measurement was performed at 600 kHz which does not correspond to any energy gap. In figures 5.10 a) and b) the RF field is clearly having a significant impact on the system, the 400 kHz measurement has a slightly greater impact suggesting that it is closer to the true transition. As was expected, the

600 kHz transition has a much smaller impact.

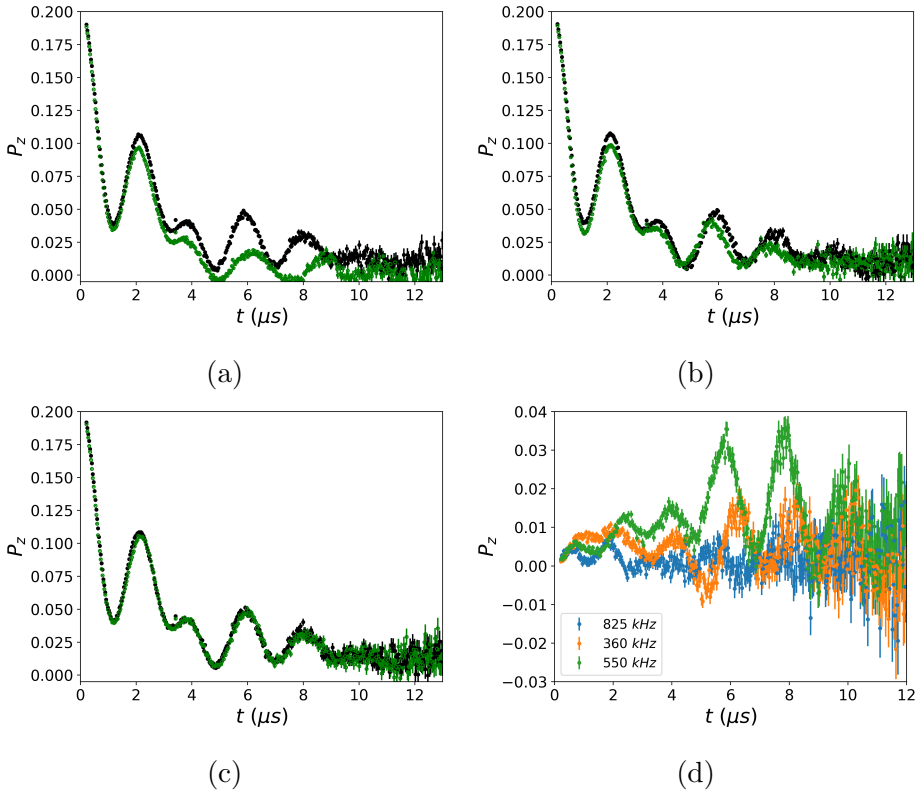

Figure 5.11: *a), b) and c) show the muon polarisation in LYHF with the RF field off (black) and RF field on (green) for 550 kHz, 360 kHz and 825 kHz respectively. d) Difference between the RF on and RF off measurements.*

Figure 5.11 a) shows the impact of the RF photon field in LYHF for an RF field applied at 550 kHz, which roughly corresponds to the transition between the $|0\rangle$ $|1\rangle$ energy level and the $|6\rangle$ $|7\rangle$ level. These values are based on the energy levels using r=0.1195 nm [142], which differs very slightly from the value obtained in the previous section. A value from the literature had to be used because, at the time of performing the experiment, the RF-off results had not yet been fitted. However, this is not expected to be an issue; the Q-value of the RF coil was such that a distribution of photon frequencies were produced. Consequently, there ought to still be a significant number of photons at the correct value of the

transition, provided the centre point of the distribution is not very far off.

Measurements were also performed at 360 kHz and 825 kHz. 360 kHz was intended to correspond to the transition between the $|2\rangle$ $|3\rangle$ energy level and the $|6\rangle$ $|7\rangle$ level. 825 kHz was chosen as a control measurement and does not correspond to any transition, it was expected that the RF field at 825 kHz would make little/no difference to the observed polarisation.

The RF field at 550 kHz has a large impact on the muon polarisation, appearing to damp the observed oscillations. The impact of the RF field becomes more prominent as t increases. At 360 kHz the impact of the RF field is less significant but there is still a noticable change in the polaristion. A possible explanation for this is that 360 kHz is not as close to the true frequency of the transition as 550 kHz is to its relevant transition. The $|0\rangle$ $|1\rangle$ and $|2\rangle$ $|3\rangle$ levels have the same probability of occupation so that is not expected to be responsible for the reduced impact. As expected, applying the RF field at 825 kHz has a very limited impact on the muon polarisation, although some difference can be observed in figure 5.11.

Clearly then, the application of the Rf field to the F-μ-F state is having some impact on the evolution of the system. In order to understand and quantify this effect it is necessary to model the RF field. To do this another term must be added to the system Hamiltonian, which takes the form of a rotating magnetic field (as is found in circularly polarised light) given by

$$\boldsymbol{B}(t) = B_1 \left(\cos(\omega t)\hat{\boldsymbol{e}}_{\mathbf{1}} + \sin(\omega t)\hat{\boldsymbol{e}}_{\mathbf{2}}\right) \tag{5.35}$$

where B_1 is the amplitude of the rotating magnetic field and, $\hat{\boldsymbol{e}}_{\mathbf{1}}$ and $\hat{\boldsymbol{e}}_{\mathbf{2}}$ are orthogonal unit vectors defining the plane that the magnetic field rotates in. In

these experiments, $\hat{\boldsymbol{e}}_\mathbf{1}$ and $\hat{\boldsymbol{e}}_\mathbf{2}$ are unit vectors in the x and y directions. The new Hamiltonian is then given by

$$\mathcal{H}(t) = \mathcal{H}_{F\mu F} + \gamma_\mu \boldsymbol{I} \cdot \boldsymbol{B}(t) + \gamma_F \boldsymbol{S_1} \cdot \boldsymbol{B}(t) + \gamma_F \boldsymbol{S_2} \cdot \boldsymbol{B}(t). \tag{5.36}$$

The Hamiltonian is now time dependent, so equation 5.10 is used to evolve the density matrix.

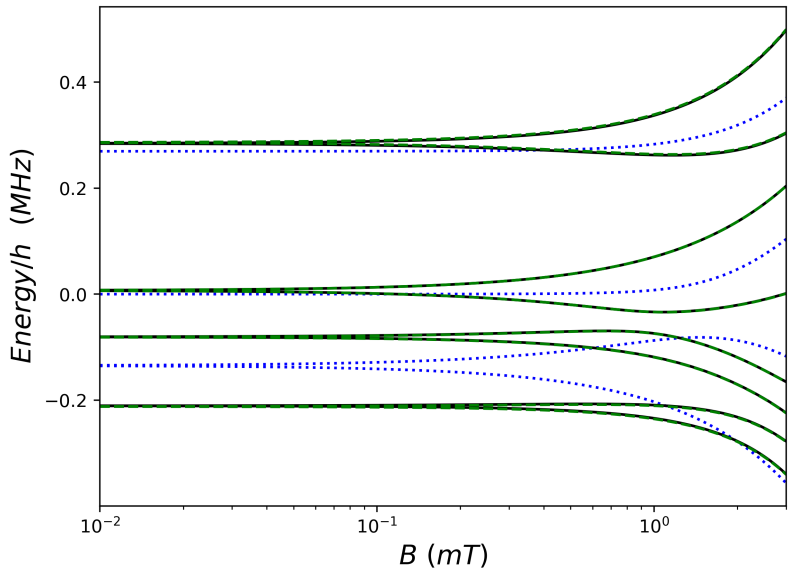

Figure 5.12: *Splitting of the energy levels due to the application of the B_1 magnetic field for r=0.11974 nm (black lines) and r=0.1195 nm (dashed green lines) in the F-μ-F state as well as r=0.1101 nm (blue dotted lines) in the F-μ state. The splitting is not dependent on the frequency of the B_1 field. The splitting at t=0 is shown.*

The B_1 rotating magnetic field will lead to a splitting of the energy levels, shown in figure 5.12. In the case that $\hat{\boldsymbol{e}}_\mathbf{1}$ and $\hat{\boldsymbol{e}}_\mathbf{2}$ are perpendicular to the F-μ-F bond then the splitting is time independent, however, if they are not both perpendicular then the splitting will vary in time. The splitting at several times was checked but only the splitting at t=0 is shown in figure 5.12. In order to

ensure that the splitting is not so great as to significantly change the energy levels and therefore change the photon frequency required, it is important to know the magnitude of B_1.

The value of B_1 was calibrated during the experiment by first applying a longitudinal magnetic field, the strength of which causes the muon to precess at the same frequency as the rotating magnetic field. Typically this longitudinal field is strong enough to decouple the F-μ or F-μ-F state. When this field is applied there will be a difference between the RF on and RF off measurements which will oscillate. By fitting a cosine function to the difference between the RF on and RF off measurements it is then possible to determine B_1[181]. It should be noted this method is not sensitive to small changes in B_1 and so all quoted values of B_1 have an associated uncertainty of around 0.05 mT.

The calibrated B_1 field amplitudes for the PVDF experiment are 0.15 mT, 0.18 mT and 0.12 mT at 400 kHz, 450 kHz and 600 kHz respectively. In the LYHF experiment B_1 is 0.15 mT, 0.18 mT and 0.19 mT for the fields rotating at 550 kHz, 360 kHz and 825 kHz respectively. These fields are small enough to keep the splitting within acceptable levels (<10 kHz change in the energy gap for PVDF and<5 kHz for LYHF). This is true at all values of t.

The fit parameters from the RF off measurements were used in order to produce the results in figure 5.13, showing the impact of the rotating magnetic field. It is quite clear that using the calibrated B_1 values predicts a change in polarisations that is much smaller than what was observed in the experiments. However, when inputting a value for B_1 that is 4 times greater than the calibrated values, the predicted polarisation change is much more in line with what was observed.

At 825 kHz, the inclusion of the rotating magnetic field with 4 times the calibrated B_1 appears to provide a strong agreement with the experimental data,

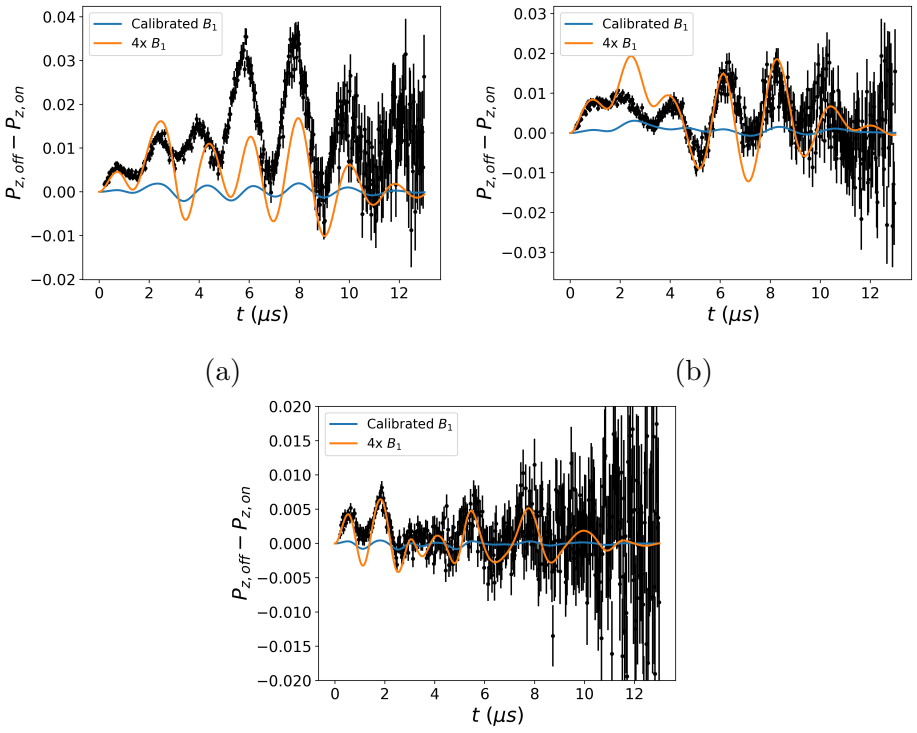

Figure 5.13: *Simulation of muon polarisations with the rotating magnetic field. Each panel shows the RF off data subtracted from the RF on in LYHF. The frequencies of the rotating magnetic fields are a) 550 kHz, b) 360 kHz and c) 825 kHz. In each panel the black points show the difference in the data, the blue lines show the simulated subtraction using the calibrated B_1 values and the orange line the subtraction with 4 times B_1.*

suggesting that it is accurately modelling its effect. Why multiplying the calibrated B_1 by 4 should yield the correct result is not currently known. It is possible there is some factor of 4 mistake in the model code or in the calibration of the B_1 field amplitudes, however one has not been identified. It is worth noting that figures 5.12 and 5.13 used the same code, so if there is a factor of 4 mistake in the code for figure 5.13 then it is also in figure 5.12.

In the 550 kHz and 360 kHz measurements, the predicated change in polarisation is clearly qualitatively different to the experimental data. Changing the

4 times factor is unlikely to yield an accurate prediction. This is especially clear in the 360 kHz result, where the agreement at some times is very good however at other times there is a strong disagreement. Clearly at these frequencies the inclusion of the rotating magnetic field is not accurately modelling the full effect of the RF photon field.

This analysis has not been performed on the PVDF experiment because of the difficulties in fitting to the RF off data, which are expected to be the result of the amorphous background.

This can be interpreted as evidence that the application of the RF field is fundamentally altering the quantum state and is not just perturbing the Hamiltonian. Therefore the RF field has had its intended purpose.

5.7 Collapse Operators

Use of a rotating magnetic field proved insufficient to quantify the impact of the RF photons on the F-μ-F in the previous section. It was decided to use a new approach and model the impact of the RF field directly by using creation and annihilation operators to introduce excitations to the system.

When doing so, it was also decided to attempt to model the loss of asymmetry directly, and so fit the muon polarisation without needing to multiply by a stretched exponential. This can be done by introducing collapse operators, which model the effect of the environment on the system, without needing to model the environment directly. To do this it is necessary to use a new formula to compute the time dependence of the density matrix. Such a formula is provided by the Lindblad master equation which is given by[182],

$$i\hbar\frac{\partial\rho(t)}{\partial t} = [\mathcal{H}(t), \rho(t)] + \sum_n \frac{1}{2}[2C_n\rho(t)C_n^+ - \rho(t)C_n^+C_n - C_n^+C_n\rho(t)] \qquad (5.37)$$

where C_n are the collapse operators for which $C_n = \sqrt{\gamma_n}A_n$. γ_n describes the time scale over which the coupling to the environment has an effect and A_n are the operators that mediate that coupling. It should be noted that the $\rho(t)$ in equation 5.37 is the result of a partial trace over the full total system-environment density matrix and so the environment is not included, just its influence on the system.

Solving equation 5.37 is more difficult than the von-Neumann equation and so from here on the QuTiP Python module is used[183, 184]. QuTiP is a free package in the Python programming language for simulating open and closed quantum systems. In particular the *mesolve()* function was used, which evolves the density matrix of the system according to equation 5.37 by integrating the set of differential equations that define the system, for a given Hamiltonian and set of collapse operators.

Collapse operators are often used to model: energy loss from the system to the environment (relaxation), energy gain in the system from the environment (thermal excitation), and the loss of quantum information from the system to the environment (dephasing) [185]. In the experiments in this chapter, the thermal energy of the environment is much larger than the gaps in energy levels of the F-μ and F-μ-F systems (which are of the order of 10 μK). Therefore, energy transfer between the system and environment is expected to be insignificant, meaning that relaxation and excitation operators are not required. Dephasing effects however are expected to be significant and the relevant collapse operator is given by

$$C_{dephasing,i} = \sqrt{\frac{2}{T_{dph,i}}}\sigma_i^+\sigma_i^- \tag{5.38}$$

where $T_{dph,i}$ is the dephasing rate, σ_i^+ is the relevant raising operator acting on the i^{th} particle and σ_i^- is the corresponding lowering operator. The dephasing environment is expected to be long range and so is assumed to dephase each of the constituent particles individually, therefore a term of equation 5.38 is included for each particle. The individual particle operators are defined by $\sigma_1^+ = \sigma^+ \otimes \mathbb{I} \otimes ....$, $\sigma_2^+ = \mathbb{I} \otimes \sigma^+ \otimes ....$ and so on[186], where $\sigma^+ = |\uparrow\rangle\langle\downarrow|$.

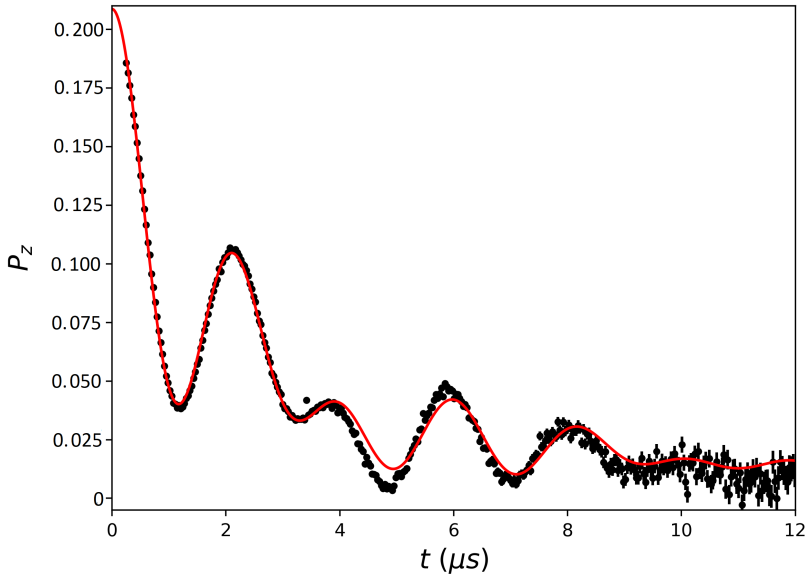

Figure 5.14: *Best fit of equation 5.34 to LYHF data at 50 K, where the density matrix is evolved according to equation 5.37 with the collapse operators in equation 5.38.*

The new fitting function is very similar to equation 5.34, however the exponential factor in front of the sum sign is removed and $\rho_n(t)$ is instead evolved according to equation 5.37. Three dephasing operators are used, one for each particle. The two fluorines are expected to interact with the environment in the same way and so in the fit they share a $T_{dph,i}$ parameter. Because the result of

the previous fit found bonds that were only very slightly buckled, they have been assumed to be linear in this fit to reduce the number of computations required for the fit. As before, four bond alignments were used that shared a common fitting parameter for r.

The fit using equation 5.37 is shown in figure 5.14 and finds an F-μ distance of r=0.195 nm. The four bonds were found to make angles of 61.650°, 89.998°, 90.001° and 90.000° with the z axis suggesting that there are only two distinct orientations. However, because each orientation was equally weighted in the fit, it would suggest there are 3 times as many bonds at 90° to z than there are at 61.65°. In the implementation of the fit the $T_{dph,i}$ terms were optimised using a dummy parameter: $D_{dph,i} = \sqrt{\frac{2}{T_{dph,i}}}$. For the fluorines $D_{dph,F}$=730.9 $s^{-1/2}$, and so $T_{dph,F}$=3.74 μs. For the muon, $D_{dph,\mu}$ was fitted to be exactly 0 meaning that $T_{dph,\mu}$ is extremely large, suggesting that the environment does not have any dephasing effect on the muon. The amplitude of the F-μ-F contribution is 0.1817. For the back ground, the fit found B=0.02689 with λ=0.354μs^{-1} and β=3.0 and A_{bkg}=0. The value of β was at the upper limit of the bounds set in the fitting, however because of the small amplitude of B it was decided there was no need to redo the fit with greater range. The reduced χ^2 statistic of the fit is 10.995.

5.8 Ongoing and Future Work

The decision was made to attempt to account for the dephasing effect of the environment directly. The dephasing environment is expected to consist of nearby spins interacting with the constituent parts of the F-μ-F state through the magnetic dipole-dipole interaction. It is possible to incorporate their effects simply by adding more dipole interaction terms to the Hamiltonian using the known crystal-

lographic locations of nearby spins. This approach has previously been successful at modelling the F-μ-F state in polycrystalline CaF_2 and NaF[187][165].

In LHYF there is a single crystal phase and so the relative positions of other nearby spins is known. Adding additional fluorine ions to the model does indeed have have a damping effect on the oscillations, especially if there are multiple F-μ-F bonds in the sample with different alignments. Some preliminary trial calculations are shown in figure 5.15, where the the 8 nearest fluorine spins to the F-μ-F site identified in figure 5.7 are added and interact with the muon and two fluorines through the dipole-dipole interaction. Figure 5.15 does not make use of the fit parameters discussed earlier.

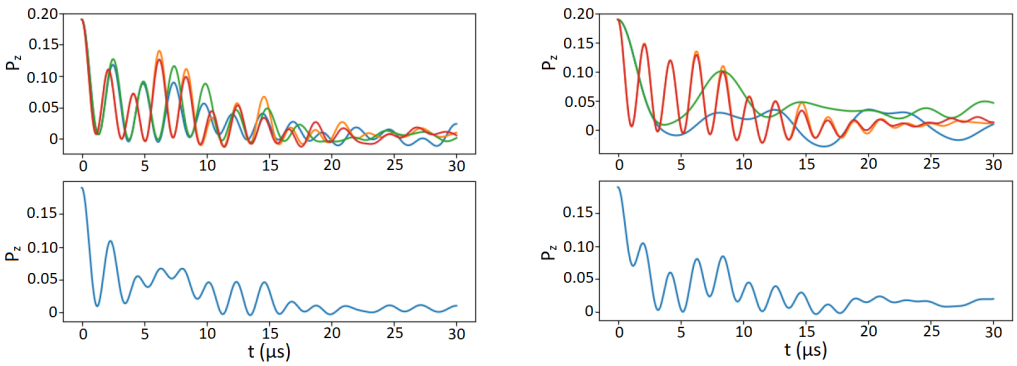

Figure 5.15: *Preliminary results showing the muon polarisation when the effect of additional nearby fluorine nuclei is taken into account. For a crystal aligned such that the crystallographic c axis forms an angle of a) 18° and b) 126° with the inital muon polarisation. Upper panels show the polarisations from each of the 4 bonds identified in 5.7. Lower panels show the resulting average polarisation.*

The most significant hurdle to overcome with this approach is that the computational expense of the simulation increases rapidly with the number of particles. This is because each new degree of freedom doubles the size of the relevant matrices, rapidly increasing the number of computations required. For N spin 1/2 particles, the sizes of the matrices scale with 2^N so for 8 additional fluorines (11

particles in total) as in figure 5.15 each matrix is now 2048×2048 in size. The QuTiP package is capable of taking advantage of any sparsity in the matrices to improve calculation times, however given the large number of matrix operations required to evolve the density matrix simulation times can be very long. The length of time required to perform a fit to experimental data is prohibitive on an ordinary computer (not a super computer). In fact, the QuTiP package itself can limit the number of extra particles that can be considered because it uses 32-bit integers to index the sparse matrices.

At the current stage of research, the F-μ-F project is being led by David Billington (a postdoctoral researcher at Cardiff University), who has secured access to a supercomputer with optimisations being performed on the HAWK supercomputer which is part of the ARCA project at Cardiff University. Current optimisations are finding that extra fluorines are not needed to accurately model the dephasing effect. Instead, nearby lithium nuclei and holmium spins are included which is proving to be successful at modelling the observed decay.

The stable isotopes of lithium are ^{6}Li and ^{7}Li which occur with relative abundances of 7.59% and 92.41% respectively. ^{6}Li has a spin quantum number $I = 1$ and ^{7}Li has spin $I = 3/2$. Because ^{7}Li is by far more abundant and the moment of ^{6}Li is smaller, only ^{7}Li is considered in the model.

Although the sample of LYHF contains only 5% holmium atoms on the Y/Ho site, that is still enough for them to have an impact. Statistically, the chances of there being a Ho atom in the same unit cell as the muon is 20% and the expected number of holmium atoms in the neighbouring unit cells is 5.4 (assuming the Ho atoms are uniformly distributed). Additionally in the crystal field ground state the Ho ions have a large magnetic moment that is highly Ising like, with an effective spin 1/2 moment of $7\mu_B$ in the crystallographic c direction[172]. At 50 K

(the measurement temperature) higher crystal field levels are accessible[173, 188, 189] in which the holmium spin state is different. In the model it is assumed to maintain an effective spin 1/2 state to reduce the computational power required. The implication of this is that the F-μ-F bond is highly likely to form in the vicinity of at least one Ho atom, which because of its large magnetic moment is expected to influence the evolution of the system. Although it is possible that because the dipole interactions of the holmium atoms are long range, then there may be some screening effect, limiting their impact. Evidence for a screening effect may be found as a consequence of the measurements in ref. [171] where it was found that changing the holmium concentration did not have an impact on their F-μ-F fit parameters.

Ongoing fits using the previously described method have been successful in fitting the muon asymmetry well in the RF off case. In order to model the impact RF field, the new approach is to use a modified version of the Jaynes-Cummings model. In this model the RF photon field can be modelled by photons in a quantised photon cavity or field. The modified Hamiltonian is proposed to be

$$\mathcal{H} = \mathcal{H}_{F\mu F+} + \hbar\omega a^{\dagger}a + \hbar g\left(\sigma_T^{+}a + a^{\dagger}\sigma_T^{-}\right) \tag{5.39}$$

where, $\mathcal{H}_{F\mu F+}$ is the Hamiltonian for the F-μ-F system and additional spins. ω is the cavity frequency, a and $a^{\dagger}$ are the cavity creation and annihilation operators, g is the interaction strength between the system and the cavity and, σ_T^{+} and σ_T^{-} are the raising and lowering operators for the system, given by $\sigma_T^{+} = \sum_i \sigma_i^{+}$ and $\sigma_T^{-} = \sum_i \sigma_i^{-}$. The preliminary results of this model have been promising and an example simulation for the RF field at 550 kHz is shown in figure 5.16.

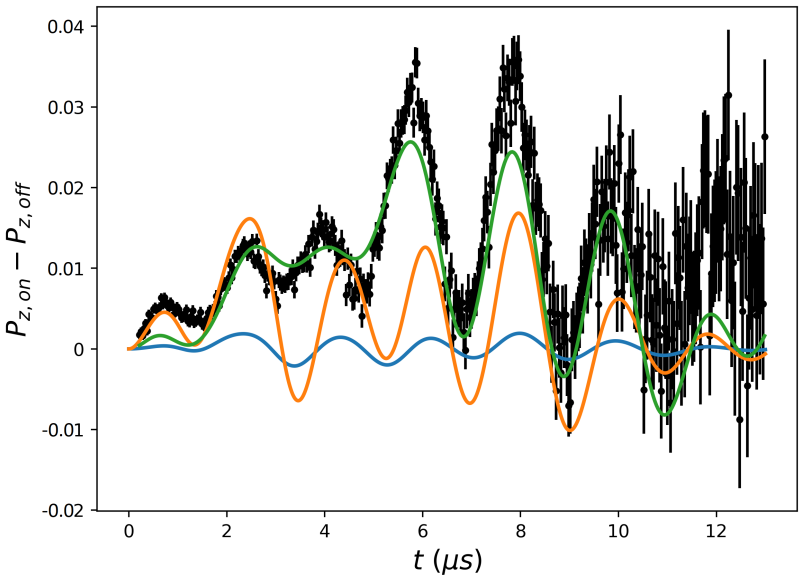

Figure 5.16: *Effect of the RF field modelled using the modified Jaynes-Cummings model in equation 5.39 (green line). The black points, blue line and orange line are the same as in figure 5.13 a).*

Chapter 6

Summary & Key Results

In summary, this thesis has focused primary on the application of ac susceptibility and muon spin rotation in magnetic systems. A particular focus was given to the ac susceptibility technique at the start of the thesis where initially a new instrument is discussed and tested, before moving on to novel measurements in the spinel spin ice samples $CdEr_2Se_4$ and $CdEr_2S_4$ using ac susceptibility. Other techniques such as dc magnetisation and specific heat measurements were used to try and interpret the data. In the latter part of the thesis the focus was much more on the muon spin rotation technique, with a muon experiment in $CdEr_2Se_4$ to aid the understanding of the ac susceptibility results. Then in the final chapter the focus was entirely on the muon spin rotation technique and the quantum states that can form during a muon experiment in fluorinated materials.

The key advancements made by this work include:

- **Implementation of the high frequency ac susceptometer**

  An ac susceptometer has been developed that has a unique capability to easily measure the ac susceptibility at high frequency over a wide range of temperatures. Its development has many possible applications. An exam-

ple application is the characterisation of magnetic nano particles which is demonstrated here and in reference [104], in fact it has already been used for this purpose in reference [105]. Another example is the characterisation of magnetic spin systems such as spin ice, which has also been demonstrated here and in reference [49].

- **Measurement of quantum tunnelling plateau in $CdEr_2Se_4$ and $CdEr_2S_4$**

  The temperature independent quantum tunnelling plateau was shown to exist in $CdEr_2Se_4$ and $CdEr_2S_4$ between 2 and 5 K at a relaxation time of $\tau \approx 4.9 \times 10^{-7}$ s, these results were published in reference [49]. This had previously not been observed in these materials and is evidence that $CdEr_2Se_4$ and $CdEr_2S_4$ behave like the pyrochlore spin ice materials.

- **Field induced coexisting relaxation mechanisms**

  ac susceptibility measurements on powder $CdEr_2Se_4$ and $CdEr_2S_4$ in an applied dc magnetic field have led to the discovery of a field induced slow relaxation mechanism that coexists with the faster mechanism present in the absence of a field. Similar behaviour has previously been observed in references [139, 138, 140] however none fully explained the origin of the field induced peak and an attempt to understand it in more detail was made here. The combined frequency range of the high frequency susceptometer and ACMS was used to measure the field and temperature dependence of both relaxation mechanisms in detail. Low temperature measurements at the Néel institute have shown that the two mechanisms stay distinct from one another to low temperatures. Measurements in single crystals did not provide any evidence of the origin of the field induced relaxation mechanism.

- **Measurement of single crystal $CdEr_2Se_4$**

  Single crystal samples of $CdEr_2Se_4$ were made available towards the end of the project, although they were small in size and fragile. These measurements mark the first time that magnetic properties of single crystal $CdEr_2Se_4$ have been measured. A Laue camera was used to try and align the sample along the [111], [110] and [100] axes (or equivalent). dc magnetisation measurements suggest that the [110] alignment was lost and a visual inspection of the sample indicated that the [111] axis was misaligned by around 10° in the > 2 K measurements. Measurements at the Néel institute focussed only on the [111] direction which was well aligned. Along the [111] direction there is a feature in the magnetisation at $\approx 0.333\mu_{FI}$ which is consistent with the magnetisation observed for the Kagomé plateau in pyrochlore spin ices, although in those materials the plateau is flat and the observed feature is not. Additionally the spin freezing temperature in the single crystal has been observed and is found to be at a lower temperature than in the powder sample.

- **Fitting of F-μ state in PVDF**

  A reasonable fit was obtained to the F-μ state in PVDF up to around 8 μs yielding similar fit parameters to that seen in a previous μSR experiment in ref.[164]. Looking to to longer times (>8 μs) the fit and data disagree. It is speculated that a contribution from the amorphous regions of PVDF is responsible for the disagreement although it has not yet been possible to fit to the data using a model that would account for those regions.

- **Fitting of F-μ-F in $LiY_{0.95}Ho_{0.05}F_4$**

  Several approaches to fitting the F-μ-F state in $LiY_{0.95}Ho_{0.05}F_4$ were used

to achieve a fit. Fitting using an analytic equation and stretched exponentials to model decoherence (as in reference [171]) achieved a reasonable fit. Evolving the density matrix using the Liouville-von Neumann equation was found tried in order to do away with some of the assumptions required for the analytic equation, this approach was found to improve the fit to experimental data. Finally the Lindblad master equation was used to include dephasing operators in the model to provide a more physical way of modelling the environment than using stretched exponentials. This was found to find the best fit of the three methods.

- **Manipulation of F-μ and F-μ-F states**

  An RF field was produced around the sample by an RF saddle coil. The purpose was to manipulate the population of the levels in the F-μ and F-μ-F states. The muon asymmetry was found to be different in the RF-on and RF-off cases indicating an alteration of the state. The difference could not be explained by the perturbing effect of a rotating magnetic field (from the RF coil) which is evidence that photons from the RF field are being absorbed and exciting the systems, altering the populations of the levels.

Bibliography

[1] S. Blundell, *Magnetism in Condensed Matter*. OUP Oxford, 2003.

[2] C. Kittel, P. McEuen, and P. McEuen, *Introduction to solid state physics*. Wiley New York, 8 ed., 1996.

[3] J. Jensen and a.R. Mackintosh, *Rare earth magnetism: structures and excitations*. Clarendon Press Oxford, 1991.

[4] M. Nikolo, "Superconductivity: A guide to alternating current susceptibility measurements and alternating current susceptometer design," *Am. J. Phys.*, vol. 63, no. 1, pp. 57–65, 1995.

[5] D. Martien, "Introduction to: ac susceptibility," *Quantum Des.*, p. 4, 1994.

[6] C. V. Topping and S. J. Blundell, "A.C. susceptibility as a probe of low-frequency magnetic dynamics," *J. Phys. Condens. Matter*, vol. 31, p. 013001, 2019.

[7] R. Kubo, "The fluctuation-dissipation theorem," *Reports Prog. Phys.*, vol. 29, p. 255, 1966.

[8] P. J. W. Debye, *Polar Molecules*. Chemical Catalog Company, Incorporated, 1929.

[9] K. S. Cole and R. H. Cole, "Dispersion and Absorption in Dielectrics I. Alternating Current Characteristics," *J. Chem. Phys.*, vol. 9, p. 341, 1941.

[10] D. W. Davidson and R. H. Cole, "Dielectric relaxation in glycerine," *J. Chem. Phys.*, vol. 18, p. 1417, 1950.

[11] S. Havriliak and S. Negami, "A complex plane representation of dielectric and mechanical relaxation processes in some polymers," *Polymer (Guildf).*, vol. 8, pp. 161–210, 1967.

[12] W. R. Abel, A. C. Anderson, and J. C. Wheatley, "Temperature measurements using small quantities of cerium magnesium nitrate," *Rev. Sci. Instrum.*, vol. 35, no. 4, pp. 444–449, 1964.

[13] E. H. Brandt, "Superconductor disks and cylinders in an axial magnetic field. I. Flux penetration and magnetization curves," *Phys. Rev. B*, vol. 58, no. 10, pp. 6506–6522, 1998.

[14] C. A. Mulder, A. J. Van Duyneveldt, and J. A. Mydosh, "Susceptibility of the Cu Mn spin-glass: Frequency and field dependences," *Phys. Rev. B*, vol. 23, no. 3, pp. 1384–1396, 1981.

[15] F. Ludwig, C. Balceris, C. Jonasson, and C. Johansson, "Analysis of AC Susceptibility Spectra for the Characterization of Magnetic Nanoparticles," *IEEE Trans. Magn.*, vol. 53, no. 11, p. 6100904, 2017.

[16] J. Kötzler, G. Nakielski, M. Baumann, R. Behr, F. Goerke, and E. H. Brandt, "Universality of frequency and field scaling of the conductivity measured by ac susceptibility of a $YBa_2Cu_3O_7$ film," *Phys. Rev. B*, vol. 50, no. 5, pp. 3384–3391, 1994.

[17] R. M. Wilcox, "Bounds for the isothermal, adiabatic, and isolated static susceptibility tensors," *Phys. Rev.*, vol. 174, no. 2, pp. 624–629, 1968.

[18] R. Orbach, "Spin-lattice relaxation in rare-earth salts," *Proc. R. Soc. Lond. A. Math. Phys. Sci.*, vol. 264, no. 1319, pp. 458–484, 1961.

[19] J. C. Gill, "A theory of the 'phonon bottleneck' in the Orbach process of spin-lattice relaxation," *J. Phys. C Solid State Phys.*, vol. 6, no. 1, pp. 109–120, 1973.

[20] B. Tomasello, C. Castelnovo, R. Moessner, and J. Quintanilla, "Single-ion anisotropy andmagnetic field response in the spin-icematerials $Ho_2Ti_2O_7$ and $Dy_2Ti_2O_7$," *Phys. Rev. B*, vol. 92, no. 15, p. 155120, 2015.

[21] J. C. Maxwell, *A treatise on electricity and magnetism*, vol. 1. Clarendon Press Oxford, 1873.

[22] Original artwork. Author: Geek3. Last accessed: 28/09/2020 11:40. URL: https://commons.wikimedia.org/wiki/File:VFPt_magnets_BHM.svg.

[23] E. Pardo, D. X. Chen, and A. Sanchez, "Demagnetizing factors for completely shielded rectangular prisms," *J. Appl. Phys.*, vol. 96, no. 6, pp. 5365–5369, 2004.

[24] J. A. Osborn, "Demagnetizing factors of the general ellipsoid," *Phys. Rev.*, vol. 67, no. 11-12, pp. 351–357, 1945.

[25] E. Stoner, "XCVII. The Demagnetizing Factors for Ellipsoids.," *London, Edinburgh, Dublin Philos. Mag. J. Sci.*, vol. 36, no. 263, pp. 803—-821, 1945.

[26] D. X. Chen, J. A. Brug, and R. B. Goldfarb, "Demagnetizing factors for cylinders," *IEEE Trans. Magn.*, vol. 27, no. 4, pp. 3601–3619, 1991.

[27] a. Aharoni, "Demagnetizing factors for rectangular ferromagnetic prisms," *J. Appl. Phys.*, vol. 83, no. 6, p. 3432, 1998.

[28] R. Bjørk and C. R. Bahl, "Demagnetization factor for a powder of randomly packed spherical particles," *Appl. Phys. Lett.*, vol. 103, no. 10, p. 1102403, 2013.

[29] B. Bleaney and R. A. Hull, "The effective susceptibility of a paramagnetic powder," *Proc. R. Soc. London. Ser. A. Math. Phys. Sci.*, vol. 178, no. 972, pp. 86–92, 1941.

[30] M. Twengström, L. Bovo, M. J. Gingras, S. T. Bramwell, and P. Henelius, "Microscopic aspects of magnetic lattice demagnetizing factors," *Phys. Rev. Mater.*, vol. 1, no. 4, p. 044406, 2017.

[31] J. A. Quilliam, L. R. Yaraskavitch, H. A. Dabkowska, B. D. Gaulin, and J. B. Kycia, "Dynamics of the magnetic susceptibility deep in the Coulomb phase of the dipolar spin ice material $Ho_2Ti_2O_7$," *Phys. Rev. B*, vol. 83, no. 9, p. 094424, 2011.

[32] P. Anderson, "Ordering and Antiferromagnetism in Ferrites," *Phys. Rev.*, vol. 102, no. 4, p. 1008, 1956.

[33] S. T. Bramwell and M. J. Gingras, "Spin ice state in frustrated magnetic pyrochlore materials," *Science*, vol. 294, no. 5546, pp. 1495–1501, 2001.

[34] J. D. Bernal and R. H. Fowler, "A theory of water and ionic solution, with

particular reference to hydrogen and hydroxyl ions," *J. Chem. Phys.*, vol. 1, no. 8, pp. 515–548, 1933.

[35] L. Pauling, "The Structure and Entropy of Ice and of Other Crystals with Some Randomness of Atomic Arrangement," *J. Am. Chem. Soc.*, vol. 57, no. 12, pp. 2680–2684, 1935.

[36] A. P. Ramirez, A. Hayashi, R. J. Cava, R. Siddharthan, and B. S. Shastry, "Zero-point entropy in 'spin ice'," *Nature*, vol. 399, pp. 333–335, 1999.

[37] M. J. Harris, S. T. Bramwell, D. F. McMorrow, T. Zeiske, and K. W. Godfrey, "Geometrical Frustration in the Ferromagnetic Pyrochlore $Ho_2Ti_2O_7$," *Phys. Rev. Lett.*, vol. 79, no. 13, pp. 2554–2557, 1997.

[38] S. Rosenkranz, A. P. Ramirez, A. Hayashi, R. J. Cava, R. Siddharthan, and B. S. Shastry, "Crystal-field interaction in the pyrochlore magnet $Ho_2Ti_2O_7$," *J. Appl. Phys.*, vol. 87, no. 9, pp. 5914–5916, 2000.

[39] L. D. C. Jaubert and P. C. W. Holdsworth, "Magnetic monopole dynamics in spin ice.," *J. Phys. Condens. Matter*, vol. 23, p. 164222, 2011.

[40] M. J. Gingras and B. C. Den Hertog, "Origin of spin-ice behavior in Ising pyrochlore magnets with long-range dipole interactions: An insight from mean-field theory," *Can. J. Phys.*, vol. 79, pp. 1339–1351, 2001.

[41] R. Siddharthan, B. S. Shastry, A. P. Ramirez, A. Hayashi, R. J. Cava, and S. Rosenkranz, "Ising pyrochlore magnets: Low-temperature properties, "ice rules," and beyond," *Phys. Rev. Lett.*, vol. 83, no. 9, pp. 1854–1857, 1999.

[42] S. T. Bramwell, M. J. Harris, B. C. den Hertog, M. J. P. Gingras, J. S. Gardner, D. F. McMorrow, A. R. Wildes, A. L. Cornelius, J. D. M. Champion, R. G. Melko, and T. Fennell, "Spin Correlations in $Ho_2Ti_2O_7$: a Dipolar Spin Ice System," *Phys. Rev. Lett.*, vol. 87, no. 4, p. 047205, 2001.

[43] B. C. den Hertog and M. J. P. Gingras, "Dipolar Interactions and Origin of Spin Ice in Ising Pyrochlore Magnets," *Phys. Rev. Lett.*, vol. 84, no. 15, pp. 3430–3433, 2000.

[44] K Matsuhira et al, "Low temperature magnetic properties of frustrated pyrochlore ferromagnets Ho_2Sn-2O_7 and $Ho_2Ti_2O_7$," *J. Phys. Condens. Matter*, vol. 12, no. 40, pp. L649–L656, 2000.

[45] H. Kadowaki, Y. Ishii, K. Matsuhira, and Y. Hinatsu, "Neutron scattering study of dipolar spin ice $Ho_2Sn_2O_7$: Frustrated pyrochlore magnet," *Phys. Rev. B*, vol. 65, no. 14, p. 144421, 2002.

[46] K. Matsuhira, Y. Hinatsu, K. Tenya, H. Amitsuka, and T. Sakakibara, "Low-Temperature Magnetic Properties of Pyrochlore Stannates," *J. Phys. Soc. Japan*, vol. 71, no. 6, pp. 1576–1582, 2002.

[47] X. Ke, B. G. Ueland, D. V. West, M. L. Dahlberg, R. J. Cava, and P. Schiffer, "Spin-ice behavior in $Dy_2Sn_{2-x}Sb_xO_{7+x/2}$ and Dy_2NbScO_7," *Phys. Rev. B - Condens. Matter Mater. Phys.*, vol. 76, no. 21, p. 214413, 2007.

[48] J. Lago, I. Živković, B. Z. Malkin, J. Rodriguez Fernandez, P. Ghigna, P. Dalmas De Réotier, A. Yaouanc, and T. Rojo, "$CdEr_2Se_4$: A new erbium spin ice system in a spinel structure," *Phys. Rev. Lett.*, vol. 104, no. 24, p. 247203, 2010.

[49] S. Gao, O. Zaharko, V. Tsurkan, L. Prodan, E. Riordan, J. Lago, B. Fåk, A. R. Wildes, M. M. Koza, C. Ritter, P. Fouquet, L. Keller, E. Canévet, M. Medarde, J. Blomgren, C. Johansson, S. R. Giblin, S. Vrtnik, J. Luzar, A. Loidl, C. Rüegg, and T. Fennell, "Dipolar Spin Ice States with a Fast Monopole Hopping Rate in $CdEr_2X_4$ (X=Se,S)," *Phys. Rev. Lett.*, vol. 120, no. 13, p. 137201, 2018.

[50] I. a. Ryzhkin, "Magnetic relaxation in rare-earth oxide pyrochlores," *J. Exp. Theor. Phys.*, vol. 101, no. 3, pp. 481–486, 2005.

[51] C. Castelnovo, R. Moessner, and S. L. Sondhi, "Magnetic monopoles in spin ice," *Nature*, vol. 451, pp. 42–45, 2008.

[52] L. D. C. Jaubert and P. C. W. Holdsworth, "Signature of magnetic monopole and Dirac string dynamics in spin ice," *Nat. Phys.*, vol. 5, pp. 258–261, 2009.

[53] D. J. P. Morris, D. A. Tennant, S. A. Grigera, B. Klemke, C. Castelnovo, R. Moessner, C. Czternasty, M. Meissner, K. C. Rule, J.-U. Hoffmann, K. Kiefer, S. Gerischer, D. Slobinsky, and R. S. Perry, "Dirac Strings and Magnetic Monopoles in the Spin Ice $Dy_2Ti_2O_7$," *Science (80-.).*, vol. 326, pp. 411–414, 2009.

[54] P. A. M. Dirac, "Quantised singularities in the electromagnetic field," *Proc. R. Soc. London. Ser. A, Contain. Pap. a Math. Phys. Character*, vol. 133, no. 821, pp. 60–72, 1931.

[55] C. Paulsen, S. R. Giblin, E. Lhotel, D. Prabhakaran, G. Balakrishnan, K. Matsuhira, and S. T. Bramwell, "Experimental signature of the attrac-

tive Coulomb force between positive and negative magnetic monopoles in spin ice," *Nat. Phys.*, vol. 12, pp. 661–666, 2016.

[56] C. Castelnovo, R. Moessner, and S. L. Sondhi, "Debye-Hückel theory for spin ice at low temperature," *Phys. Rev. B - Condens. Matter Mater. Phys.*, vol. 84, no. 14, p. 144435, 2011.

[57] Y. Levin, "Reports on Progress in Physics Related content Electrostatic correlations : from plasma to biology Electrostatic correlations : from plasma to biology," *Rep. Prog. Phys.*, vol. 65, pp. 1577–1632, 2002.

[58] L. Bovo, J. a. Bloxsom, D. Prabhakaran, G. Aeppli, and S. T. Bramwell, "Brownian motion and quantum dynamics of magnetic monopoles in spin ice," *Nat. Commun.*, no. 1535, 2013.

[59] S. T. Bramwell, S. R. Giblin, S. Calder, R. Aldus, D. Prabhakaran, and T. Fennell, "Measurement of the charge and current of magnetic monopoles in spin ice," *Nature*, vol. 461, pp. 956–959, 2009.

[60] S. R. Giblin, S. T. Bramwell, P. C. W. Holdsworth, D. Prabhakaran, and I. Terry, "Creation and measurement of long-lived magnetic monopole currents in spin ice," *Nat. Phys.*, vol. 7, pp. 252–258, 2011.

[61] J. Snyder, B. G. Ueland, J. S. Slusky, H. Karunadasa, R. J. Cava, and P. Schiffer, "Low-temperature spin freezing in the $Dy_2Ti_2O_7$ spin ice," *Phys. Rev. B*, vol. 69, no. 6, p. 064414, 2004.

[62] M. Ruminy, S. Chi, S. Calder, and T. Fennell, "Phonon-mediated spin-flipping mechanism in the spin ices $Dy_2Ti_2O_7$ and $Ho_2Ti_2O_7$," *Phys. Rev. B*, vol. 95, no. 6, p. 060414, 2017.

[63] G. Ehlers, A. L. Cornelius, M. Orenda, M. Kajnakova, T. Fennell, S. T. Bramwell, and J. S. Gardner, "Dynamical crossover in 'hot' spin ice," *J. Phys. Condens. Matter*, vol. 15, pp. L9–L15, 2003.

[64] B. Tomasello, C. Castelnovo, R. Moessner, and J. Quintanilla, "Correlated Quantum Tunneling of Monopoles in Spin Ice," *Phys. Rev. Lett.*, vol. 123, no. 6, p. 067204, 2019.

[65] J. Snyder, J. S. Slusky, R. J. Cava, and P. Schiffer, "How 'spin ice' freezes.," *Nature*, vol. 413, pp. 48–51, 2001.

[66] C. Paulsen, S. R. Giblin, E. Lhotel, D. Prabhakaran, K. Matsuhira, G. Balakrishnan, and S. T. Bramwell, "Nuclear spin assisted quantum tunnelling of magnetic monopoles in spin ice," *Nat. Commun.*, vol. 10, no. 1509, 2019.

[67] J. Lago, S. J. Blundell, and C. Baines, "μSR investigation of spin dynamics in the spin-ice material $Dy_2Ti_2O_7$," *J. Phys. Condens. Matter*, vol. 19, p. 326210, 2007.

[68] S. J. Blundell, "Monopoles, magnetricity, and the stray field from spin ice," *Phys. Rev. Lett.*, vol. 108, no. 14, p. 147601, 2012.

[69] A. Yaouanc, P. Dalmas De Réotier, A. Bertin, C. Marin, E. Lhotel, A. Amato, and C. Baines, "Evidence for unidimensional low-energy excitations as the origin of persistent spin dynamics in geometrically frustrated magnets," *Phys. Rev. B - Condens. Matter Mater. Phys.*, vol. 91, no. 10, p. 104427, 2015.

[70] H. Fukazawa, R. Melko, R. Higashinaka, Y. Maeno, and M. Gingras, "Mag-

netic anisotropy of the spin-ice compound $Dy_2Ti_2O_7$," *Phys. Rev. B*, vol. 65, no. 5, p. 054410, 2002.

[71] A. Petrenko, R. Lees, and G. Balakrishnan, "Magnetization process in the spin-ice compound $Ho_2Ti_2O_7$," *Phys. Rev. B*, vol. 68, no. 1, p. 012406, 2003.

[72] R. Higashinaka, H. Fukazawa, K. Deguchi, and Y. Maeno, "Low temperature specific heat of $Dy_2Ti_2O_7$ in the Kagome ice state," *J. Phys. Soc. Japan*, vol. 73, no. 10, pp. 2845–2850, 2004.

[73] R. Higashinaka, H. Fukazawa, Y. Maeno, and Y. Maeno, "Anisotropic release of the residual zero-point entropy in the spin ice compound $Dy_2Ti_2O_7$: Kagome ice behavior," *Phys. Rev. B - Condens. Matter Mater. Phys.*, vol. 68, no. 1, p. 014415, 2003.

[74] R. Moessner and L. Sondhi, "Theory of the [111] magnetization plateau in spin ice," *Phys. Rev. B - Condens. Matter Mater. Phys.*, vol. 68, no. 6, p. 064411, 2003.

[75] A. L. Cornelius and J. S. Gardner, "Short-range magnetic interactions in the spin-ice compound $Ho_2Ti_2O_7$," *Phys. Rev. B - Condens. Matter Mater. Phys.*, vol. 64, no. 6, p. 060406, 2001.

[76] Z. Hiroi, K. Matsuhira, S. Takagi, T. Tayama, and T. Sakakibara, "Specific heat of kagomé ice in the pyrochlore oxide $Dy_2Ti_2O_7$," *J. Phys. Soc. Japan*, vol. 72, no. 2, pp. 411–418, 2003.

[77] E. Lhotel, S. Petit, M. Ciomaga Hatnean, J. Ollivier, H. Mutka, E. Ressouche, M. R. Lees, and G. Balakrishnan, "Evidence for dynamic kagome ice," *Nat. Commun.*, vol. 9, no. 3786, 2018.

[78] T. Fennell, S. T. Bramwell, D. F. McMorrow, P. Manuel, and A. R. Wildes, "Pinch points and Kasteleyn transitions in kagome ice," *Nat. Phys.*, vol. 3, pp. 566–572, 2007.

[79] T. Fennell, O. A. Petrenko, G. Balakrishnan, S. T. Bramwell, J. D. Champion, B. Fåk, M. J. Harris, and D. M. K. Paul, "Field-induced partial order in the spin ice dysprosium titanate," *Appl. Phys. A Mater. Sci. Process.*, vol. 74, pp. S889–S891, 2002.

[80] Z. Hiroi, K. Matsuhira, and M. Ogata, "Ferromagnetic Ising spin chains emerging from the spin ice under magnetic field," *J. Phys. Soc. Japan*, vol. 72, no. 12, pp. 3045–3048, 2003.

[81] J. P. Clancy, J. P. Ruff, S. R. Dunsiger, Y. Zhao, H. A. Dabkowska, J. S. Gardner, Y. Qiu, J. R. Copley, T. Jenkins, and B. D. Gaulin, "Revisiting static and dynamic spin-ice correlations in $Ho_2Ti_2O_7$ with neutron scattering," *Phys. Rev. B - Condens. Matter Mater. Phys.*, vol. 79, no. 1, p. 014408, 2009.

[82] S. I. Yoshida, K. Nemoto, and K. Wada, "Ordered phase of dipolar spin ice under [110] magnetic field," *J. Phys. Soc. Japan*, vol. 73, no. 7, pp. 1619–1622, 2004.

[83] R. Higashinaka, H. Fukazawa, and Y. Maeno, "Specific heat of single crystal of spin ice compound $Dy_2Ti_2O_7$," *Phys. B Condens. Matter*, vol. 329-333, pp. 1040–1041, 2003.

[84] H. Diep, S. T. Bramwell, M. J. P. Gingras, and P. C. Holdsworth, "Frustrated Spin Systems," ch. 7, World Scientific, 2013.

[85] J. P. Ruff, R. G. Melko, and M. J. Gingras, "Finite-temperature transitions in dipolar spin ice in a large magnetic field," *Phys. Rev. Lett.*, vol. 95, no. 9, p. 097202, 2005.

[86] S. J. Blundell, "Spin-polarized muons in condensed matter physics," *Contemp. Phys.*, vol. 40, no. 3, pp. 175–192, 1999.

[87] S. L. Lee, R. Cywinski, and S. Kilcoyne, *Muon science: Muons in physics, chemistry and materials*. CRC Press, 1999.

[88] A. Schenck, *Muon spin rotation spectroscopy: principles and applications in solid state physics*. CRC Press, 1985.

[89] A. Yaouanc and d. R. Pierre Dalmas, *Muon spin rotation, relaxation, and resonance: applications to condensed matter*. Oxford University Press, 2011.

[90] A. D. Hillier, D. M. Paul, and K. Ishida, "Probing beneath the surface without a scratch - Bulk non-destructive elemental analysis using negative muons," *Microchem. J.*, vol. 125, pp. 203–207, 2016.

[91] J. Sugiyama, I. Umegaki, H. Nozaki, W. Higemoto, K. Hamada, S. Takeshita, A. Koda, K. Shimomura, K. Ninomiya, and M. K. Kubo, "Nuclear Magnetic Field in Solids Detected with Negative-Muon Spin Rotation and Relaxation," *Phys. Rev. Lett.*, vol. 121, no. 8, p. 87202, 2018.

[92] T. D. Lee and C. N. Yang, "Parity Nonconservation and a Two-Component Theory of the Neutrino," *Phys. Rev.*, vol. 105, no. 5, pp. 1671–1675, 1957.

[93] B. D. Patterson, "Muonium states in semiconductors," *Rev. Mod. Phys.*, vol. 60, no. 1, pp. 69–159, 1988.

[94] R. Garwin, L. Lederman, and M. Weinrich, "Observations of the Failure of Conservation of Parity and Charge Conjugation in Meson Decays: the Magnetic Moment of the Free Muon," *Phys. Rev.*, vol. 105, p. 141, 1957.

[95] A. Keren, "Generalization of the Abragam relaxation function to a longitudinal field," *Phys. Rev. B*, vol. 51, no. 14, pp. 10039–10042, 1994.

[96] R. S. Hayano, Y. J. Uemura, J. Imazato, N. Nishida, T. Yamazaki, and R. Kubo, "Zero-and low-field spin relaxation studied by positive muons," *Phys. Rev. B*, vol. 20, no. 3, pp. 850–859, 1979.

[97] J. N. Mundy, *Solid state: nuclear methods.* Academic Press, 1983.

[98] R. B. Clover and W. P. Wolf, "Magnetic susceptibility measurements with a tunnel diode oscillator," *Rev. Sci. Instrum.*, vol. 41, no. 5, pp. 617–621, 1970.

[99] J. N. Fox and J. U. Trefny, "Experiments using a tunnel diode oscillator," *Am. J. Phys.*, vol. 43, no. 7, pp. 622–625, 1975.

[100] E. D. Dahlberg, M. Hardiman, R. Orbach, and J. Souletie, "High-frequency ac susceptibility and ESR of a spin-glass," *Phys. Rev. Lett.*, vol. 42, no. 6, pp. 401–404, 1979.

[101] W. L. Pillinger, P. S. Jastram, and J. G. Daunt, "Electronic ac mutual inductance bridge for measuring small susceptibilities at low temperatures," *Rev. Sci. Instrum.*, vol. 29, no. 2, pp. 159–162, 1958.

[102] A. D. Hibbs, R. E. Sager, S. Kumar, J. E. McArthur, A. L. Singsaas, K. G. Jensen, M. A. Steindorf, T. A. Aukerman, and H. M. Schneider, "A SQUID-

based ac susceptometer," *Rev. Sci. Instrum.*, vol. 65, no. 8, pp. 2644–2652, 1994.

[103] F. R. Foronda, F. Lang, J. S. Möller, T. Lancaster, A. T. Boothroyd, F. L. Pratt, S. R. Giblin, D. Prabhakaran, and S. J. Blundell, "Anisotropic local modification of crystal field levels in Pr-based pyrochlores: A muon-induced effect modeled using density functional theory," *Phys. Rev. Lett.*, vol. 114, no. 1, p. 017602, 2015.

[104] E. Riordan, J. Blomgren, C. Jonasson, F. Ahrentorp, C. Johansson, D. Margineda, A. Elfassi, S. Michel, F. Dell'ova, G. Klemencic, and S. Giblin, "Design and development of a low temperature, inductance based high frequency ac susceptometer," *Rev. Sci. Instrum.*, vol. 90, p. 073908, 2019.

[105] H. Chen, D. Billington, E. Riordan, J. Blomgren, S. R. Giblin, C. Johansson, and S. A. Majetich, "Tuning the dynamics in Fe_3O_4 nanoparticles for hyperthermia optimization," *Appl. Phys. Lett.*, vol. 117, p. 073702, 2020.

[106] J. Grambow and G. Weber, "Measurement at the magnetic a.c. susceptibility at frequencies between 2 MHz and 1 GHz: Zero field spin-spin relaxation of cerium- and neodymium-magnesium nitrate at 4.2 K," *J. Phys. E.*, vol. 4, no. 11, pp. 865–867, 1971.

[107] P. Fannin, B. Scaife, and S. Charles, "New Technique For Measuring the Complex Susceptibility of Ferrofluids," *J. Phys. E.*, vol. 19, pp. 238–239, 1986.

[108] M. Hanson and C. Johansson, "Interaction effects in the dynamic response of magnetic liquids," *J. Magn. Magn. Mater.*, vol. 101, no. 1–3, pp. 45–46, 1991.

[109] F. Ahrentorp, A. P. Astalan, C. Jonasson, J. Blomgren, B. Qi, O. T. Mefford, M. Yan, J. Courtois, J. F. Berret, J. Fresnais, O. Sandre, S. Dutz, R. Müller, and C. Johansson, "Sensitive high frequency AC susceptometry in magnetic nanoparticle applications," *AIP Conf. Proc.*, vol. 1311, pp. 213–223, 2010.

[110] S. T. Boyd, V. Kotsubo, R. Cantor, A. Theodorou, and J. A. Hall, "Miniature thin-film SQUID susceptometer for magnetic microcalorimetry and thermometry," *IEEE Trans. Appl. Supercond.*, vol. 19, no. 3, pp. 697–701, 2009.

[111] J. Eisenstein, "Superconducting elements," *Rev. Mod. Phys.*, vol. 26, no. 3, pp. 277–291, 1954.

[112] M. Couach, A. F. Khoder, and F. Monnier, "Study of superconductors by a.c. susceptibility," *Cryogenics (Guildf).*, vol. 25, no. 12, pp. 695–699, 1985.

[113] N. Shirakawa, J. E. McArthur, and J. R. O'Brien, "SQUID-based AC magnetometry down to 0.5 K made available on a widely-accessible platform," *J. Phys. Conf. Ser.*, vol. 150, p. 012045, 2009.

[114] J. Tafur, A. P. Herrera, C. Rinaldi, and E. J. Juan, "Development and validation of a 10 kHz-1 MHz magnetic susceptometer with constant excitation field," *J. Appl. Phys.*, vol. 111, no. 7, p. 07E349, 2012.

[115] D. X. Chen, V. Skumryev, and B. Bozzo, "Calibration of ac and dc magnetometers with a Dy_2O_3 standard," *Rev. Sci. Instrum.*, vol. 82, no. 4, p. 045112, 2011.

[116] M. Ciszek, K. Rogacki, K. Oganisian, N. Zhigadlo, and J. Karpinski, "Influence of the carbon substitution on the critical current density and AC losses in MgB_2 single crystals," *Eur. Phys. J. B*, vol. 78, pp. 359–365, 2010.

[117] Miltenyi Biotec GmbH, "FeraSpin ™ Series : FeraSpin ™," 2011.

[118] J. C. Q. A. Pankhurst S. K. Jones, J. Dobson, "Applications of magnetic nanoparticles in biomedicine," *J. Phys. D. Appl. Phys.*, vol. 36, pp. R167–R181, 2003.

[119] S. Bogren, A. Fornara, F. Ludwig, M. d. P. Morales, U. Steinhoff, M. F. Hansen, O. Kazakova, and C. Johansson, "Classification of magnetic nanoparticle systems—synthesis, standardization and analysis methods in the nanomag project," *Int. J. Mol. Sci.*, vol. 16, no. 9, pp. 20308–20325, 2015.

[120] R. M. Ferguson, A. P. Khandhar, C. Jonasson, J. Blomgren, C. Johansson, and Krishnan, "Size-dependent relaxation properties of monodisperse magnetite nanoparticles measured over seven decades of frequency by ac susceptometry," *IEEE Trans. Magn.*, vol. 49, no. 7, pp. 3441–3444, 2013.

[121] V. L. Calero-Ddelc, D. I. Santiago-Quiñonez, and C. Rinaldi, "Quantitative nanoscale viscosity measurements using magnetic nanoparticles and SQUID AC susceptibility measurements," *Soft Matter*, vol. 7, pp. 4497–4503, 2011.

[122] E. Wetterskog, A. Castro, L. Zeng, S. Petronis, D. Heinke, E. Olsson, L. Nilsson, N. Gehrke, and P. Svedlindh, "Size and property bimodality in magnetic nanoparticle dispersions: single domain particles vs. strongly coupled nanoclusters," *Nanoscale*, vol. 9, no. 12, pp. 4227–4235, 2017.

[123] P. Bender, J. Fock, M. F. Hansen, L. K. Bogart, P. Southern, F. Ludwig, F. Wiekhorst, W. Szczerba, L. J. Zeng, D. Heinke, N. Gehrke, M. T. Fernández Díaz, D. González-Alonso, J. I. Espeso, J. Rodríguez Fernández, and C. Johansson, "Influence of clustering on the magnetic properties and hyperthermia performance of iron oxide nanoparticles," *Nanotechnology*, vol. 29, p. 425705, 2018.

[124] L. Ben-Dor and I. Shilo, "Structure and Magnetic properties of sulfides of the type $CdRE_2S_4$ and $Mg(Gd_xTb_{1-x})_2S_4$," *J. Solid State Chem.*, vol. 35, no. 2, pp. 278–285, 1980.

[125] A. Tomas, I. Shilo, and M. Guittard, "Structure cristalline du spinelle $CdEr_2S_4$," *Mater. Res. Bull.*, vol. 13, no. 8, pp. 857–859, 1978.

[126] H. Fujii, T. Okamoto, and T. Kamigaichi, "Crystallographic and Magnetic Studies of Rare Earth Chalcogenide Spinels," *J. Phys. Soc. Japan*, vol. 32, p. 1432, 1972.

[127] L. Ben-Dor, I. Shilo, and I. Felner, "$CdEr_2S_4$: Magnetic and Mössbauer measurements," *J. Solid State Chem.*, vol. 39, pp. 257–258, 1981.

[128] G. C. Lau, R. S. Freitas, B. G. Ueland, P. Schiffer, and R. J. Cava, "Geometrical magnetic frustration in rare-earth chalcogenide spinels," *Phys. Rev. B - Condens. Matter Mater. Phys.*, vol. 72, no. 5, p. 054411, 2005.

[129] H. Cao, A. Gukasov, I. Mirebeau, P. Bonville, C. Decorse, and G. Dhalenne, "Ising versus XY anisotropy in frustrated $R_2Ti_2O_7$ compounds as "seen" by polarized neutrons," *Phys. Rev. Lett.*, vol. 103, no. 5, p. 056402, 2009.

[130] P. Dasgupta, Y. Jana, and D. Ghosh, "Crystal field effect and geometric

frustration in $Er_2Ti_2O_7$ -an XY antiferromagnetic pyrochlore," *Solid State Commun.*, vol. 139, pp. 424–429, 2006.

[131] A. Bertin, Y. Chapuis, P. Dalmas De Réotier, and A. Yaouanc, "Crystal electric field in the $R_2Ti_2O_7$ pyrochlore compounds," *J. Phys. Condens. Matter*, vol. 24, p. 256003, 2012.

[132] A. Legros, D. H. Ryan, P. Dalmas De Réotier, A. Yaouanc, and C. Marin, "^{166}Er Mössbauer spectroscopy study of magnetic ordering in a spinel-based potential spin-ice system: $CdEr_2S_4$," *J. Appl. Phys.*, vol. 117, no. 17, p. 17C701, 2015.

[133] Y. P. Huang, G. Chen, and M. Hermele, "Quantum spin ices and topological phases from dipolar-octupolar doublets on the pyrochlore lattice," *Phys. Rev. Lett.*, vol. 112, no. 16, p. 167203, 2014.

[134] D. Reig-I-Plessis, S. V. Geldern, A. A. Aczel, D. Kochkov, B. K. Clark, and G. J. Macdougall, "Deviation from the dipole-ice model in the spinel spin-ice candidate $MgEr_2Se_4$," *Phys. Rev. B*, vol. 99, no. 13, p. 134438, 2019.

[135] S. Gao, *Neutron Scattering Investigation of the Spin Correlations in Frustrated Spinels*. PhD thesis, University of Geneva, 2017.

[136] V. G. Fleisher, V. I. Kozub, and Y. P. Stepanov, "Slow relaxation of AC-susceptibility of YBaCuO microcrystalline powders: magnetic field-induced dynamical alignment of crystallites," *Phys. C Supercond. its Appl.*, vol. 206, pp. 305–317, 1993.

[137] M. J. Jackson, E. Lhotel, S. R. Giblin, S. T. Bramwell, D. Prabhakaran,

K. Matsuhira, Z. Hiroi, Q. Yu, and C. Paulsen, "Dynamic behavior of magnetic avalanches in the spin-ice compound $Dy_2Ti_2O_7$," *Phys. Rev. B*, vol. 90, no. 6, p. 064427, 2014.

[138] J. Snyder, B. G. Ueland, J. S. Slusky, H. Karunadasa, R. J. Cava, A. Mizel, and P. Schiffer, "Quantum-Classical Reentrant Relaxation Crossover in $Dy_2Ti_2O_7$ Spin Ice," *Phys. Rev. Lett.*, vol. 91, no. 10, p. 107201, 2003.

[139] H. Xing, H. Guo, C. Feng, Z. A. Xu, and H. Zeng, "On the origin of the two thermally driven relaxations in diluted spin ice $Dy_{1.6}Y_{0.4}Ti_2O_7$," *J. Phys. Condens. Matter*, vol. 25, p. 046005, 2013.

[140] J. Snyder, B. G. Ueland, A. Mizel, J. S. Slusky, H. Karunadasa, R. J. Cava, and P. Schiffer, "Quantum and thermal spin relaxation in the diluted spin ice $Dy_{2-x}M_xTi_2O_7$ (M=Lu,Y)," *Phys. Rev. B*, vol. 70, no. 18, p. 184431, 2004.

[141] B. Z. Malkin, M. V. Vanyunin, M. J. Graf, J. Lago, F. Borsa, A. Lascialfari, A. M. Tkachuk, and B. Barbara, "^{19}F nuclear spin relaxation and spin diffusion effects in the single-ion magnet $LiYF_4$:Ho^{3+}," *Eur. Phys. J. B*, vol. 66, pp. 155–163, 2008.

[142] M. J. Graf, J. Lago, A. Lascialfari, A. Amato, C. Baines, S. R. Giblin, J. S. Lord, A. M. Tkachuk, and B. Barbara, "Muon spin rotation studies of spin dynamics at avoided level crossings in $LiY_{0.998}Ho_{0.002}F_4$," *Phys. Rev. Lett.*, vol. 99, no. 26, p. 267203, 2007.

[143] G. Ehlers, E. Mamontov, M. Zamponi, K. C. Kam, and J. S. Gardner, "Direct observation of a nuclear spin excitation in $Ho_2Ti_2O_7$," *Phys. Rev. Lett.*, vol. 102, no. 1, p. 016405, 2009.

[144] H. D. Zhou, C. R. Wiebe, J. A. Janik, L. Balicas, Y. J. Yo, Y. Qiu, J. R. D. Copley, and J. S. Gardner, "Dynamic spin ice: $Pr_2Sn_2O_7$," *Phys. Rev. Lett.*, vol. 101, no. 22, p. 227204, 2008.

[145] P. A. M. Dirac, *The principles of quantum mechanics*. Oxford university press, fourth ed., 1981.

[146] D. J. Griffiths and D. F. Schroeter, *Introduction to quantum mechanics*. Cambridge University Press, 2018.

[147] D. Manzano, "A short introduction to the Lindblad master equation," *AIP Adv.*, vol. 10, p. 025106, 2020.

[148] W. K. Wootters, "Entanglement of formation of an arbitrary state of two qubits," *Phys. Rev. Lett.*, vol. 80, no. 10, pp. 2245–2248, 1998.

[149] C. G. Timpson, *Quantum information theory and the foundations of quantum mechanics*. OUP Oxford, 2013.

[150] K. Blum, *Density matrix theory and applications*. Springer Science & Business Media, 64 ed., 2012.

[151] J. Von Neumann, "Wahrscheinlichkeitstheoretischer aufbau der quantenmechanik," *Nachrichten von der Gesellschaft der Wissenschaften zu Göttingen, Math. Klasse*, vol. 1927, pp. 245–272, 1927.

[152] J. Lord, S. Cottrell, and W. Williams, "Muon spin relaxation in strongly coupled systems," *Phys. B Condens. Matter*, vol. 289-290, pp. 495–498, 2000.

[153] M. Celio and P. F. Meier, "Exact calculation of the muon polarization function," *Hyperfine Interact.*, vol. 18, pp. 435–440, 1984.

[154] F. J. Dyson, "The radiation theories of Tomonaga, Schwinger, and Feynman," *Phys. Rev.*, vol. 75, no. 3, pp. 486–502, 1949.

[155] K. Kormann, S. Holmgren, and H. O. Karlsson, "Accurate time propagation for the Schrödinger equation with an explicitly time-dependent Hamiltonian," *J. Chem. Phys.*, vol. 128, no. 18, p. 184101, 2008.

[156] A. L. Fetter and J. D. Walecka, *Quantum theory of many-particle systems*. Courier Corporation, 2012.

[157] G. Mazzi, *Numerical Treatment of the Liouville-von Neumann Equation for Quantum Spin Dynamics*. Doctor of philosophy, University of Edinburgh, 2010.

[158] S. J. Blundell, "Spin-polarized muons in condensed matter physics," *Contemp. Phys.*, vol. 40, no. 3, pp. 175–192, 1999.

[159] E. Roduner and H. Fischer, "Muonium substituted organic free radicals in liquids. Theory and analysis of μSR spectra," *Chem. Phys.*, vol. 54, pp. 261–276, 1981.

[160] D. G. Fleming, D. M. Garner, J. H. Brewer, J. B. Warren, G. M. Marshall, G. Clark, A. E. Pifer, and T. Bowen, "The chemical reaction of muonium with Cl_2 in the gas phase," *Chem. Phys. Lett.*, vol. 48, no. 2, pp. 393–398, 1977.

[161] P. W. Percival, "Muonium Chemistry," *Radiochim. Acta*, vol. 26, pp. 1–14, 1979.

[162] J. H. Brewer, S. R. Kreitzman, D. R. Noakes, E. J. Ansaldo, D. R. Harsh-

man, and R. Keitel, "Observation of muon-fluorine "hydrogen bonding" in ionic crystals," *Phys. Rev. B*, vol. 33, no. 11, pp. 7813–7816, 1986.

[163] B. R. Hahn, O. Herrmann-Schönherr, and J. H. Wendorff, "Evidence for a crystal-amorphous interphase in PVDF and PVDF/PMMA blends," *Polymer (Guildf).*, vol. 28, pp. 201–208, 1987.

[164] T. Lancaster, F. L. Pratt, S. J. Blundell, I. McKenzie, and H. E. Assender, "Muon-fluorine entanglement in fluoropolymers.," *J. Phys. Condens. Matter*, vol. 21, p. 346004, 2009.

[165] J. M. Wilkinson and S. J. Blundell, "Information and decoherence in a muon-fluorine coupled system," *Phys. Rev. Lett.*, vol. 125, no. 8, p. 87201, 2020.

[166] K. Nishiyama, S. W. Nishiyama, and W. Higemoto, "Asymmetric F-μ-F interaction of the muon in polyfluorocarbons," *Phys. B Condens. Matter*, vol. 326, no. 1-4, pp. 41–45, 2003.

[167] D. R. Noakes, E. J. Ansaldo, S. R. Kreitzman, and G. M. Luke, "The $(F\mu F)^-$ ion in solid fluorides," *J. Phys. Chem. Solids*, vol. 54, no. 7, pp. 785–792, 1993.

[168] I. McKenzie, Z. Salman, S. R. Giblin, Y. Y. Han, G. W. Leach, E. Morenzoni, T. Prokscha, and A. Suter, "Polymer dynamics near the surface and in the bulk of poly(tetrafluoroethylene) probed by zero-field muon-spin-relaxation spectroscopy," *Phys. Rev. E*, vol. 89, no. 2, p. 022605, 2014.

[169] J. S. Möller, D. Ceresoli, T. Lancaster, N. Marzari, and S. J. Blundell,

"Quantum states of muons in fluorides," *Phys. Rev. B*, vol. 87, no. 12, p. 121108, 2013.

[170] F. L. Pratt, S. J. Blundell, I. M. Marshall, T. Lancaster, A. Husmann, C. Steer, W. Hayes, C. Fischmeister, R. E. Martin, and A. B. Holmes, "μSR in polymers," *Phys. B Condens. Matter*, vol. 326, pp. 34–40, 2003.

[171] R. C. Johnson, K. H. Chen, S. R. Giblin, J. S. Lord, A. Amato, C. Baines, B. Barbara, B. Z. Malkin, and M. J. Graf, "μSR study of spin dynamics in $LiY_{1-x}Ho_xF_4$," *Phys. Rev. B*, vol. 83, no. 17, p. 174440, 2011.

[172] J. Rodriguez, S. Dunsiger, J. Kycia, G. MacDougall, J. Quilliam, P. Russo, A. Savici, Y. Uemura, C. Wiebe, and G. Luke, "Study of the "Anti-Glass" $LiHo_{0.045}Y_{0.955}F_4$," *Phys. B Condens. Matter*, vol. 374-375, pp. 13–16, 2006.

[173] M. Schechter and P. C. Stamp, "Derivation of the low- T phase diagram of $LiHo_xY_{1-x}F_4$: A dipolar quantum Ising magnet," *Phys. Rev. B - Condens. Matter Mater. Phys.*, vol. 78, no. 5, p. 054438, 2008.

[174] J. S. Möller, P. Bonfà, D. Ceresoli, F. Bernardini, S. J. Blundell, T. Lancaster, R. De Renzi, N. Marzari, I. Watanabe, S. Sulaiman, and M. I. Mohamed-Ibrahim, "Playing quantum hide-and-seek with the muon: localizing muon stopping sites," *Phys. Scr.*, vol. 88, p. 068510, 2013.

[175] A. Vaidya, *What do muons tell us about order, entanglement and dynamics in magnets?* M.sci., Durham University, 2015.

[176] T. Lancaster, S. J. Blundell, P. J. Baker, M. L. Brooks, W. Hayes, F. L. Pratt, J. L. Manson, M. M. Conner, and J. A. Schlueter, "Muon-fluorine

entangled states in molecular magnets," *Phys. Rev. Lett.*, vol. 99, no. 26, p. 267601, 2007.

[177] R. Storn and K. Price, "Differential Evolution – A Simple and Efficient Heuristic for global Optimization over Continuous Spaces," *J. Glob. Optim.*, vol. 11, pp. 341–359, 1997.

[178] J. M. Raimond, M. Brune, and S. Haroche, "Colloquium: Manipulating quantum entanglement with atoms and photons in a cavity," *Rev. Mod. Phys.*, vol. 73, no. 3, pp. 565–582, 2001.

[179] S. Thiele, F. Balestro, R. Ballou, S. Klyatskaya, M. Ruben, and W. Wernsdorfer, "Electrically driven nuclear spin resonance in single-molecule magnets," *Science (80-.).*, vol. 344, no. 6188, pp. 1135–1138, 2014.

[180] D. D. Awschalom, L. C. Bassett, A. S. Dzurak, E. L. Hu, and J. R. Petta, "Quantum spintronics: Engineering and manipulating atom-like spins in semiconductors," 2013.

[181] S. P. Cottrell, S. F. Cox, J. S. Lord, and C. A. Scott, "Radio-frequency μSR experiments at the ISIS pulsed muon facility," *Appl. Magn. Reson.*, vol. 15, pp. 469–476, 1998.

[182] G. Lindblad, "On the Generators of Quantum Dynamical Semigroups," *Commun. Math. Phys.*, vol. 48, pp. 119–130, 1976.

[183] J. R. Johansson, P. D. Nation, and F. Nori, "QuTiP: An open-source Python framework for the dynamics of open quantum systems," *Comput. Phys. Commun.*, vol. 183, no. 8, pp. 1760–1772, 2012.

[184] J. R. Johansson, P. D. Nation, and F. Nori, "QuTiP 2: A Python framework for the dynamics of open quantum systems," *Comput. Phys. Commun.*, vol. 184, no. 4, pp. 1234–1240, 2013.

[185] A. D. O'Connell, M. Hofheinz, M. Ansmann, R. C. Bialczak, M. Lenander, E. Lucero, M. Neeley, D. Sank, H. Wang, M. Weides, J. Wenner, J. M. Martinis, and A. N. Cleland, "Quantum ground state and single-phonon control of a mechanical resonator," *Nature*, vol. 464, pp. 697–703, 2010.

[186] F. Bodoky, O. Gühne, and M. Blaauboer, "Modeling the decay of entanglement for electron spin qubits in quantum dots," *J. Phys. Condens. Matter*, vol. 21, no. 39, p. 395602, 2009.

[187] D. R. Harshman and M. Celio, "Positive muons in single crystal sodium fluoride: A simple spin system," *Hyperfine Interact.*, vol. 32, pp. 683–686, 1986.

[188] P. E. Hansen, T. Johansson, and R. Nevald, "Magnetic properties of lithium rare-earth fluorides: Ferromagnetism in $LiErF_4$ and $LiHoF_4$ and crystal-field parameters at the rare-earth and Li sites," *Phys. Rev. B*, vol. 12, no. 11, pp. 5315–5324, 1975.

[189] H. M. Rønnow, J. Jensen, R. Parthasarathy, G. Aeppli, T. F. Rosenbaum, D. F. McMorrow, and C. Kraemer, "Magnetic excitations near the quantum phase transition in the Ising ferromagnet $LiHoF_4$," *Phys. Rev. B - Condens. Matter Mater. Phys.*, vol. 75, no. 5, p. 054426, 2007.